NSF ATM-8814913

# Numerical and Observational Investigations of Long-lived, MCS-induced, Severe Surface Wind Events: The Derecho

by Jerome M. Schmidt



William R. Cotton, P.I.

Colorado State University

## DEPARTMENT OF ATMOSPHERIC SCIENCE



PAPER NO. 479

# NUMERICAL AND OBSERVATIONAL INVESTIGATIONS OF LONG-LIVED, MCS-INDUCED, SEVERE SURFACE WIND EVENTS: THE DERECHO

by

**Jerome M. Schmidt**

Department of Atmospheric Science

Colorado State University

Fort Collins, CO 80523

Research Supported by

**The National Science Foundation**

under grant ATM-8814913

March 27, 1991

Atmospheric Science Paper No. 479

ABSTRACT OF DISSERTATION

# NUMERICAL AND OSBERVATIONAL INVESTIGATIONS OF LONG-LIVED, MCS-INDUCED, SEVERE SURFACE WIND EVENTS: THE DERECHO

This study addresses the production of sustained, straight-line, severe surface winds associated with mesoscale convective systems (MCSs) of extratropical origin otherwise known as derechos. Derechos are particularly violent summertime systems capable of producing a swath of damaging outflow winds and/or severe wind gusts ($> 25$ m s$^{-1}$) having a major axis of at least 400 km in length. Climatological data compiled for several derechos in the United States have shown that they typically occur in the upper Midwest, have average propagation speeds of 24 m s$^{-1}$, average lifetimes of 9 hours, and typically form in environments characterized by strong static stability within the lowest few kilometers of the atmosphere.

In this dissertation the physical processes which govern the observed derecho characteristics are identified and their possible forcing mechanisms are determined. To address these problems, detailed observations of two derechos are presented along with simulations using the Colorado State University Regional Atmospheric Modeling System (CSU-RAMS). The observations revealed a derecho environment characterized by strong vertical wind shear through the depth of the troposphere and large values of convective available potential energy (CAPE). The thermodynamic environment of the troposphere in each case had a distinct three-layer structure consisting of: (i) a surface-based stable layer of 1-to-2 km in depth, (ii) an elevated well-mixed layer of 2-4 km in depth, and (iii) an upper tropospheric layer of intermediate stability that extended to the tropopause. Note that this profile is in stark contrast to the neutral subcloud layer which typifies the downburst

environment. This suggests that mechanisms other than strong penetrating downdrafts may be responsible for the severe surface winds.

Two primary sets of simulations were performed to assess the impact of the observed environmental profiles on the derecho structure, propagation, and longevity. The first set consisted of nested-grid regional-scale simulations initialized from the standard NMC analyses on a domain having relatively coarse horizontal resolution (75 km). These simulations were useful for identifying features of the regional-scale environment which affected the derecho longevity and track. They also provided further insight into the temporal and spatial characteristics of observed environmental features, such as the nocturnal low-level jet and static stability profiles.

The second set of simulations consisted of two and three-dimensional experiments initialized in a horizontally homogeneous environment having a relatively fine horizontal resolution (2 km) and explicit microphysics. These experiments were particularly useful for depicting the convective and meso$\beta$-scale (20-200 km) aspects of the simulated MCS which impacted the severe surface wind development, system longevity, and propagation characteristics. The results from these experiments indicate the importance of convectively-induced gravity waves on the MCS structure, propagation, longevity, and severe surface wind development. The sensitivity of the simulated convection and gravity waves to variations in the vertical wind shear and moisture profiles are described.

Finally, observations of derechos reveal their convective structure typically consists of bow echo squall lines. Detailed Doppler radar analyses and 3-D simulations of a severe, bow echo squall line are presented which reveal the unique 3-D circulation features which accompany these mesoscale convective systems. We will illustrate how the mesoscale and convective-scale flow fields within the bow echo establish the severe surface wind maximum which is often located within the vertex region of the bow echo.

Jerome M. Schmidt
Department of Atmospheric Science
Colorado State University
Fort Collins, Colorado 80523
Spring, 1991

## ACKNOWLEDGEMENTS

I would like to thank my advisor, Dr. William R. Cotton, for his support and guidance during this project. His openness to new ideas has been greatly appreciated. I would also like to thank my other committee members Dr. Richard Johnson, Dr. Graeme Stephens, and Dr. Viswanathan Bringi for useful discussions and comments which improved the text. I would also like to thank Dr. Craig Tremback and Dr. Robert Walko for their advice on using the CSU-RAMS and scientific discussions which clarified many aspects of the research. Conversations with Dr. James E. Bossert, Ray McAnelly, Dr. Melville Nicholls, Hahns Verlinde, and Mike Weissbluth had a valuable impact on the material presented in this dissertation. Special thanks to Piotr Flatau for many interesting discussions. I would also like to thank Dr. William Moninger and Dr. Joseph Kasper for their initial guidance.

I am greatly indebted to my family and in particular my wife, Sue Chen. Her support and patience made the pursuit of this degree possible.

Brenda Thompson is acknowledged for her patient and professional assistance. The figures were expertly drafted by Lucy McCall. This research was funded by the National Science Foundation under grant ATM-8814913. The computing was done of the National Center for Atmospheric Research's Cray-XMP computer. NCAR is supported by the National Science Foundation.

TABLE OF CONTENTS


**1 Introduction** 1

**2 Background** 4
2.1 Derecho characteristics . . . . . 4
2.1.1 Convective Structure . . . . . 12
2.2 Possible derecho forcing mechanisms . . . . . 12
2.2.1 Convective-scale downdraft structure . . . . . 15
2.2.2 Surface mesohigh structure . . . . . 21
2.2.3 Surface mesolow structure . . . . . 26
2.2.4 Meso$\beta$-scale (20-200km) gravity waves . . . . . 26
2.2.5 Severe meso$\beta$-scale wave events . . . . . 30
2.2.6 Forcing mechanisms for meso$\beta$-scale gravity waves . . . . . 34
2.2.7 Environmental factors affecting wave longevity . . . . . 34
2.2.8 Wave/convective interactions . . . . . 35
2.3 Summary . . . . . 37

**3 Experiment Strategy** 38
3.1 Observational data base . . . . . 38
3.2 Model description and experimental design . . . . . 41
3.2.1 Non-homogeneous experiments . . . . . 42
3.2.2 Description of the two-dimensional, horizontally homogeneous experiments . 43
3.2.3 3-D horizontally homogeneous experiments . . . . . 51

**4 Case studies** 54
4.1 The 12-13 May 1985 PRE-STORM derechos . . . . . 54
4.1.1 Severe surface wind characteristics . . . . . 54
4.1.2 Regional-scale environment . . . . . 55
4.1.3 Thermodynamic and vertical wind shear characteristics . . . . . 62
4.2 Numerical results from the 12-13 May derecho . . . . . 71
4.2.1 Low-level jet dynamics . . . . . 74
4.3 The 2-3 August 1981 CCOPE derecho . . . . . 90
4.3.1 System overview . . . . . 90
4.3.2 Environmental features of the 2-3 August 1981 derecho . . . . . 96
4.3.3 Regional-scale aspects of the 2-3 August derecho . . . . . 96
4.3.4 Evolutionary characteristics of the flow and thermodynamic fields . . . . . 108
4.3.5 Meso$\beta$-scale aspects of the CCOPE derecho . . . . . 108
4.4 Summary . . . . . 118

**5 2-D horizontally homogeneous explicit simulations** **122**
5.1 Idealized simulations in variable vertical wind shear . . . . . 122
5.2 Temporal evolution of the high shear case LS2 . . . . . 130
5.3 Surface wind dynamics . . . . . 133
5.3.1 Temporal evolution of the maximum surface wind gusts. . . . . 133
5.3.2 Surface outflow characteristics . . . . . 133
5.3.3 Role of the middle-level, rear-to-front jet . . . . . 145
5.4 Other sensitivity experiments . . . . . 148
5.5 Summary of the two-dimensional simulations . . . . . 150

**6 3-D homogeneous experiments** **153**
6.1 The unidirectional vertical wind shear experiment . . . . . 154
6.2 An experiment with a clockwise turning hodograph . . . . . 159
6.3 Summary . . . . . 173

**7 Summary and Conclusions** **174**
7.1 Regional-scale environmental structure and forcing mechanisms . . . . . 174
7.2 Results from the two-dimensional homogeneous experiments . . . . . 176
7.3 Results from the three-dimensional horizontally homogeneous experiments . . . 178
7.4 Conceptual Derecho Model . . . . . 180

**8 Suggestions for further research** **187**

LIST OF FIGURES


2.1 Area affected by widespread downburst activity during derecho occurrence of 19-20 July 1983. From Johns and Hirt (1987) . . . . . 6
2.2 Surface mesoanalysis for 0000 GMT 20 July 1983. From Johns and Hirt (1985) 7
2.3 Skew-T log-P plot of the 1200 GMT 19 July 1983, sounding at St. Cloud, Minnesota. From Johns and Hirt (1985). . . . . 8
2.4 The spatial distribution of summertime derechos occurring in the United States. From Johns and Hirt (1987) . . . . . 9
2.5 The distribution of derecho propagation speeds. From Johns and Hirt (1987) . 10
2.6 Idealized sketch of a middle-latitude, synoptic-scale situation especially favorable for development of severe thunderstorms. From Johns et al. (1990) . . 11
2.7 Schematic bow echo morphology and flow. From Fujita (1978) . . . . . 13
2.8 Detailed analysis of radar imagery from the NWS radar at Pittsburgh, PA. From Johns and Hirt 1987 . . . . . 14
2.9 Schematic of updraft, downdraft, and entrainment flows within a typical Cb. From Knupp and Cotton (1985) . . . . . 18
2.10 Doppler radar analyses of a low-level roll vortex. From Wakimoto (1982) . . . 19
2.11 Conceptual model illustrating the physical processes along mature downdraft flow branches. From Knupp (1988) . . . . . 20
2.12 Schematic of surface pressure field in a squall-line thunderstorm. From Fujita (1955) . . . . . 22
2.13 Schematic structure of the windshift-pressure jump and gust front associated with the 31 May 1969 squall line. From Charba (1974) . . . . . 23
2.14 High resolution numerical simulations of a density current. From Droegemeier and Wilhelmson (1987) . . . . . 25
2.15 A time plot of the maximum surface wind gusts within a high resolution simulation of a density current. From Droegemeier and Wilhelmson (1987) . . 27
2.16 Schematic illustrating the relationship between the radar reflectivity and surface pressure fields of a mid-latitude squall line. From Johnson and Hamilton (1988) . . . . . 28
2.17 Analysis of winds and pressure within a wake low. From Fujita (1955) . . . . . 29
2.18 Hourly movement of pressure pulsation 10-11 April 1944. From Brunk (1949) . 31
2.19 The synoptic setting of meso$\beta$-scale gravity wave events. From Uccellini and Koch (1987) . . . . . 33

3.1 Experimental setup of the CCOPE field program. . . . . 39
3.2 The May-June 1985 Oklahoma-Kansas PRE-STORM observational network . . 40
3.3 Skew-T log-P plot of the 2346 Knowlton sounding of 2 August 1981. . . . . 44
3.4 Environmental hodograph of the 2346 UTC 2 August Knowlton sounding . . . 46

3.5 Environmental sounding of temperature and dewpoint temperature of the presquall environment from the Powderville, Montana site at 0111 UTC 3 August 1981. 47
3.6 Vertical wind shear profiles used to initialize the 2-D homogeneous experiments. 48
3.7 Mean number of lid days for April-September 1983-1986. From Farrell and Carlson (1989) . . . . . 49
3.8 Vertical wind shear profiles used to initialize the 3-D horizontally homogeneous experiments . . . . . 52

4.1 Satellite perspective of the 12-13 May 1985 derechos . . . . . 56
4.1 Continued. . . . . 57
4.2 Standard NMC analyses of the 70 and 50 kPa constant pressure charts at 0000 and 1200 UTC 13 May 1985 . . . . . 58
4.2 Continued. . . . . 59
4.3 Standard surface analyses of the 12-13 May 1985 derecho . . . . . 60
4.3 Continued. . . . . 61
4.4 Skew-T log-P plots from Pratt, Kansas . . . . . 63
4.5 Skew-T log-P plot from CSM . . . . . 64
4.6 Vertical profiles of the $v$-component of flow from Pratt, Kansas on 13 May 1985 65
4.7 Vertical profiles of the $u$-component of flow from Pratt, Kansas on 13 May 1985 66
4.8 Vertical cross-section of the warm frontal zone at 0600 UTC 13 May 1985 . . . 68
4.9 Skew-T log-P plot of the 0903 UTC 13 May 1985 sounding from CNU. . . . . 69
4.10 Time plots of surface temperature, pressure, and winds from the PAM stations P03 and P24 . . . . . 70
4.11 Vertical profiles of $\theta_e$ near 0700 UTC 13 May 1985 . . . . . 72
4.12 Model generated horizontal flow vectors on the coarse grid at the 2.5 and 5 km levels . . . . . 73
4.13 Model generated horizontal flow vectors and perturbation Exner function ($\pi'$) on the fine grid . . . . . 75
4.13 Continued. . . . . 76
4.14 Vertical $x$-$z$ cross-section of the model generated $v$-component of flow showing the southerly low-level jet . . . . . 77
4.14 Continued. . . . . 78
4.15 Vertical $y$-$z$ cross-section of the model generated $v$-component of flow showing the north-south structure of the low-level southerly jet. . . . . 79
4.15 Continued. . . . . 80
4.16 Vertical $x$-$z$ cross-section of the model generated $u$-component of flow showing the development of the easterly low-level jet . . . . . 81
4.16 Continued. . . . . 82
4.17 Vertical $y$-$z$ cross-sections of the model generated $u$-component of flow showing horizontal extent of the easterly low-level jet . . . . . 83
4.17 Continued. . . . . 84
4.18 Vertical $x$-$z$ cross-sections of the model generated potential temperature ($\theta$) surfaces . . . . . 86
4.18 Continued. . . . . 87
4.19 Schmatic representation of the warm and cold conveyor belt circulations adapted from Carlson 1981. From Cotton (1990). . . . . 88

4.20 Vertical $x$-$z$ cross-sections of the model generated perturbation Exner function ($\pi'$) and its relationship to the southerly low-level jet. . . . . 91
4.20 Continued. . . . . 92
4.21 Surface synoptic surface conditions at 0300 UTC 3 August 1981. . . . . 93
4.22 Low-elevation radar PPI from Huron, South Dakota at 0900 UTC 3 August 1981 showing radar reflectivity structure of the bow echo squall line . . . . 94
4.23 Infrared satellite imagery depicting the growth of the MCC. . . . . 95
4.24 The 0000 UTC 3 August 1981 50 and 70 kPa height and temperature analyses. From Cotton et al. (1984). . . . . 97
4.25 Vertical east-west cross-section of the model generated potential temperature and vertical motion at 0000 UTC 3 August 1981 depicting the relationship between the MCC and eastward advecting mountain-plains solenoid. From Tremback (1990). . . . . 99
4.26 Vertical east-west cross-section of the model generated potential temperature and vertical motion at 0800 UTC 3 August 1981 depicting the relationship between the MCC and eastward advecting mountain-plains solenoid. From Tremback (1990). . . . . 100
4.27 Vertical east-west cross-section of the model generated potential temperature and vertical motion at 1200 UTC 3 August 1981 depicting the relationship between the MCC and eastward advecting mountain-plains solenoid. From Tremback (1990) . . . . . 101
4.28 Low-level model generated horizontal flow vectors and perturbation Exner function ($\pi'$) . . . . . 102
4.28 Continued. . . . . 103
4.29 Vertical $x$-$z$ cross-sections through the model generated surface low pressure at 0600 UTC 3 August 1981. . . . . 104
4.29 Continued. . . . . 105
4.30 Vertical $x$-$z$ cross-sections through the model generated surface low pressure at 1200 UTC 3 August 1981. . . . . 106
4.30 Continued. . . . . 107
4.31 Time plots of surface wind speed from the CCOPE PROBE station MOS . . . 110
4.32 Illustration of the relationship between the CP-2 radar echo and the surface wind field at 0009 UTC on 2 August 1981 for system A. From Wade (1982). 111
4.33 Horizontal mid-level radar reflectivity cross-sections at 0300 UTC 3 August 1981 obtained from the SKWR 5 cm radar . . . . . 112
4.34 Objectively analyzed surface parameters derived from the CCOPE mesonet at 0305 UTC 3 August 1981. . . . . 113
4.34 Continued. . . . . 114
4.35 Storm kinematic fields derived from a multiple Doppler radar analysis of the CCOPE bow echo at 0303 UTC 3 August 1981. . . . . 116
4.35 Continued. . . . . 117
4.36 Air parcel trajectory released near the primary downdraft on the northern flank of G1. . . . . 119
4.37 Schematic thermodynamic and vertical wind shear profiles summarizing the primary features of the 12-13 May 1985 and 2-3 August 1981 derechos. . . . 120

5.1 Vertical $x$-$z$ cross-sections of experiment S0 at 3600 s showing the perturbation flow, Exner function, and thermodynamic fields . . . . . 125

5.2 Vertical $x$-$z$ cross-sections of experiment S1 at 3600 s showing the perturbation flow, Exner function, and thermodynamic fields . . . 126
5.3 Vertical $x$-$z$ cross-sections of experiment S2 at 7200 s showing the perturbation flow, Exner function, and thermodynamic fields . . . 127
5.4 Vertical $x$-$z$ cross-sections of experiment S3 at 5400 s showing the perturbation flow, Exner function, and thermodynamic fields . . . 128
5.5 Vertical $x$-$z$ cross-sections of experiment LS2 at 18000 s showing the perturbation flow, Exner function, and thermodynamic fields. . . . 131
5.5 Continued. . . . 132
5.6 Time series of the maximum surface wind gusts the two-dimensional simulations listed in Table 3.1. . . . 134
5.7 Vertical $x$-$z$ cross-sections of experiment LNU at 18000 s showing the perturbation flow, Exner function, and thermodynamic fields . . . 136
5.7 Continued. . . . 137
5.8 Windowed in view of the convective region of experiment LNU at 18000 s showing the perturbation flow, Exner function, and thermodynamic fields . 139
5.8 Continued. . . . 140
5.9 Windowed in view of the convective region of experiment LS2 at 18000 s showing the perturbation flow, Exner function, and thermodynamic fields . . . . 141
5.9 Continued. . . . 142
5.10 Breakdown of total perturbation Exner function into the hydrostatic and non-hydrostatic components . . . 143
5.10 Continued. . . . 144
5.11 Conceptual model showing the interaction between the vertical wind shear and the storm induced buoyancy fields . . . 147
5.12 Jet structure produced by a two-dimensional vorticity model. From Weisman (1990) . . . 149

6.1 Horizontal $x$-$y$ cross-sections of the near surface (z= 146 m) model generated storm-relative flow showing bow echo development in unidirectional shear . 155
6.1 Continued. . . . 156
6.2 Horizontal $x$-$y$ cross-sections of the middle-level model generated storm-relative flow vectors and perturbation Exner function ($\pi'$) showing bow echo development in unidirectional vertical wind shear. . . . 157
6.2 Continued. . . . 158
6.3 Vertical $x$-$z$ cross-sections of the unidirectional experiment at 10800 s taken through the vertex region of the bow echo . . . 160
6.3 Continued. . . . 161
6.4 Horizontal $x$-$y$ cross-sections of the near surface (z= 146 m) model generated flow fields for the curved hodograph experiment at 10800 s. . . . 162
6.4 Continued. . . . 163
6.5 Horizontal $x$-$y$ cross-sections of the middle-level model generated flow fields for the curved hodograph experiment at 10800 s. . . . 165
6.5 Continued. . . . 166
6.6 Vertical $x$-$z$ cross-sections of the model generated flow fields for the curved hodograph experiment at 10800 s taken through the vertex region of the bow echo . . . 167

6.6 Continued. . . . . 168
6.6 Continued. . . . . 169
6.7 Vertical $y$-$z$ cross-sections of the model generated flow fields for the curved hodograph experiment at 10800 s taken along the convective line . . . . . 170
6.7 Continued. . . . . 171
6.7 Continued. . . . . 172

7.1 Conceptual diagram illustrating the primary two-dimensional features of the simulated MCS structure derived from the idealized three-layered thermodynamic and strong vertical wind shear profiles. . . . . 182
7.2 Schematic flow structure of the 2 August 1981 CCOPE bow echo squall line showing a planar view of the storm . . . . . 184
7.3 Three-dimensional schematic depiction summarizing the 3-D flow features of the 2 August, 1981 CCOPE squall line. . . . . 185

LIST OF TABLES

2.1 Severe Meso-$\beta$-scale gravity wave events. Data compiled from Table 1 of Uccelini and Koch (1987) and from author's own research. . . . . 32

3.1 Experiment Design . . . . . 50

# Chapter 1

## INTRODUCTION

The association between propagating extratropical mesoscale convective systems and the occurrence of non-tornadic but otherwise severe "straight-line" surface outflows (gusts $> 25$ m $s^{-1}$) have been known since the time of Hinrichs (1888) who termed such systems derechos (a Spanish derivative meaning "straight-ahead"). More recent studies of derechos have shown them to be particularly violent mesoscale convective systems capable of producing swaths of severe surface wind gusts and/or property damage exceeding 400 km in length (Johns and Hirt 1987). Each year in the United States, derechos inflict millions of dollars in property damage and occasional loss of life, yet little is known of their structure or of the physical mechanisms governing their longevity and/or ability to produce sustained severe surface winds.

The purpose of this dissertation is to attempt to gain a better understanding of the environmental setting and possible physical processes governing the development, longevity, and propagation of derecho-type MCSs. Use is made of both relevant observationally-derived case studies and numerical simulations employing the Colorado State University Regional Atmospheric Modeling System (CSU-RAMS). Particular emphasis is placed on derechos which form in environments characterized by strong low-level static stability. This choice is based on the climatology of Johns and Hirt (1987) which showed that a significant percentage of derechos (90% of the derechos in their sample) initiate on the cold side of synoptic-scale frontal boundaries. The central question to be addressed then becomes one of how storms overriding a deep surface-based stable layer, a thermodynamic condition which inhibits the penetration of middle-level convective-scale downdrafts into the subcloud layer, are able to produce damaging surface outflow for extended periods of time. The emphasis of this study thus differs from previous numerical studies of severe convection which are

typically initialized with near neutral static stability near the surface. Nevertheless, we will show that the lower stable layer, particularly when capped by an elevated well-mixed layer, has many interesting affects on the evolution of the flow field within the simulated MCS which lead to both long-lived systems and systems which readily produce severe surface winds.

Two aspects of derechos which make them particularly challenging to study in complete detail, either observationally or numerically, is their longevity and speed ( 9 hours and 24 m $s^{-1}$, respectively [Johns and Hirt 1987]). Since data networks are typically limited in areal extent and 3-D simulations quickly become cost prohibitive, such length and time scales dictate choices which must be made to accommodate both realistic model design and feasibility. With this in mind the basic goals of this observational and numerical study are as follows: (i) to identify significant features of the regional-scale environment which may impact the derecho development and longevity in each case study, and (ii) to investigate the convective-scale and meso$\beta$-scale (20-200 km) circulations of the observed and simulated MCS which may have further contributed to the strength of the surface outflow and system longevity. The first goal is accomplished by supplementing detailed observations of the two case studies with regional-scale simulations having a relatively coarse horizontal resolution (75 km) and which are initialized from the standard NMC analyses of each case day. The second goal is accomplished by supplementing detailed surface and Doppler observations of the MCS described by Schmidt and Cotton (1989) with simulations initialized in either a two or three-dimensional, horizontally homogeneous environment having relatively fine horizontal resolution (2 km) and explicit microphysics. By presenting both regional and mesoscale simulations, this dissertation represents one of the initial attempts to address the wide range of space and time scales which characterize derecho-type events.

The material presented in this dissertation will adhere to the following basic outline. Chapter 2 will review the derecho characteristics as outlined by Johns and Hirt (1987) and present a review of possible derecho forcing mechanisms. Chapter 3 contains a description of the data sets used in the analyses, a description of the CSU-RAMS, and an outline of the experimental strategy. In chapter 4 we introduce the observational case studies and present the results from the regional-scale simulations. Significant findings here include the

first ever Doppler radar derived flow fields of a meso-$\beta$-scale bow echo squall line, and the first regional-scale observational and numerical analyses of a derecho event. We then turn to the two and three dimensional explicit simulations in Chapters 5 and 6, respectively. These chapters will illustrate, in detail not presented in previous studies, the role of vertical wind shear, gravity waves, and the thermodynamic structure of the observed cases on the evolution and character of the internal flow structure of the simulated MCS and surface flow fields. We stress the role of a surface-based stable layer on the severe surface wind development and system maintenance in a way not previously described. We also present a unique description of the middle-level rear-to-front jet development typically associated with squall line type MCSs in terms of gravity wave dynamics and the possible relationship of the jet magnitude to the thermodynamic and vertical wind shear profiles of the ambient environment. The primary conclusions and a schematic derecho model are presented in Chapter 7. The recommendations for further research are presented in Chapter 8.

# Chapter 2

# BACKGROUND

To provide the reader with a background of derecho type systems, we review the derecho case study presented by Johns and Hirt (1985) and present highlights of their derecho climatological study which most clearly distinguish derecho characteristics from other types of MCSs (section 2.1). This is followed by a more general review of MCS circulation features which may impact the development of severe surface winds, such as convective-scale downdrafts, meso$\beta$-scale surface pressure fields, and meso$\beta$-scale gravity waves (section 2.2). A summary of the primary derecho features and possible forcing mechanisms may be found in section 2.3.

## 2.1 Derecho characteristics

A mesoscale analyses of a typical derecho event is illustrated in Figs 2.1- 2.3. The derecho produced a swath damaging surface winds (in excess of 25 m $s^{-1}$) from northwest North Dakota to southwestern Michigan (Fig 2.1) as it tracked rapidly southeastward at 23 m $s^{-1}$ along and to the north of a quasi-stationary surface front during its 15 hour life span (Fig 2.2). Vertical soundings of the wind and temperature taken in the pre-derecho environment north of the frontal zone (at St. Cloud Minnesota) revealed an environment characterized by strong vertical wind shear through the depth of the troposphere (winds were nearly calm at the surface and greater than 40 m $s^{-1}$ at 20 kPa) and large values of convective available potential energy (CAPE)[Fig 2.3]. Note the three layer thermodynamic structure within the troposphere consisting of: (i) a lower layer of moist but statically stable air from the surface to 80 kPa exhibiting a nearly isothermal temperature profile, (ii) a deep neutral layer from 80 to 50 kPa, and (iii) an upper tropospheric layer of intermediate stability which extended to the tropopause. Similar profiles were evident at other stations

north of the frontal zone (not shown) resulting in a large region of lifted indices in excess of -12 in the derecho environment.

The above example illustrates many of the characteristic features noted for a number of summertime derechos (May-August) studied by Johns and Hirt (1987). A summary of their work, presented in Figs 2.4 and 2.5, reveals a frequency maximum of derecho occurrence within the upper midwest[1] (Fig 2.4), an average propagation speed of 24 m $s^{-1}$ (Fig 2.5), and an average duration of nine hours. Over 90% of the derechos were found to initiate along, or to the cold side of, synoptic scale frontal boundaries. Despite the low-level static stability which may exist in such cases, average lifted indices of -9 were common in the derecho environment. This strongly suggests that an elevated well mixed layer, such as in Fig 2.3, may be present in many of these systems.

Johns et al. (1990) have shown that the vertical wind shear profile in the derecho environment have many distinct differences from the classic severe storm pattern (Fig 2.6). The winds in the derecho environment are typically light and variable at the surface reflecting the fact that many of these systems occur at night when the flow is decoupled from the surface. As in the classic severe weather pattern, the flow aloft in the derecho genesis region is characterized by significant veering of the winds with height and strong low-level warm air advection. They note, however, that the derechos do not appear to occur in the region of intersection between the upper and lower-level jets. Further, they showed that as the derecho progresses toward the upper level ridge, little if any directional shear is present within the lower to middle-troposphere (70 to 50 kPa layer). Above 50 kPa, the thermal wind vector appears to have a large variance from case to case (Dr. Robert Maddox, personal communication) suggesting that the lower-to-middle level unidirectional flow is perhaps the most characteristic signature of the wind in the derecho environment.

---

[1]Since the climatology covers the three month period between June and August, the observed maximum in the upper midwest may be biased by the normal tendency of the severe weather events to occur farther northward during the summertime.

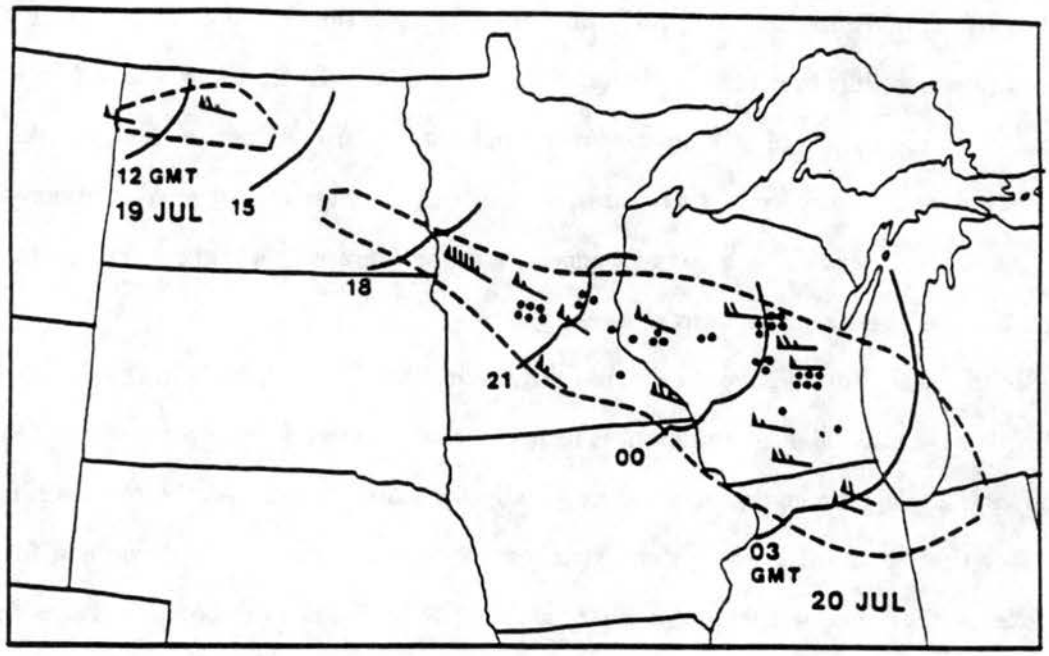


Figure 2.1: Area affected by widespread downburst activity during derecho occurrence of 19-20 July 1983 (bounded by dashed line). Surface wind gusts indicated by wind flag = 50 kt, full barb = 10 kt, half barb = 5 kt. Dots represent personal injuries. Three-hourly squall front positions indicated in Greenwich Mean Time (GMT). From Johns and Hirt (1985).

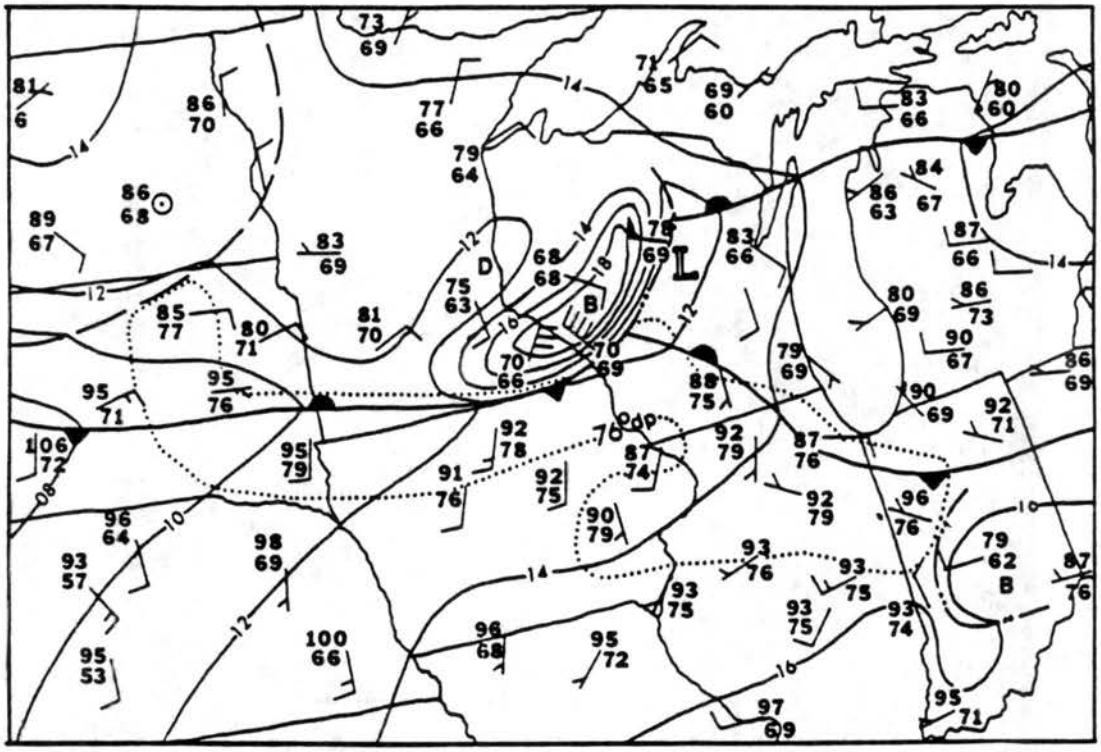


Figure 2.2: Surface mesoanalysis for 0000 GMT 20 July 1983. Isobars in millibars with first two digits omitted. Wind in knots (gust values plotted when applicable). Temperatures and dew points in deg. Fahrenheit. From Johns and Hirt (1985).

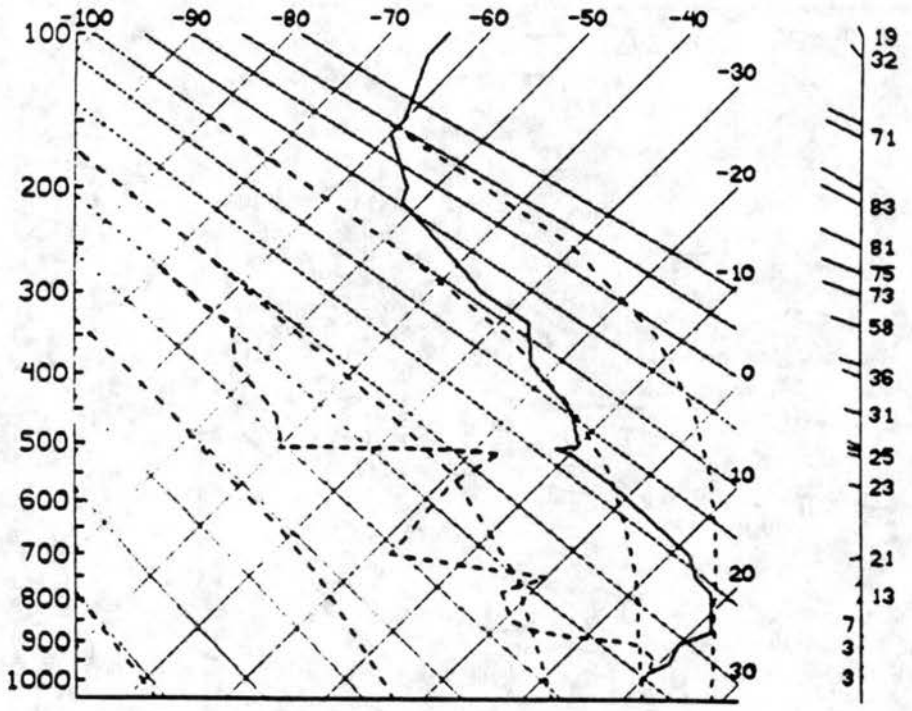


Figure 2.3: Skew-T log-P plot of the 1200 GMT 19 July 1983, sounding at St. Cloud, Minnesota. Temperatures and dew points in C°. Heights in millibars. Wind direction rose and speeds (kt.) on right. From Johns and Hirt (1985).

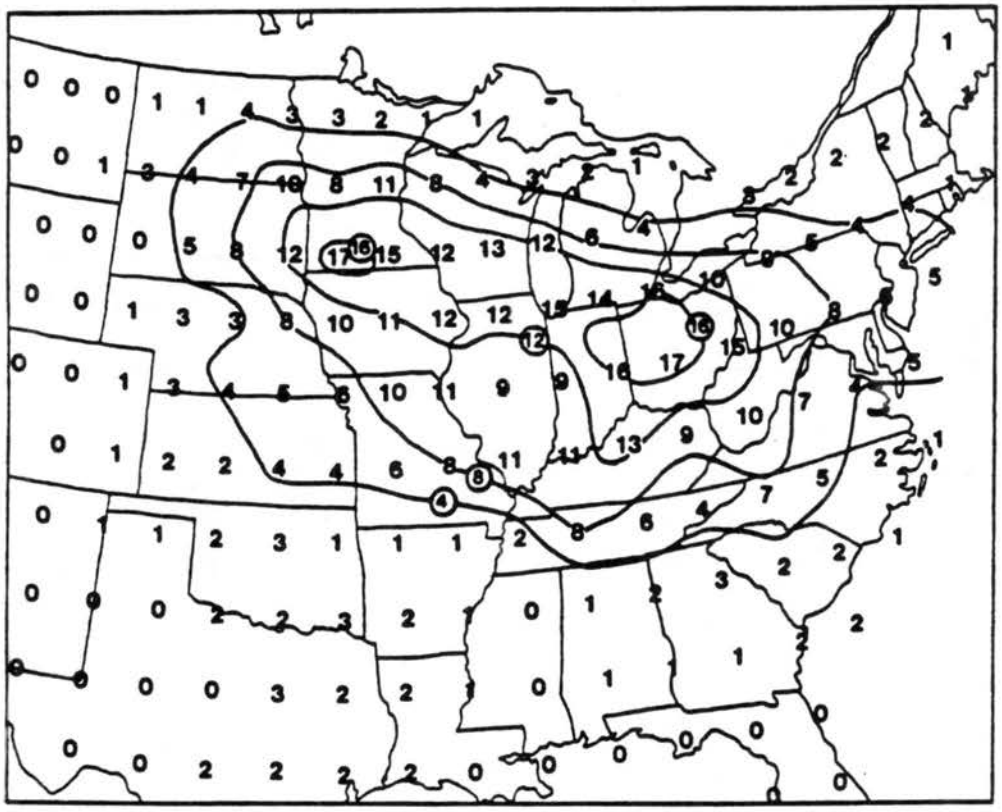

Figure 2.4: Total number of derechos occurring in 2° lat by 2° long squares during the months of May through August for the period 1980-1983. From Johns and Hirt (1987).

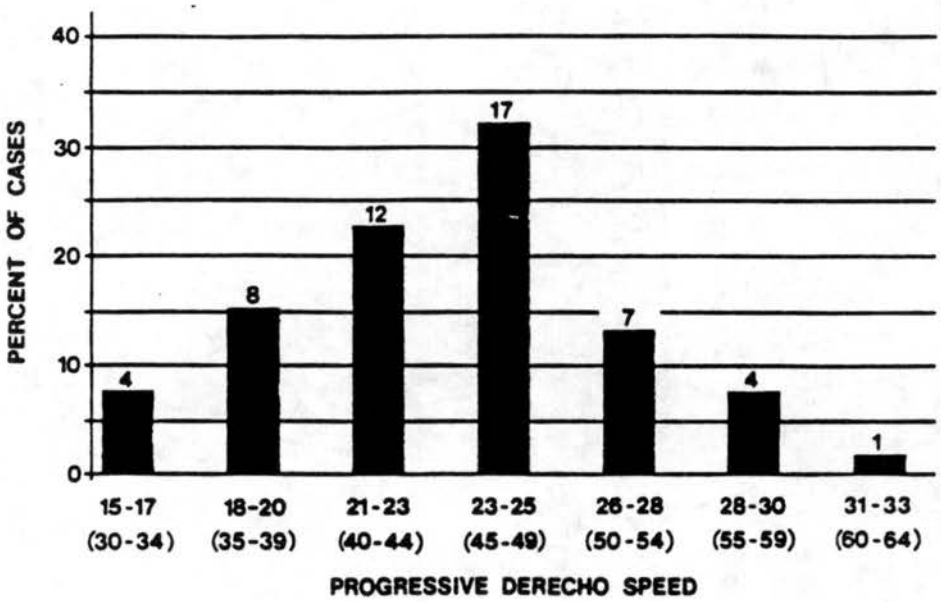


Figure 2.5: Frequency distribution of the speeds of progressive derechos (53 cases). Speeds in m $s^{-1}$ with kt in parentheses. Total number of cases in each speed category indicated above bar. From Johns and Hirt (1987).

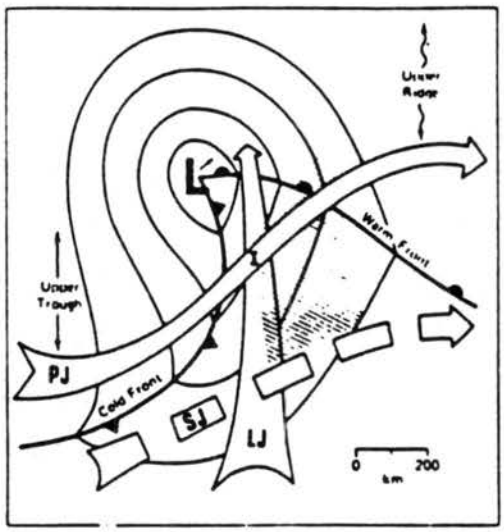


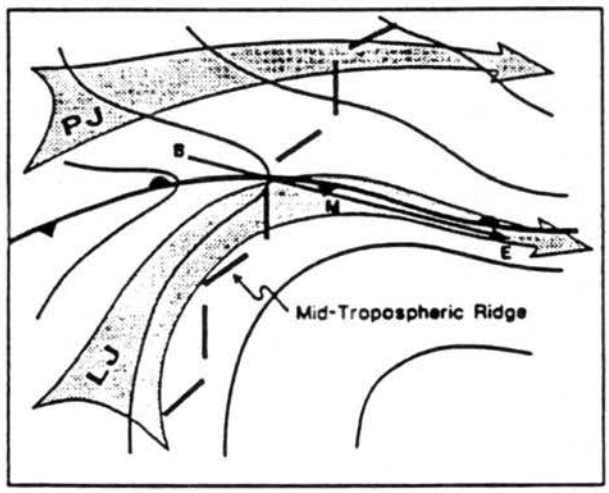


Figure 2.6: Idealized sketch of a middle-latitude, synoptic-scale situation especially favorable for development of severe thunderstorms. Thin lines denote sea-level isobars around a low-pressure center with cold and warm fronts. Broad arrows represent low-level jet stream (LS), polar jet (PJ) in upper troposphere, and subtropical jet (SJ) at a somewhat higher level in the upper troposphere [after Barnes and Newton (1985)]. (b) Similar sketch for the composite large-scale pattern associated with long-lived derechos. Note that damage axis B-E is 750 nm (approximately 1400 km in length!). Both Figs. from Johns et al. (1990).

### 2.1.1 Convective Structure

The MCS structure accompanying the derecho is, to date, one of the least known features of these systems. This may reflect the rapid propagation speed of the accompanying MCSs which would make it difficult for ground based sensors to sample the entire evolution of the meso$\beta$-scale components. Since the derecho frequency at a given location is also relatively low, only a few have been sampled in observational field experiments. By using satellite imagery, Johns and Hirt (1987) determined that the convective organization of the derechos in their sample divided equally between squall lines, nonlinearly organized MCSs, and MCCs. The large number of MCCs in the derecho climatology (approximately 1/3 of the 70 cases) was surprising given the results of Cunning (1986) which showed that the severe weather associated with MCCs generally occur early in the lifecycle of the MCC.

The few known examples of the radar-derived convective structure suggest that bow echo squall lines (Fujita 1978) may be an integral component of derecho systems. This is suggested by the isochrones analyses denoting the leading edge of the radar reflectivity echo in Fig 2.1 and by a few other documented cases (Przybylinski and DeCaire 1985; Johns and Hirt 1987). While the bow echo is thought to derive its shape from convective-scale downburst activity (Fujita 1978, Fig 2.7), radar depictions of bow echoes whose along-line dimension is in excess of 80 km (Fig 2.8) suggest that organization on the mesoscale may also be important for these structures. Recent studies by Schmidt and Cotton (1989) and Weisman (1990) suggest that the bow echo is a distinctly three-dimensional meso$\beta$-scale system which has an enhanced middle-level rear-to-front flow situated between anticyclonically and cyclonically rotating middle-level vortices. These vortices force the middle-level rear-to-front jet locally near the vertex of the bow echo, a region where the severe surface winds are often observed (Fujita 1978). We will demonstrate later how the the organization of the middle and upper level flow within bow echo MCSs play an important role on the development of severe surface winds within the vertex region of the bow echo.

## 2.2 Possible derecho forcing mechanisms

Though derechos are capable of sustaining severe surface winds for several hours and, consequently, inflicting millions of dollars in property damage each year, there is very little

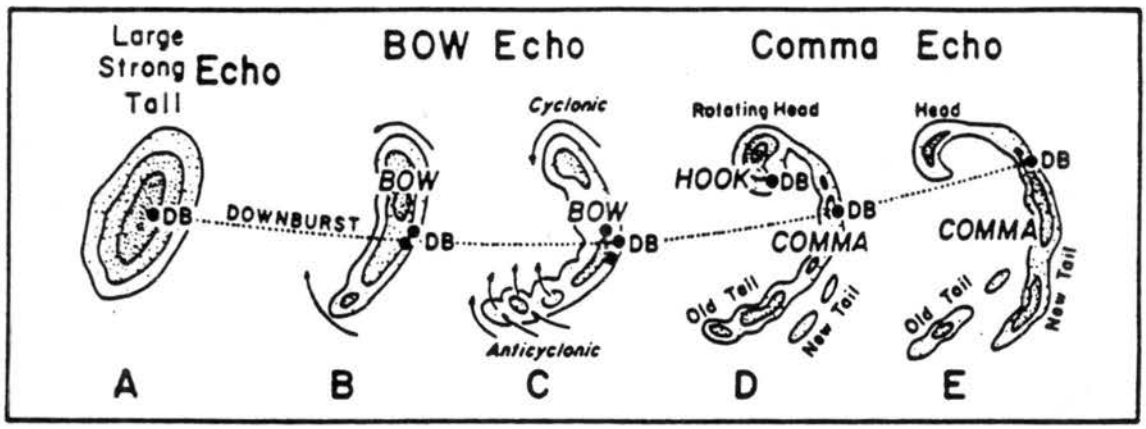


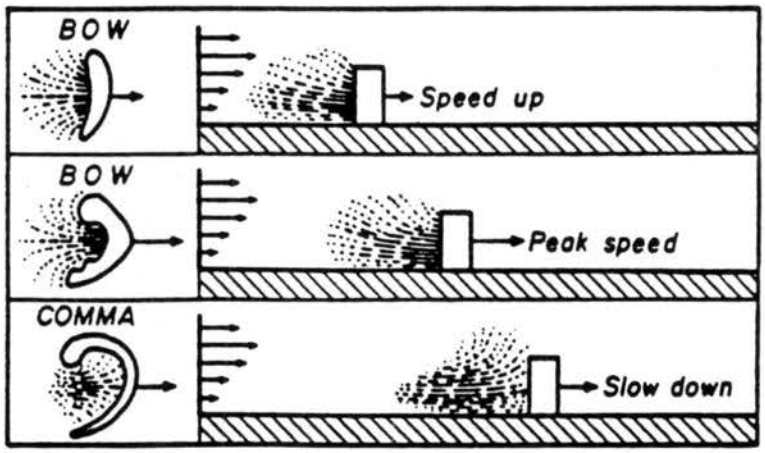


Figure 2.7: A typical morphology of radar echoes associated with strong and extensive downbursts. Some bow echoes disintegrate before turning into comma echoes. During the period of strongest downbursts, the echo often takes the shape of a spearhead or a kink pointing along the direction of motion (top panel). A conceptual model of a wake flow behind a bow echo that evolves into a comma echo (bottom panel). Both panels from Fujita (1978).

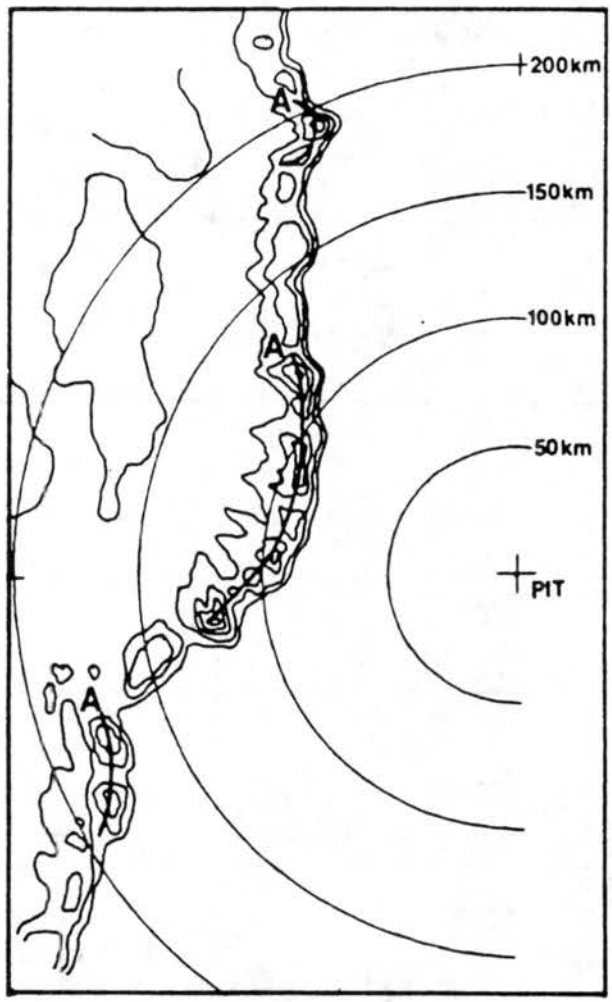


Figure 2.8: Detailed analysis of radar imagery from the NWS radar at Pittsburgh, PA, for 2210 UTC 4 July 1983. A serial derecho is in progress. The contours represent video integrator and processor intensity (VIP) levels with the outside contour indicating VIP level 1, and interior contours generally representing successively higher VIP levels. The dark solid lines marked with an "A" connect the higher VIP levels and represent bow echoes. A well-defined crest of a LEWP is evident at the north end of the southern bow (near the lowest A). (This detailed analysis was prepared by Ron Przybylinski of WSFO Indianapolis). From Johns and Hirt (1987).

known of their governing dynamics. It is apparent that any successful explanation of these systems must account for both the the longevity of the parent MCS and the mechanisms acting within the MCS to produce the sustained severe surface winds. With these two primary objectives in mind, we begin a general review of the possible forcing mechanisms for convectively-induced severe surface winds. The discussion first focuses on the structure of the convective-scale updraft and downdraft and their impact on the surface flow and pressure fields that develop beneath maturing storm cells. We then work upscale to review the structure and dynamics of the surface meso-$\beta$-scale pressure fields which typically accompanying more mature MCSs and the impact these pressure fields have on the longevity of the MCS and the surface flow fields. Finally we address a different type of surface pressure perturbation which may also accompany severe MCS development, namely, meso-$\beta$-scale gravity waves. Such waves have been implicated in a number of severe surface wind events and may, therefore, play an important role in the derecho development.

### 2.2.1 Convective-scale downdraft structure

In their initial study of derechos, Johns and Hirt (1987) suggested that exceptionally strong convective-scale downdrafts were most likely responsible for producing the swath of damaging winds which accompany derecho systems. Of the many types of downdrafts which occur in the vicinity of convective storms, the most likely candidate to initiate severe surface winds is what Knupp and Cotton (1985) referred to as the low-level precipitation downdraft (labeled PR in Fig 2.9). Such a downdraft may modify the subcloud layer in two important ways in terms of its affect on the surface flow: (i) through a downward momentum transport, or (ii) through a downward transport of lower-valued, middle-tropospheric, equivalent potential temperature ($\theta_e$). Both processes affect the structure and magnitude of the surface pressure fields which in turn drive the surface outflow and generate fields of low-level convergence which affect storm regeneration and/or maintenance.

The structure and magnitude of the PR downdraft and its impact on the subcloud momentum and thermodynamic fields is determined by a number of factors such as storm type, precipitation characteristics, downdraft maturity, and subcloud thermodynamic structure. For a detailed review of how these downdraft controls operate the reader is referred

to Knupp and Cotton (1985). Our interest for the present discussion lies in the structure and dynamics of the two primary flow branches (labeled a and b) entering the mature PR downdraft depicted in Fig 2.9. These flow branches, though shown merging into one common downdraft region, have significantly different source regions, governing dynamics, and evolutionary characteristics. The middle-level trajectory (labeled b) originates above cloud base at a level near the top of the well-mixed layer [referred to as the transition level by Knupp (1988)] and is primarily a buoyancy-driven downdraft. In isolated congestus towers, these trajectories are prevalent during the initial stages of the downdraft development and reflect the initial development of negative bouyancy forces above cloud base resulting from precipitation loading, melting, and evaporation.

The magnitude of the bouyancy-driven downdrafts below cloud base appears to be strongly governed by the ambient thermodynamic static stability profile within the subcloud layer, the precipitation characteristics of the parent cloud, and the type and maturity of the convective system. Small precipitation particles and nearly dry adiabatic lapse rates below cloud base have been noted to exert a strong control on producing downbursts in isolated convective towers (Kamburova and Ludlam 1966; Srivastava 1987; Knupp 1988). These locally intense downdrafts are well known for their ability to produce damaging surface wind gusts (Fujita and Wakimoto 1981). The strong surface winds appear to result from divergent outflow from a locally intense surface high pressure zone generated as the downburst impacts the ground (Proctor 1989). In some situations the surface winds within the outflow are locally enhanced as a result of a rotor circulation which develops near the leading edge of the outward flowing air (Wakimoto 1982) [Fig 2.10]. Since these are rather transient phenomenon (by definition lasting less than 6 minutes [Fujita and Byers 1977]), repeated downburst formation would be required to produce a derecho lasting on the order of nine hours. Since one expects the subcloud layer to stabilize with time, particularly if the storms develop in the late afternoon, this type of downdraft may serve as an effective wind producer perhaps only during a limited time near the initial stages of derecho development.

Downdraft parcels which originate near the surface, such as the "up-down" downdraft (labeled a in Fig 2.9), on the other hand, may be a persistent circulation feature of the maturing storm. Knupp (1988) has found that as the subcloud layer stabilizes (a possible result

of surface radiational cooling, downshear precipitation, or previous convection), the mass flux into the precipitation downdraft is increasingly dominated by the "up-down" downdraft circulation. The "up-down" downdraft trajectories originate near the surface within the low-level updraft. Since such parcels are often negatively buoyant (Marwitz 1973), an upward-directed pressure gradient force is needed to generate the initial lift (Fig 2.11). As the parcels are swept upward into the storm, increased water loading, melting, and evaporation generate additional negative bouyancy, thus slowing the parcel's upward progress and ultimately initiating the downdraft portion of the circulation. Since the parcel's horizontal momentum is partially conserved within the updraft, they are eventually displaced from the region of forced uplift and are then free to rapidly descend toward the surface. This may be an effective mechanism to generate sustained strong surface outflows in situations where strong static stability is present in the low-level ambient environment.

The vertical pressure gradient required to lift the parcels along the upbranch of the "up-down" downdraft is easily established along the leading edge of many convective systems due to the surface mesohigh and the middle-level mesolow located beneath the primary updraft. These pressure fields may result from either hydrostatic affects (LeMone et al. 1984) or through nonhydrostatic affects associated with the rotation, curvature, and shearing of the flow near the updraft (Weisman and Klemp 1984). The Weisman and Klemp (1984) study suggested that the middle-level, dynamically-induced low pressure contributed to nearly 60% of the updraft strength on the right flank of a simulated supercell. Clearly, the ability of these systems to draw up the lower level air may have important consequences for potentially strong downdraft development, particularly as the lower levels become increasingly stable.

Dynamic forcing within supercells, resulting from differential rotation in the low-to-middle levels of the storm, may also force a strong low-level downdraft termed the occlusion downdraft (Weisman and Klemp 1984). Due to the strong dynamical forcing, these downdrafts are likely to reach downburst intensity irregardless of the underlying low level static stability. This example illustrates the complex interactions and feed back mechanisms which can occur between the storm type and the resulting downdraft magnitude and structure. In the supercell, the local cooling associated with the downdraft provides a source of horizontal vorticity which may then be tilted into the vertical and stretched in the primary updraft.

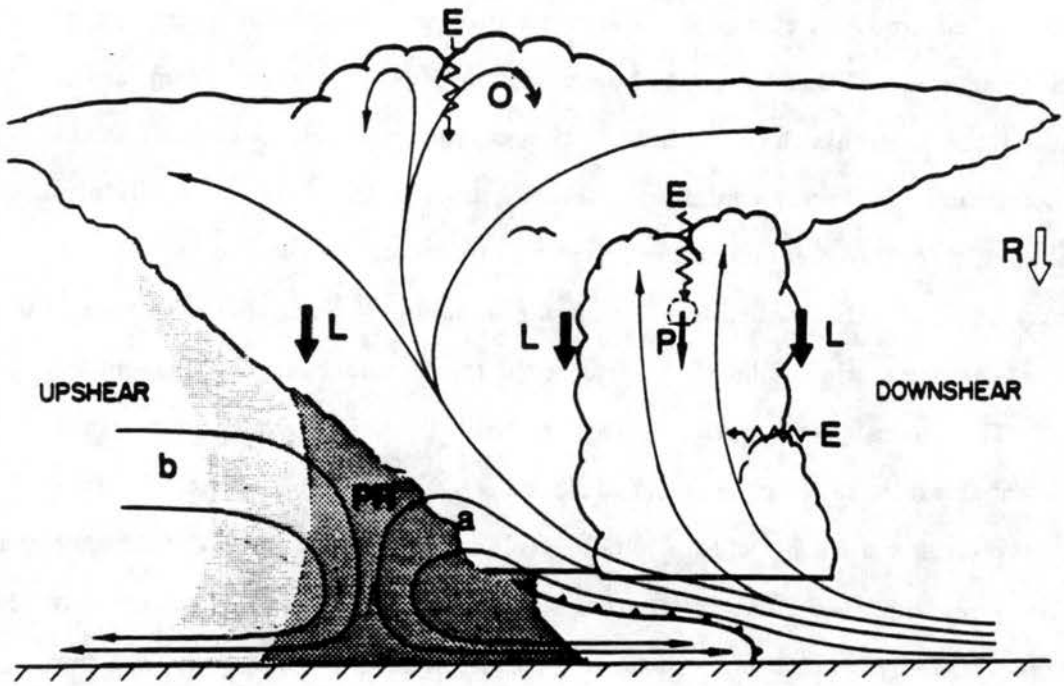


Figure 2.9: Schematic of updraft, downdraft, and entrainment flows within a typical Cb based on a composite of observational studies, numerical model studies, and research by the authors. All flows are storm relative. E denotes entrainment. Other symbols label downdraft circulations which are defined in Table 1 of Knupp and Cotton (1985). From Knupp and Cotton (1985).

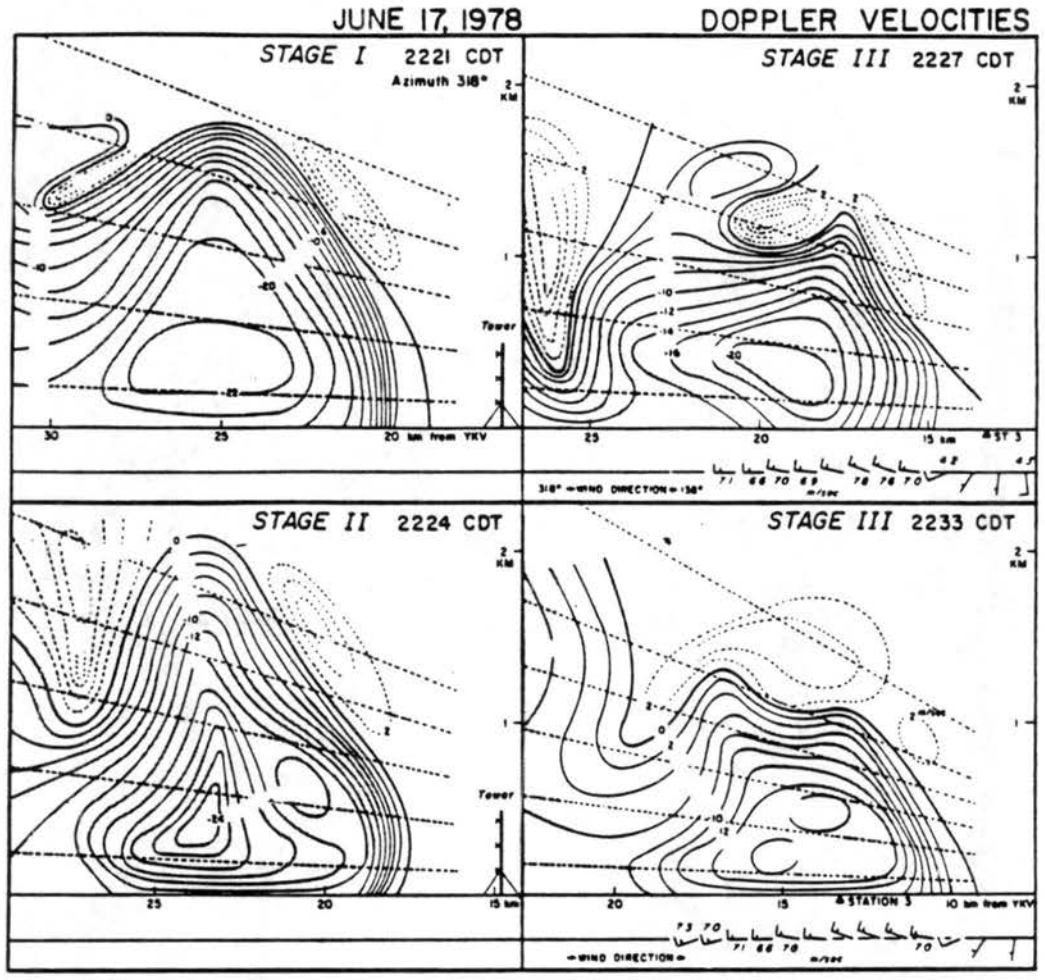


Figure 2.10: RHI cross sections of Case C at 2221 (stage I), 2224 (stage II), 2227 (stage III) and 2233 (stage III) CDT. Dashed lines are Doppler velocities away from the radar and solid lines are velocities toward the radar. Gray areas have $> 10$ dB(Z) reflectivity. Distances are measured from YKV. Surface data are obtained from station 3. Located in the lower right hand corner of the 2221 and 2224 CDT analyses is a 500 m tower. From Wakimoto (1982).

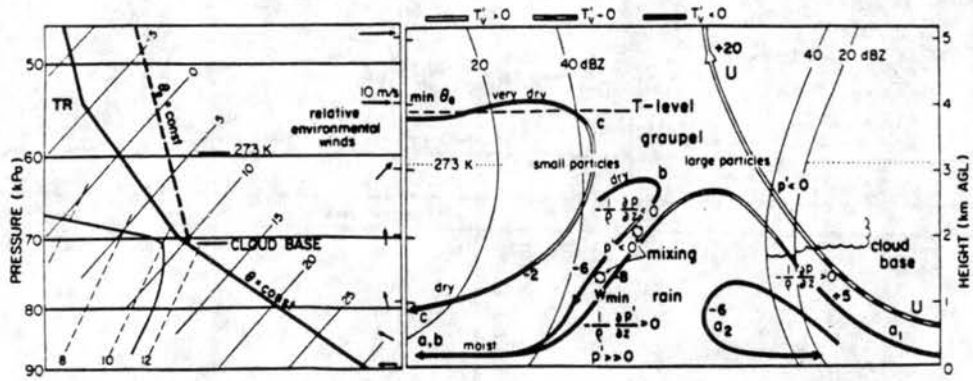


Figure 2.11: Conceptual model illustrating the physical processes along mature downdraft flow branches. A representative sounding upon which the physical model is based appears on the left. From Knupp (1988).

Since this may lead to a further spin up of the parent mesocyclone, surface wind speeds around the cell may increase either from enhanced low-level rotation or from a stronger dynamically-induced downdraft. Consequently, severe surface wind gusts associated with the developing mesocyclone circulations have been recorded in both the inflow region and outflow region of these storms (Wade 1982). Since supercells are particularly long-lived features, they become attractive subjects for explaining the development of derecho type systems.

### 2.2.2 Surface mesohigh structure

Another aspect of the the low-level cooling associated with the low-level PR downdraft is its impact on the surface mesohigh development. The importance of the surface mesohigh on the maintenance, regeneration, motion, and surface flow fields of MCSs has been recognized for over a century (Hinrichs 1888; Humphreys 1914; Byers and Braham 1949; Newton 1950, 1966; Fujita 1955; Thorpe et al. 1982; Rotunno et al. 1988). In this and the subsequent subsection, we review the structure of the mesohigh and the wake mesolow, their impact on the surface flow fields, and their relation to the internal flow structure of the associated MCS.

Studies documenting the meso$\beta$-scale convectively-induced surface mesohigh have revealed that the flow emanating from these systems is highly ageostrophic (Fujita 1955)[Fig 2.12]. The cross-isobaric flow, which may occur at right angles to the isobars, tends to produce two primary zones of strong surface winds, one located at the leading edge of the mesohigh termed the gust front, and the other located near the trailing wake low. Most of the attention of past research has centered on the flow structure along the leading gust front. The primary structural characteristics of the gust front include the head, which is an elevated region of cold air consisting of strongly rotational flow, the turbulent wake, and the body which is typically 0.5 to 2 km deep and provides the hydrostatic motive force which drives the current (Fig 2.13).

Numerical and observational studies suggest that the strongest flow within the density current typically occurs within a frictionally-induced elevated jet located approximately 500 m AGL and at the surface directly beneath the head of the current. The surface wind

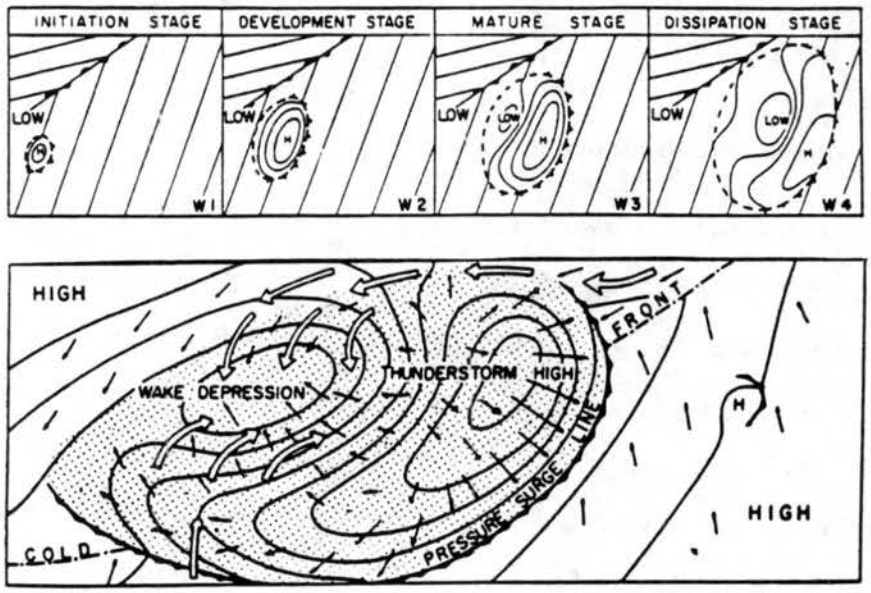


Figure 2.12: Isobar patterns for four stages of squall-mesosystems (top, from Fujita 1963). The W designates warm sector type systems. Schematic of surface pressure field in a squall-line thunderstorm (bottom, from Fujita 1955). Small arrows indicate surface wind; large arrows relative flow into the wake. Stippling indicates extent of precipitation-cooled air. From Johnson and Hamilton (1988).

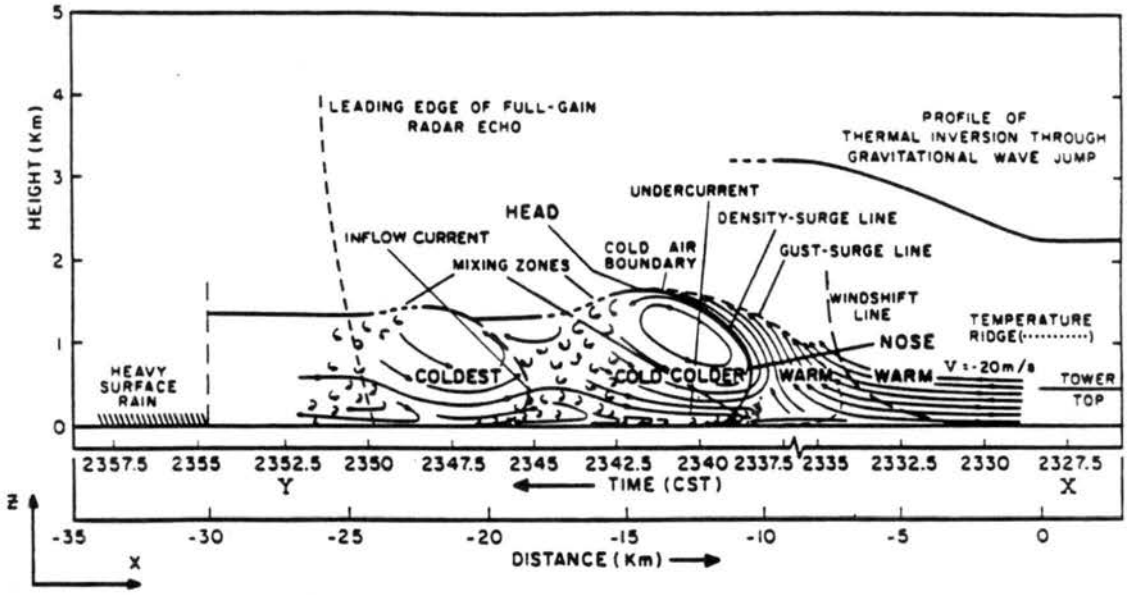


Figure 2.13: Schematic structure of the windshift-pressure jump and gust front associated with the 31 May 1969 squall line. From Charba (1974).

maximum within the the density current head arises from two primary sources. First, this is a region of rapid pressure increases within the current. It is not uncommon to observe pressure rises of 4-7 hPa in stronger density currents within a few tens of minutes after the initial wind shift. Numerical and observational studies have shown that the pressure increase is bimodal in nature with an initial rapid increase in pressure, termed the pressure jump, followed by a slight pressure lull before a more gradual increase to the peak pressure. The peak surface winds are typically located near the peak pressure following the lull (Charba 1974).

The total pressure rise within the current reflects both nonhydrostatic and hydrostatic affects which arise near its leading edge. Charba (1974) attributed the initial pressure jump in his analyses to hydrostatic affects associated with a gravitational wave that formed in the nocturnal stable layer immediately ahead of the density current (Fig 2.13). Such waves are also present in the studies by Crook (1988), Crook and Moncrieff (1988), and Fulton et al. (1990). Other studies have suggested that the initial pressure jump is nonhydrostatically-induced as a result of the rapid deceleration of the flow along the leading edge of the density current (Wakimoto 1982; Droegemeier and Wilhelmson 1987). In the Wakimoto (1982) study, this nonhydrostatic component accounted for nearly one-half of the total pressure increase.

A second factor influencing the intensity of the surface flow near the head of the current is the presence of a strong rotor circulation. The rotor results from the strong horizontal gradients in potential temperature which exist between the current and the ambient environment. Numerical studies by Droegemeier and Wilhelmson (1987) have also shown that the rotor is affected by the presence of a cyclostrophically balanced low pressure region near the top of the density current head (Fig 2.14). They argued that the circulation about this low accounted for the increase in the surface winds located directly beneath the low.

Their simulations also showed that turbulence within the leading edge of the gust front, a result of mixing and entrainment between the cold air mass and the ambient environment, may provide an additional source of severe surface wind gusts. This mixing gives rise to the characteristic appearance of the density current and appears in nearly all gust front schematics. In their simulations, the passage of turbulent billow circulations were found

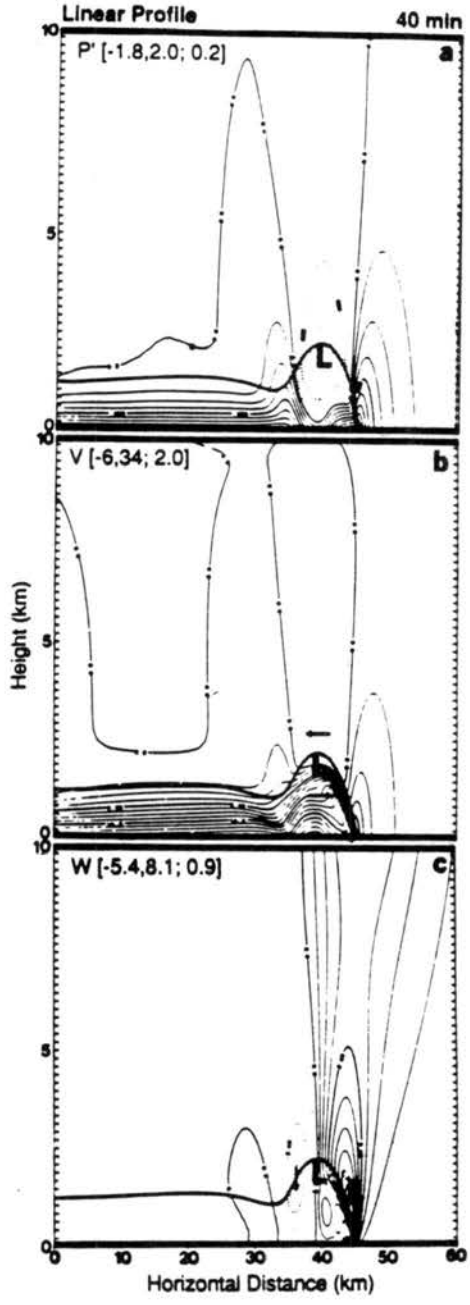


Figure 2.14: Contour plots at 40 min in the Linear Profile simulation of (a) perturbation pressure (mb), (b) the horizontal velocity (m $s^{-1}$), and (c) the vertical velocity (m $s^{-1}$). The bold solid line denotes the outflow boundary (-0.1 K perturbation isentrope), and the L indicates the region of lowest pressure. The arrow in panels b and c depict the general flow (ground-relative) around the low center. From Droegemeier and Wilhelmson (1987).

to increase the surface winds from 30 to 40 m $s^{-1}$ (Fig 2.15). Their study illustrates the relatively fine horizontal resolution which may be necessary to to capture the complete detail and magnitude of the flows impacting the development of severe surface wind gusts in derecho-like systems.

### 2.2.3 Surface mesolow structure

The intense pressure gradients and turbulence marking the leading edge of the mesohigh appear to apply as well to a companion feature which often hugs the trailing flank of the mesohigh, *i.e.*, the wake low. The mesolow appears to owe its origin to mesoscale subsidence-induced warming within the trailing stratiform region of the convective system (Williams 1953; Koch and McCarthy 1982; Zipser 1977; Johnson and Hamilton 1988). Johnson and Hamilton (1988), presenting the most detailed study to date of the wake low and its relationship to the precipitation and internal flow characteristics of the MCS, suggested that the wake low is a surface manifestation of the descending rear inflow jet (Fig 2.16). The location of the strong pressure gradient and the low itself were found to correspond with the back edge of the trailing precipitation field. Such strong gradients in the wake of squall lines have, on occasion, produced surface wind gusts in excess of 25 m $s^{-1}$ (Fig 2.17). More extreme surface wind speeds appear to be limited by the relatively short time air parcels actually spend within the pressure field (Vescio 1990). Even so, the surface wind speeds which may be obtained in the mesohigh-mesolow gradient is remarkable given the fact that they may arise 50 to 200 km behind the leading convective line.

### 2.2.4 Meso$\beta$-scale (20-200km) gravity waves

Another type of mesoscale surface pressure field that may develop in association with convective storms, result from the pressure perturbations generated by internal gravity waves. Internal gravity waves represent one of the fundamental responses of a stratified fluid to an imposed heat source/sink and, therefore, are probably excited whenever convective motions are present. In the atmosphere, internal gravity waves provide an effective mechanism to redistribute momentum and heat over a wide spectrum of length and time scales. We will restrict our attention here to meso-$\beta$-scale (20-200 km) gravity waves which

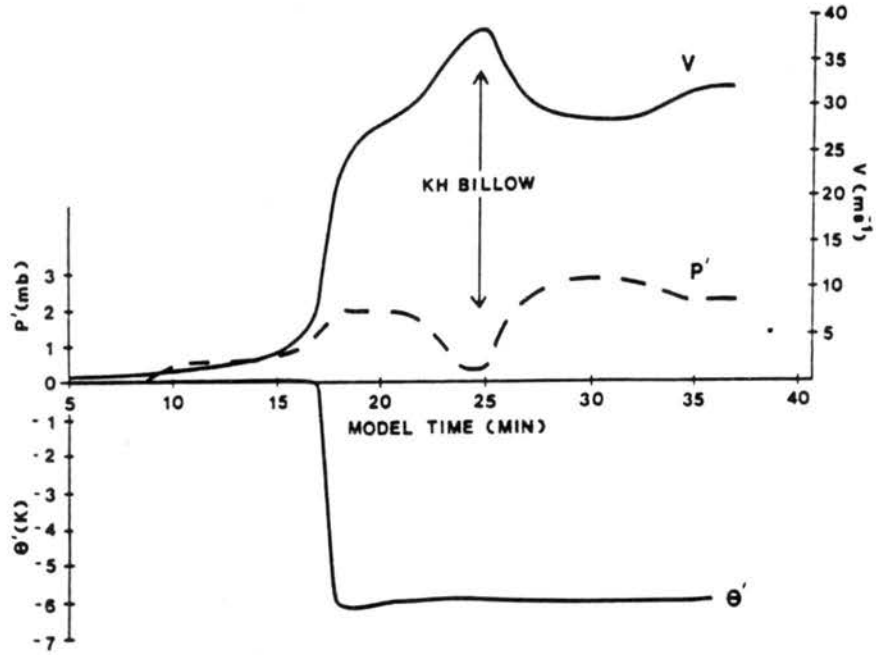


Figure 2.15: Time series plots of the surface horizontal velocity v (m $s^{-1}$), perturbation pressure p′ (mb), and perturbation potential temperature $\theta'$ (K). The point of measurement is 16 km from the cold-air source region (approximately the position of the gust front). From Droegemeier and Wilhelmson (1987)].

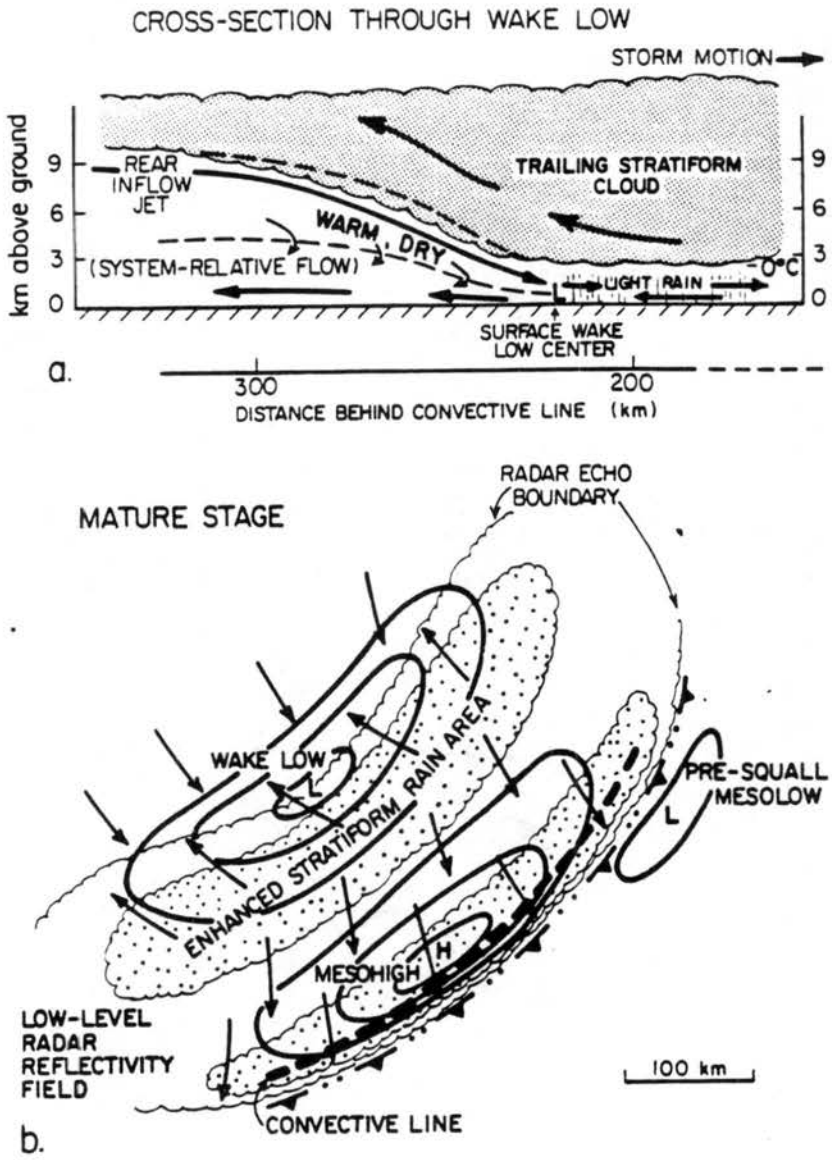


Figure 2.16: Schematic cross section through the wake low (a) and surface pressure and wind fields and precipitation distribution during the squall line mature stage (b). Winds in (a) are system relative with the dashed line denoting zero relative wind. Arrows indicate streamlines, not trajectories, with those in (b) representing actual winds. Note that horizontal scales differ in the two schematics. From Johnson and Hamilton (1988).

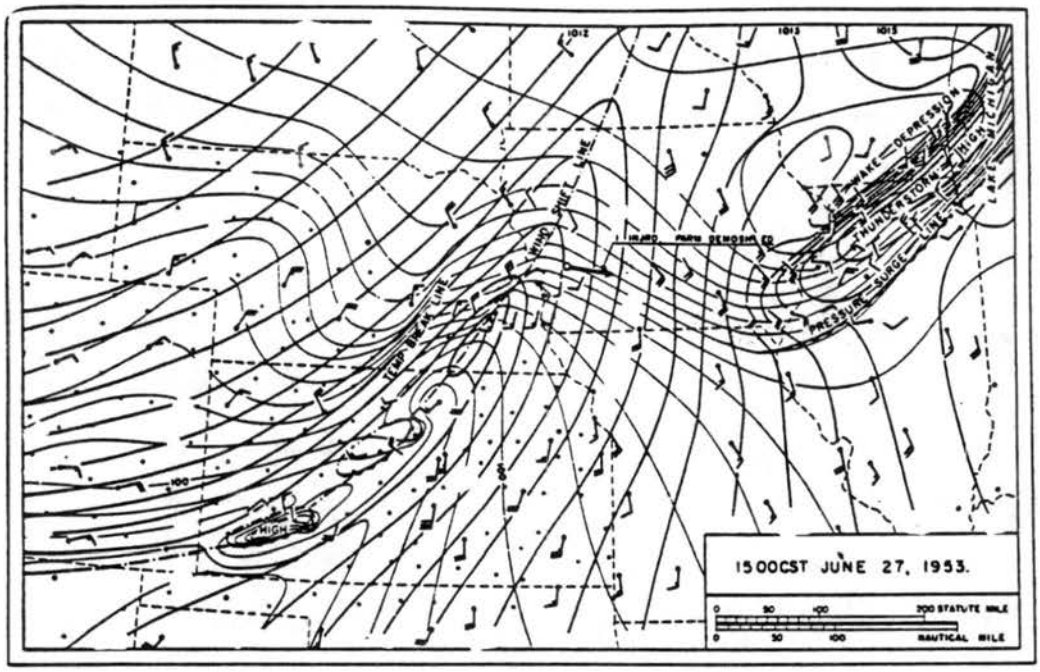


Figure 2.17: Analysis of winds and pressure within a wake low. From Fujita (1955).

exhibit long lifetimes (several hours). Waves of such length and time scales have been implicated in a number of severe weather events (cf. Eom 1975; Uccellini 1975; Miller and Sanders 1980; Stobie et al. 1983; Bosart and Seimon 1988; Koch et al. 1988). We begin this subsection, therefore, with a review of the gravity wave cases which are known to have been associated with severe surface wind producing MCSs (section 2.6.1). We then review the possible forcing mechanisms for meso$\beta$-scale gravity waves and the environmental conditions which lead to a prolonged wave lifetime (sections 2.6.2 and 2.6.3). Finally the issue of how wave/convective interactions may affect the structure, propagation, and longevity of mesoscale convective systems is addressed (section 2.6.4).

### 2.2.5 Severe meso$\beta$-scale wave events

A classic example of a severe, long-lived, meso$\beta$-scale wave event was presented by Brunk (1949). In his case, a mesoscale wave ($\lambda$= 150-200 km) was tracked for a 24 hour period as it propagated rapidly eastward at 20 m $s^{-1}$ along and to the north of an east-west warm frontal boundary (Fig 2.18). The wave passage at a particular station was marked by rapid pressure falls and severe, easterly surface wind gusts of 25-45 m $s^{-1}$.

Figure 2.19 and Table 2.1, compiled in part from Uccellini and Koch (1987), summarize the characteristics of a number of other strong-to-severe surface wind events which have been attributed to the presence of gravity waves. Note that the wave events generally occurred in the springtime on the cold side of synoptic scale frontal boundaries, and are characterized by rapid pressure falls, fast propagation speeds, strong-to-severe easterly surface winds, and a several hour life span[2]. The study of Uccellini and Koch (1987) has further shown that the waves are typically confined to the west of an upper level ridge and/or within the exit region of an upper-level jet streak. The only notable exception to this general pattern being the warm sector gravity waves discussed Miller and Sanders (1980). The speed, longevity, location, and severity of these gravity wave events are remarkably similar to the derecho characteristics listed above making them attractive candidates for explaining derecho events.

---

[2]We were unable, in many cases, to determine whether the severe winds persisted throughout the entire life span of the wave event.

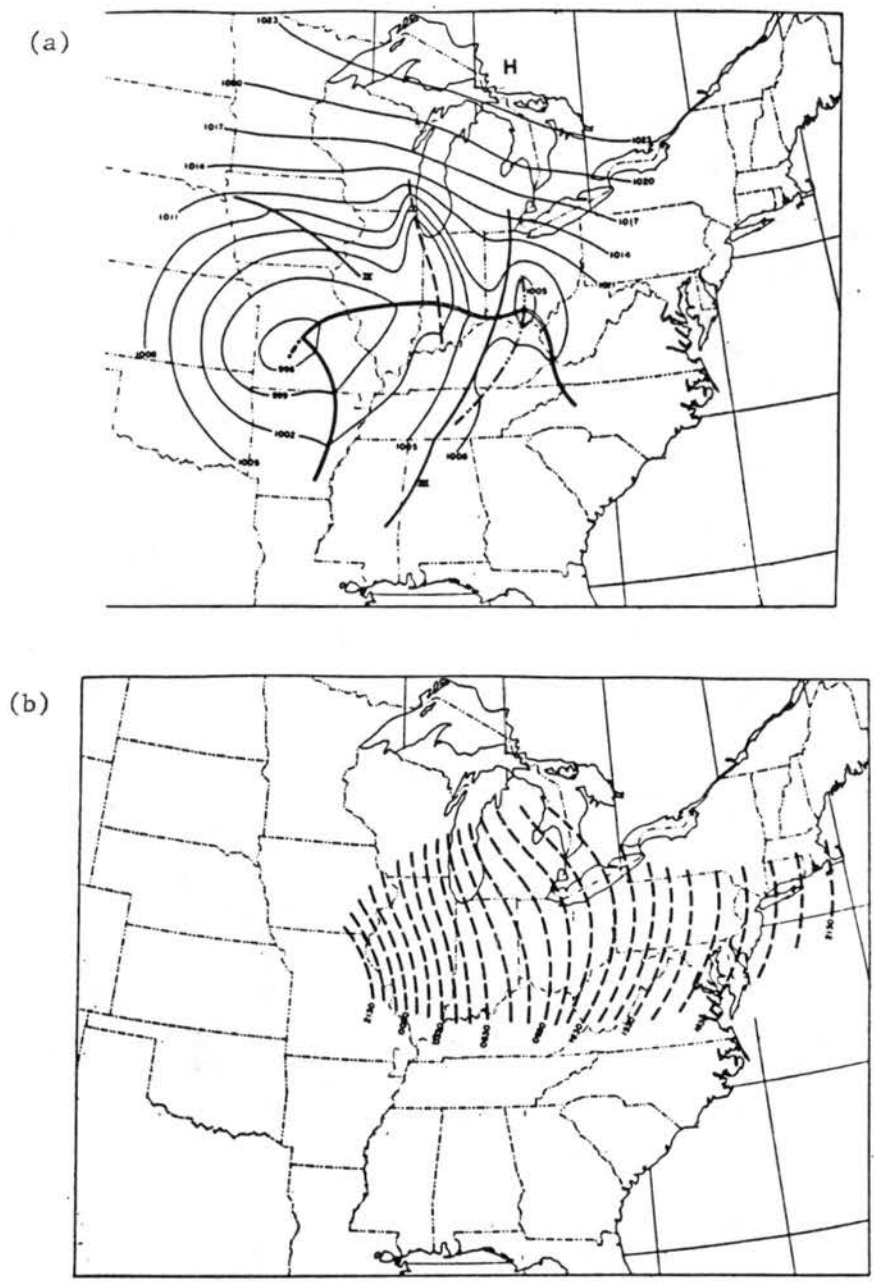


Figure 2.18: Enlarged section of surface map, 0630 CST 11 April 1944 (a) and (b) hourly movement (CST) of pressure pulsation 10-11 April 1944. From Brunk (1949).

Table 2.1: Severe Meso-$\beta$-scale gravity wave events. Data compiled from Table 1 of Uccelini and Koch (1987) and from author's own research.

| Reference | Date | Wave Type | $\lambda$ (km) | $\Delta$p (hPa) | Duration (hours) | c (m s$^{-1}$) | Max. Surface Gust (m s$^{-1}$) | Direction |
|---|---|---|---|---|---|---|---|---|
| Brunk (1949) | 11 Apr 1944 | Wave of depression | 150-200 | -6 | 36 | 20 | 40 | Easterly |
| Mayor (1958) | 1 Jan 1955 | Wave of depression | – | – | 14 | 20 | 35 | Easterly |
| Ferguson (1967) | 13 Mar 1963 | Wave of depression | 18-60 | -3.3 | 13 | 20 | 19 | East/N.E. |
| Eom (1975) | 19 Apr 1970 | Wave of depression | 500 | -11.5 to -14.6 | 9 | 50 | 26 | Easterly |
| Pecnick and Young (1984) | 27 Mar 1975 | Wave of depression | 120 | -4.4 to -7.4 | 21 | 32 | 33 | Easterly |
| Koch and Golus (1988) | 11/12 Jul 1981 | Wave Packet | 160 | .5 to 1 | up to 33 | 20 | Derecho | ? |
| Bosart and Seimon (1988) | 27 Feb 1984 | Wave of depression | 150-200 | -3 to -14 | up to 30 | 15-20 | 30 | Easterly |

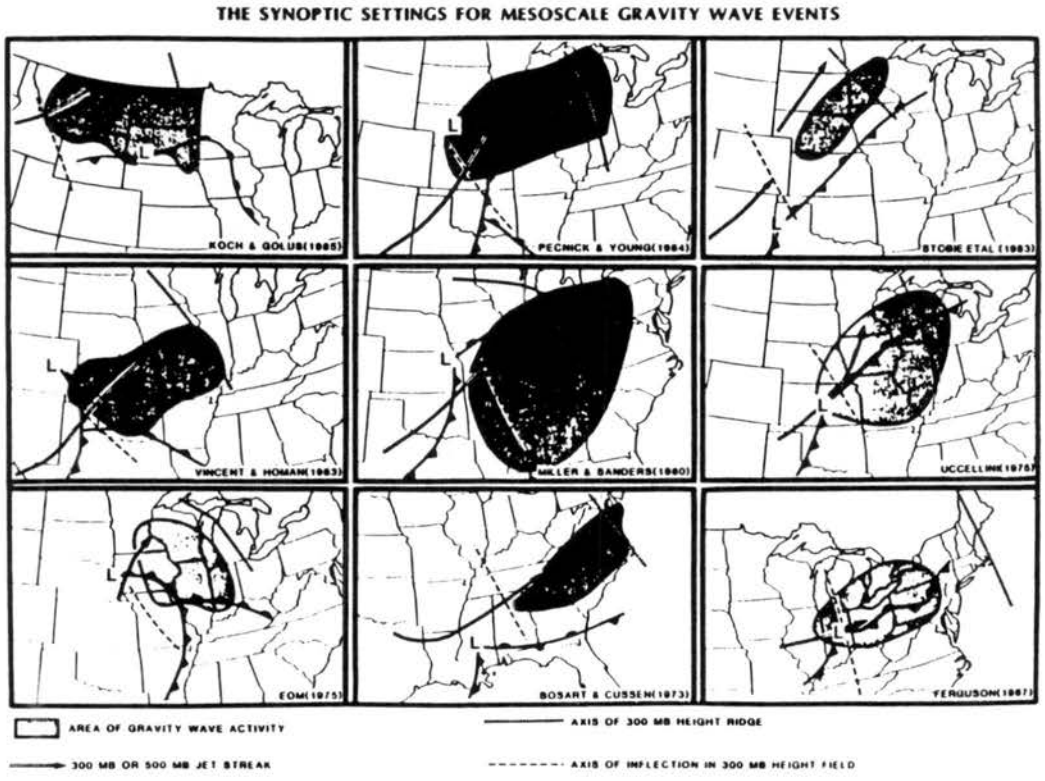


Figure 2.19: The synoptic settings for wave cases 2 through 10 listed in Table 1 of Uccellini and Koch (1987). Positions of all atmospheric features shown on maps are approximate means during first half of wave episode, during which wave source mechanisms are assumed to operate most efficiently. Shaded regions represent areas of wave activity during the entire wave episode as determined from surface microbarograph analyses. Jet streak positions (double arrow) represent core of maximum wind speeds within the 300 mb jet stream (if unavailable, 500 mb data are used). Dotted line refers to the ridge axis. Dashed line refers to the inflection axis between the trough and ridge in the 300 mb height field. From Uccellini and Koch (1987).

### 2.2.6 Forcing mechanisms for meso$\beta$-scale gravity waves

The generation of meso-$\beta$-scale gravity waves in the atmosphere may arise in a number of ways. These include topographical or mechanical forcing, vertical wind shear instabilities, geostrophic adjustment processes, or convective excitation (see Uccellini and Koch (1987) for a more detailed discussion of the forcing mechanisms). Uccellini and Koch (1987) suggested that the geostrophic adjustment process and shear instabilities were the most likely forcing mechanism for the wave events presented in Fig. 2.19. Shear excitation of gravity waves refers to the ability of the wave to extract energy from the basic state sheared flow. This requires a critical level to be present in a region where the Richardson number is less than 0.25. Wave encounters with critical levels with Richardson numbers greater than 0.25 result in the absorbtion of wave energy at that level (Booker and Bretherton 1967).

The presence of gravity-inertia waves, on the other hand, reflect an inability of the ageostrophic circulations to restore quasi-geostrophic balance (Van Tuyl and Young 1982). To see why this may occur, consider the classic circulation about an upper-level jet streak as it approaches an upper level ridge axis. In this case the ageostrophic circulation in the exit region of the jet attempts to build high pressure on the cyclonic or left exit region of the jet axis. This pressure field acts to decrease the flow within the jet in an attempt to restore geostrophy. This tendency is opposed, however, by the increase in pressure in the right exit region of the jet as it approaches the upper level ridge axis. The pressure tendency disrupts the ability of the ageostrophic circulation to restore geostrophic balance and the result is an excitation of gravity-inertia waves near the exit region of the jet. Once excited, gravity-inertia waves may ultimately alter both the orientation and strength of the classic 4-cell ageostrophic circulation about the jet streak and the expected location of MCS development.

### 2.2.7 Environmental factors affecting wave longevity

Once a gravity wave is forced, its behavior and amplitude is strongly governed by the environmental conditions within the surrounding fluid. Thus, the favored locations for wave development not only reflect the regions where the forcing mechanisms listed above are operative, but also where conditions are favorable to promote wave longevity (such as in a

wave duct). Without some trapping mechanism most waves, due to their tendency to propagate energy vertically, would rapidly decrease in amplitude before traveling horizontally for even a few cycles (Lindzen and Tung 1976).

The atmospheric conditions conducive to ducted meso-$\beta$-scale gravity waves within the lower troposphere were described by Lindzen and Tung (1976). They showed the most efficient wave ducts occur when a layer of low static stability containing a steering level (*i.e.* the level where the environmental flow speed equals the wave phase speed) overlies a deep and stable ABL (referred to as the ducting layer). Their analysis suggests that wave ducts of a few kilometers in depth would be adequate to support wave phase speeds of 10 to 50 m $s^{-1}$. These environmental constraints for wave trapping are quite common and, as we'll show later, appear in the two derecho case studies discussed in Chapter 4.

Wave guides may also form in the upper troposphere as well [Tripoli and Cotton (1989a,b)]. In their numerical study, gravity waves were trapped in and beneath the upper tropospheric cirrus cloud shield associated with a simulated MCS. The wave duct resulted from radiative cooling at cloud top which produced a rapid decrease in the Scorer parameter just above the cloud top. Consequently, gravity waves emitted from the convective region of the MCS had a lasting effect on the simulated flow fields within the stratiform region of the system.

### 2.2.8 Wave/convective interactions

Though convective activity was not cited by Uccellini and Koch (1987) as the most likely source of meso$\beta$-scale waves, convectively-excited waves nonetheless appear to have an important role modifying both the vertical wind shear and static stability profiles within the near environment of mesoscale convective systems and MCS internal circulation features (Emanuel 1982; Bolton 1984; Raymond 1984,1986; Lin and Smith 1986; Orlanski and Ross 1986; Lin and Li 1988; Baliji and Clark 1988; Nicholls et al 1990; Schmidt and Cotton 1990). Some of the initial studies of convective/gravity wave interactions attempted to show the importance of gravity waves on the propagation and orientation of squall lines (Hamilton and Archbold 1945; Freeman 1948; Brunk 1949; Tepper 1950; Abdullah 1954). In these studies, the squall line was modelled as a hydraulic jump propagating on a thin elevated

inversion separating the moist ABL from the dry ambient air aloft. Their calculations of the hydraulic jump speed appeared to give reasonable predictions for the propagation speed of observed squall lines and the low-level lift generated by the jump provided a mechanism to aid the low-level convective-scale updraft.

Within the past two decades, the research efforts have focused on the synergistic relationship which may develop between the waves and the convective systems (Lindzen 1974; Ley and Peltier 1978; Xu and Clark 1984; Raymond 1986; Nehrkorn 1986; Zhang and Fritsch 1988). The primary premise of this relationship, termed WAVE-CISK by Lindzen (1974), is that the wave generates the low-level lift required to initiate the convection, while the convection in turn, through latent heat release, provides the energy to maintain the wave. It is further assumed that the convection and the wave remained phase-locked. This type of synergistic relationship may be distinguished from other cases where the waves, once generated by the convection, rapidly propagate away from the region of forcing (cf. Baliji and Clark 1988; Schmidt and Cotton 1990). While an appealing idea, several problems have been noted with the current formulation of the WAVE-CISK problem, such as its failure to generate realistic wave growth rates (Nehrkorn 1986) [for a more detailed review of WAVE-CISK and its problems see Xu and Clark (1984); Cotton and Anthes (1989)].

Other researchers within the past decade have focused on the affect of gravity waves on the initiation and internal MCS flow structure (Emanuel 1982; Bolton 1984; Raymond 1984,1986; Lin and Smith 1986; Orlanski and Ross 1986; Lin and Li 1988; Baliji and Clark 1988; Nicholls et al 1990; Schmidt and Cotton 1990). The waves in these papers are typically studied within a linearized framework using simplified environments consisting of one or more layers of constant static stability and constant vertical wind shear. Despite the simplifications, these studies have shown that many squall line circulation features, such as the surface pressure distribution, broad regions of mesoscale inflow and outflow within the middle and upper troposphere, and the updraft structure are well represented within the linearized framework. We will make extensive use of these similarities in the discussion presented in Chapter 5.

## 2.3 Summary

In summary, we have shown that derechos are long-lived, convectively-induced, straight-line surface wind storms which produce damage paths of at least 400 km in length. A review of their characteristics reveal that they typically persist for an average of nine hours, have rapid propagation speeds (24 m $s^{-1}$ on average), and tend to form in environments having a low-level layer of strong static stability and significant convective instability aloft. We also described the known convective structure of derechos and listed a few their possible forcing mechanisms such as strong convective-scale downdrafts, convectively-induced meso$\beta$-scale surface pressure fields, and meso$\beta$-scale gravity waves. The problems that remain are to determine how these systems arise and to identify the possible physical mechanisms which govern some of their characteristics and ability to produce sustained damaging surface winds. In the following chapter we outline the experimental strategy used to approach these problems.

# Chapter 3

# EXPERIMENT STRATEGY

## 3.1 Observational data base

In this dissertation data are presented for two nocturnal, summertime derechos which occurred on 2-3 August 1981 and 12-13 May 1985. The observations of these derechos were obtained from two primary sources, (i) the Convective Cooperative Precipitation Experiment (CCOPE, Knight [1982]), conducted in the High-Plains region of southeastern Montana during the months of May-August 1981 (Fig 3.1), and (ii) the Oklahoma-Kansas Preliminary Regional Experiment for STORM-CENTRAL (PRE-STORM, Cunning [1986]), conducted during the months of May and June 1985 (Fig 3.2). The main observational data platforms of both experiments included a multiple Doppler radar network for the retrieval of storm relative winds, a surface mesonet, aircraft operations, and a dense network of rawinsonde stations.

Choices made in the use of these data were dictated by the location of the storms in and around the specific network. In the PRE-STORM case the derecho skirted the northwest portion of the data network and, therefore, was not observed by radar or aircraft. Primary use is made of the PRE-STORM supplemental rawinsonde sites and surface mesonet which captured important details of the regional-scale airmass structure within the pre-derecho environment. The surface mesonet consisted of forty NCAR/FOF PAM-II and forty NSSL SAM stations distributed over a network having an approximately 50 km station spacing. The rawinsondes sites consisted of regional National Weather Service stations and supplemental sites operated by the military.

In the CCOPE case, on the other hand, two of the three MCSs associated with the derecho passed directly through the network providing an excellent opportunity to assess the impact of these meso$\beta$-scale systems on the derecho development. Use is made of

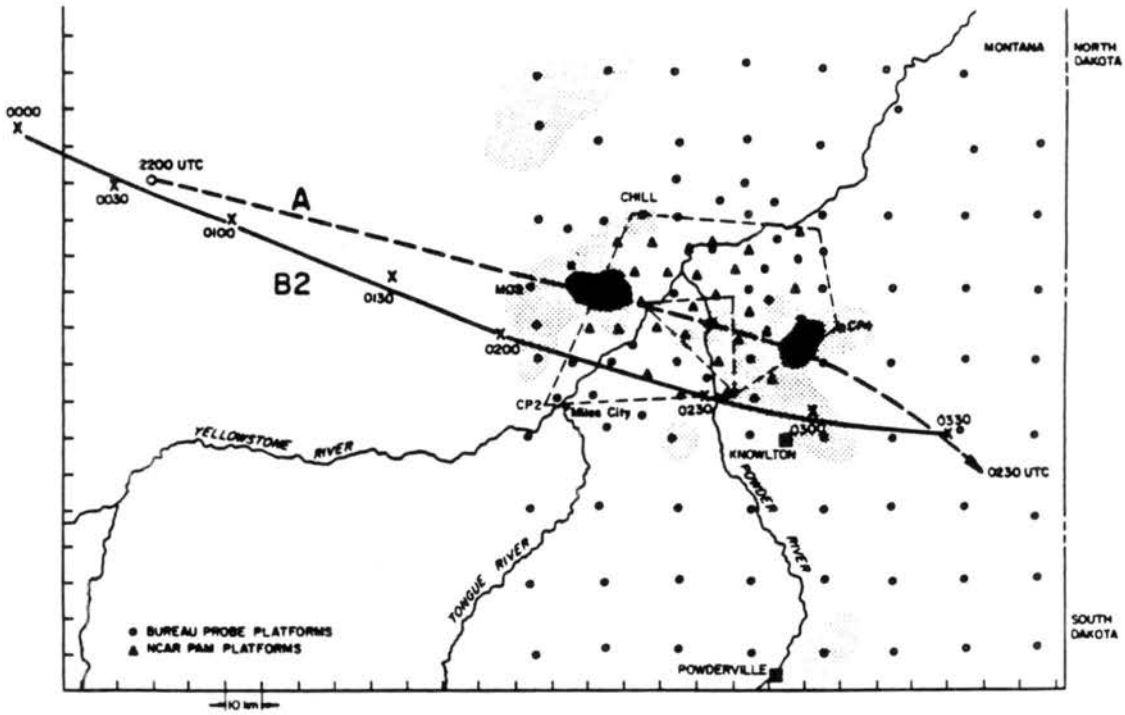


Figure 3.1: Experimental setup of the CCOPE field program showing Doppler radar network (dashed polygon), surface mesonetwork (circles and triangles), and the Knowlton rawinsonde station. The tracks labeled A and B represent the movement of the storm cores associated with the two meso$\beta$-scale systems discussed in the text. Track A was taken from Wade (1982). Light and dark stippling indicate, respectively, regions of surface wind gusts of 25 and 30 m $s^{-1}$ which were associated with system B between 0200 to 0330 UTC 3 August 1981.

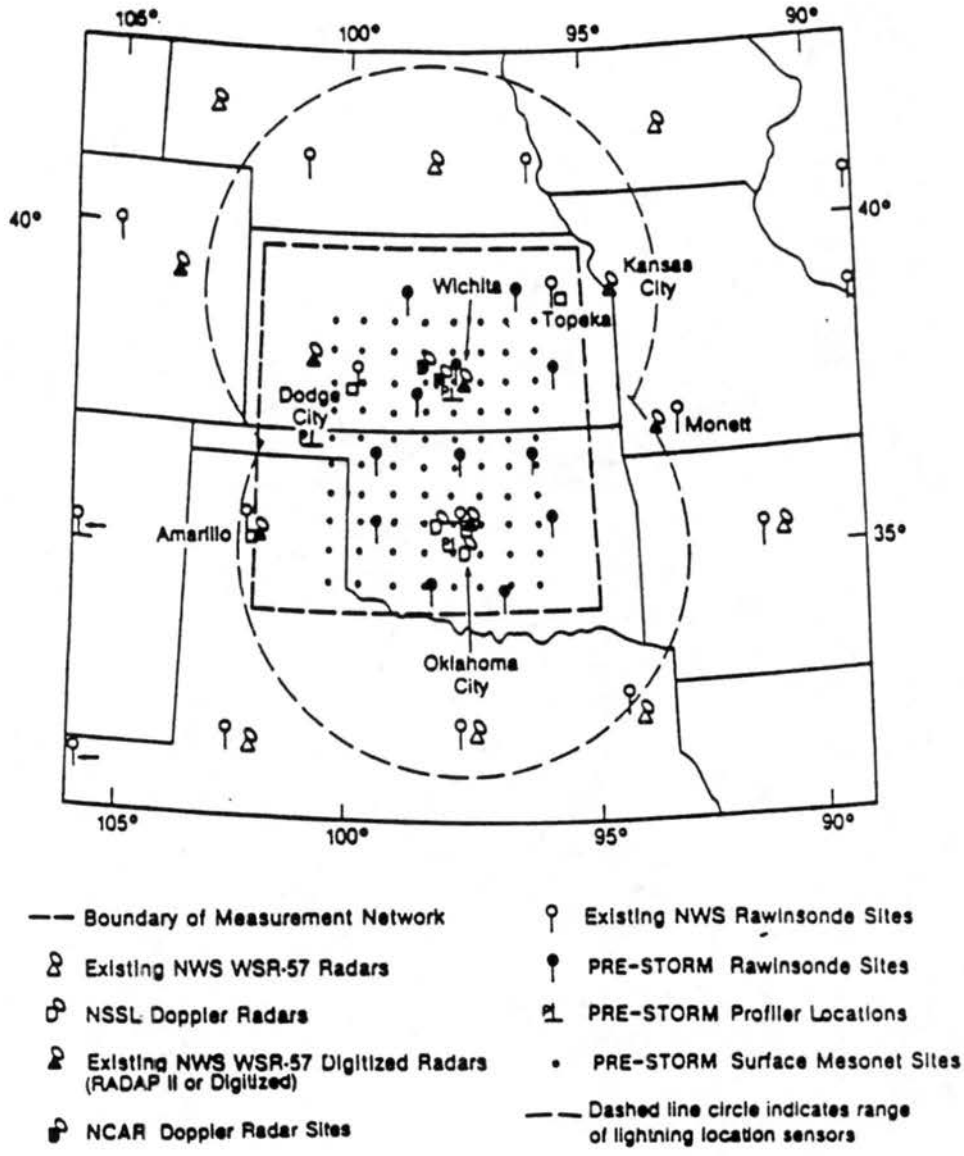


Figure 3.2: The May-June 1985 Oklahoma-Kansas PRE-STORM observational network.

the CCOPE mesonetwork, aircraft measurements, rawinsonde and Doppler radar derived data. The CCOPE surface mesonet consisted of an inner array of 27 NCAR/FOF PAM stations which recorded data averaged over one minute time intervals, and an outer network of 96 Portable Remote Observation of the Environment (PROBE) stations provided by the Bureau of Reclamation and operated by the Montana State Department of Natural resources. The PROBE stations were spaced approximately every 20 km and recorded data averaged over a five minute time interval. The aircraft data were obtained from the University of Wyoming King Air and the upper air stations were operated by Texas A&M University. Details of the Doppler radars used in this study and the Doppler radar analyses techniques may be found in Schmidt and Cotton (1989).

Because this experiment covered a much smaller area than that of PRE-STORM, detailed observations of the regional scale thermodynamics and vertical shear profiles were not available through the entire episode. For this reason, the regional scale data presented for this case consists primarily of standard NMC analyses and rawinsondes released over southeastern Montana from the CCOPE network during the initial stages of the derecho. Details of the evolutionary characteristics of the regional-scale flow will be supplemented with the regional-scale numerical simulations described in the next section and from the simulations of this case described previously by Tremback (1990).

### 3.2 Model description and experimental design

The primary tool used in the analyses of the two derecho case studies is the Colorado State University Regional Atmospheric Modeling System (CSU-RAMS). The CSU-RAMS resulted from a merger of two modeling programs, one the mesoscale model program directed by Dr. Roger A. Pielke (i.e. Pielke 1974; Mahrer and Pielke 1977) and the cloud/mesoscale modeling program directed by Dr. William R. Cotton (i.e. Cotton and Tripoli 1978; Tripoli and Cotton 1982; 1986; 1989a,b). The combination of a cloud and mesoscale model makes the CSU-RAMS well suited to study the wide range of time and spatial scales inherent with derecho type systems. The model equation set consists of the nonhydrostatic compressible dynamic equations of motion, a thermodynamic equation, and a set of microphysical equations that account for interactions between all phases of water [A description of the

model equations and formulation of the CSU-RAMS may be found in Nicholls (1987) and Tremback (1990)]. The user has the option to include a variety of modular routines for the calculation of the surface energy budget, short and longwave radiation budgets, or ice-phase microphysical affects on the storm evolution. The user also has the option to include multiple nests within the outer domain to improve the horizontal resolution in areas of key interest.

The simulations performed in this study fall into two primary classes. In the first set of experiments, presented in Chapter 4, the model is configured as in Tremback (1990) except the nonhydrostatic option is utilized. These experiments are conducted on a large domain with relatively coarse horizontal resolution and parameterized convection to investigate the meso$\alpha$-scale (200-2000 km) circulations associated with the two observed derecho case studies. The second primary set of simulations employ a much finer horizontal resolution so that the convection could be resolved explicitly on either a two- or three-dimensional domain using the full set of microphysical parameterizations available in RAMS. The two-dimensional experiments employ a relatively large horizontal domain to assess the impact of rapidly moving gravity waves (which on smaller domains would otherwise rapidly pass beyond the lateral boundaries) on both the internal flow characteristics of the simulated MCS and the ambient environmental wind shear and thermodynamic profiles beyond the MCS cloud shield. The three-dimensional experiments were designed (by necessity) on a smaller horizontal domain to assess the impact of the three-dimensional circulations of the observed CCOPE squall line on the severe surface wind development. The following subsections outline in greater detail the specific design of the various experiments to be presented in Chapters 4-6.

### 3.2.1 Non-homogeneous experiments

For the regional-scale experiments, the model was initialized in each case with the standard NMC analyses at 1200 UTC 12 May, 1985 and 1200 UTC 2 August, 1981 for the PRE-STORM and CCOPE derechos, respectively. The NMC data were interpolated onto isentropic surfaces on a domain extending from from 155° W to 60° W and 10° N to 70° N and then analyzed with a Barnes (1973) objective analysis scheme. The gridded data were

then interpolated onto a model grid having a horizontal resolution of approximately 75 km. The vertical resolution was varied from 300 m near the surface to a constant value of 750 m aloft. In each experiment an inner nest was placed within the large domain to give a fine grid horizontal resolution of approximately 25 km. The convective parameterization scheme used in the simulations was the modified Kuo (1974) scheme described by Tremback (1990). The Klemp-Wilhelmson (1978a,b) radiative boundary condition was applied on the lateral boundaries, and the top boundary for these experiments consisted of a solid wall placed at 17.5 km. The results will be shown after 12 to 24 hours of simulation for each case.

### 3.2.2 Description of the two-dimensional, horizontally homogeneous experiments

The two-dimensional experiments (Chapter 5) used a $x$-$z$ domain of either 400 x 23 km or 800 x 23 km. Both domains had a horizontal grid spacing of 2 km and a vertical resolution which varied from 300 m near the surface to a constant value of 500 m aloft. Tests made with a finer horizontal resolution (1 and 0.5 km) showed a nearly identical development of the squall line as the coarse resolution simulations. Results will thus be shown for the coarse resolution simulations exclusively. The lateral boundary conditions are as described above and, to prevent unwanted wave reflection from the top of the model (located at 23 km) in this convective environment, an energy absorbing layer 5 km thick was used as the top boundary condition.

To initialize the convection in the homogeneous environment, a positive tendency was added to the initial fields of potential temperature and mixing ratio for the first 600 s of the simulation. The tendencies were applied to an area 10 km across and 2 km deep and produced a maximum potential temperature ($\theta'$) and mixing ratio perturbations (q') of 2° C and 2 g kg$^{-1}$, respectively. To provide a smooth transition to the undisturbed environment, these tendencies were reduced outward from the center of the heated region to a value of zero at the edge using a sine squared function. The tendencies generated a buoyant bubble within the domain which accelerated upward and activated the microphysical routines.

The thermodynamic and vertical wind shear profiles chosen for the homogeneous experiments were based on soundings taken from the 2-3 August 1981 derecho (Fig 3.3, Fig 3.4,

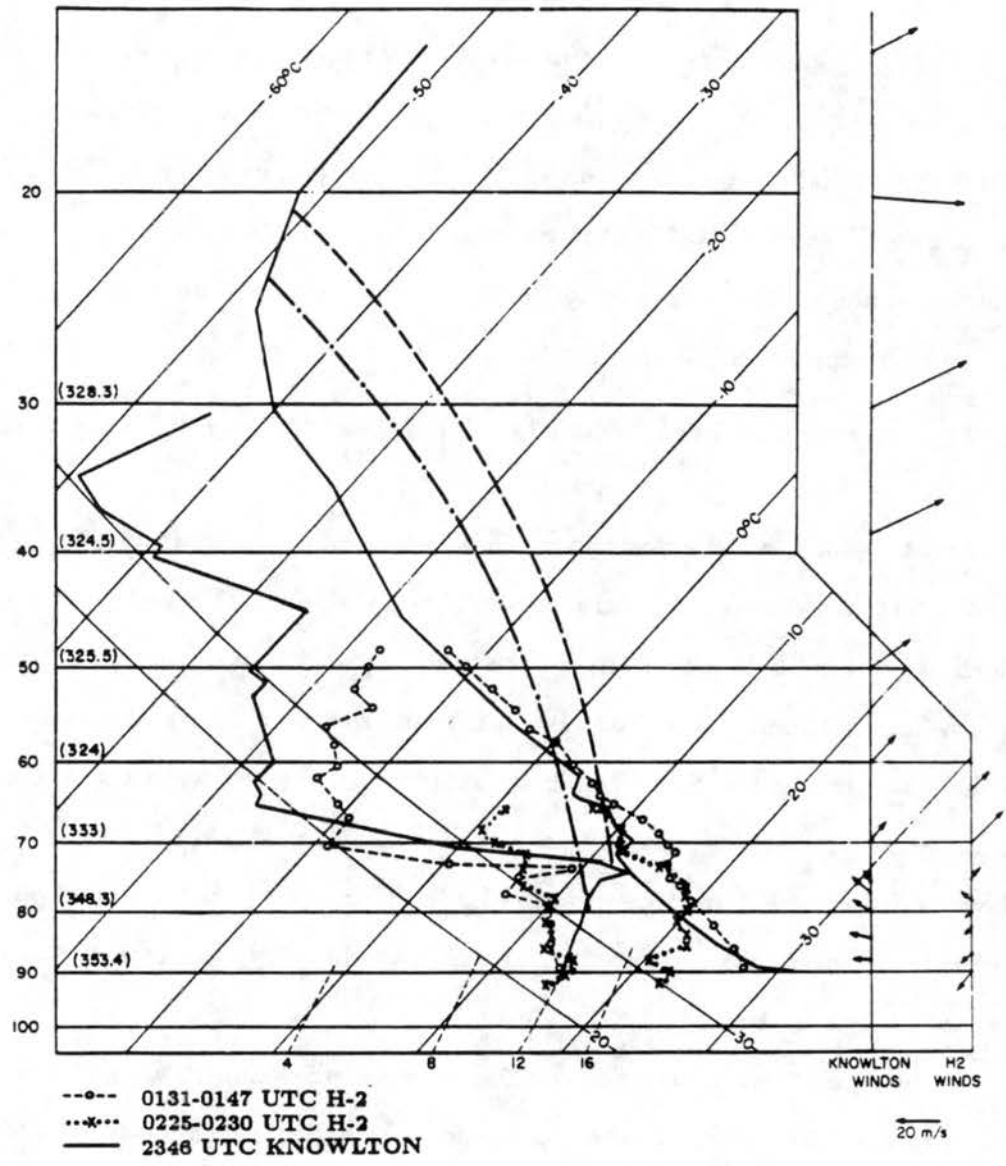


Figure 3.3: Skew-T log-P plot of the 2346 UTC 2 August 1981 Knowlton sounding (solid lines), and two University of Wyoming King Air aircraft soundings near 0131 UTC (open circles) and 0225 UTC (x's) 3 August 1981. Parcel ascents based on average conditions near the surface are shown for the Knowlton (dashed curve) and the 0225 UTC H2 (dot-dashed) soundings. The winds from the Knowlton and 0225 UTC H2 soundings are plotted to the right. Numbers in parentheses represent values of ($\theta_e$) derived from the Knowlton sounding and are plotted at 10 kPa intervals beginning at 90 kPa. (From Schmidt and Cotton 1989)

and Fig 3.5). Results will be shown for an idealized thermodynamic profile shown in Fig 3.5. The idealized thermodynamic profile was chosen to eliminate the smaller scale temperature fluctuations in the actual sounding, while at the same time retaining the three thermodynamically distinct layers present within the observed troposphere (*i.e.* the surface-based stable layer, the elevated well-mixed layer, and the upper tropospheric stable layer). This alteration has three main benefits: (i) it simplifies the interpretation of the results, (ii) it allows the results to be generalized to other situations which exhibit similar thermodynamic characteristics, and (iii) it should allow for future comparisons with linear analytical solutions.

The choice of the idealized sounding, though somewhat arbitrary, is also based on the following: 90% of all derechos studied by Johns and Hirt (1987) formed on the cold side of synoptic scale boundaries and yet had an average lifted index of -9. This strongly suggests that the low-level stable and elevated mixed layer combination in the observed and idealized sounding may be a representative thermodynamic profile of a number of derecho cases.

The three-layered thermodynamic structure may arise in a variety of situations. The surface-based stable layer may arise from nocturnal cooling, shallow frontal zones, or diabatic cooling resulting from convectively-induced, meso$\beta$-scale surface cold pools. The overlying layer of low static stability may result from differential temperature advection (Newton 1966; Carr and Millard 1985) or, as often the case in the West-Central United States, from the eastward advection of the daytime mountain ABL over the Central Plains (Benjamin and Carlson 1986). Results from Fawbush and Miller (1954) and the climatological study of Farrell and Carlson (1989) have shown that the mountain-induced, elevated well-mixed layer typically extends from 70 to 50 kPa and may remain intact several hundred kilometers to the lee of the Rocky Mountains (Fig 3.7). Examples supporting this basic thermodynamic structure include Fig 2.3 and the case studies to be presented in Chapter 4.

With the thermodynamics fixed, we then set out to test the response of the model to variations in the vertical wind shear profile. The vertical wind shear profiles used in the two-dimensional experiments are shown in Fig 3.6 and a list of experiments using these profiles are shown in Table 3.1. In experiment S0 the initial flow was set to zero everywhere in

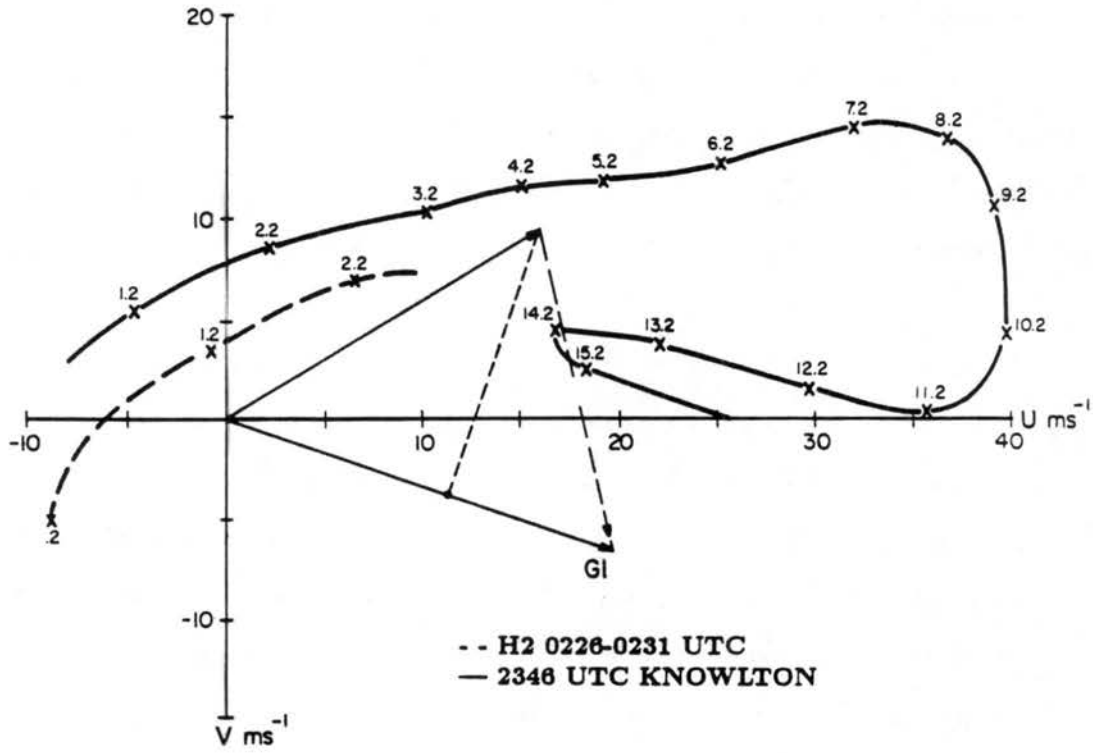


Figure 3.4: Hodograph corresponding to the environmental soundings plotted in Fig 3.3 Labeled x's refer to height in km Above Ground Level. Average cell and storm motion vectors are included for system B from 0233 to 0330 UTC 3 August 1981.

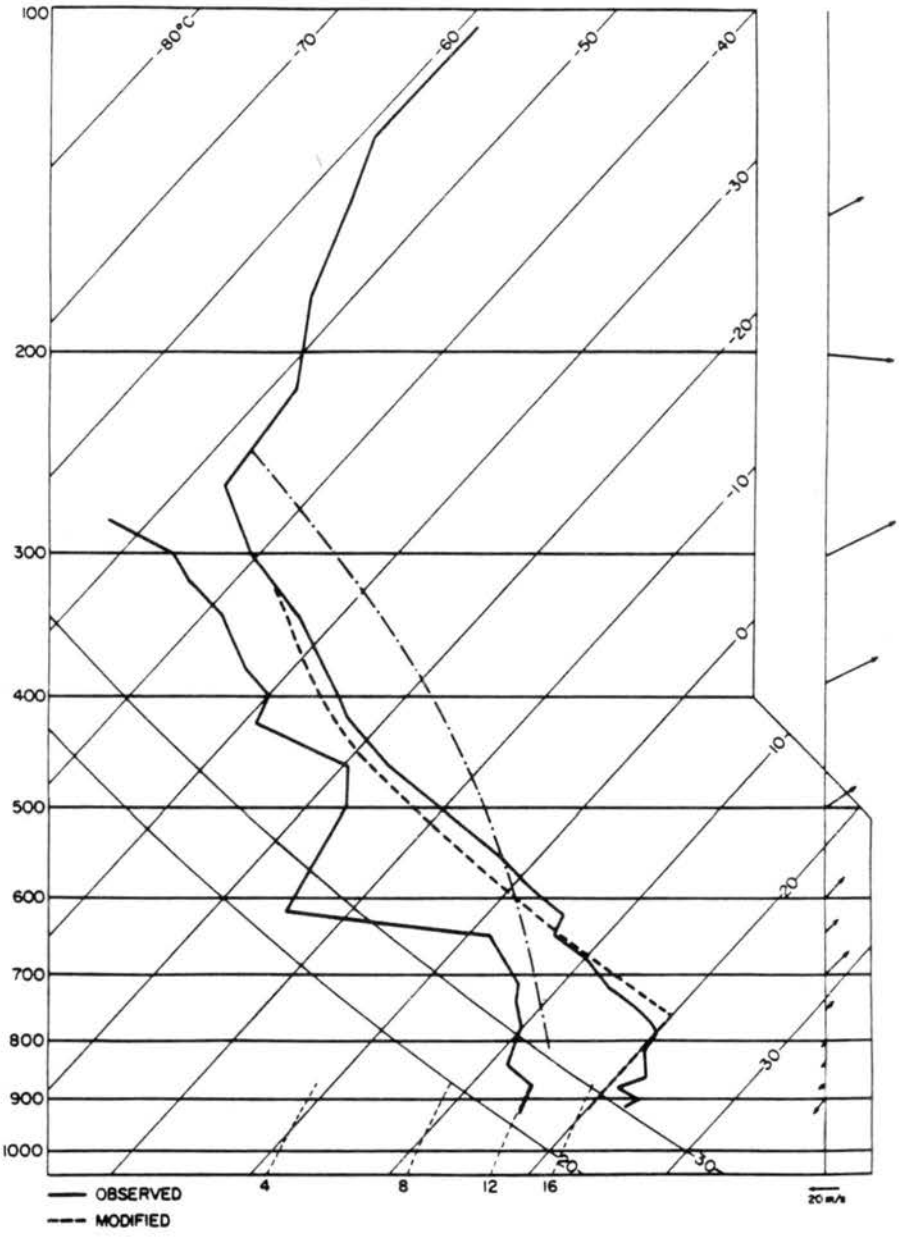


Figure 3.5: Environmental sounding of temperature and dewpoint temperature of the presquall environment from the Powderville, Montana site at 0111 UTC 3 August 1981 (solid lines). The sounding was modified below 50 kPa with aircraft soundings taken immediately ahead of the squall line. The thin dashed line represents the simplifications made to the observed temperature profile used to initialize experiments listed in Table 3.1. Parcel ascent based on the observed environment is shown as the dot-dash line.

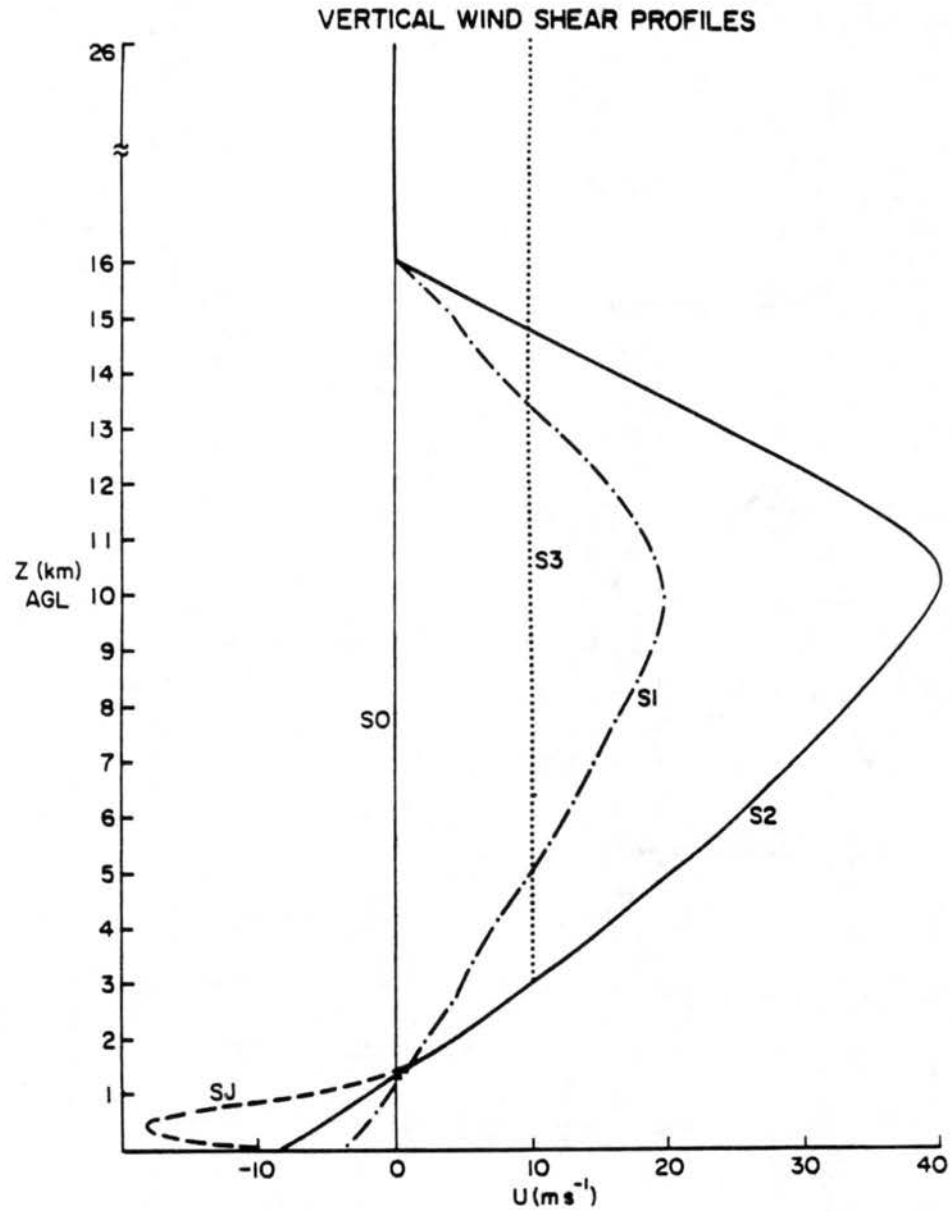


Figure 3.6: Vertical wind shear profiles used to initialize the 2-D homogeneous experiments. The labels S0,S1, S2, S3, SJ refer to the specific experiments discussed in the text.

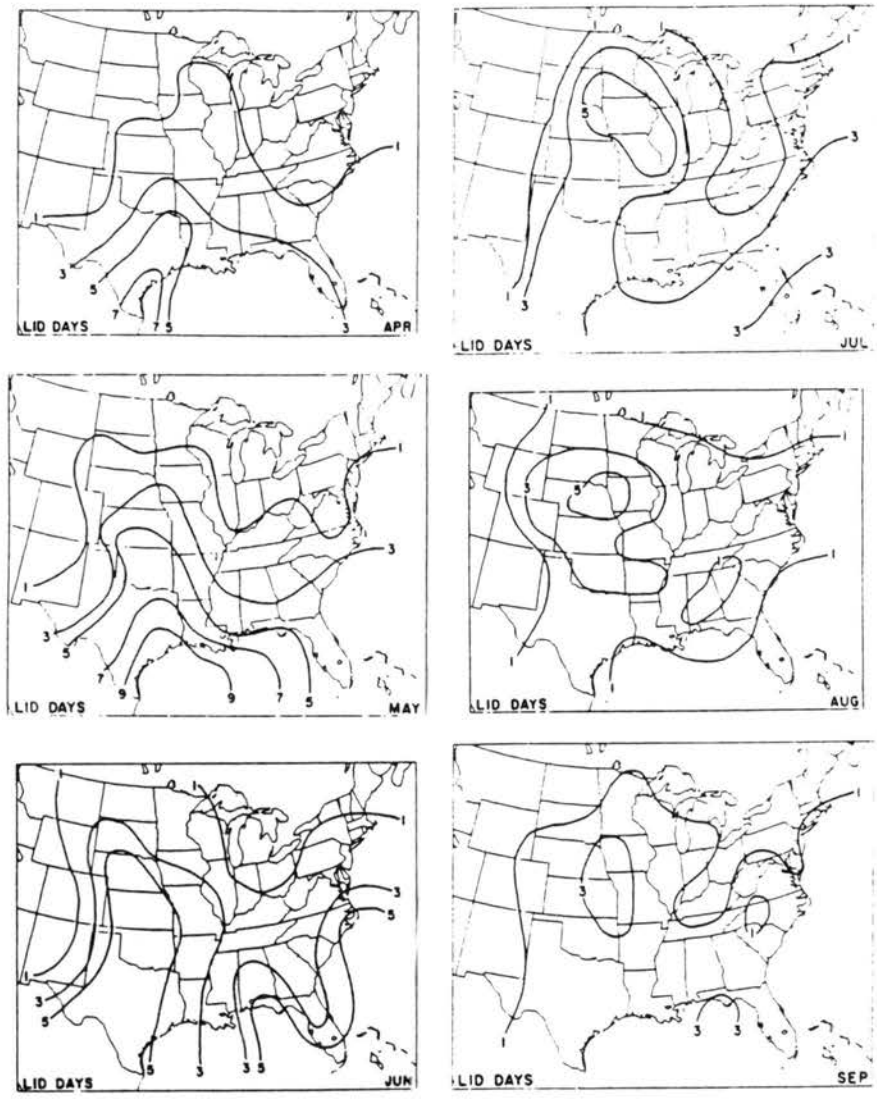


Figure 3.7: Mean number of lid days for April-September 1983-1986. From Farrell and Carlson (1989)

Table 3.1: Experiment Design

| Experiment | Description | Domain |
|---|---|---|
| S0 | No flow | x-z 400 × 23 km |
| S1 | Weak Shear | " |
| S2 | Strong Shear | " |
| S3 | Low-level Shear | " |
| LS2 | S2 Shear | x-z 800 × 23 km |
| LNU | Neutral ABL (S2 Shear) | " |
| SJ | Low-level Jet Profile | " |
| LNmix | Mixing Ratio (q=0) in ABL (S2 Shear) | " |
| LNcor | No Coriolis (S2 Shear) | " |
| 3D S2 | 3-D Unidirectional Shear (S2) | x-y-z 110 × 110 × 17 km |
| 3Ddir | 3-D Curved Hodograph | " |

the domain. Though not a very realistic representation of the atmosphere, this experiment was particularly useful in showing the structure of the primary gravity waves resulting from the initial convection. In experiments S1 and S2, shear is re-introduced in the model by specifying a quasi-linear profile over the depth of troposphere. These experiments illustrate the important affects of vertical wind shear on both the gravity waves and the convective development within the model. In an attempt to replicate the observed wind profile of Fig 3.5, the u-component in experiment S2 ranged from a surface minimum of -8 m $s^{-1}$ to a maximum of 40 m $s^{-1}$ at 10.5 km AGL. The u-component in the stratosphere was reduced linearly to zero by 16 km and held constant above that point. The u-component in experiment S1 was simply set to half the value used in experiment S2 at each level within the domain. The u-component in experiment S3 was identical to S2 up to a level of 3 km and set to a constant value of 10 m $s^{-1}$ above that level. Experiment SJ is identical to S2 above 1500 m but was modified below that point to form a low-level jet profile.

Experiments S0-S3 were initialized at $t$=0 and integrated for four hours. Experiments initialized on the larger domain (LS2, SJ, LNU, LDRY, and LCOR) were initialized at $t$=0 and integrated for five hours. The longer simulation times allow a detailed study of the evolutionary characteristics of the system and illustrate the ability of the simulated systems to produce sustained severe surface winds.

### 3.2.3 3-D horizontally homogeneous experiments

The second set of horizontally homogeneous experiments will be performed in a 3-D framework. The horizontal and vertical resolution and the top and lateral boundary conditions used for the 3-D experiments remain as stated for the 2-D experiments. The primary difference here will be the domain size and the vertical wind shear profiles chosen for study. Initial experiments suggested that a $x$-$y$-$z$ domain of 110 x 130 x 17.5 km would be required to capture the essential features of the squall line development. Because this was also the largest domain which could be placed into the CRAY-XMP computer at NCAR, we are limited in our ability to determine the affects of the gravity waves once they move beyond the convective region of the simulation. The discussion will focus instead on the character of the flow near the primary cells within the line. Since these experiments were

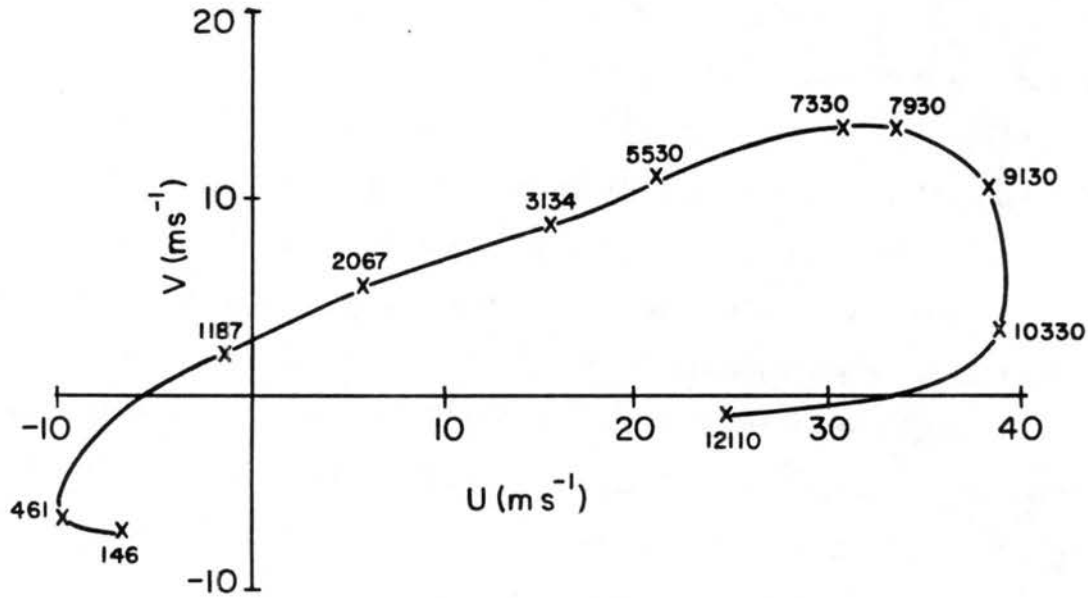


Figure 3.8: Vertical wind shear profiles used to initialize the 3-D horizontally homogeneous experiments.

expensive to run, the focus will center on the evolution of the flow during the first four hours of the simulation.

Experiments utilizing two vertical wind shear profiles will be presented. Experiment 3DS2 uses an identical profile to experiment S2, *i.e.* strong unidirectional shear through the entire troposphere. A second experiment was also run to determine the affects of directional shear on the simulated storm (3DDIR). The shear profile used to initialize the model in this simulation will be based on the observed CCOPE soundings (Fig 3.8).

# Chapter 4

# CASE STUDIES

In this chapter we present observational and numerical data for the 12-13 May 1985 PRE-STORM and the 2-3 August 1981 CCOPE derechos. The two case studies were chosen as representative examples of derechos which occur in environments characterized by strong static stability with the lowest few kilometers of the atmosphere. The primary goals of this chapter are: (i) to establish the regional-scale environmental thermodynamic and vertical wind shear profiles which accompanied the derecho development, and (ii) to identify possible mechanisms on the regional-scale and meso-scale which may have aided the production of the severe surface winds and system longevity. These goals will be accomplished by supplementing detailed observational analyses of the two case studies with regional-scale simulations described in 3.2.1. Details of the convective and meso-$\beta$-scale explicit cloud simulations will be the subject of Chapters 5 and 6. The chapter will be outlined as follows. Observational analyses and numerical simulations of the 12-13 May 1985 PRE-STORM derecho are presented in sections 4.1 and 4.2, respectively. Section 4.3 details the regional and mesoscale aspects of the 2-3 August 1981 CCOPE derecho and the main findings for these two cases are summarized in section 4.4.

## 4.1 The 12-13 May 1985 PRE-STORM derechos

### 4.1.1 Severe surface wind characteristics

An overview of the derecho development between 0000 and 1200 UTC 13 May is shown from a satellite perspective in Fig 4.1. The two derecho candidates during the period include the dry-line MCS in west-central Texas and the northwest Kansas MCS. The initial storms for the Texas derecho developed rapidly near 1000 UTC 13 May along the dry line and moved eastward through northeastern Texas, southeastern Oklahoma and central Arkansas.

These storms produced a swath of winds gusting from 25 to 36 m $s^{-1}$ and numerous reports of crop and property damage between 1300 UTC 13 May and 0000 UTC 14 May. The initial storms for the northwest Kansas derecho developed in southeastern Colorado near 0000 UTC 13 May and propagated northeastward to the Kansas-Nebraska border by 1200 UTC 13 May (Fig 4.1). Between 0600 and 1200 UTC 13 May, this MCS produced a swath of severe wind gusts and property damage extending from Syracuse City, Kansas (located southwest of Garden City, Kansas) to the border town of Superior, Nebraska. Peak surface winds of 36 m $s^{-1}$ were accompanied by golf ball size hail and heavy rain. Because of its nocturnal character and its location to the north of the warm frontal zone, the northwest Kansas derecho will become the focus of discussion for the remainder of this section.

### 4.1.2 Regional-scale environment

The regional-scale flow shows the PRE-STORM region was being influenced by the passage of a large trough over the Rocky Mountains and the development of a closed low at 70 kPa in eastern Colorado by 1200 UTC 13 May (Fig 4.2). Conditions ahead of the trough quickly changed during the night as a weak middle-level jet streak, accompanied by a narrow tongue of extremely dry air and large lapse rates in the 70-50 kPa layer ($>$ 22 K), rotated around the trough axis and into the lee of the Rocky Mountains by 1200 UTC. This layer appeared in the satellite imagery as a distinct dry slot which advected over the warm frontal zone and into the region of the northwest Kansas derecho by 1200 UTC (Fig 4.1).

Conditions at the surface were dominated by a quasi-stationary, but deepening low pressure center in the Texas Panhandle and a high pressure region that passed into central Iowa during the night (Fig 4.3). The surface low was associated with a pronounced dry line that extended southward across Texas and a slow-moving warm frontal zone that extended eastward across the Kansas-Oklahoma border. A secondary trough, characterized by surface pressure falls of 4 to 6 hPa, extended northward from the surface low just ahead of the windshift line in central Kansas. This trough, when coupled with increasing pressure to the north in the anticyclone, served to intensify the east-west pressure gradient across Kansas during the night.

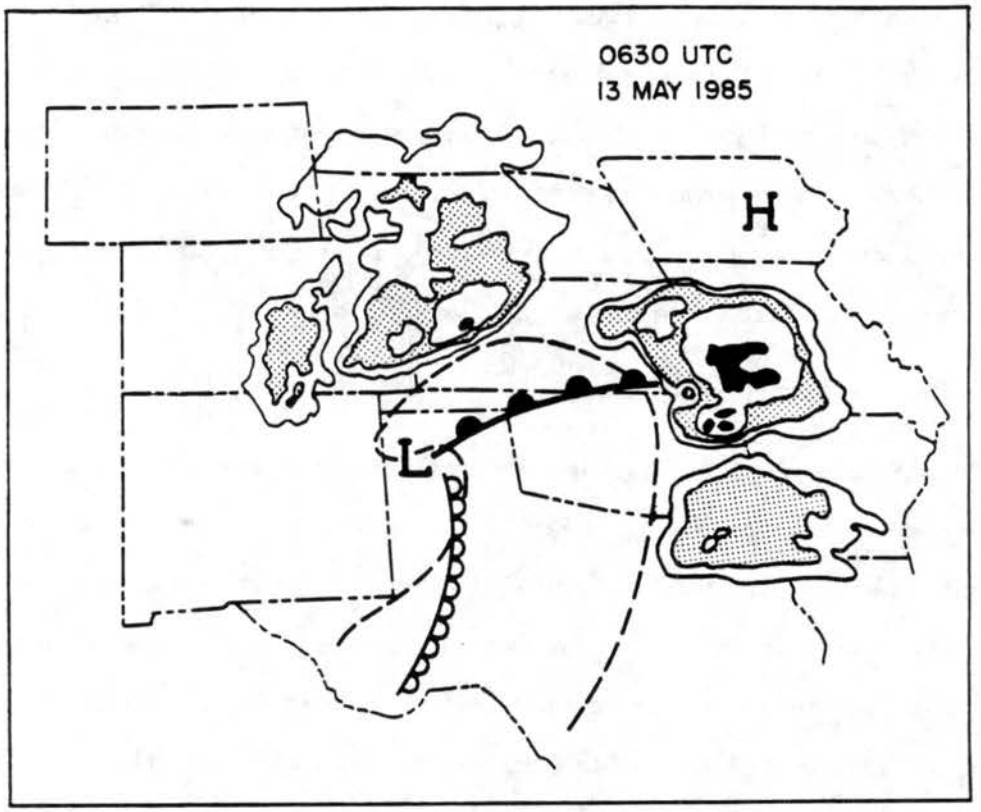


Figure 4.1: Satellite perspective of the 12-13 May 1985 derechos showing their relationship to the primary frontal zones and surface pressure fields (a) 0630 UTC 13 May 1985 and (b) 1200 UTC 13 May 1985. Scalloped regions in (b) outline derecho paths while triangles, circles, and x's denote individual reports of severe surface winds taken from Storm Data. Time of occurrence is as follows: triangles, 0600 to 1200 UTC 13 May; x's, 1300 UTC 13 May to 0000 UTC 14 May; circles, 0000 to 0400 UTC 13 May.

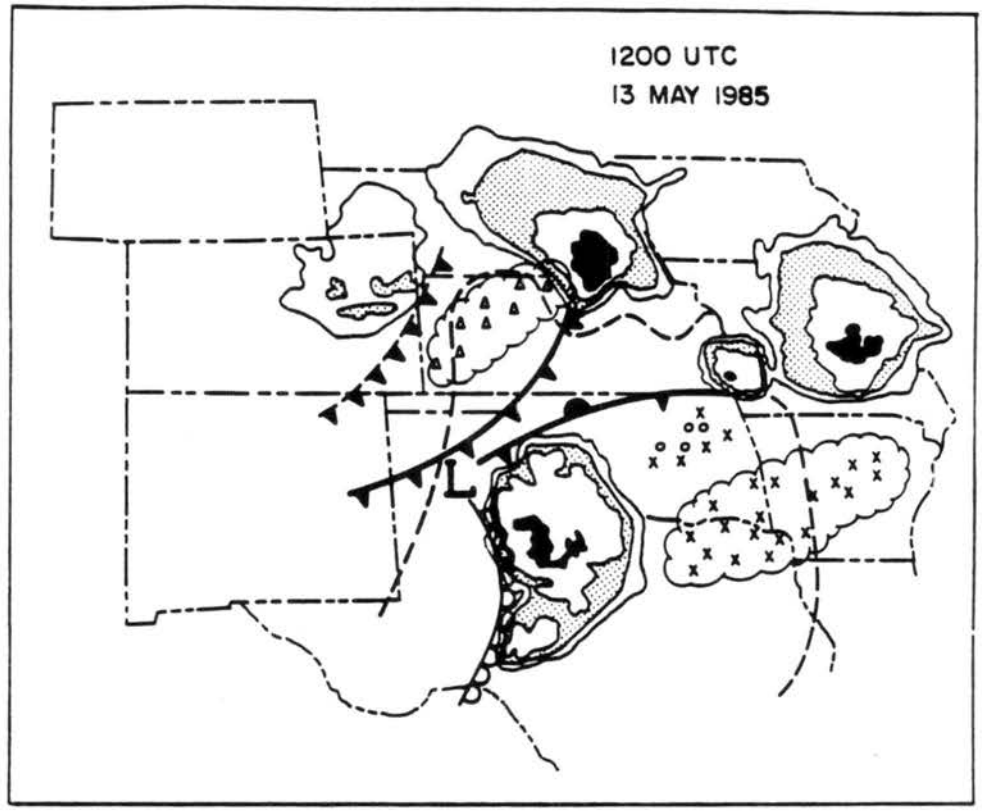


Figure 4.1: Continued.

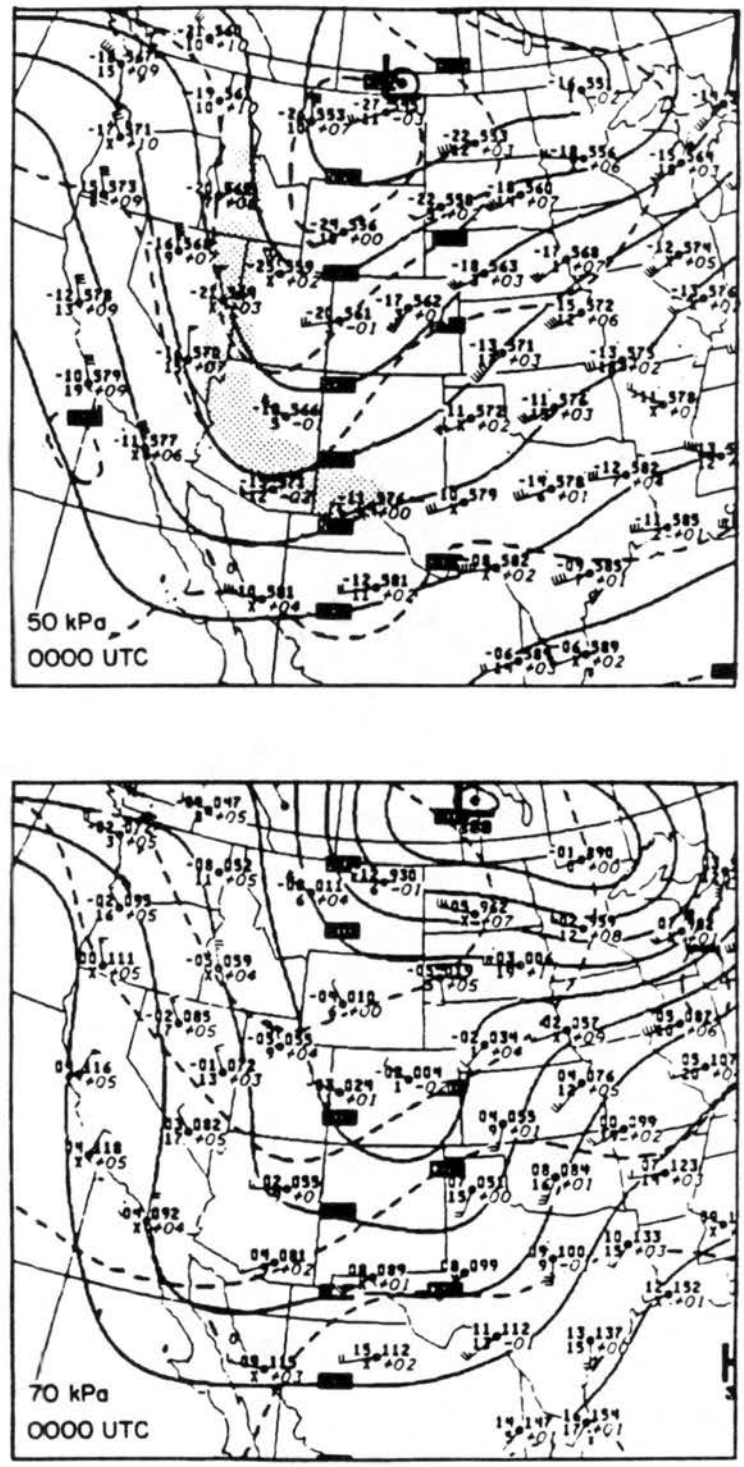


Figure 4.2: Standard NMC analyses of the 70 and 50 kPa constant pressure charts at 0000 and 1200 UTC 13 May 1985. Shaded region on the 50 kPa charts denote wind speeds in excess of 25 m $s^{-1}$.

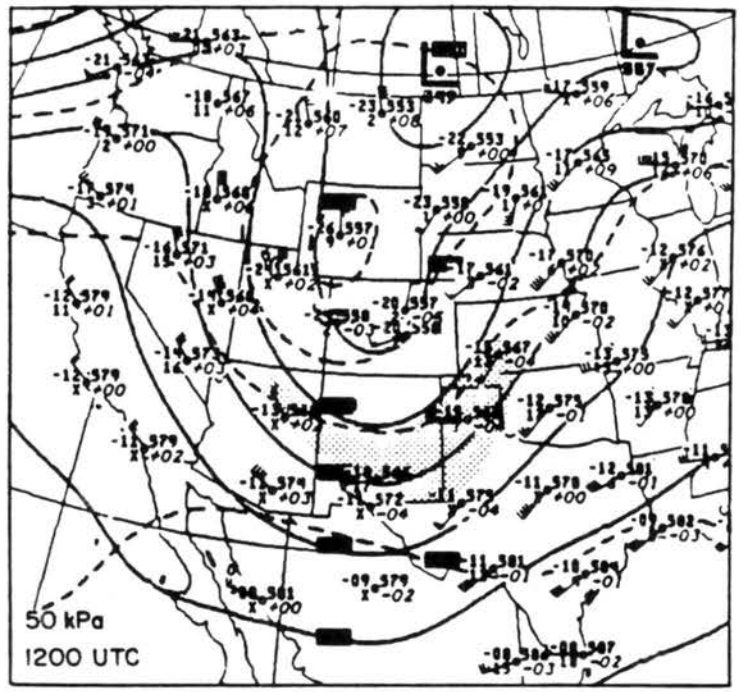


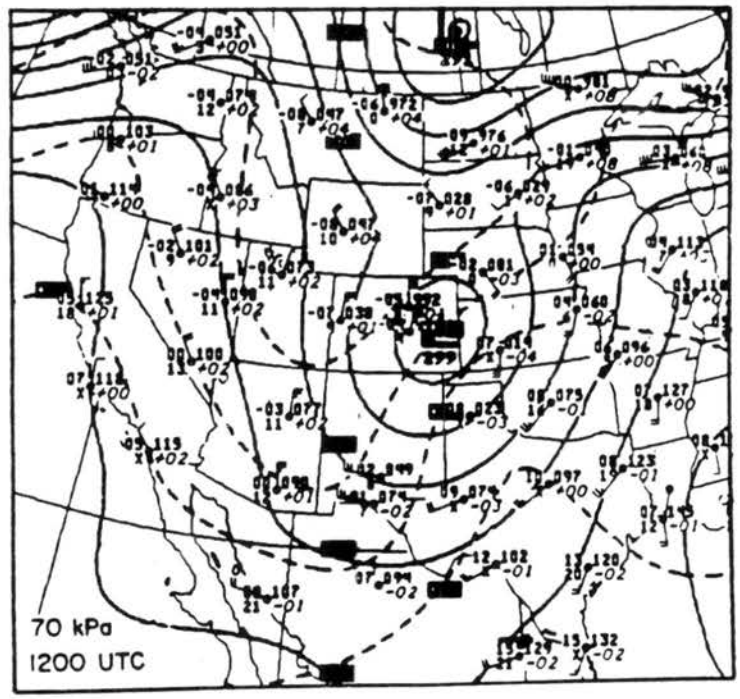


Figure 4.2: Continued.

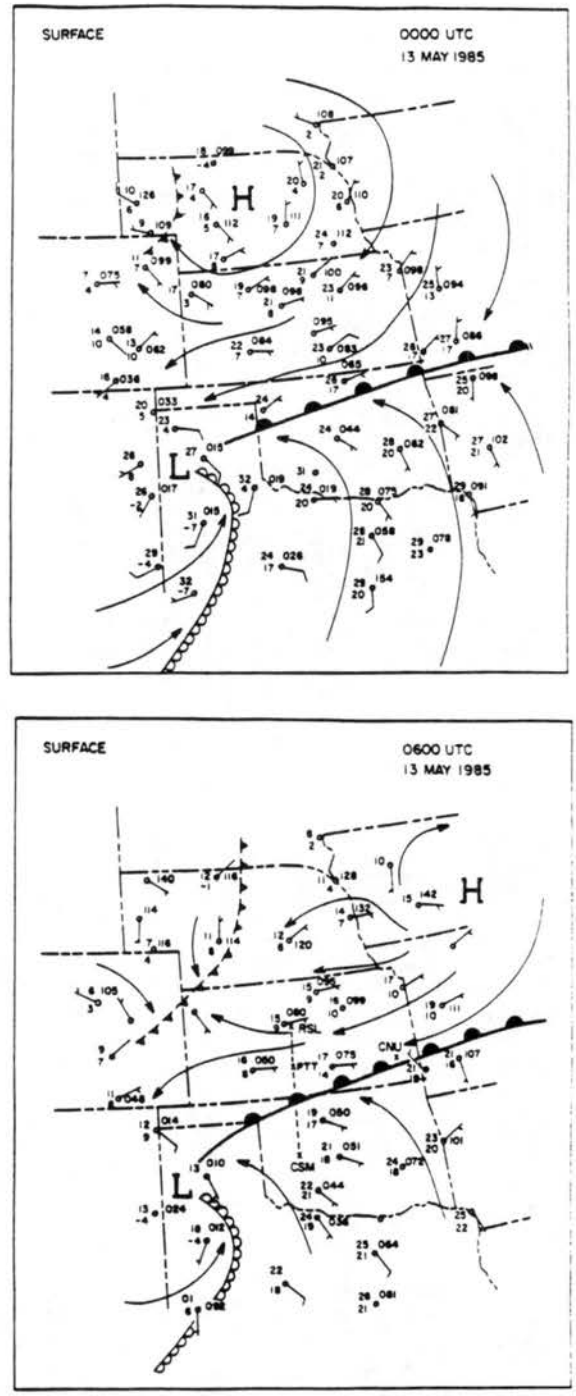


Figure 4.3: Standard surface analyses at (a) 0000 UTC, (b) 0600 UTC, and (c) 1200 UTC 13 May 1985. Temperature and dewpoint temperatures are in C°. The labels RSL, PTT, CSM, and CNU in (b) denote the PRE-STORM supplemental rawinsonde sites used in the analyses. The bold dashed line between RSL and CSM denotes the approximate location of a vertical cross-section shown in Fig 4.8.

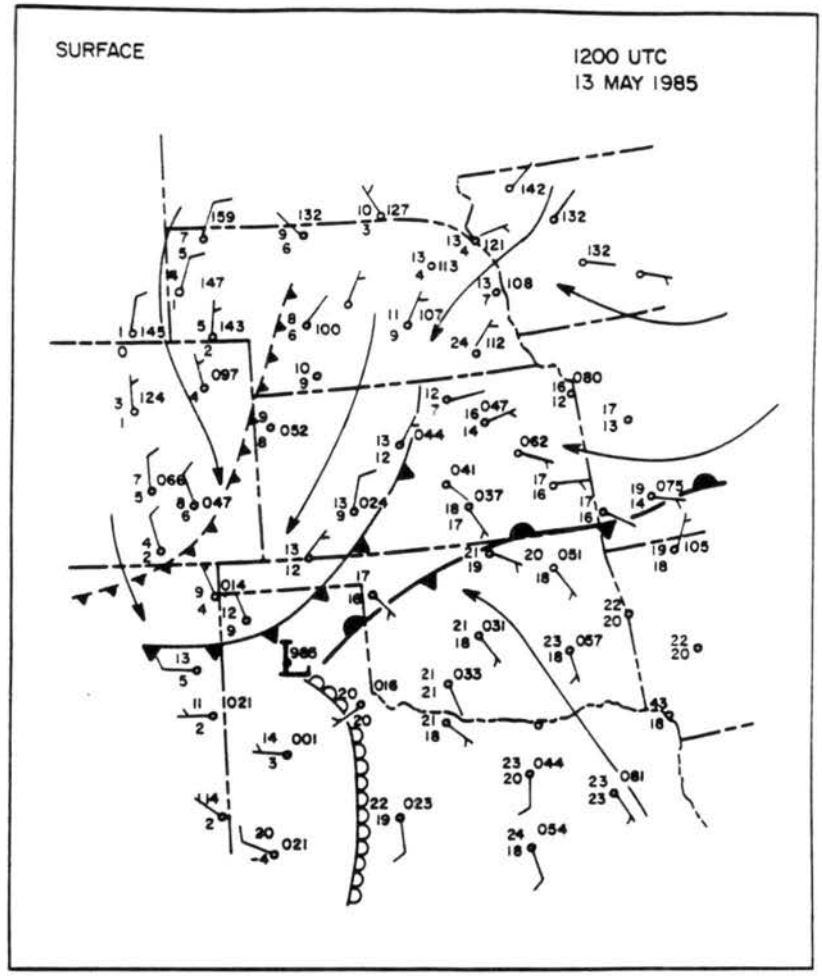


Figure 4.3: Continued.

### 4.1.3 Thermodynamic and vertical wind shear characteristics

The vertical structure of the airmass over the PRE-STORM region is shown in greater detail in Figs 4.4- 4.8. Soundings representative of the developments occurring in the western half of the network, and north of the warm frontal zone, are shown from the Pratt Kansas site (PTT) [Fig 4.4]. Notable features of Fig 4.4 include the rapid destabilization of the soundings in the 80-60 kPa layer and the strong low-level flow evident below 70 kPa. The soundings reveal that the derecho environment was characterized by three distinct thermodynamic layers within the troposphere: (i) a surface-based stable layer to 78 kPa, (ii) an elevated nearly adiabatic layer from 78 to 60 kPa, and (iii) an upper layer of intermediate stability extending to the tropopause. The lower stable layer in this case reflects the pre-existing stability north of the warm frontal zone, nocturnal cooling, and strong warm air advection near 75 kPa. The elevated well-mixed layer represents the intrusion of the dry tongue over the warm frontal zone evident in the satellite imagery of Fig 4.1. The soundings suggest that the well-mixed layer resulted from differential temperature advection in the 80 to 50 kPa layer as temperatures warmed near the base of the layer and cooled aloft in advance of the trough. This well-mixed layer deepened to the south (Fig 4.5) indicating a continued infusion of low-valued equivalent potential temperature ($\theta_e < 315$ K) over the warm frontal zone during the night.

The soundings also suggest the development of southerly and easterly low-level jet systems. The southerly low-level jet (Fig 4.6) was responsible for the strong warm air and moisture advection over the warm frontal zone. This is a typical component of the plains circulation (Blackadar 1957) which has been associated with a number of severe weather outbreaks. The time series of Fig 4.6 shows a rapid increase in the $v$-component from 0 to 25 m s$^{-1}$ between 0000 and 0900 UTC near the 85 kPa level. Figure 4.7 shows that a similar increase also occurred in the easterly $u$-component during the same time interval. This easterly jet of 20-26 m s$^{-1}$ was centered near 90 kPa within the stable air mass north of, and beneath, the east-west warm frontal zone.

The distinction between the two low-level jets is more clearly revealed in a vertical $y$-$z$ cross-section taken perpendicular to the warm frontal zone at 0600 UTC (Fig 4.8). Note the

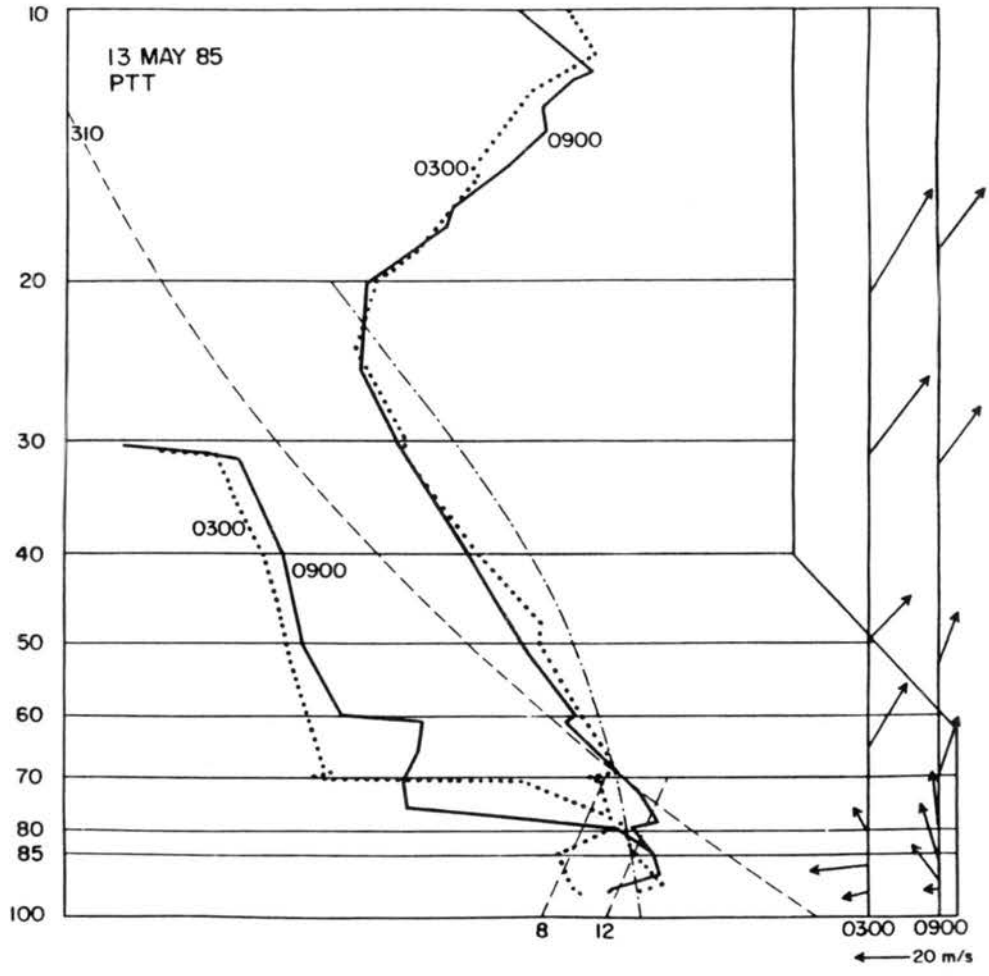


Figure 4.4: Skew-T log-P plot of the 0300 (dotted) and 0900 UTC (solid) 13 May 1985 soundings from PTT.

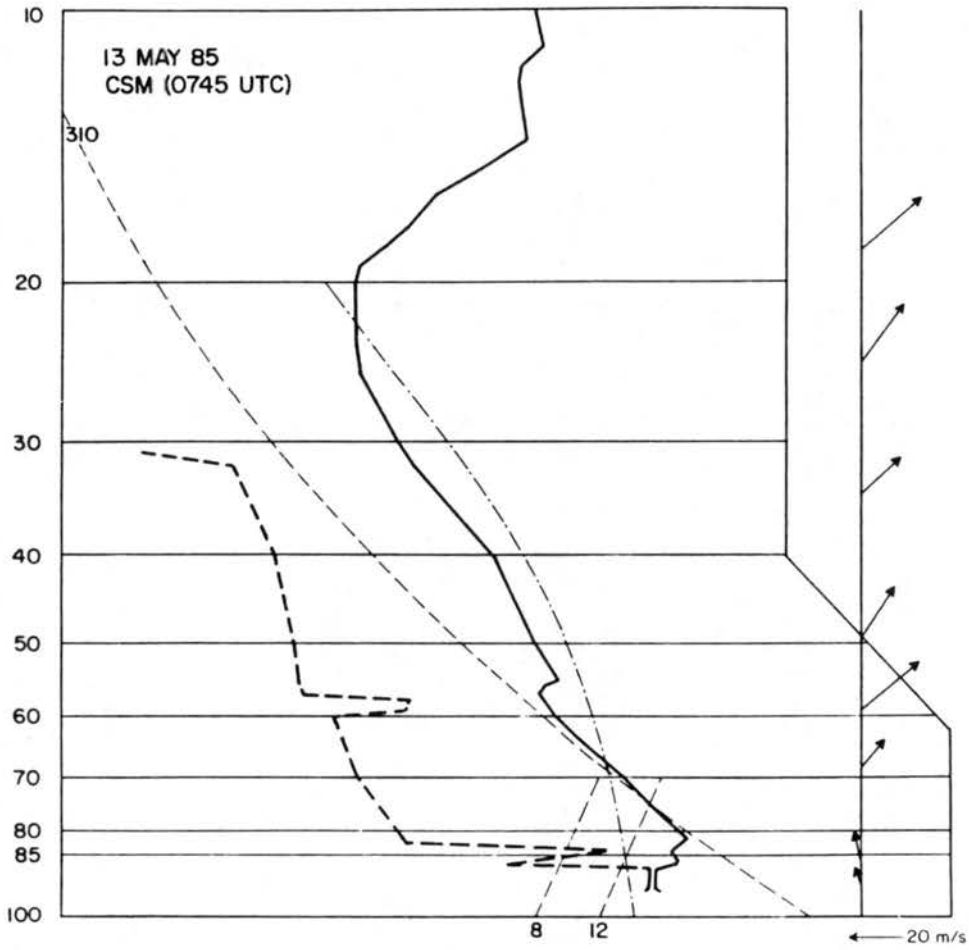


Figure 4.5: Skew-T log-P plot of the 0745 UTC 13 May 1985 sounding from CSM.

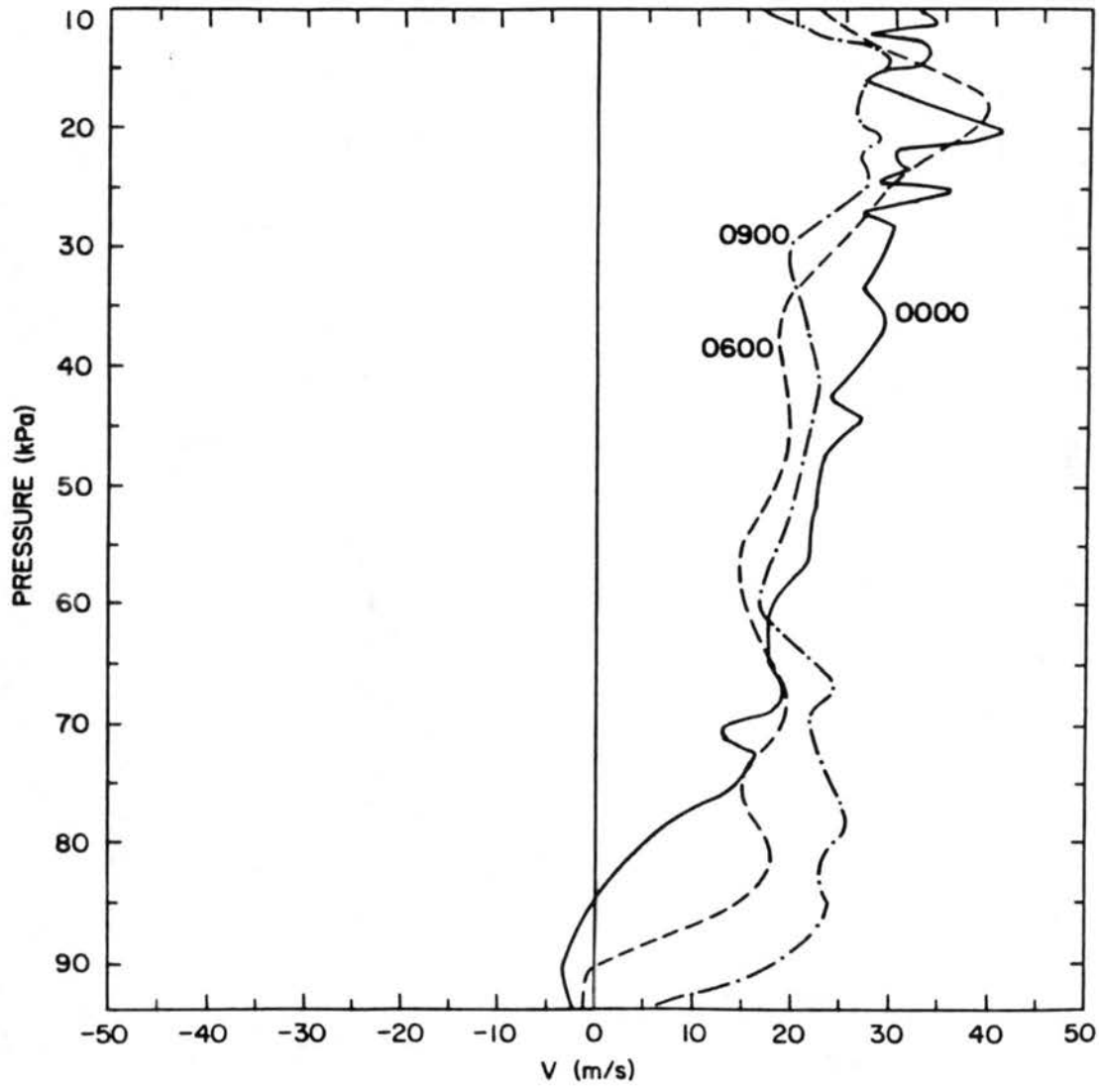


Figure 4.6: Vertical profiles of the $v$-component of flow from PTT at 0000 (solid), 0600 (dashed), and 0900 (dot-dashed) UTC 13 May 1985.

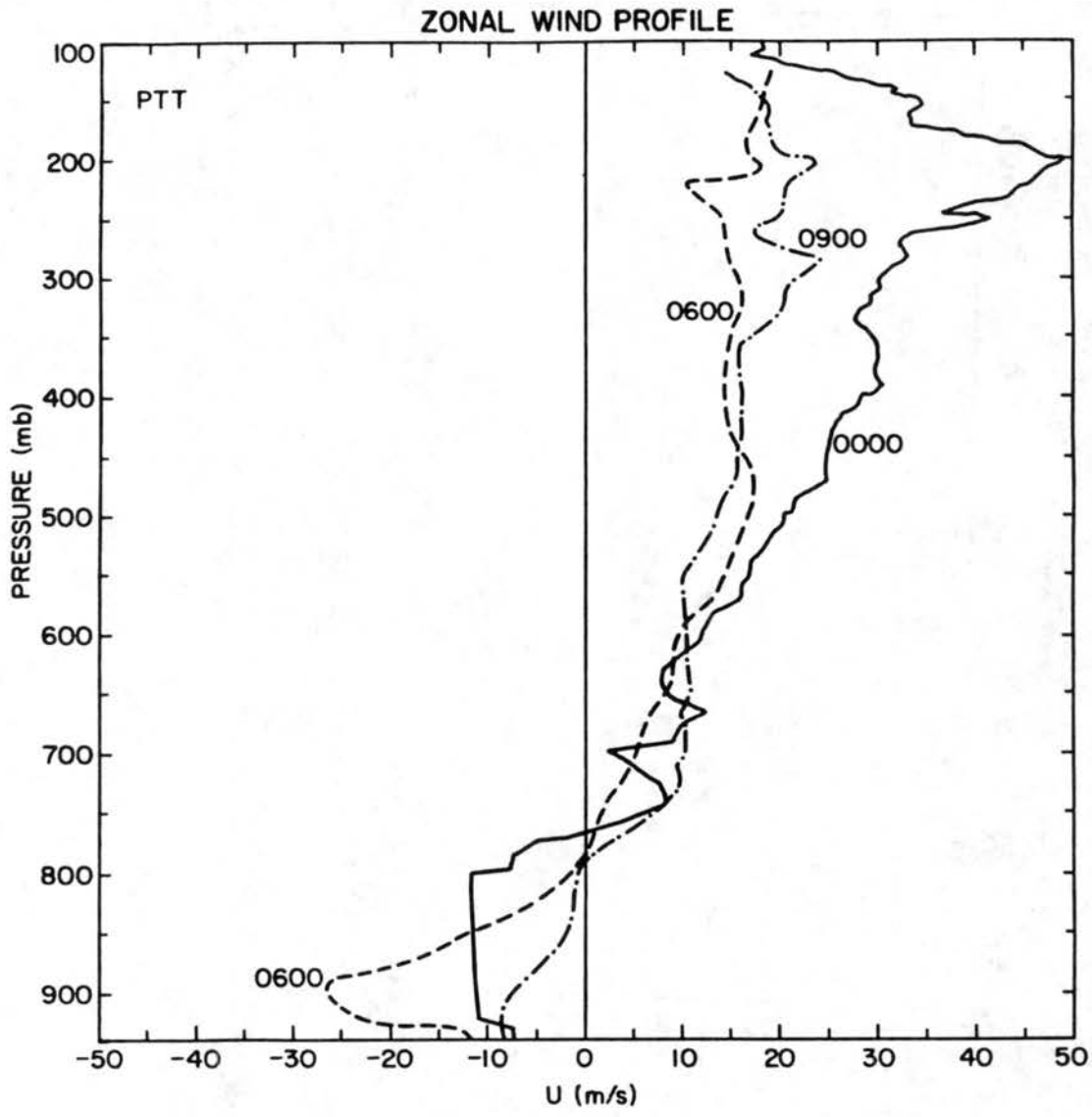


Figure 4.7: As in Fig 4.6 except for the $u$-component of flow.

correspondence between the band of strong easterly flow in excess of 15 m $s^{-1}$ extending from Russell (RSL) to Pratt (PTT) Kansas with the relatively low values of equivalent potential temperature ($\theta_e$). This suggests the air source for the easterly jet was beneath the warm frontal surface (denoted by the band of higher $\theta_e$ values within the southerly jet). This structure is similar to the cold conveyor belt discussed by Carlson (1980). Peak easterly speeds in excess of 25 m $s^{-1}$ were located within the jet core over PTT but similar values were later evident in the northern rawinsonde stations of RSL and FRI (not shown) suggesting a northward drift in the jet during the night. This may explain the sudden decrease of the easterly jet at PTT after 0600 UTC (Fig 4.7).

The rapid changes in the thermodynamic and vertical wind shear profiles evident in Figs 4.4- 4.8, appear to have been confined to the western portion of the domain. Soundings released in the eastern portion of the network (Fig 4.9), remained relatively stable and showed no signs of the strong, low-level easterly or southerly currents evident to the west. East-west differences across the network were also present in the surface pressure traces (Fig 4.10). Compare the rapid, nearly 1 hPa drop per hour in pressure in the western portion of the network to the relatively flat profiles farther to the east. Easterly surface flows increased in response to this pressure field with peak speeds of 20 m $s^{-1}$ recorded at Russell Kansas at 0900 UTC.

Behind the trough axis, the winds shifted to the northwest and the values of $\theta_e$ dropped to 310 K. An inspection of the available rawinsondes and surface data reveal two possible source regions for this air (Fig 4.11a,b). One such source was the dry air within the elevated mixed layer advecting over the warm frontal zone (Fig 4.11a). Another source was the dry and cool, easterly low-level air flow emanating from the cold anticyclone in central Nebraska (Fig 4.11b). This information, combined with the observed wind gusts from Russell at 0900 UTC, suggests that the derecho-producing storm may have processed the low-level momentum within the easterly low-level jet that formed beneath the warm frontal zone. This is consistent with the findings of Fortune (1989) whose composite flows of MCCs show a well defined inflow of cool air from the east.

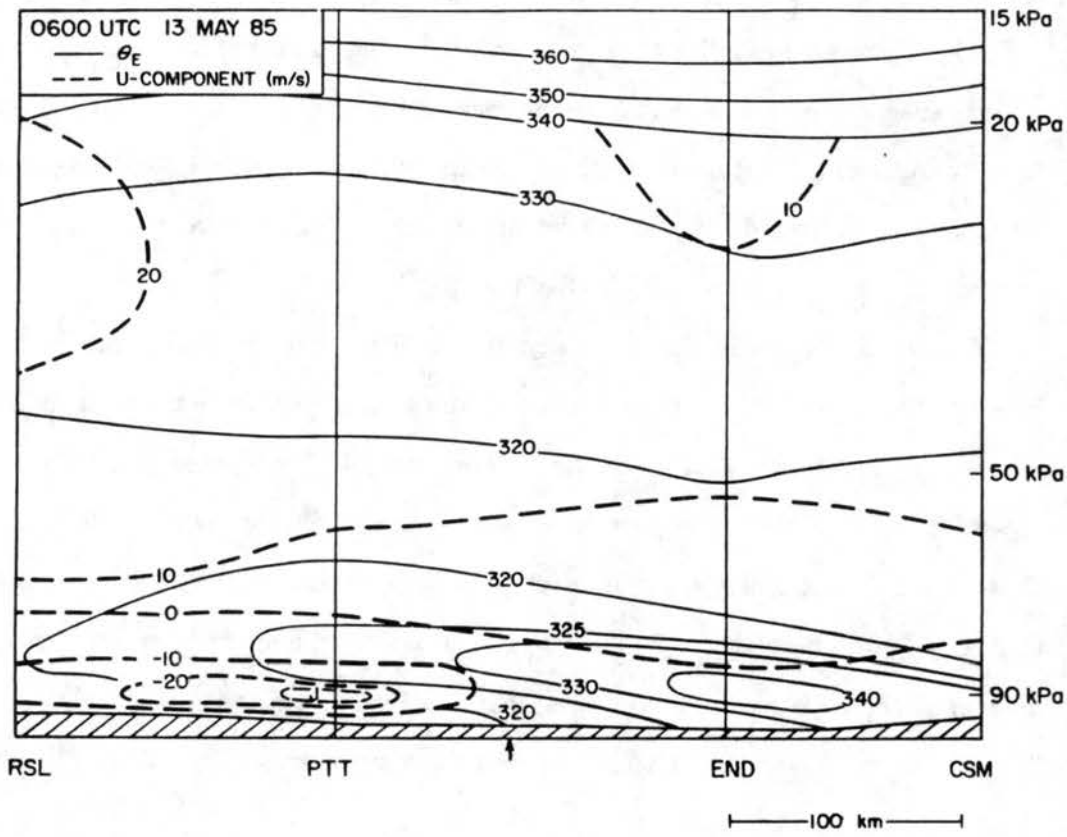


Figure 4.8: Vertical $y$-$z$ cross-section of equivalent potential temperature ($\theta_e$ in K) and the $u$-component of flow at 0600 UTC 13 May 1985. The bold arrow denotes the approximate location of the warm frontal zone. The location of the cross-section is shown as the bold dashed line in Fig 4.3.

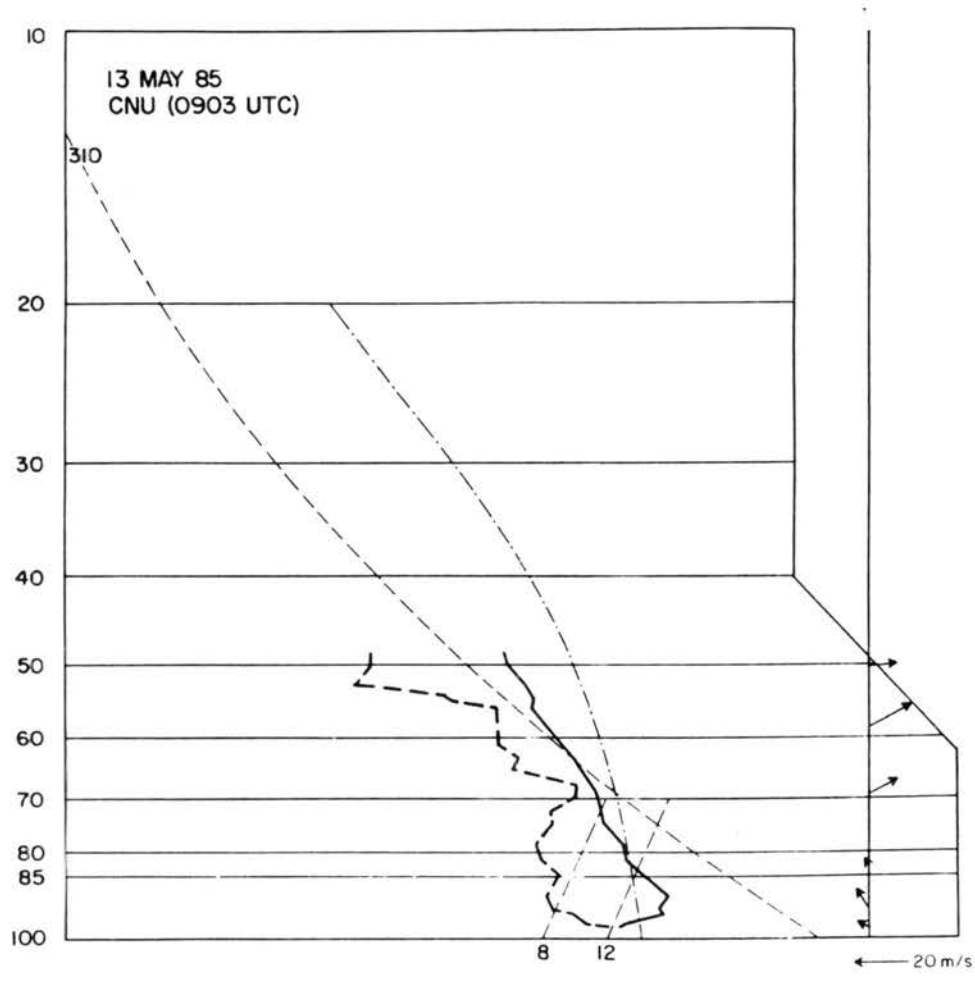


Figure 4.9: Skew-T log-P plot of the 0903 UTC 13 May 1985 sounding from CNU.

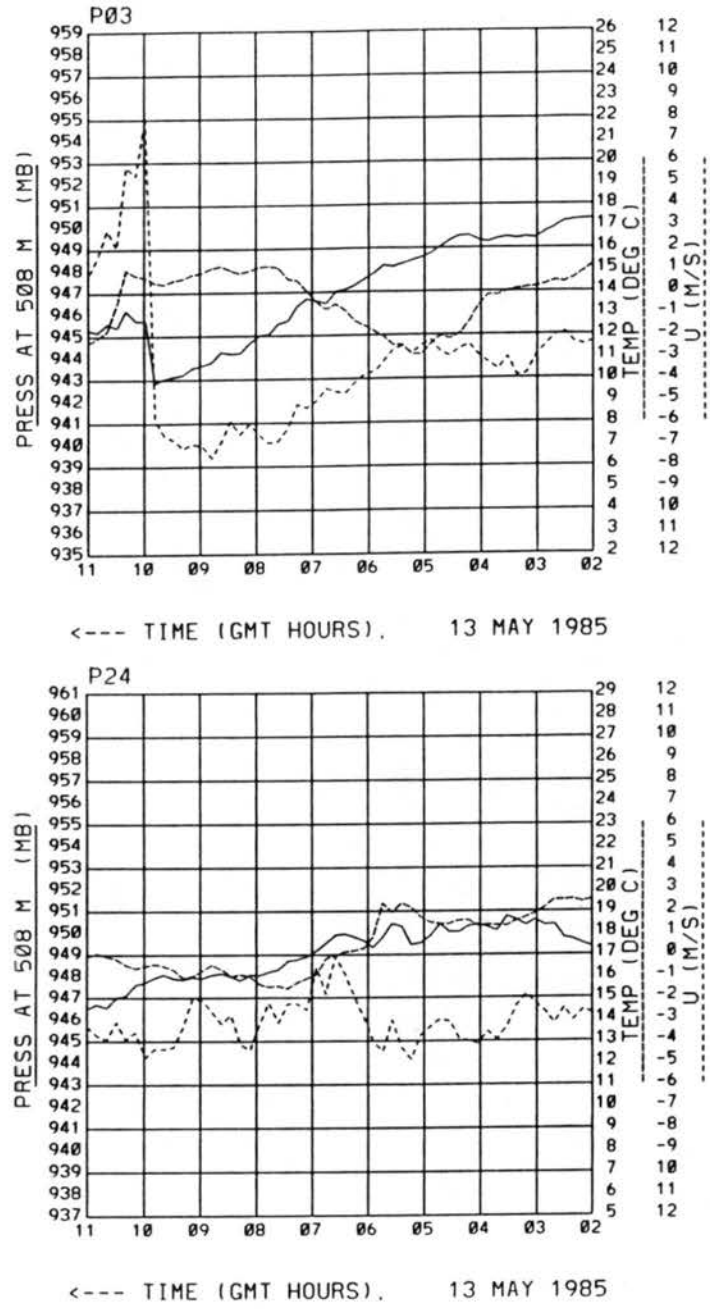


Figure 4.10: Time plots of temperature (dashed), $u$-component of flow (lightly dashed), and surface pressure (adjusted to 95 kPa)[solid] for (a) PAM station P03, and (b) PAM station P24 showing the east-west variations in the surface network that were present during the night of 12-13 May 1985.

## 4.2 Numerical results from the 12-13 May derecho

The observational data presented for the 12-13 May case study suggested several key environmental factors which may have influenced the development and timing of the northwest Kansas derecho. These include the rapid lee cyclogenesis that occurred as the middle-level jet streak rotated around the trough, the differential temperature and moisture advection which destabilized the soundings, the rapid development and northward movement of a strong low-level easterly jet which formed beneath the east-west orientated warm frontal boundary, and the east-west differences in the surface pressure tendencies across the network. Such east-west differences may begin to explain why the large MCC that developed over northeastern Oklahoma and southern Missouri between 0000 and 1200 UTC 13 May remained rather quiescent compared to the two derecho systems which formed near the jet systems in the western portion of the network.

To obtain a better understanding of the spatial and temporal characteristics of these features we now present the results from the nested, regional-scale simulations of the 12-13 May derecho. Presenting data between 00 and 1200 UTC 13 May from the large domain first shows that the model properly handled the movement of the middle-level trough axis from the Colorado-Utah border to central Colorado and the development of the closed low over northeastern Colorado [3] (compare Figs 4.2 and 4.12). During this period, the model also developed and moved a large region of upward vertical motion from eastern Colorado (Fig 4.12a) to west-central Nebraska (Fig 4.12b) along a track which closely matched the observed MCS (compare Figs 4.12 and Fig 4.1). This vertical motion was located in a region of strong positive vorticity advection ahead of the trough. This suggests that the observed MCS had strong, upper-level support on the synoptic-scale throughout its entire lifecycle.

The model generated flow fields near the surface are shown on the fine grid in Fig 4.13. Note that the model does a good job of moving the high pressure region into central Iowa and of generating the observed confluence zone along the Oklahoma-Kansas border. As observed, the lowest pressures extended southeastward from eastern Colorado to a closed low

---

[3]The cyclonic flow was more pronounced below this level suggesting the model, though underestimating its magnitude, was properly handling the development of the lee low.

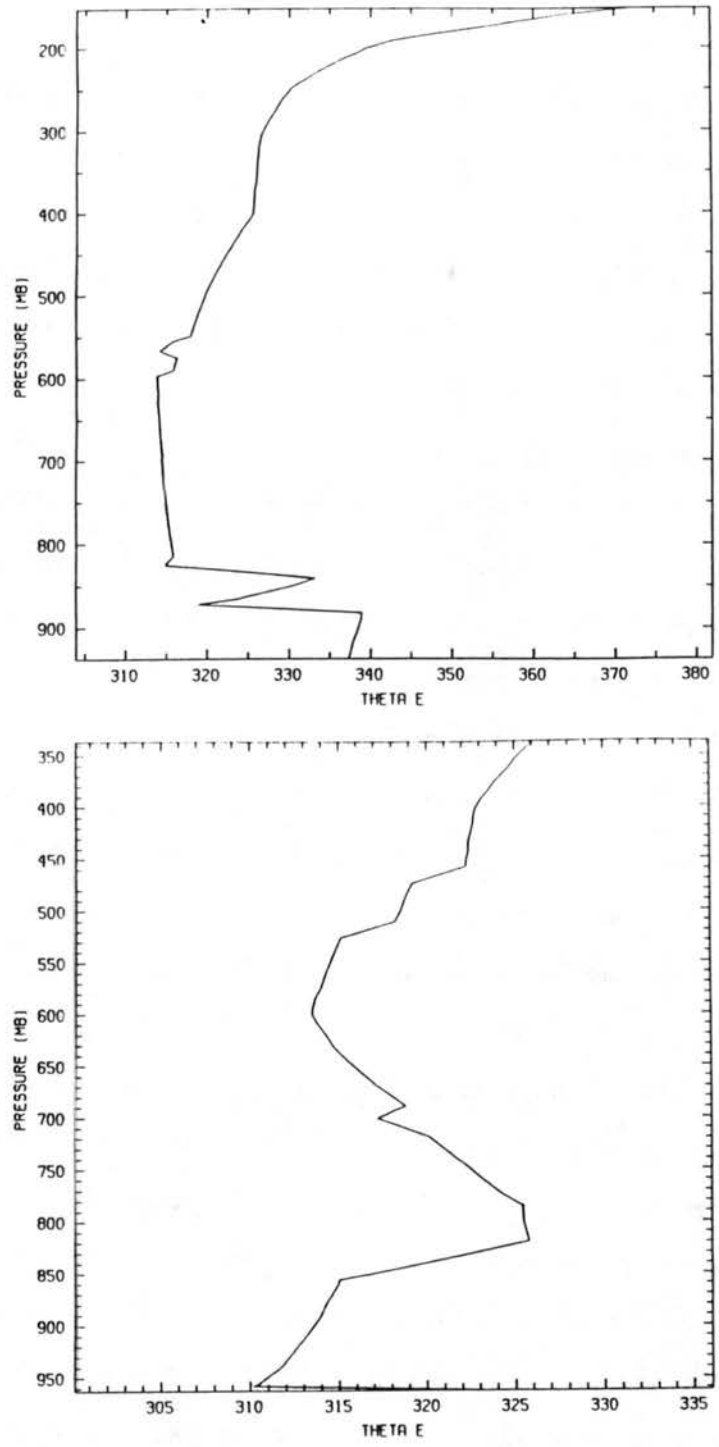


Figure 4.11: Vertical profiles of $\theta_e$ from: (a) the 0745 UTC 13 May 1985 sounding from CSM and (b) the 0720 UTC 13 May 1985 sounding from FRI.

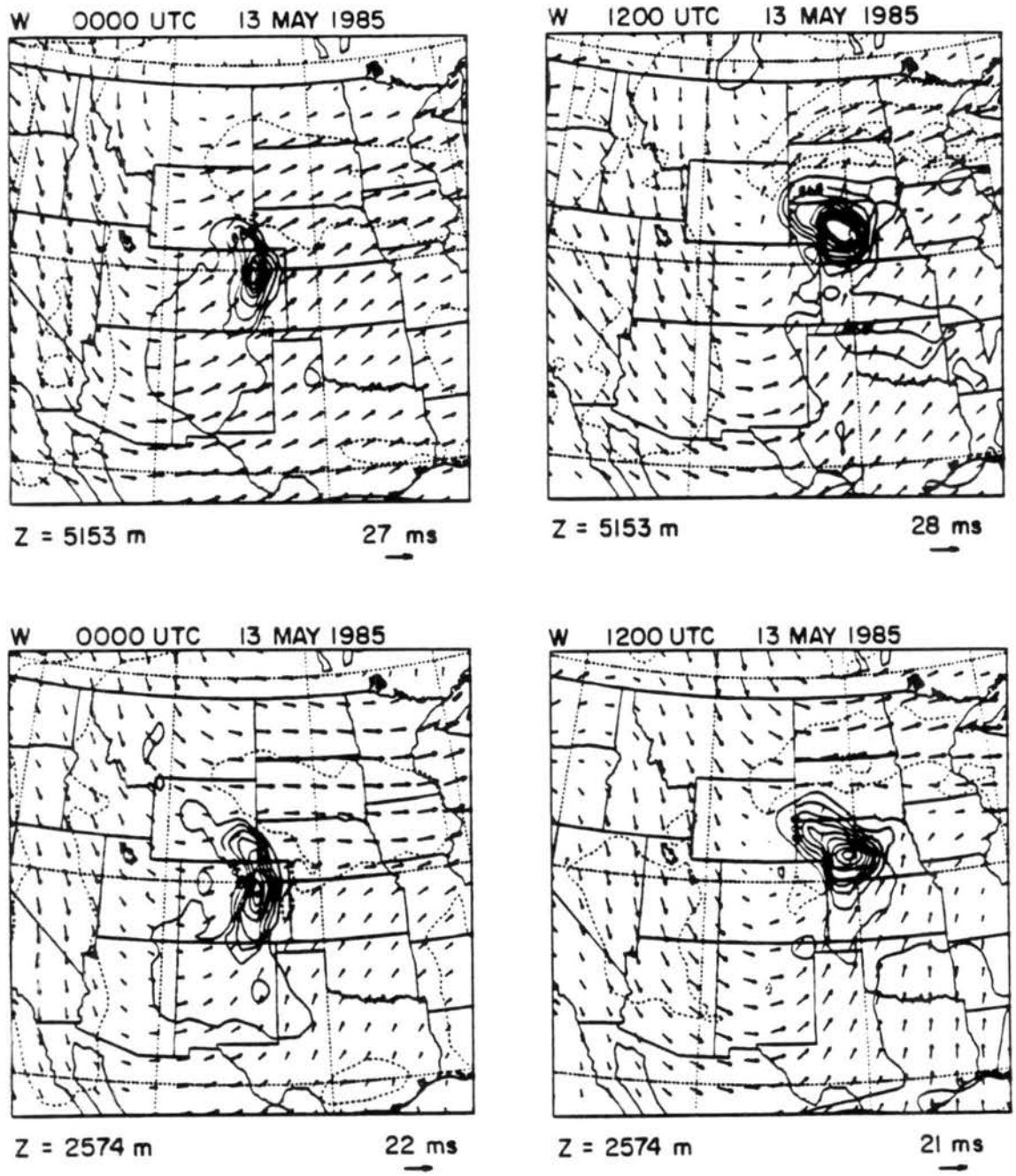


Figure 4.12: Model generated horizontal flow vectors on the coarse grid at the 2.5 and 5 km levels. Solid and dashed contours depict regions of upward/downward vertical motion fields, respectively. Contour interval is every 4 cm $s^{-1}$. Times shown are 12 and 24 hours after the initial start up of the model and correspond to the 0000 UTC and 1200 UTC 13 May 1985 time periods.

located within the Texas Panhandle region. The model also developed an inverted trough in the stable air mass north of the warm frontal zone in west-central Kansas (Fig 4.13c). The axis of this trough corresponded with the location of a low-level easterly wind maximum which intensified from 10 to 25 m $s^{-1}$ as it moved east-northeastward from eastern Colorado to the Kansas-Nebraska border between 0000 and 1200 UTC (Figs 4.13a-c). Quite remarkably, this track was nearly identical to that taken by the derecho (compare to Fig 4.1b) suggesting that the low-level wind maximum may have played a key role in the location and timing of the observed derecho.

Vertical cross-sections through the simulated wind maximum reveal it was the focal point of two low-level jet systems (Fig 4.14- 4.17). Note the similarity of the modeled jets to the observed jets in Figs 4.6 and 4.7. The model shows that the southerly low-level jet (Figs 4.14 and 4.15) formed near the Colorado border and quickly intensified as it drifted slowly eastward during the period. This jet was centered near 1500 m AGL and was responsible for the strong warm air and moisture advection which increased the values of convective available potential energy (CAPE) over the warm frontal zone in the pre-derecho environment. The easterly jet (Figs 4.16 and 4.17), as in the observations, formed parallel to and beneath the warm frontal zone (Fig 4.18). This jet extended across the state of Kansas with peak speeds of 18 to 22 m $s^{-1}$ located within the western portion of the state near the axis of the southerly low-level jet.

Significantly, both jets terminated within the primary updraft of the modeled MCS and thus represent a possible regional-scale source of low-level momentum which could have been processed by the derecho-producing MCS. Though we have not explicitly resolved the convective-scale motion within this simulation, we expect that the strong vertical pressure gradients which are typically present near intense convective systems could act to transport the momentum within either one of these low-level jets to the surface. We investigate this process in greater detail in the explicit simulations of Chapter 5.

### 4.2.1 Low-level jet dynamics

The model development, movement, and timing of the two jet systems in the western portion of the network helps to clarify the spatial and temporal characteristics of the jet

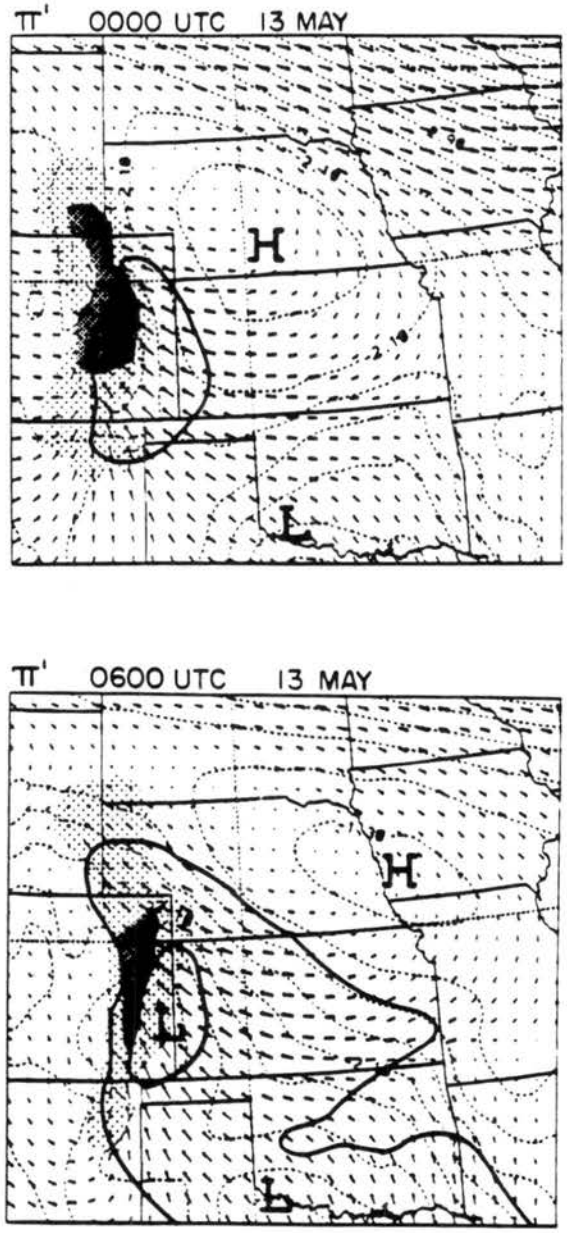


Figure 4.13: Model generated horizontal flow vectors and perturbation pressure ($\pi'$, contoured every .2 J kg$^{-1}$ K$^{-1}$) fields on the fine grid for the 460 m level at (a) 0000 UTC 13 May, (b) 0600 UTC 13 May, and (c) 1200 UTC 13 May 1985. Stippling denotes region of updraft at the 1.6 km level in excess of 6 cm s$^{-1}$ (lightly stippled) and 18 cm s$^{-1}$ (heavy stippling). The bold H and L denote regions of high and low pressure, respectively. The bold solid lines denote wind speeds in excess of 10 and 20 m s$^{-1}$.

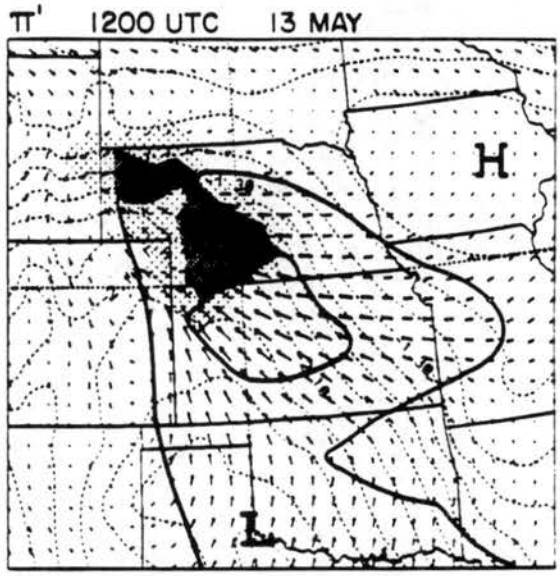


Figure 4.13: Continued.

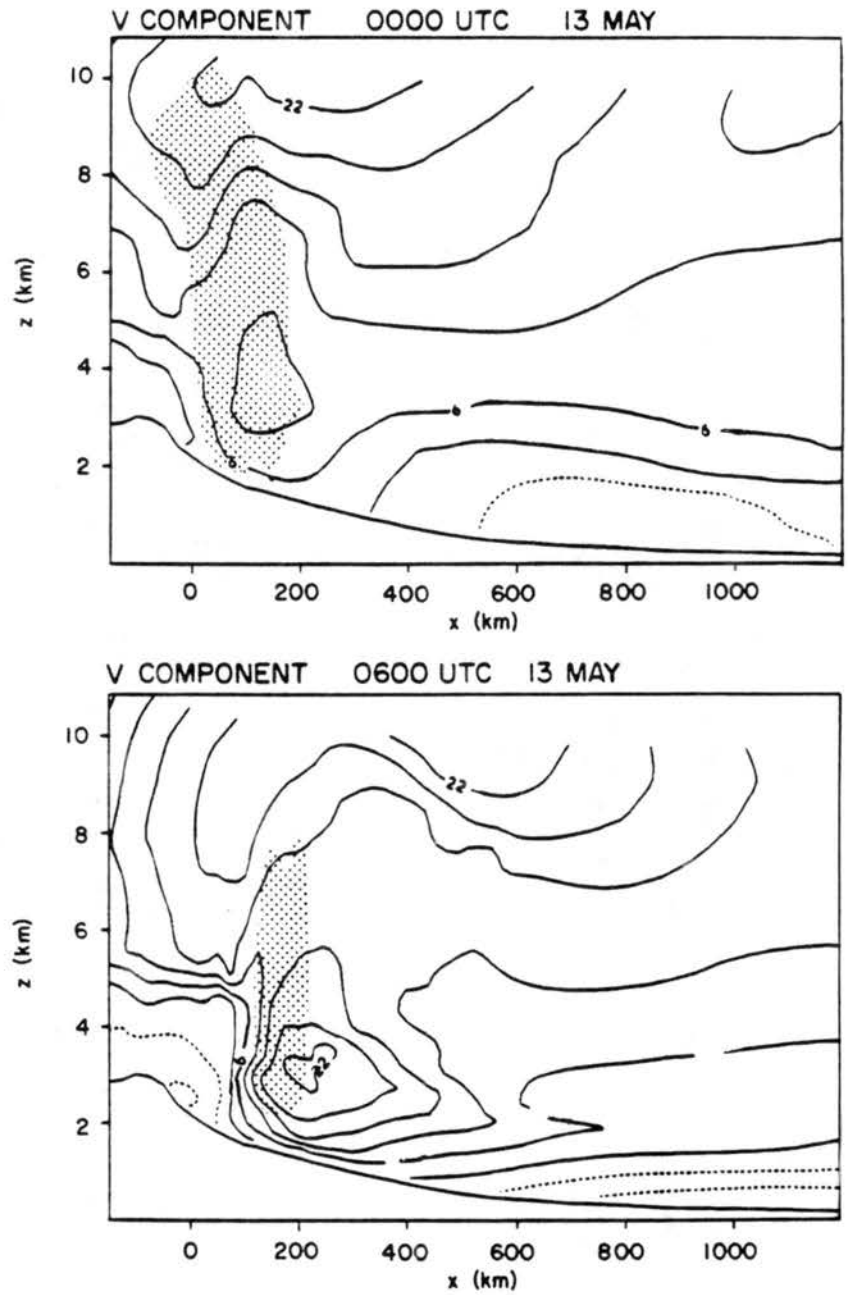


Figure 4.14: Vertical $x$-$z$ cross-section of the $v$-component of flow (contoured every 4 m $s^{-1}$) at (a) 0000 UTC, (b) 0600 UTC, and (c) 1200 UTC 13 May 1985. Stippled regions denote updraft in excess of 6 cm $s^{-1}$. The cross-sections were taken at the midpoint of the domain shown in Fig 4.13.

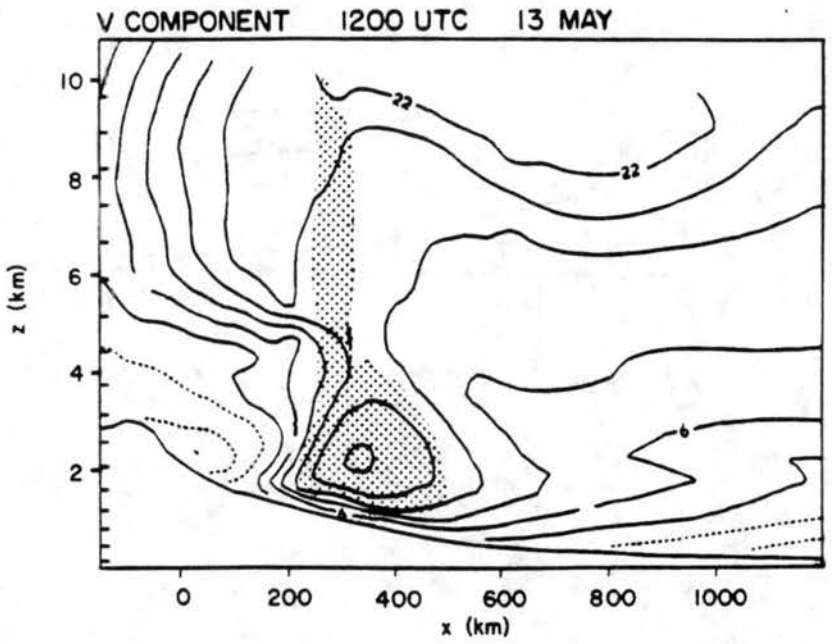


Figure 4.14: Continued.

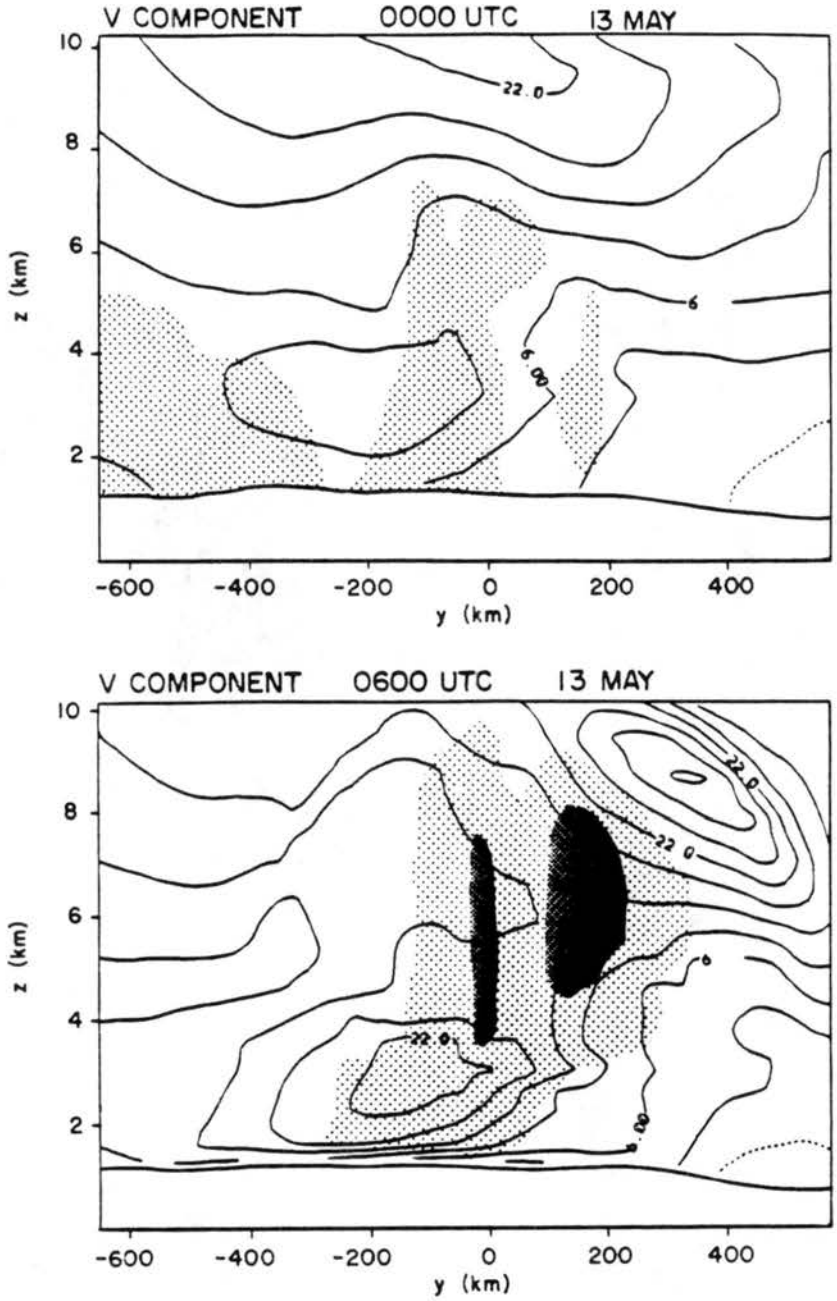


Figure 4.15: Vertical $y$-$z$ cross-section of the $v$-component of flow (contoured every 4 m $s^{-1}$) at (a) 0000 UTC, (b) 0600 UTC, and (c) 1200 UTC 13 May 1985. Stippled region in (a) denotes updraft in excess of 2 cm $s^{-1}$. Stippled region in (b) and (c) denote updraft in excess of 6 (lightly shaded) and 18 (darker shading) cm $s^{-1}$. The cross-sections were taken along the axis of the southerly low-level jet evident in Fig 4.14.

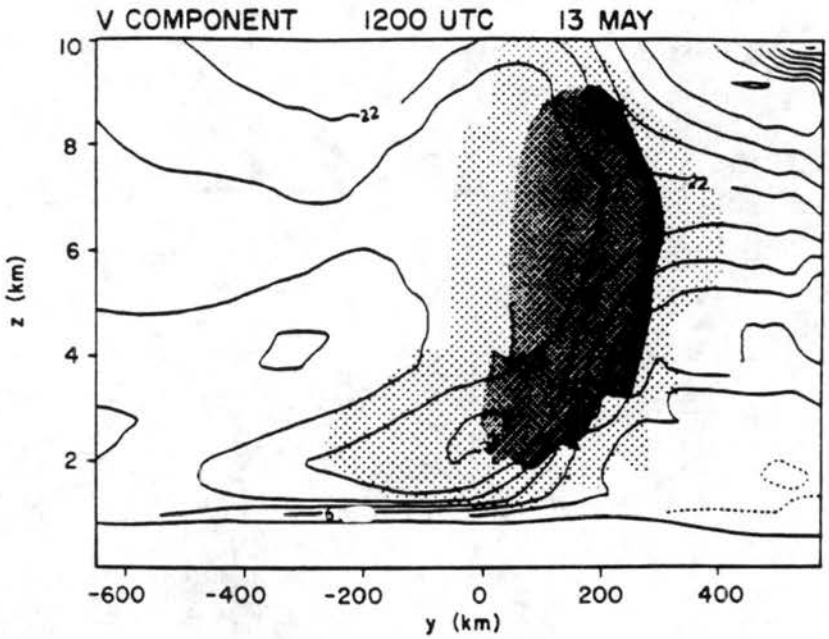


Figure 4.15: Continued.

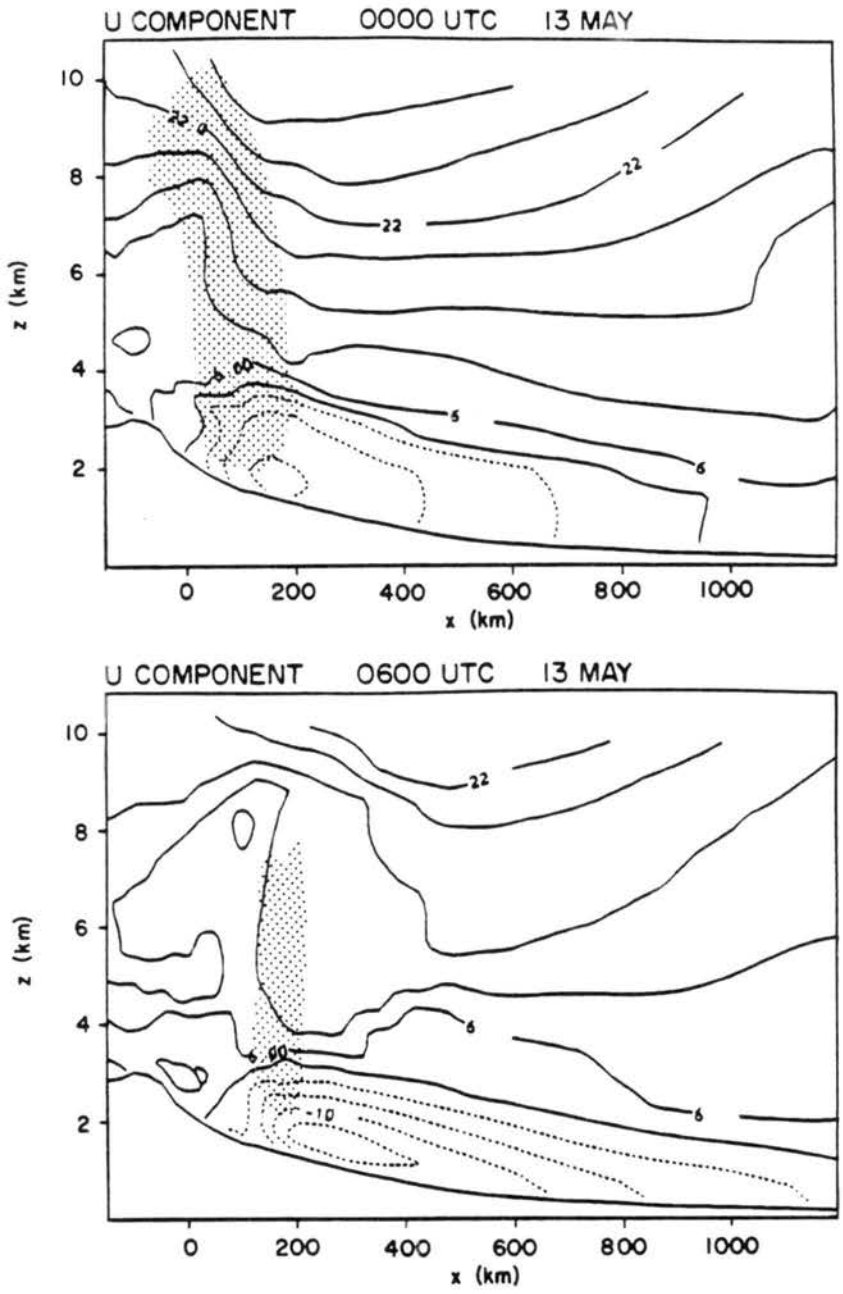


Figure 4.16: Vertical $x$-$z$ cross-sections of the $u$-component of flow (contoured every 4 m $s^{-1}$) at (a) 0000 UTC, (b) 0600 UTC, and (c) 1200 UTC 13 May 1985. Stippled regions denote updraft in excess of 6 cm $s^{-1}$. Approximate location of the cross-sections correspond to the midpoint of the domain shown in Fig 4.13.

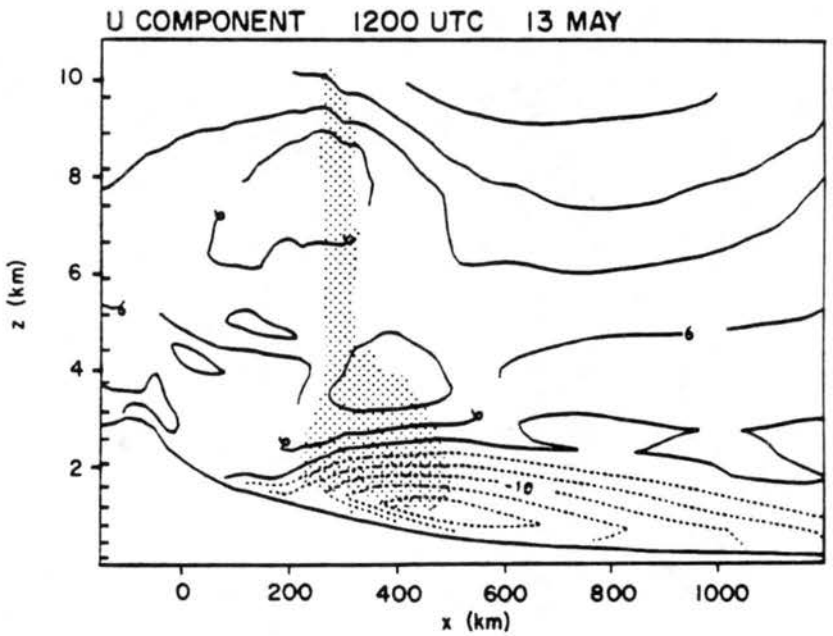


Figure 4.16: Continued.

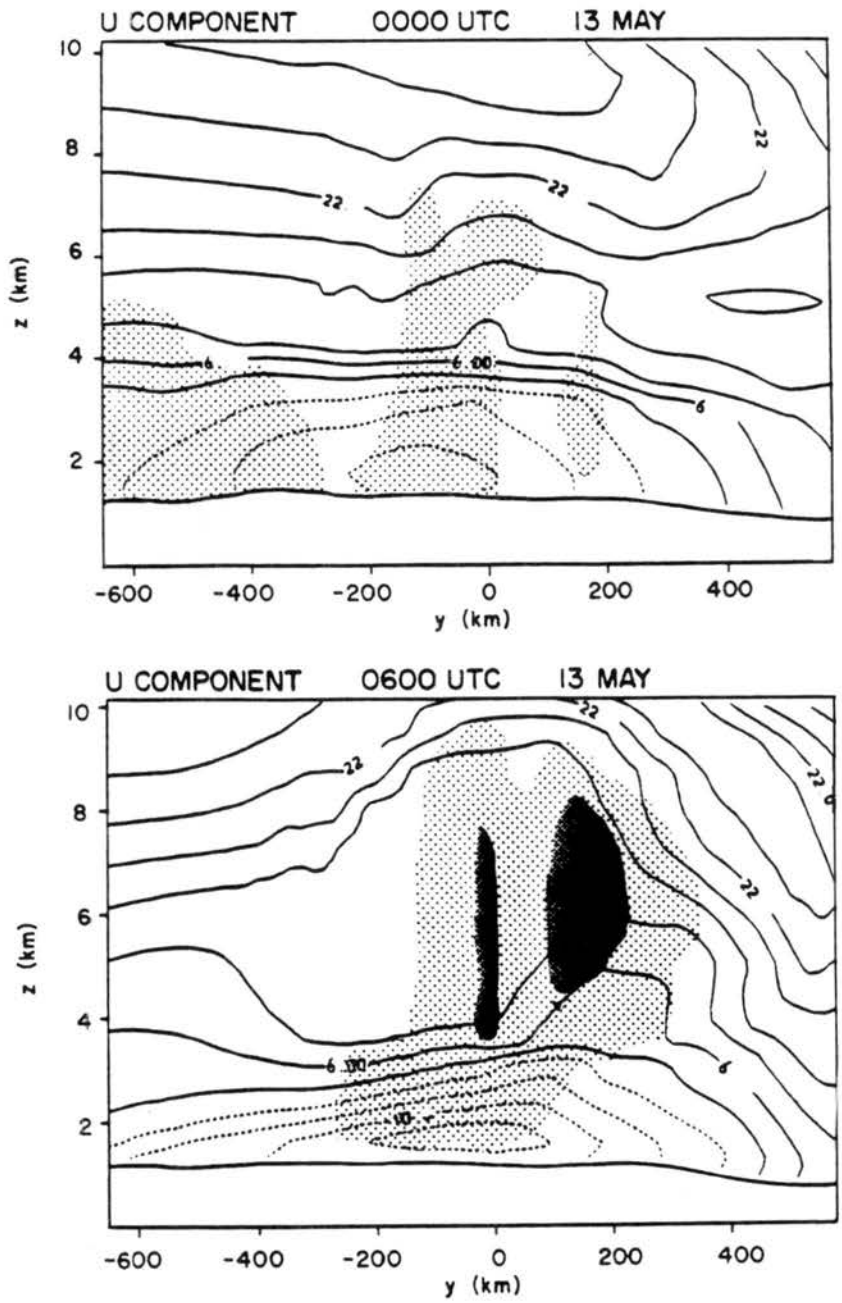


Figure 4.17: Vertical $y$-$z$ cross-sections of the $u$-component of flow (contoured every 4 m $s^{-1}$) at (a) 0000 UTC, (b) 0600 UTC, and (c) 1200 UTC 13 May 1985. Stippled region in (a) denotes updraft in excess of 2 cm $s^{-1}$. Stippled regions in (b) and (c) denote updraft in excess of 6 (lightly shaded) and 18 (darkly shaded) cm $s^{-1}$. The cross sections were taken along the axis of the low-level southerly jet evident in Fig 4.14.

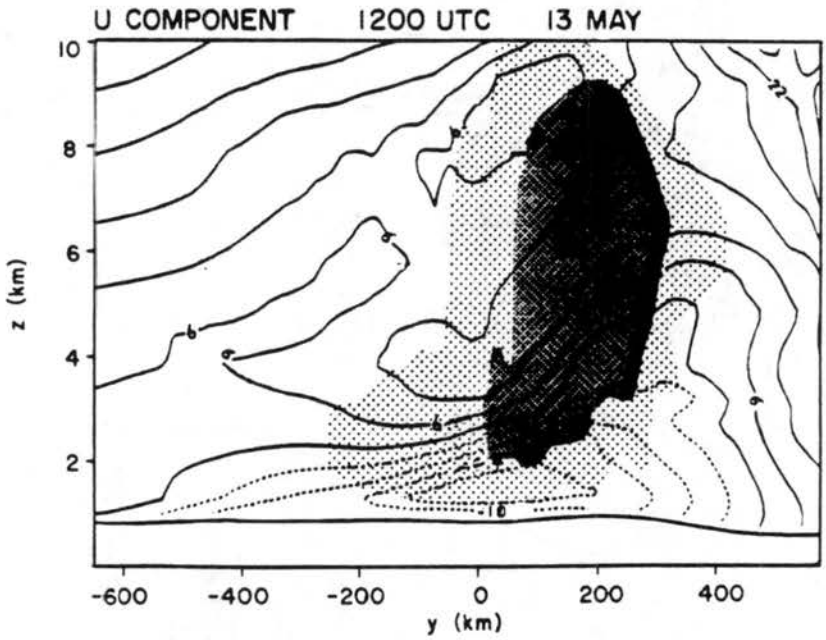


Figure 4.17: Continued.

systems observed within the PRE-STORM rawinsonde network during the night of 13 May. Since both jets terminated within the simulated MCS, it also leads to further insight into the regional scale dynamics associated with the development of the northwest Kansas derecho.

The two low-level jet systems evident in the model are examples of the cold and warm conveyor belt circulations (Carlson 1980) which often accompany the development of extra-tropical synoptic-scale cyclones (Fig 4.19). The warm conveyor belt in his model is shown to originate ahead of the cold front before rising over the warm frontal zone and merging with the southwesterly flow aloft. The cold conveyor belt originates within the cold synoptic scale high pressure north of the warm front, rises to the north of the surface low, and merges with the westerly flow aloft.

The dynamics governing the formation of the warm conveyor belt have been investigated in great detail since its discovery in the early 1950s and the reader is referred to the papers of Means (1954), Newton (1956), Bonner (1963) Bonner and Paegle (1970) Uccellini (1980), and McNider and Pielke (1981) for a review. Of interest here is the formation of the strong easterly current within the stable air mass north of the warm frontal zone. The cold conveyor belt in our case represents an intensification of the northeasterly airflow generated by the synoptic-scale high which passed to the north of the warm frontal zone (Fig 4.3).

There are three factors which may have acted to enhance this easterly synoptic current. First, convergence along the east-west frontal zone led to a packing of the low-level potential temperature surfaces between 00 and 1200 UTC 13 May. As shown by Shapiro (1982), the atmospheric response to an increased thermal gradient in confluent flow is a direct circulation about the front. To see this consider the Sawyer-Eliassen, cross-frontal circulation equation for the ageostrophic stream function $\psi$ in the vertical y-p plane:

$$-\gamma\frac{\partial\theta}{\partial p}\frac{\partial^2\psi}{\partial y^2}+2\frac{\partial m}{\partial p}\frac{\partial^2\psi}{\partial y\partial p}-\frac{\partial m}{\partial y}\frac{\partial^2\psi}{\partial p^2}=-2\gamma(-\frac{\partial V}{\partial y}\frac{\partial\theta}{\partial y}+\frac{\partial U}{\partial y}\frac{\partial\theta}{\partial x})-\frac{\partial^2U'\omega'}{\partial p^2}+\gamma\frac{\partial^2\theta'\omega'}{\partial y\partial p}+\gamma\frac{\partial}{\partial y}\frac{d\theta}{dt} \tag{4.1}$$

where U and V represent the horizontal geostrophic flow components, m is the geostrophic momentum (U - fy), $\gamma$ is a static stability parameter $(\frac{R}{fp_o}\frac{p_o}{p}^{\frac{C_v}{C_p}})$, and $\omega$ is the p-coordinate vertical velocity. Though the Sawyer-Eliassen equation is complicated in appearance, it

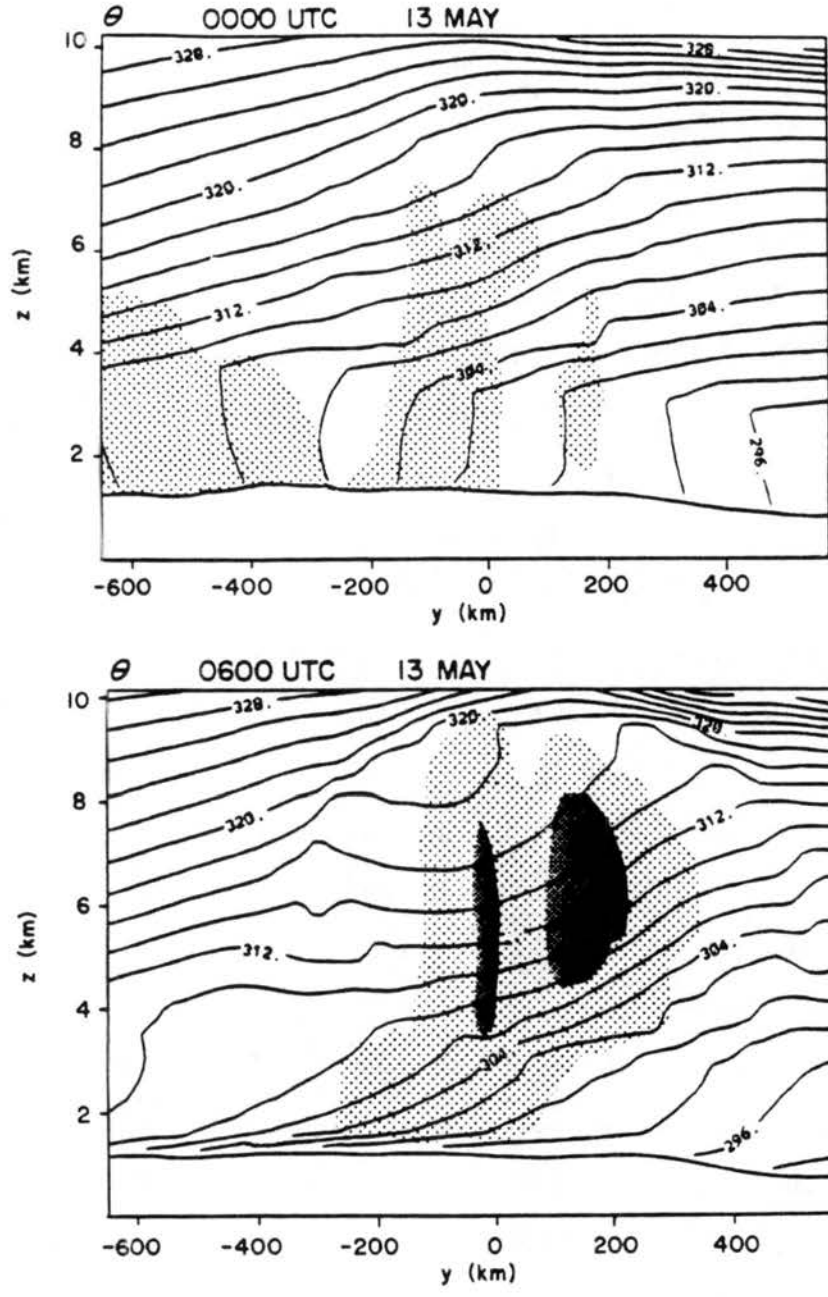


Figure 4.18: Vertical $x$-$z$ cross-sections of the potential temperature ($\theta$) surfaces at (a) 0000 UTC, (b) 0600 UTC, and (c) 1200 UTC 13 May 1985. Stippled region in (a) denotes updraft in excess of 2 cm $s^{-1}$. Stippled regions in (b) and (c) denote updraft in excess of 6 (lightly shaded) and 18 (darkly shaded) cm $s^{-1}$. Approximate location of the cross-sections correspond to the midpoint of the southerly jet shown in Fig 4.14.

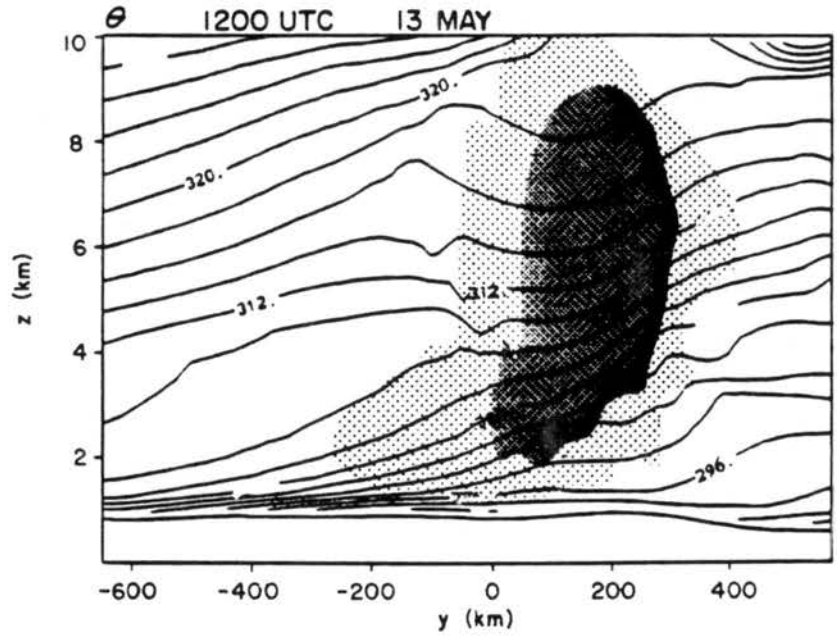


Figure 4.18: Continued.

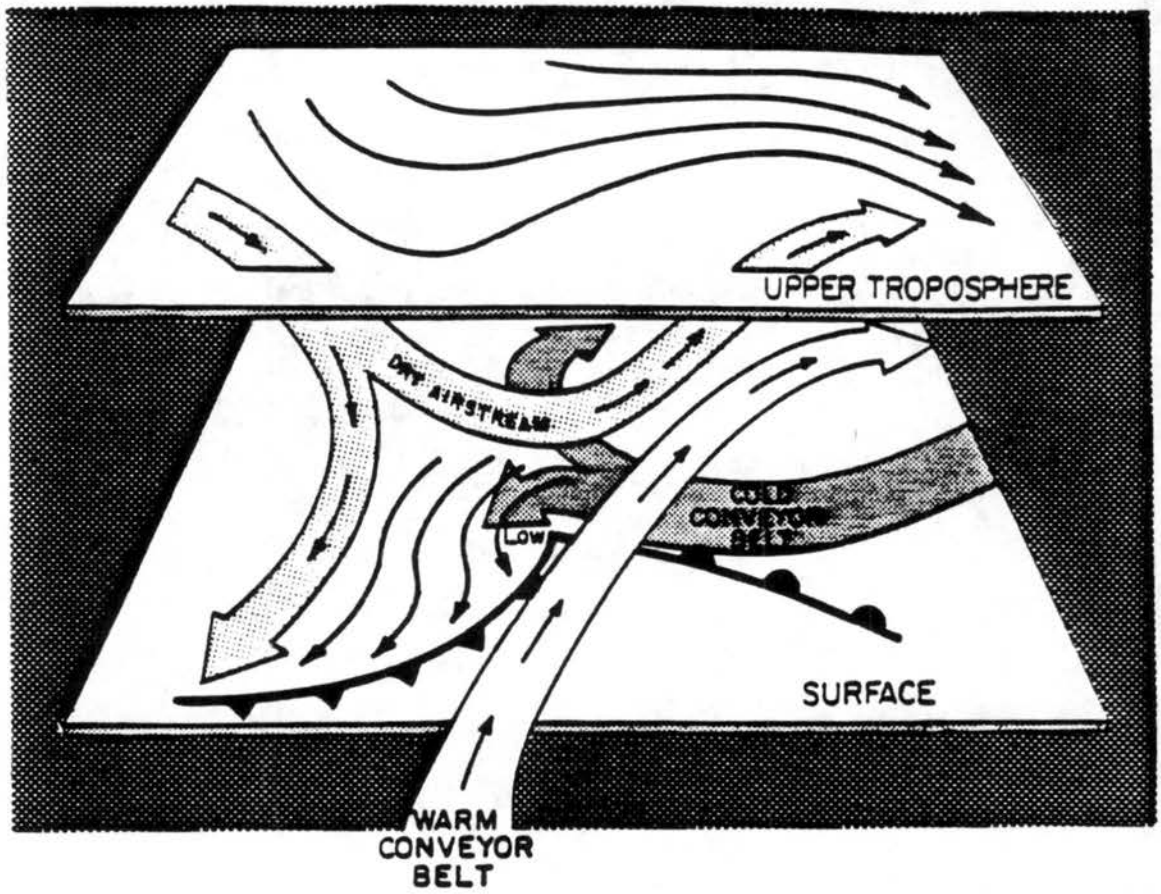


Figure 4.19: Schematic representation of the warm and cold conveyor belt circulations adapted from Carlson 1980. From Cotton (1990).

has a simple physical interpretation. The left hand side, through the leading coefficients, determines the orientation and aspect ratio of the circulation, while the right hand side determines the direction and magnitude of the spin. For an east-west orientated front viewed from the east, a positive forcing on the R.H.S. of Equation (1) results in a clockwise circulation about the front.

The terms on the R.H.S represent, respectively, the affects of geostrophic stretching and deformation, turbulent fluxes of momentum and heat, and diabatic heating. Considering the effects of the geostrophic terms only and applying this equation to the east-west oriented warm frontal zone, we expect that the first term on the right hand side of the equation is positive ($\frac{\partial V}{\partial y}\frac{\partial \theta}{\partial y} > 0$ and $\frac{\partial U}{\partial y}\frac{\partial \theta}{\partial x}$ is approximately zero) and a direct circulation about the front should arise. A direct circulation simultaneously acts to increase the along-frontal shear required to maintain thermal wind balance and to reduce the cross-frontal thermal gradient by adiabatically cooling/warming the warm/cold side of the frontal boundary, respectively. In this case the lower branch of the direct circulation within the cold air would be directed north-to-south. Coriolis turning of this flow would then produce an easterly current within the cool air mass on the northern side of the front. The idealized simulations of Hoskins et al. (1984) have shown that such processes may led to jet strengths of nearly 40 m $s^{-1}$ within a 12 hour time period. This is consistent with the rapid development of both the observed and simulated jets for this case.

A second possible factor affecting the development of the easterly jet, was the strong east-west pressure gradient that developed across Kansas during the night (Fig 4.13). This was a combination of an increase in magnitude of the high pressure zone in Nebraska and Iowa and pressure falls associated with the lee cyclogenesis. As shown in Fig 4.13, the easterly wind maximum was located in an inverted trough that extended from the low pressure center in the Texas Panhandle northward to the model resolved MCC. In the observations this trough coincided with the leading edge of the cold surge accompanying the outflow from the MCC (Fig 4.1) and the maximum easterlies in the surface time series (Fig 4.10). The model shows that the surface position of the trough corresponded with the southerly low-level jet axis (Fig 4.20) suggesting the trough was hydrostatically-induced by an increase in the depth of the warm moist air aloft. It thus appears that, in addition to

its role of providing heat and moisture to the MCS, the low-level southerly jet may also significantly increase the strength of the low-level easterly momentum within the underlying stable air mass through hydrostatically-induced pressure reductions which take the form of a narrow trough beneath the jet axis. This suggests that forecasting the strength and location of the southerly low-level jet may serve as a useful guide to forecasting the location of derecho events.

A third factor affecting the enhanced easterly current may have been the ageostrophic flow about the middle-level jet streak which rotated around the trough axis and into the lee of the Rockies between 0000 and 1200 UTC 13 May (Fig 4.2). As shown by Uccellini (1980) the low-level return branch about the upper level jet may directly contribute to an increase in the low-level jet speed if it is properly oriented. In our case, the middle-level jet axis was oriented southwest-northeast across northwest Kansas suggesting a low-level ageostrophic flow in the exit region from the southeast, or along the warm frontal boundary. As is often the case, the MCC was located in the updraft along the left exit region of this jet where further latent heat release and mass evacuation could contribute to surface pressure falls and increase in the strength of easterly flow.

## 4.3 The 2-3 August 1981 CCOPE derecho

### 4.3.1 System overview

A system exhibiting similar environmental conditions to the 12-13 May 1985 PRE-STORM derecho occurred on 2-3 August 1981. An overview of this system between 0000 and 1200 UTC 3 August, 1981 shows the derecho-producing storm moved along an east-west stationary frontal zone extending from southeastern Montana to western Minnesota (Figs 4.21 and 4.22). The frontal zone provided a trigger for two of the initial storms (labeled A and B in Fig 4.23) which later merged in southeastern Montana with a third MCS (labeled C) to form a MCC. The severe winds coincided with the movement of the MCC across the Dakotas during the night and persisted until the MCCs demise in western Minnesota near 1300 UTC 3 August. Surface wind gusts ranged from 25 to 43 m $s^{-1}$ between 0000 and 1300 UTC with peak speeds occurring between 0830 and 1000 UTC 3 August.

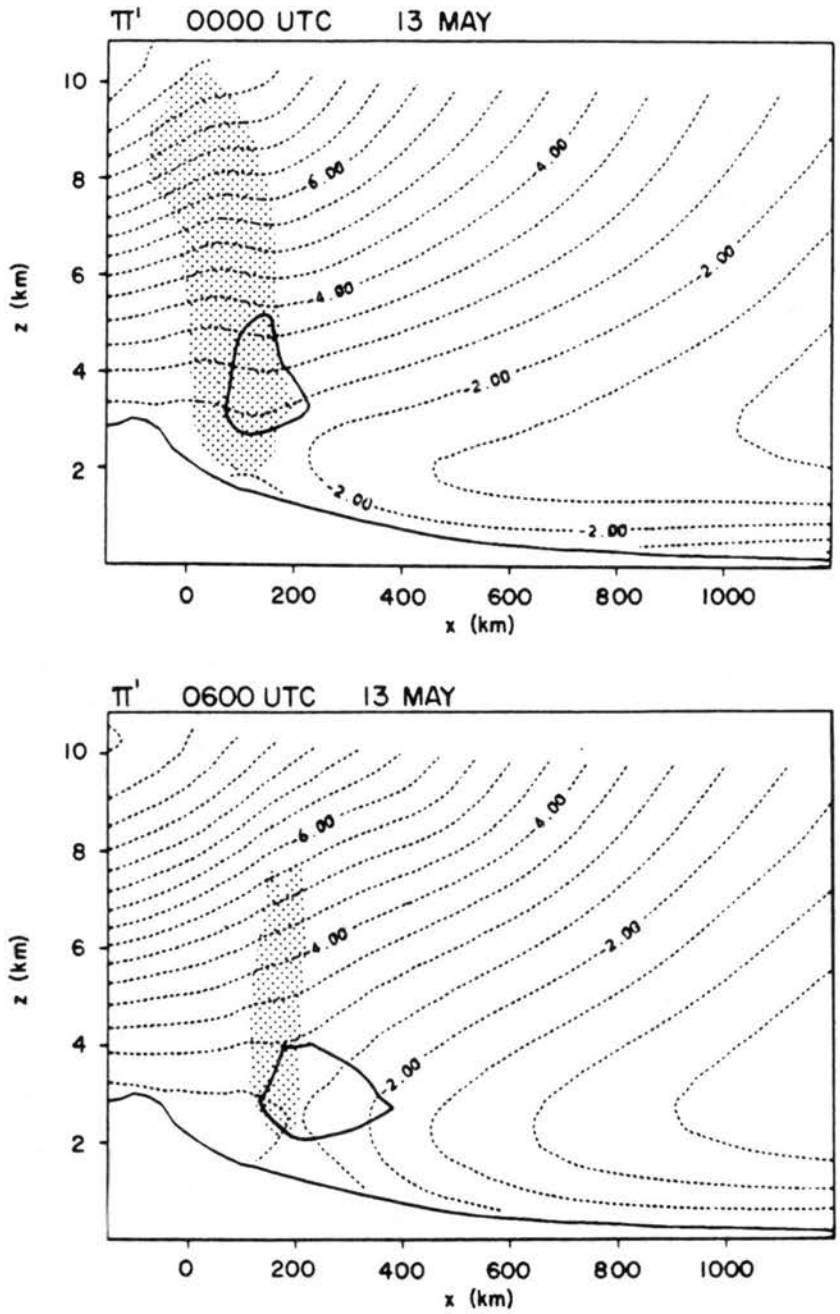


Figure 4.20: Vertical $x$-$z$ cross-sections of perturbation Exner function ($\pi'$) at (a) 0000 UTC, (b) 0600 UTC, and (c) 1200 UTC 13 May 1985. Contour interval is every 0.5 J kg$^{-1}$ K$^{-1}$. Stippled regions denote updraft in excess of 6 cm s$^{-1}$. Bold solid line denotes the location of the southerly low-level jet shown in Fig 4.14. Location of the cross sections correspond to the midpoint of the domain shown in Fig 4.13.

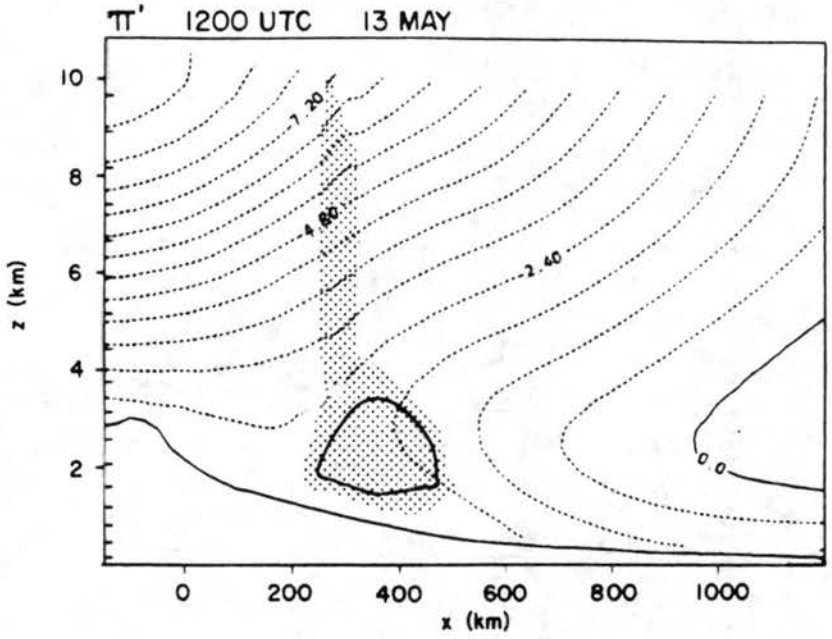


Figure 4.20: Continued.

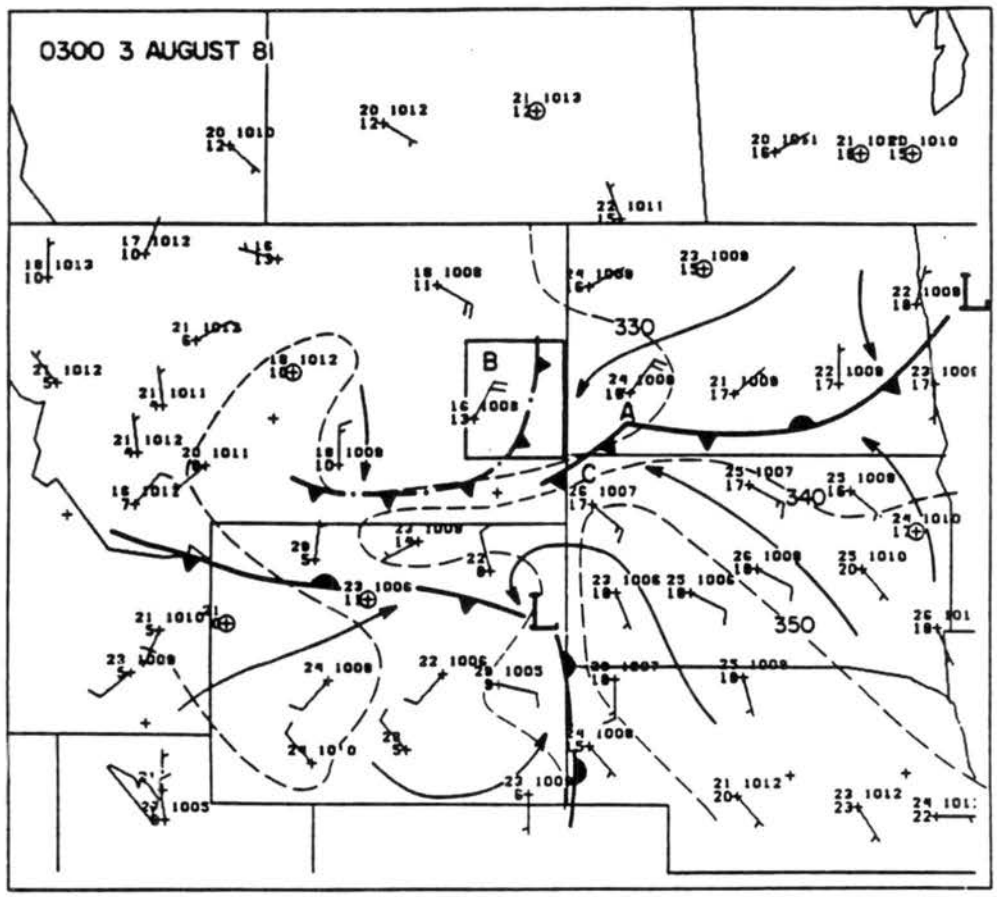


Figure 4.21: Synoptic surface conditions at 0300 UTC 3 August 1981. Plotted station parameters include temperature (C°), dewpoint (C°), pressure (hPa). Dashed lines denote values of equivalent potential temperature ($\theta_e$) at 10 K intervals. Labels A, B, and C denote the location of the three MCSs evident in the satellite imagery of Fig 4.23.

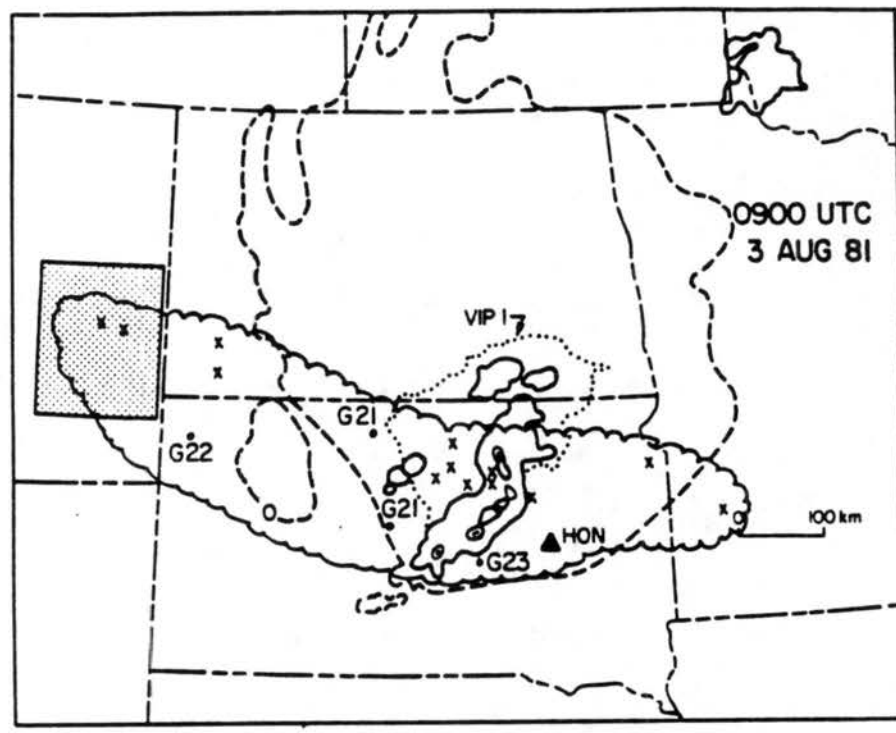


Figure 4.22: Low-elevation radar PPI from Huron, South Dakota at 0900 UTC 3 August 1981 showing VIP levels 1-4. Heavy dashed line shows -32° IR contour at 0900 UTC. The stippled region outlines the CCOPE mesonet. Severe weather occurring from 0000-1300 UTC 3 August 1981 was reported at the locations marked 'X'. Additional wind reports, plotted in m $s^{-1}$, and scalloped outline of the area affected by the derecho were provided courtesy of Robert H. Johns.

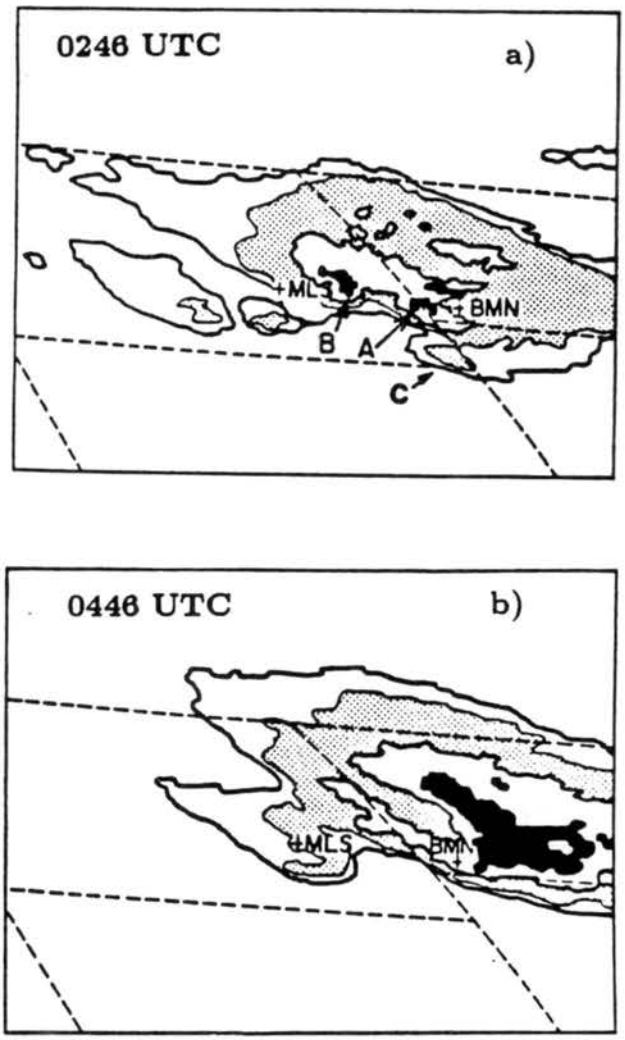


Figure 4.23: Infrared satellite imagery depicting the growth of the MCC. IR isotherms enclosing -40, -50 (shaded), -55, -60 (black) and -65°C are shown. MLS and BMN denote radar sites at Miles City, Montana and Bowman, North Dakota. The diameter of the system at 0446 UTC 3 August 1981 is approximately 500 km. (Fig. courtesy of Pat Laybe and Ray McAnelly)

### 4.3.2 Environmental features of the 2-3 August 1981 derecho

The vertical structure of the airmass in the genesis region of the derecho was characterized by high values of CAPE and strong vertical wind shear (see Fig 3.3 and 3.4). Moist, southeasterly flow in the layer between the surface and 75 kPa and a southwesterly flow within a deep, dry, elevated mixed layer between 75 and 45 kPa combined to produce lifted indices of -10 and low-level vertical wind shear of 3 x $10^{-3}$ $s^{-1}$ in the pre-frontal environment in southeastern Montana. The winds increased aloft to a maximum of nearly 40 m $s^{-1}$ near the tropopause in association with an upper level jet streak that was propagating through the broad upper level trough depicted in Fig 4.24.

### 4.3.3 Regional-scale aspects of the 2-3 August derecho

Because this case was also the focus of an extensive modeling study of Tremback (1990), relevant details of the regional-scale forcing are presented in this section from his simulations as well as the nested non-hydrostatic simulations discussed in Section 3.2.1. Results from both simulations reveal that the regional-scale pattern of the 2-3 August derecho, unlike the previous example, appeared to remain relatively unchanged throughout the episode. Two possible forcing mechanisms for the MCC appear to have been the circulations associated with the low-level frontal zone and the upper level jet streak propagating through the trough. The upward branch within the exit region of this jet streak was shown by Tremback (1990) to have an important role in both the propagation and sustenance of the MCC.

A more subtle feature aiding the development of this system appears to have been the circulation associated with the elevated well-mixed layer as it propagated eastward over the plains during the night (Tremback 1990). Using a regional scale simulation, he determined that the elevated mixed layer over the CCOPE region was a remnant of the heated ABL that developed over the elevated terrain to the west. During the late afternoon and early evening, this layer advected eastward as part of the general mountain-plains solenoidal circulation and, by 0000 UTC 3 August, it was in place to affect the development of the storm systems in east-central Montana.

Tremback's simulations suggest that the MCC development and movement was directly linked to the eastward progression of the solenoidal circulation during the night. During the

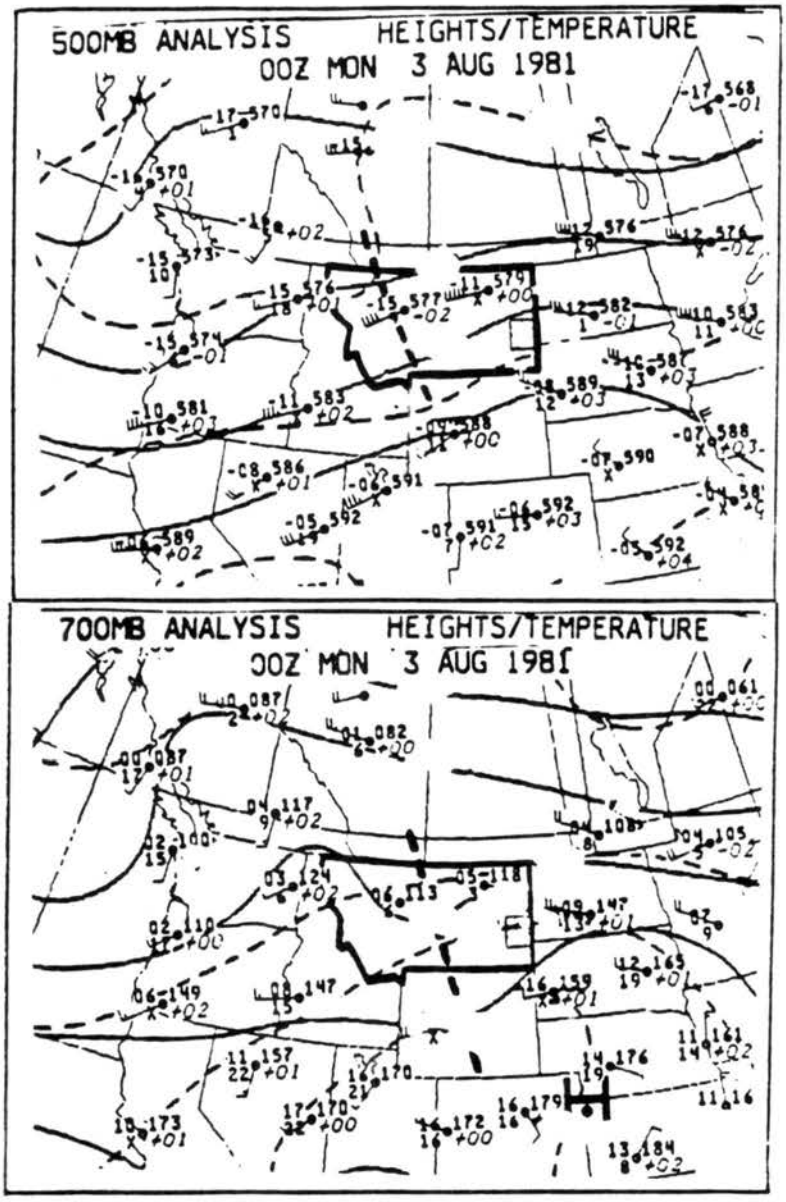


Figure 4.24: The 0000 UTC 3 August 1981 50 and 70 kPa height and temperature analyses. From Cotton et al. (1984).

early stages of development, the storms were coupled to the low-level upslope circulation associated with the inflow branch of the solenoid (Fig 4.25). As time progressed, the lower layers stabilized, the solenoidal circulation decoupled from the surface (Fig 4.26), and the primary forcing and the MCC itself shifted to the upward branch of an indirect circulation forced along the leading edge of the solenoid (Fig 4.27). This relationship between the MCC and the solenoid was maintained until 0900 UTC 3 August when the MCC suddenly accelerated and, consequently, outran the supporting solenoidal circulation before subsequently decaying in the eastern Dakotas. Tremback (1990) suggested that this final phase in the system life cycle may have resulted from the excitation of a inertia-gravity wave. The details of this phase in the MCC life cycle, however, remain under investigation.

One additional aspect of the elevated mixed layer was its affect on the the development of a southerly low-level jet. This jet formed ahead of the low pressure region located in east-central Wyoming (Fig 4.21) and was responsible for strong moisture and heat advection into the MCC (Tremback 1990). Tremback's simulations of this case have revealed the jet formed in response to a favorable horizontal potential temperature gradient associated with the advancing solenoidal circulation. This conclusion is similar to that obtained by McNider and Pielke (1981).

The relationship between the low pressure, the low-level southerly jet, and the elevated mixed layer is shown in greater detail from the nested simulations of this case described in section 3.2.1. Results from the fine grid show that the surface low (Fig 4.28) was colocated with the deepest portion of the elevated mixed layer throughout the period (Figs 4.29 and 4.30). This correspondence may be one reason for the weak low pressure troughs which are often observed in the lee of the Rockies during the summertime. The southerly low-level jet was located near the top of the lower stable layer and within the leading potential temperature gradient of the solenoid (Fig 4.29). As in the previous case, the jet directly fed the region of positive vertical motion associated with the model resolved MCC. Since peak wind speeds within the CCOPE low-level southerly jet were only 16 m $s^{-1}$, however, other processes within the MCC itself were likely responsible for the strong surface winds in this case.

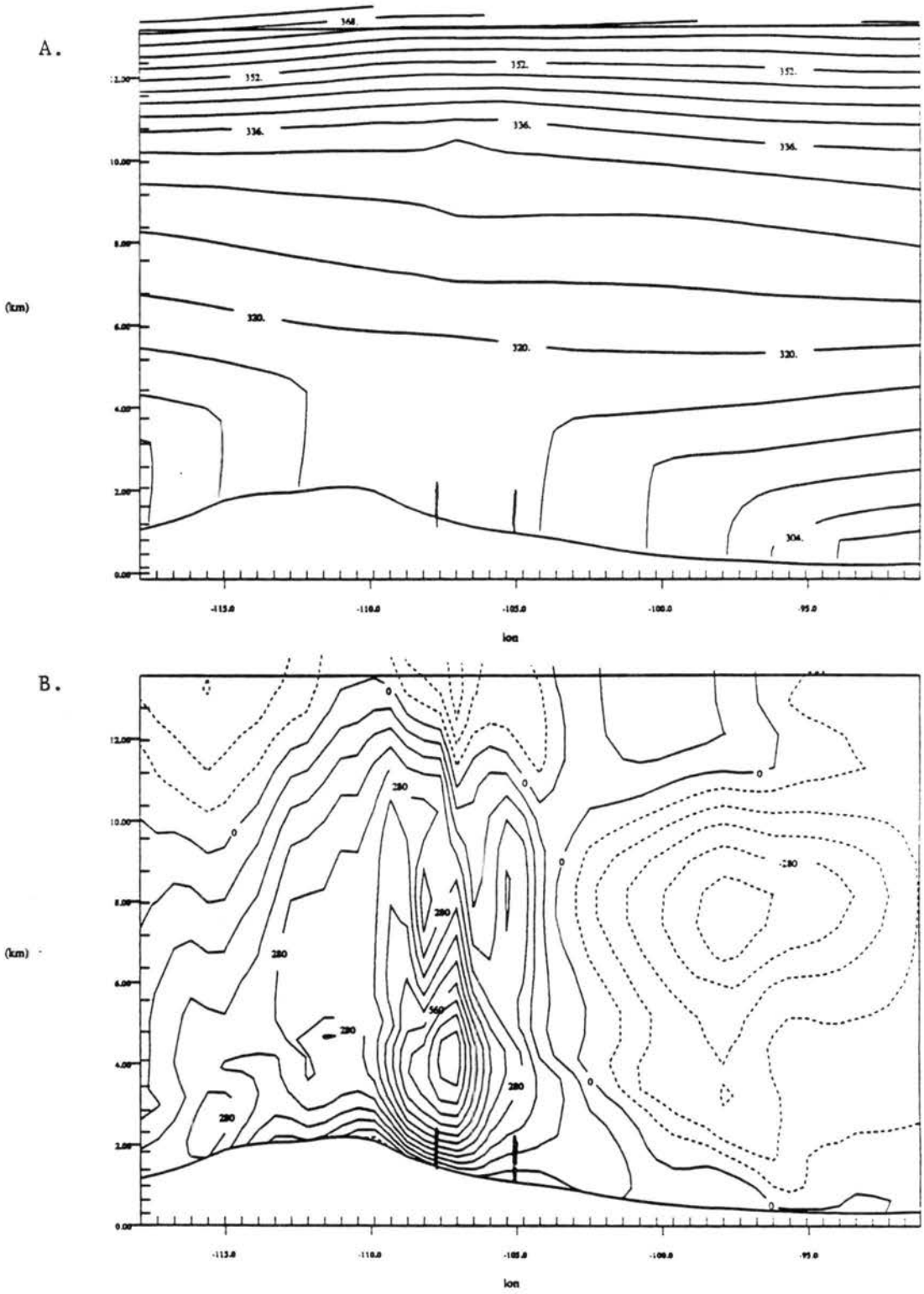


Figure 4.25: Vertical east-west cross-section of (a) potential temperature and (b) vertical velocity at 45.2° N from a high resolution control run at 0000 UTC 3 August 1981. From Tremback (1990).

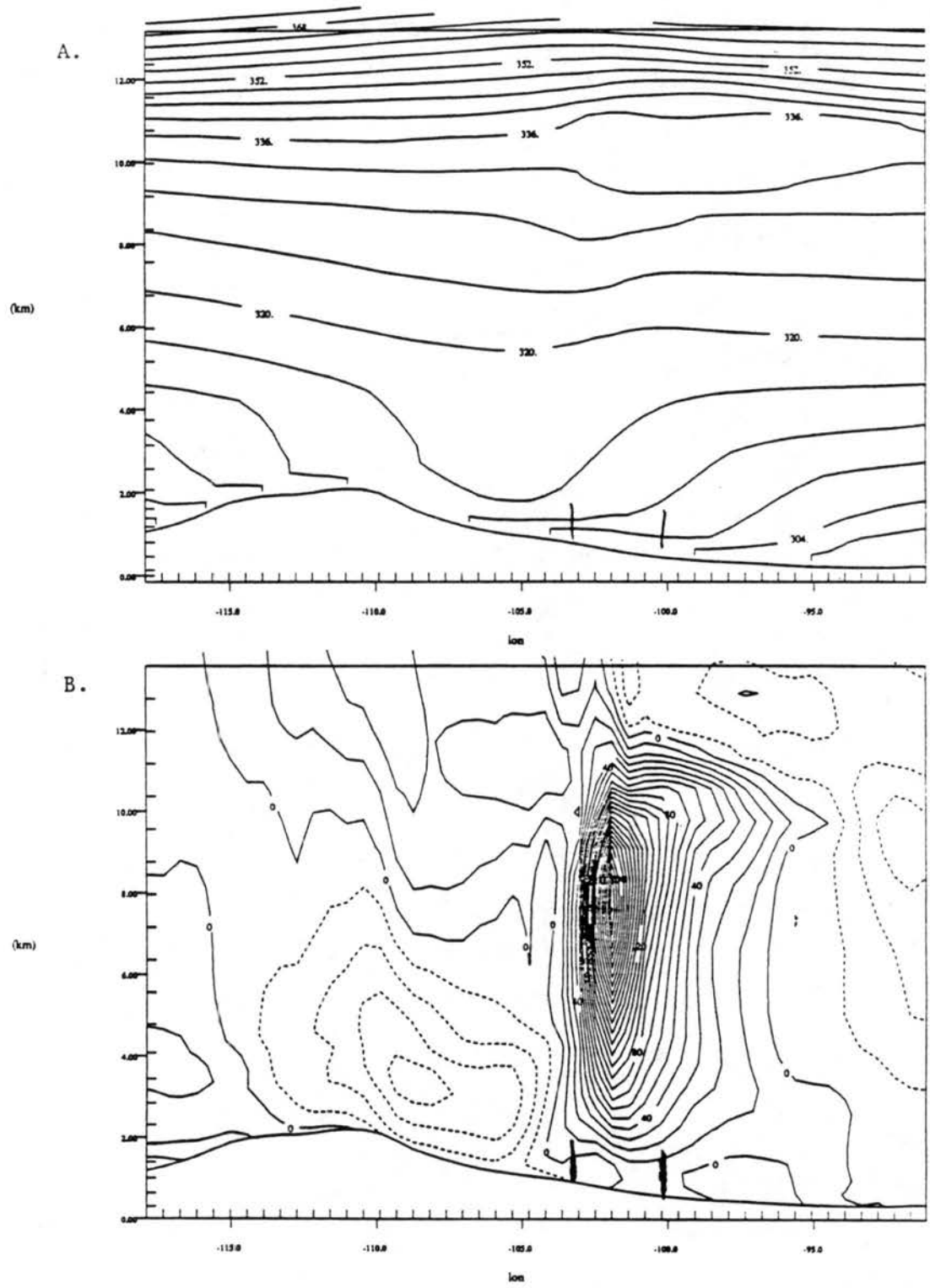


Figure 4.26: Vertical east-west cross-section of (a) potential temperature and (b) vertical velocity at 45.2° N from a high resolution control run at 0800 UTC 3 August 1981. From Tremback (1990).

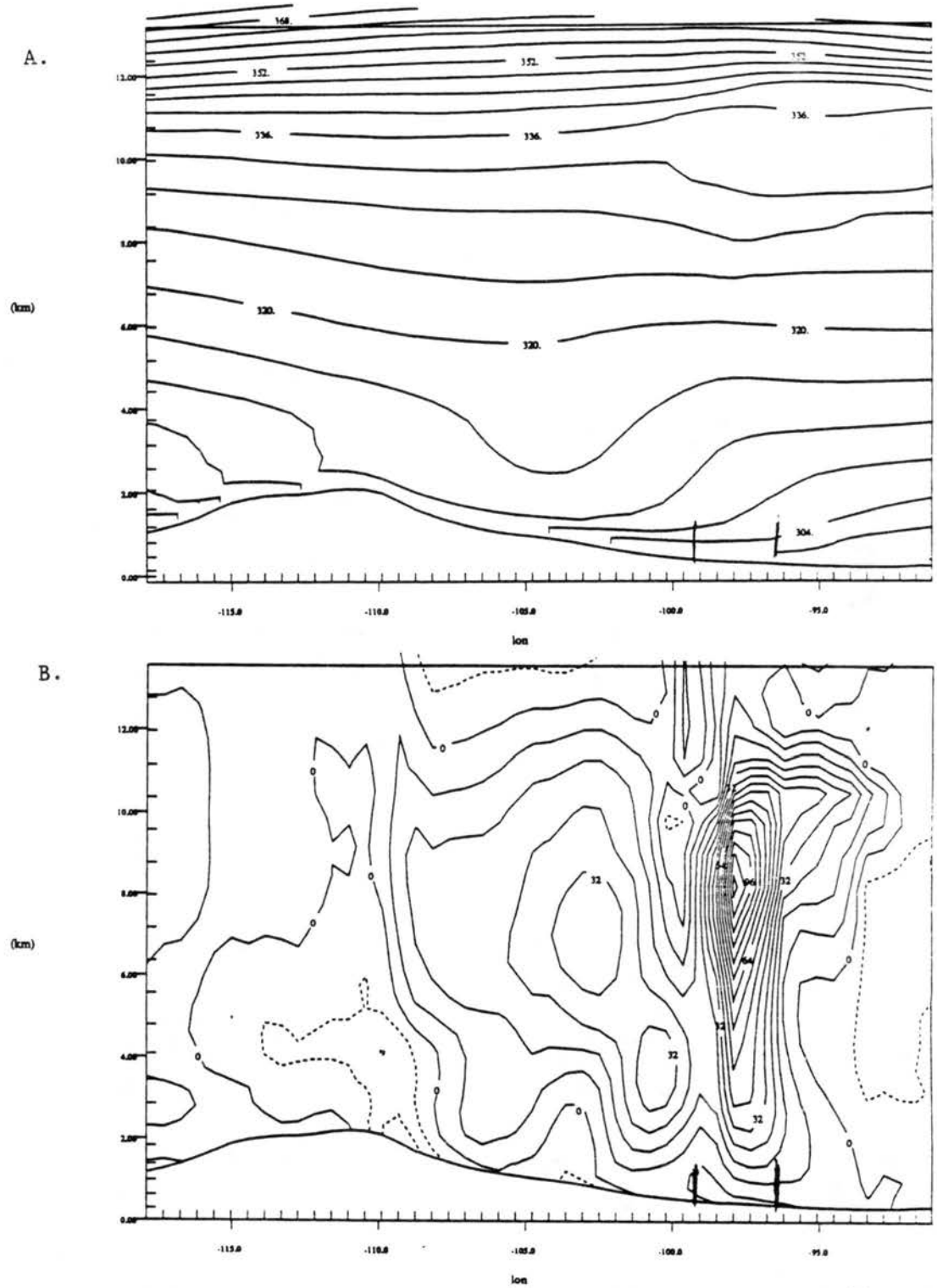


Figure 4.27: Vertical east-west cross-section of (a) potential temperature and (b) vertical velocity at 45.2° N from a high resolution control run at 1200 UTC 3 August 1981. From Tremback (1990).

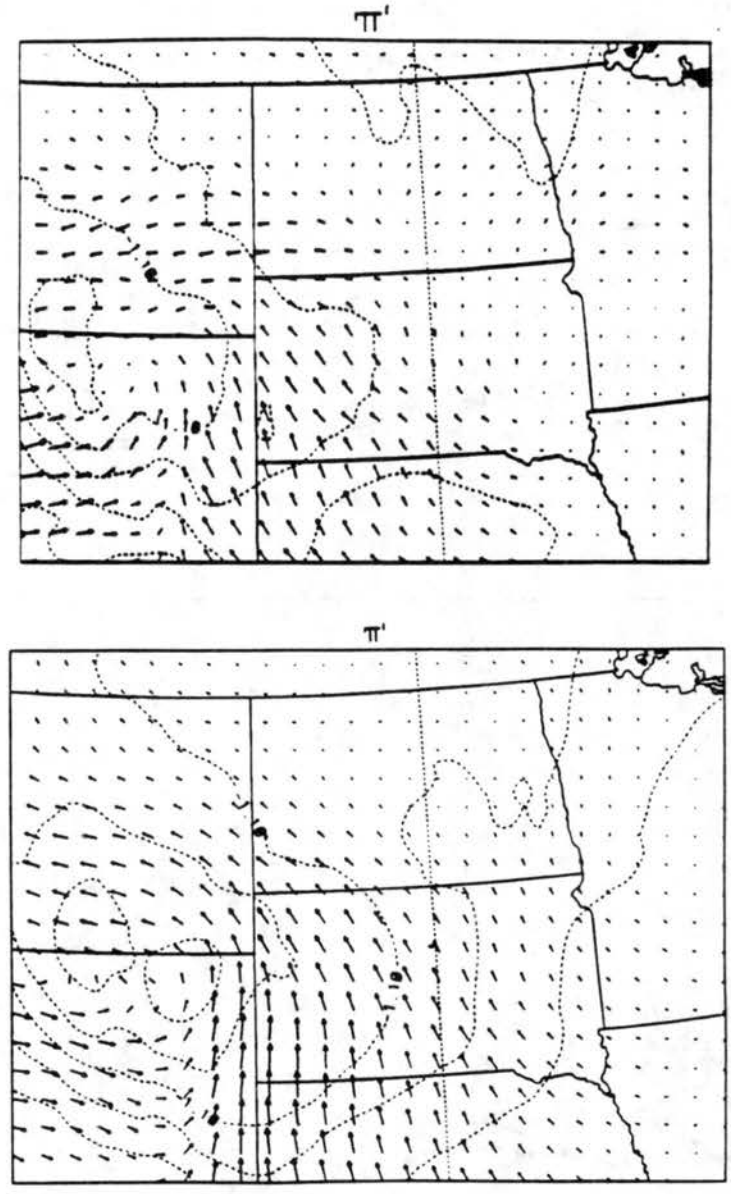


Figure 4.28: Horizontal flow vectors and perturbation Exner function ($\pi'$ contoured every .2 J kg$^{-1}$ K$^{-1}$ on the fine grid for the 2-3 August CCOPE derecho. (a) 0000 UTC, (b) 0600 UTC, and (c) 1200 UTC 3 August 1981.

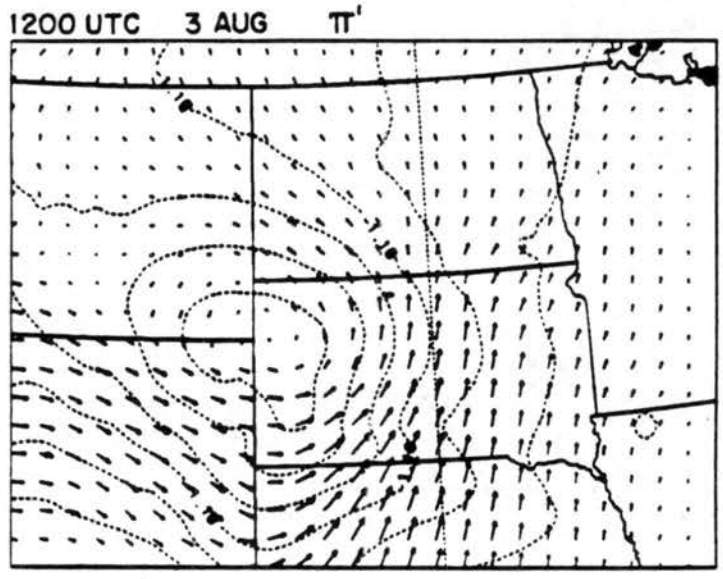


Figure 4.28: Continued.

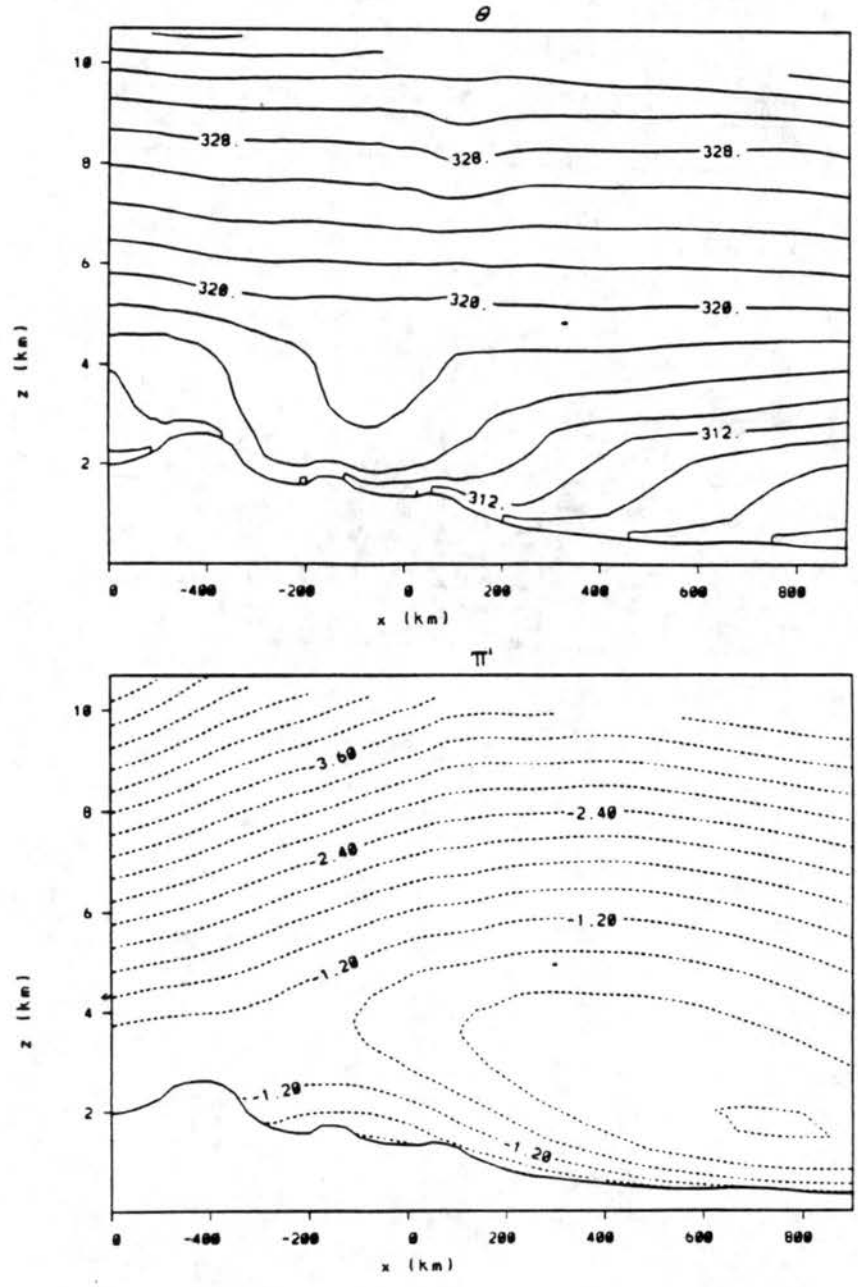


Figure 4.29: Vertical $x$-$z$ cross-sections through the surface low pressure evident in Fig 4.28 at 0600 UTC 3 August 1981. (a) potential temperature, (b) perturbation Exner function ($\pi'$) contoured every .3 J kg$^{-1}$ K$^{-1}$, and (c) the $v$-component of flow contoured every 4 m s$^{-1}$.

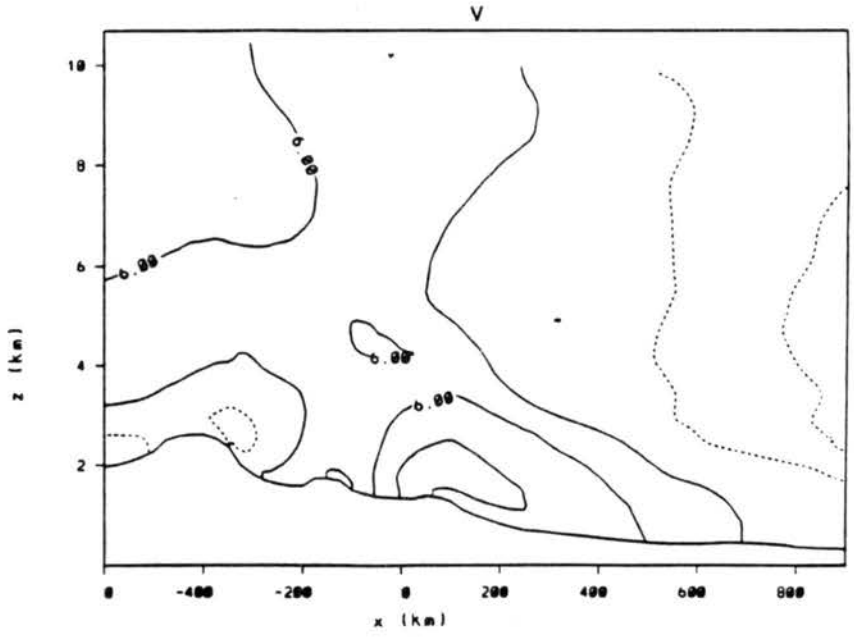


Figure 4.29: Continued.

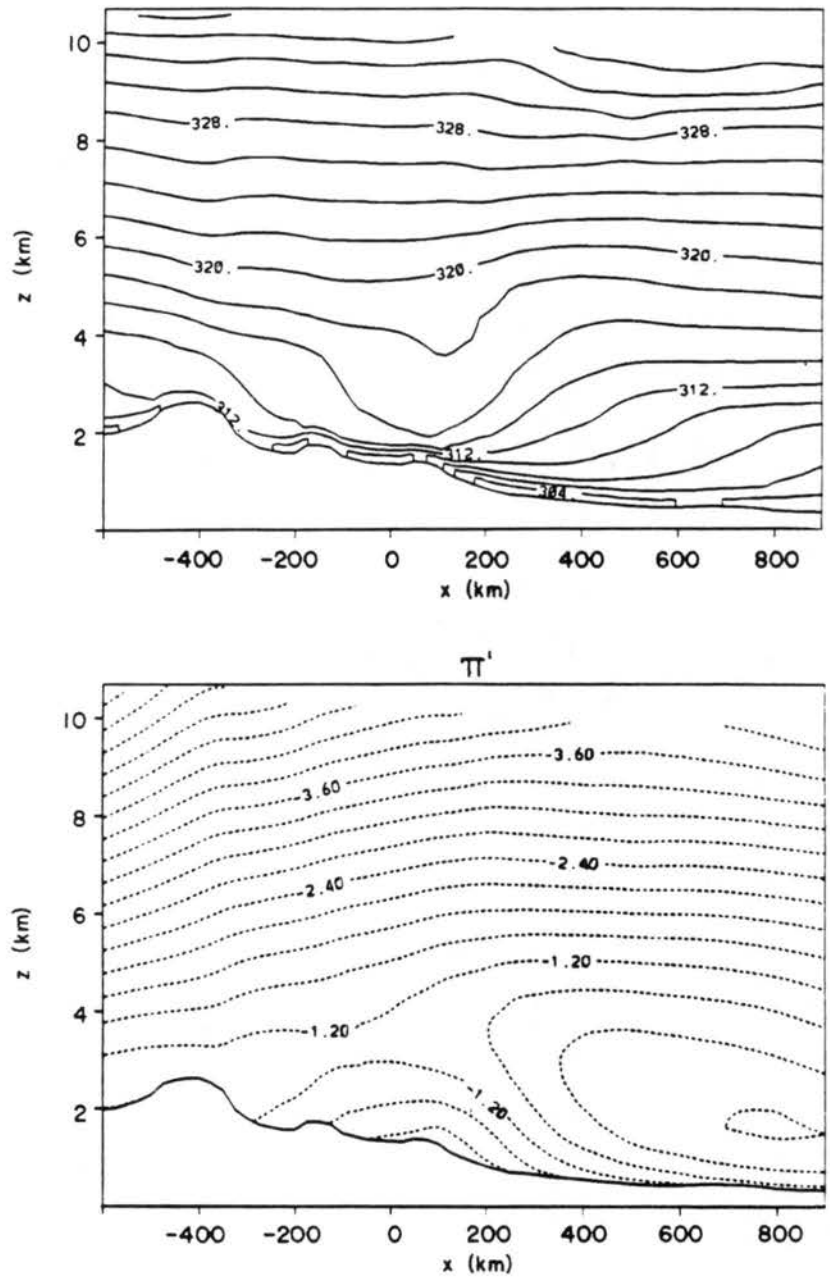


Figure 4.30: Vertical $x$-$z$ cross-sections through the surface low pressure evident in Fig 4.28 at 1200 UTC 3 August 1981. (a) potential temperature, (b) perturbation Exner function ($\pi'$) contoured every .3 J kg$^{-1}$ K$^{-1}$, and (c) the $v$-component of flow contoured every 4 m s$^{-1}$.

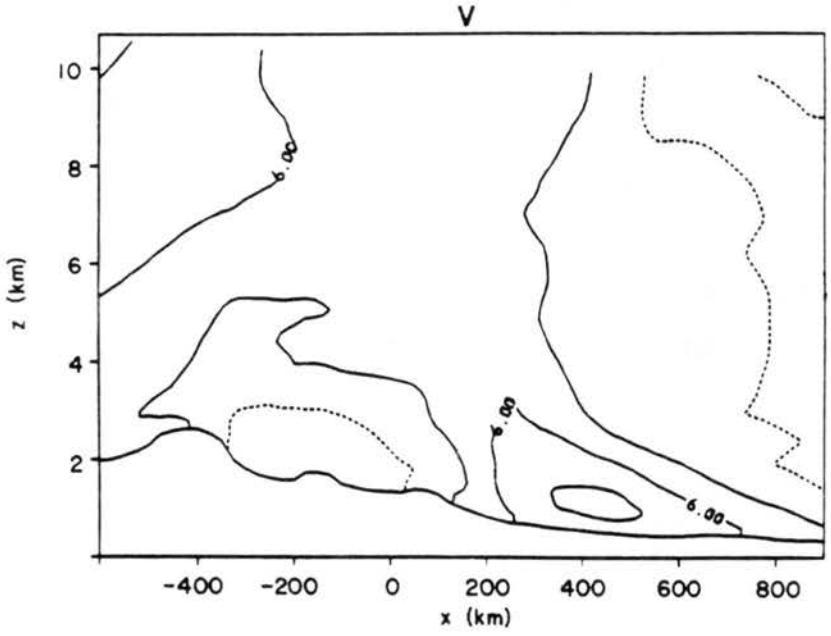


Figure 4.30: Continued.

### 4.3.4 Evolutionary characteristics of the flow and thermodynamic fields

As can be seen in Figs 4.25 through 4.27, the evolution of the low-level thermodynamic structure within the derecho environment evolved from one of nearly neutral conditions during the initial stages of the derecho, to one of increasing static stability. This was a result, in part, of the onset of nocturnal cooling in the model. Two other factors affecting the development of the low-level static stability were the presence of the pre-existing east-west stationary frontal zone (Fig 4.21) and diabatic processes associated with meso$\beta$-scale surface outflow boundaries.

The diabatic cooling was revealed by aircraft soundings taken in the outflow region between systems A and B during the initial stages of the derecho development (see Fig 3.3). An important feature of these soundings is that the low-level outflow of system A undercut, but did not entirely remove, the moist ABL evident in the pre-storm environment. Also note that the elevated well-mixed layer remained intact above the outflow air. As a result there remained a sufficient supply of CAPE to maintain the convective scale updrafts of system B even though they were over 80 km removed from the direct surface-based inflow source that fueled system A.

### 4.3.5 Meso$\beta$-scale aspects of the CCOPE derecho

The relatively weak low-level flow in the regional-scale simulations of the 2-3 August derecho suggests that the severe surface winds were likely generated by the circulations associated with the individual MCSs. One of the unique aspects of this case is that two of three MCSs involved with the initial development of the derecho, passed directly through the CCOPE data network located in southeastern Montana (Fig 3.1). It was thus possible to make a detailed assessment of the meso$\beta$-scale structure of the MCSs and their impact on the severe surface wind development.

An inspection of a single time series of pressure and surface winds reveals the range of conditions which occurred as the two systems passed through the network (Fig 4.31). Note that in each case, peak westerly winds of 15 to 20 m $s^{-1}$ (Fig 4.31a) preceeded the rapid onset of a severe northerly component of nearly 30 m $s^{-1}$ (Fig 4.31b). In the case of system A, the winds were responding to an intense surface meso-cyclone (Fig 4.31d) which

developed beneath a supercell (Wade 1982) [Fig 4.32]. As can be seen in the Fig 4.32, surface winds of 20 to 25 m $s^{-1}$ were present in both the inflow and outflow regions of this storm. The supercell produced F1 damage in the CCOPE experimental area and as it passed into western North Dakota (Weisman et al. 1983, Miller et al. 1988).

The second system to pass through the mesonetwork was a bow echo squall line (Fig 4.33) [Schmidt and Cotton 1989]. This system produced a narrow band of surface gusts in excess of 30 m $s^{-1}$ along the path taken by a supercell-like cell embedded within the vertex region of the bow echo (Fig 3.1). Regions of strong flow were concentrated along the leading gust front, where there was a northwesterly flow component, and in the trailing stratiform region of the system where there was a strong northerly component (Fig 4.31).

The bimodal nature of the surface wind speed trace for system B (Fig 4.31c) suggests that separate processes may have led to the severe surface wind development. The initial surge of northwesterly flow likely reflects the presence of a strong rotor circulation along the leading outflow boundary, such as illustrated in Fig 2.14, while the trailing wind maximum located within the vertex region of the bow echo, appears to have been associated with the mesohigh-mesolow couplet (Fig 4.34). The difference between the two surface wind peaks is also reflected in the $\theta_e$ analysis (Fig 4.34e) which shows a low-level source region for the leading surge ($\theta_e > 332$ K) and a middle-level source region for the trailing wind surge ($\theta_e < 328$ K). Since the $\theta_e$ values within the trailing wind maximum corresponded to those present within the elevated well-mixed layer, we have previously concluded (Schmidt and Cotton 1989) that parcels approaching the upshear flank of the line within the southwesterly rear-to-front flow aloft were strongly affected by the near surface pressure field and descended well behind the leading convective line. This analyses illustrates that the squall line, despite having to overcome the the pre-existing, low-level static stability, still had a significant downward transport of middle-level momentum to the surface.

The development of the trailing surface wind maximum was a reflection of the unique surface pressure distribution which accompanied this squall line. As in previous squall line studies, the shape of the surface mesohigh resembled the overlying structure of the convective and trailing stratiform precipitation radar reflectivity pattern (compare Fig 4.33 and Fig 4.34) suggesting it was primarily hydrostatically induced by diabatic cooling and

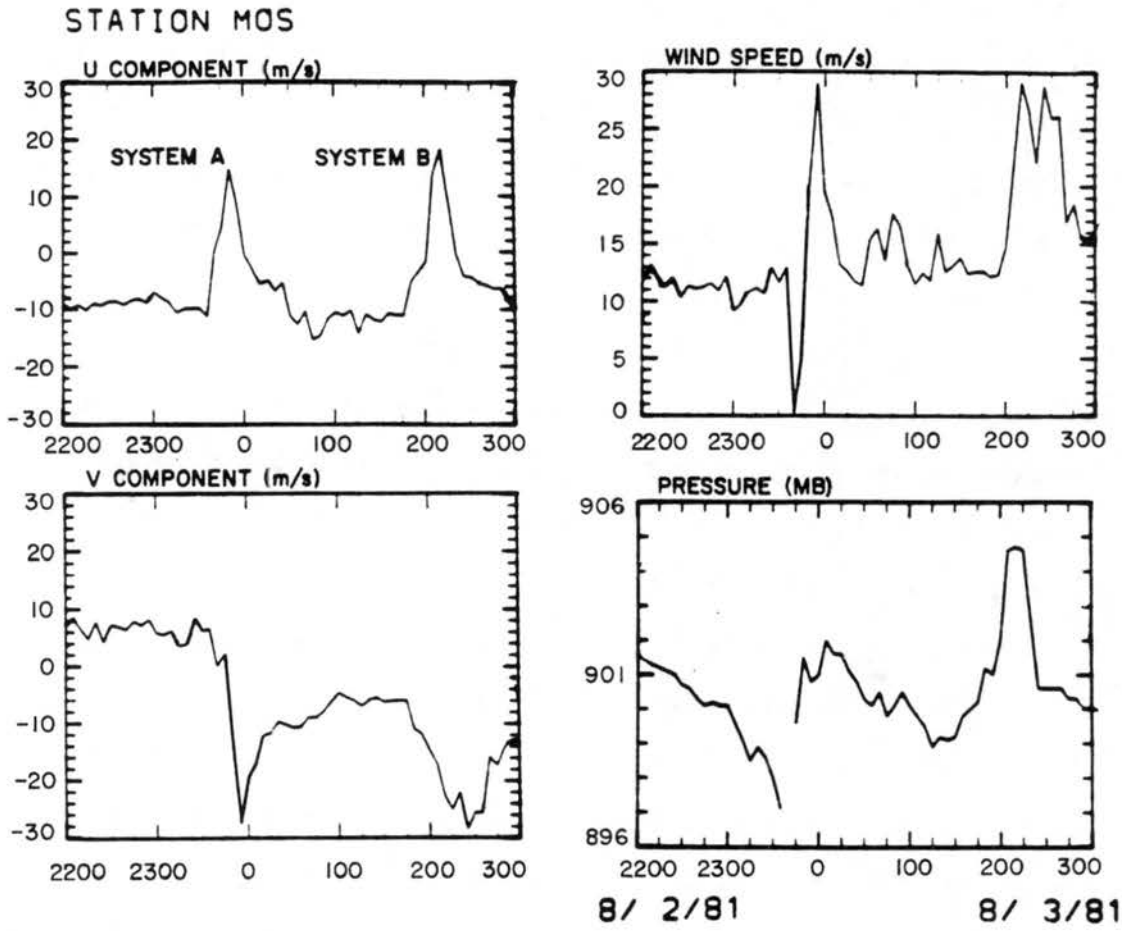


Figure 4.31: Time plots of (a) $u$-component, (b) $v$-component, (c) wind speed, and (d) surface pressure for the CCOPE PROBE surface station MOS between 2200 and 0300 UTC 2-3 August 1981.

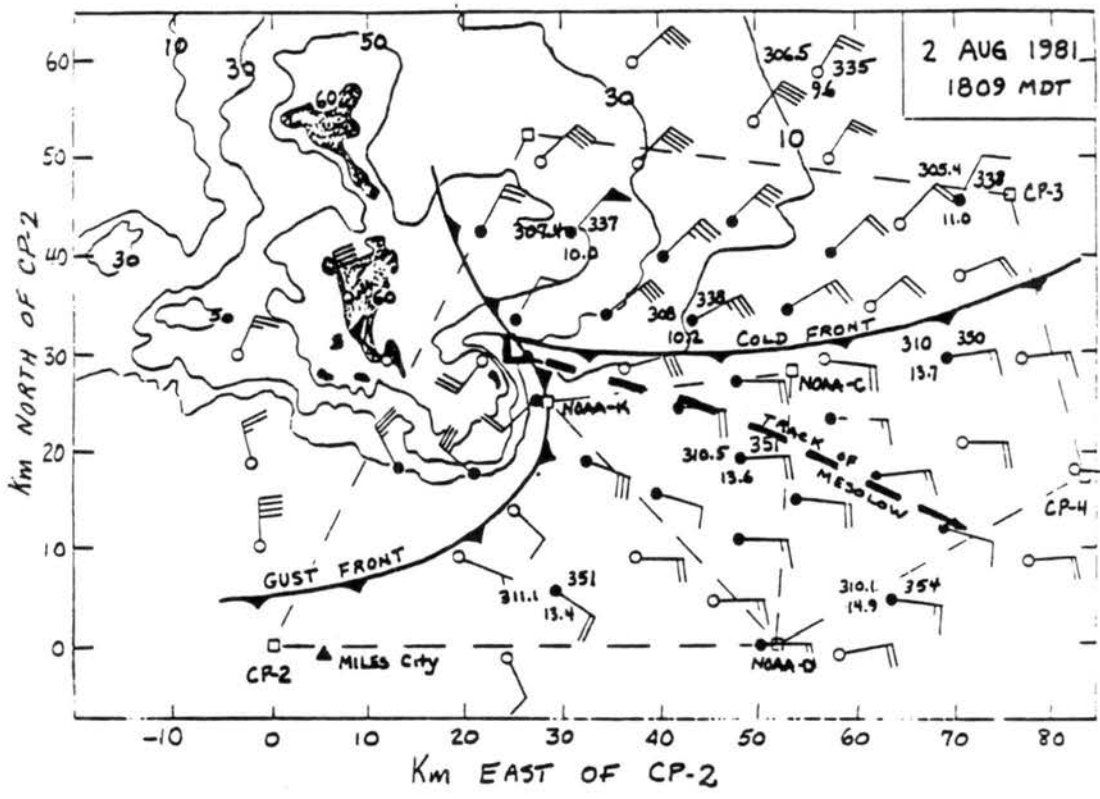


Figure 4.32: Illustration of the relationship between the CP-2 radar echo and the surface wind field at 0009 UTC on 2 August 1981 for system A. Winds are plotted with a long barb equal to 5 m $s^{-1}$ and a flag equal to 25 m $s^{-1}$. Elevation angle of the PPI is 1.5°. PAM stations are indicated by the darkened circles. Representative values of $\theta$, $\theta_e$, and mixing ratio (q) are shown for selected stations. From Wade (1982).

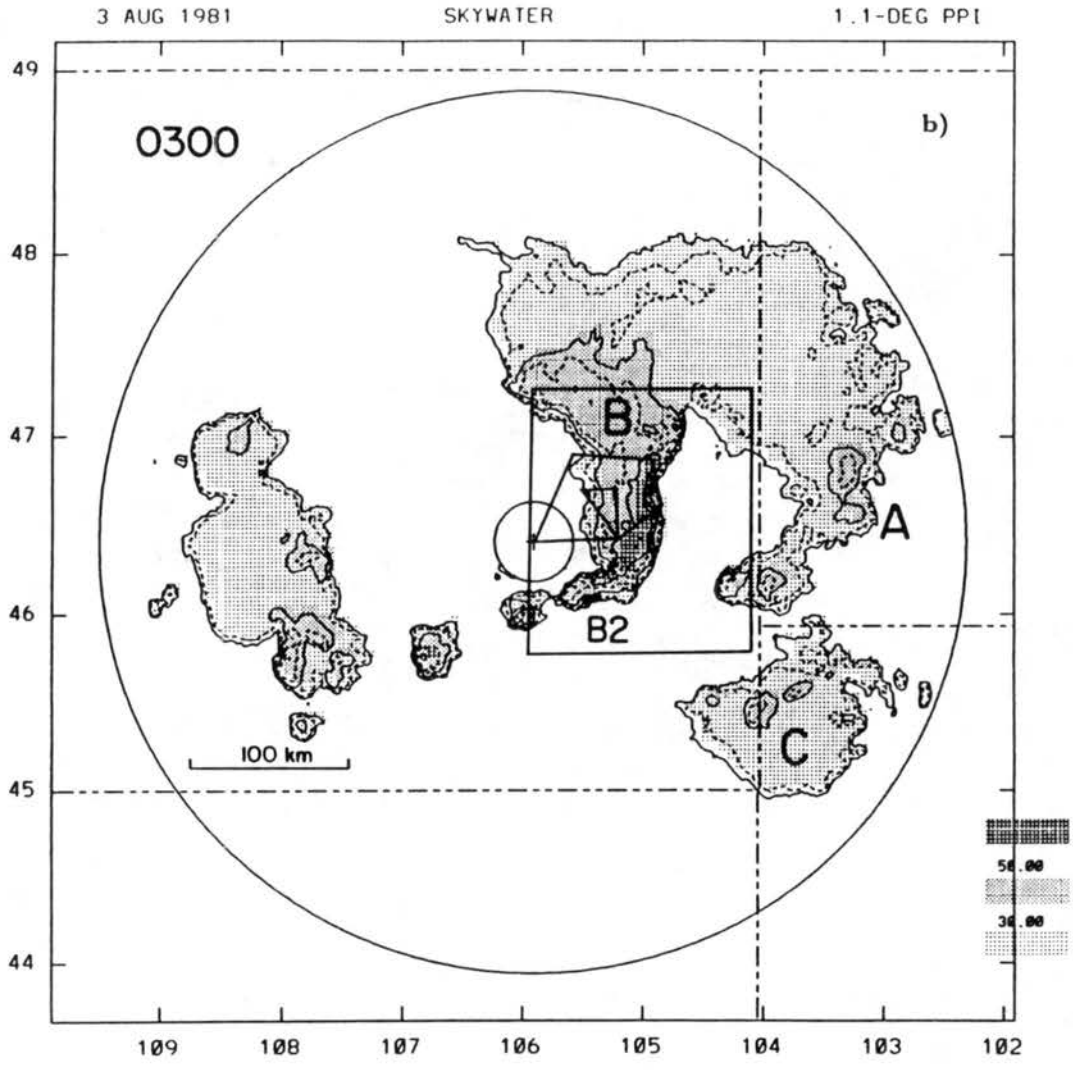


Figure 4.33: Horizontal mid-level radar reflectivity cross-sections at 0300 UTC 3 August 1981 obtained from the SKWR 5 cm radar. Labelling of the major storm systems as in Fig 4.21. The dashed lines depict the state boundaries. The large circle represents the 250 km range of the radar. The rectangle in eastern Montana represents the CCOPE mesonetwork and the polygon represents the Doppler radar array. Storms labeled B1 and B2 are discussed in the text. From Schmidt and Cotton (1989).

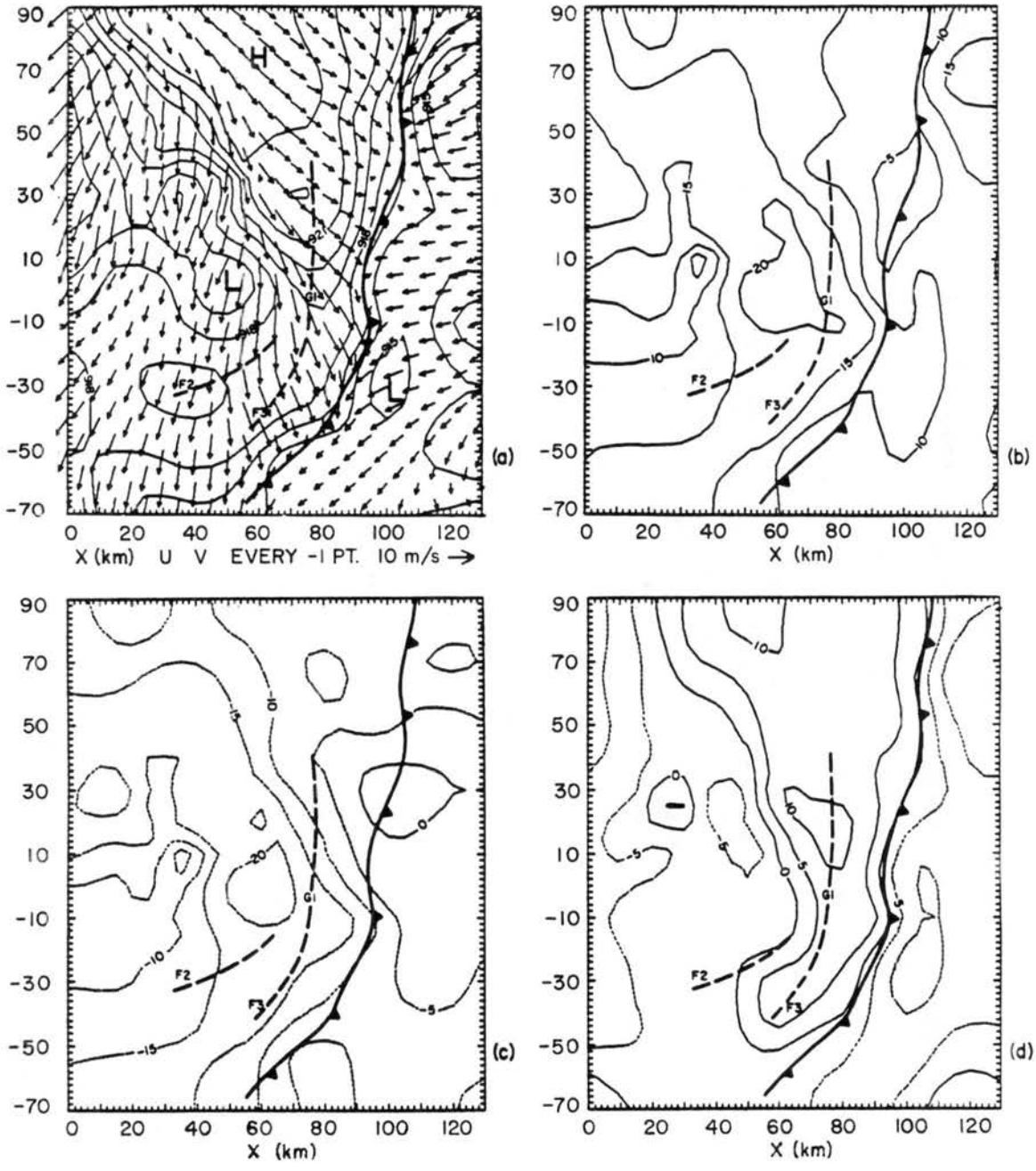


Figure 4.34: Objectively analyzed surface parameters derived from the CCOPE mesonet at 0305 UTC 3 August 1981. (a) surface pressure, reduced to Miles City, Montana, at 1hPa intervals and vector flow field, (b) wind speed, (c) v-component, (d) u-component contoured every 5 m/s, (e) values of equivalent potential temperature $\theta_e$ contoured every 2.0 K. The bold H and L mark high and low values of pressure in (a). The bold dashed lines represent position of the convective line. The labels F2,F3, and G1 represent convective groupings discussed in Schmidt and Cotton (1989).

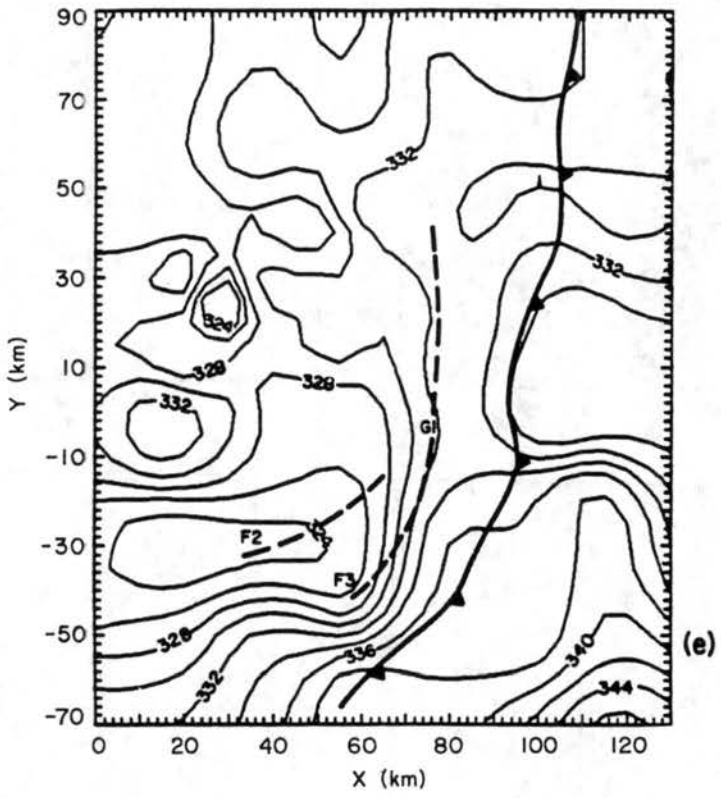


Figure 4.34: Continued.

precipitation loading. The development of the cirrus cloud shield toward the northwest in this case may have thus resulted in the northwest-southeast orientation of the surface pressure gradient established behind the line. This gradient was intensified near the vertex region of the bow echo in the vicinity of the wake low.

A detailed Doppler radar analyses of the bow echo squall line provides further details of how the convective and mesoscale flow fields within the line may have established and maintained the surface pressure fields which led to the trailing surface wind maximum (Fig 4.35). At low-levels there was strong cyclonic flow about the supercell which enhanced the low-level northerly flow near the mesolow, and the northwesterly flow along the leading edge of the system to the south of the supercell. The northward bias in the surface high pressure field was likely a result of the flow emanating from a supercell like cell within the line (labeled G1), which would have preferentially deposited precipitation particles to the north and northwest (Fig 4.35c). The location of the wake low was partly a reflection of the bow-shaped line segment but it may also have resulted from subsidence associated with the middle-level rear-to-front jet (cf. Johnson and Hamilton 1988). In this case, the jet was confined to the vertex region of the bow echo between two counter-rotating vortices located on either end of the convective line segment (Fig 4.35b). This confinement of the jet to a specific region may be a distinguishing aspect of bow echo squall lines compared to their more linear counterparts.

Another factor relevant to this storm, was the up-down downdraft circulation evident in the trajectories shown in Fig 4.36. These parcel trajectories reflect the stability of the inflowing air and the strong upward directed vertical pressure gradient force along the leading edge of the system (Knupp 1988). These parcels entered the strong downdraft evident on the northern flank of the supercell in Fig 4.34a and either turned cyclonically toward the leading convective line or exited out to the rear of the system. Note that the trajectories released closer to the supercell G1 (parcels E,F,and H), experienced greater vertical displacements before subsequently descending in the downdraft. This is likely a result of strong, dynamically-induced uplift on the flank of the supercell resulting from middle-level rotation (Weisman and Klemp 1984). Once removed from the region of uplift, such parcels may have produced strong low-level downdrafts. The rapid descent of these

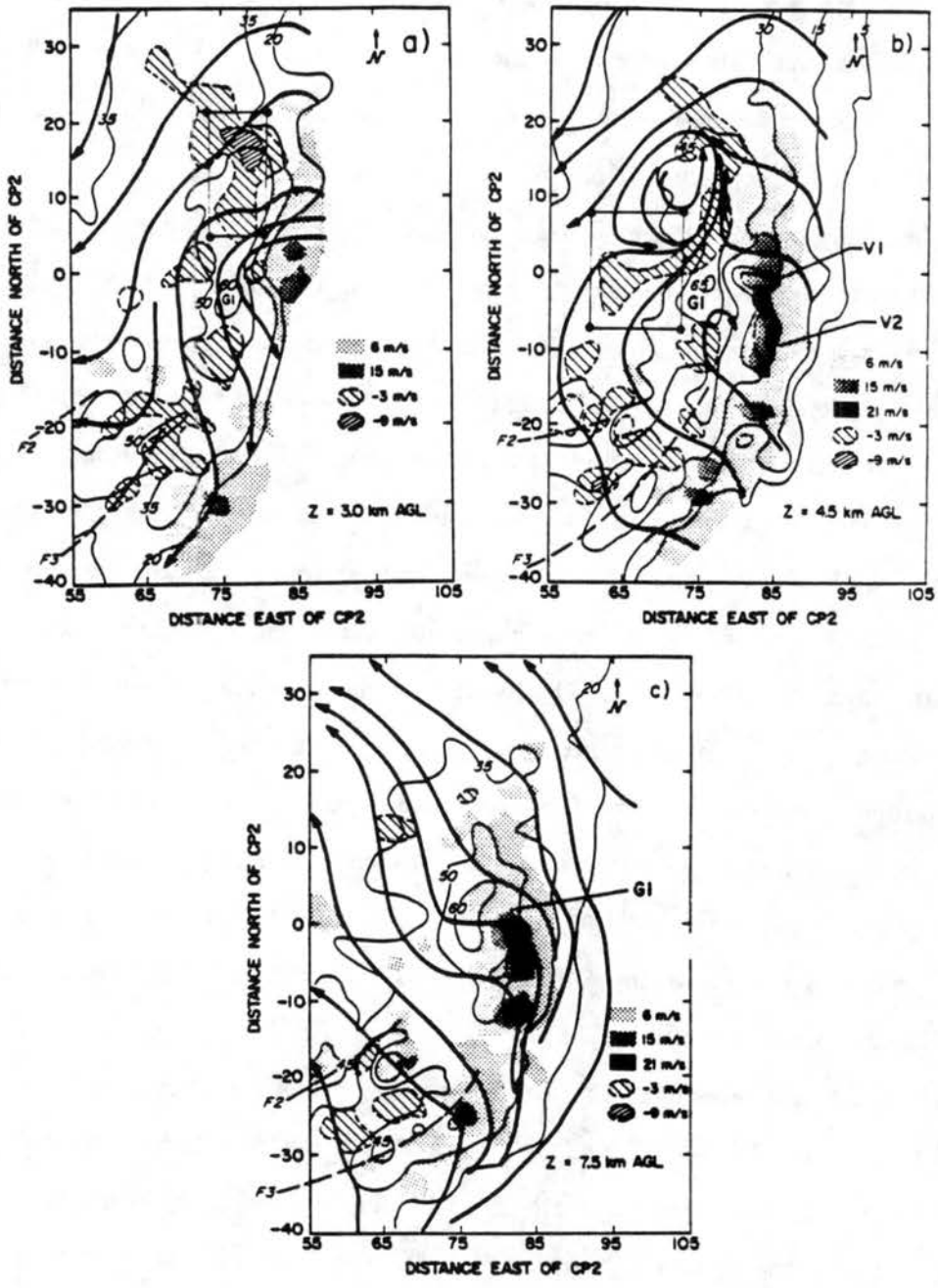


Figure 4.35: Storm kinematic fields derived from a multiple Doppler radar analysis at 0303 UTC showing horizontal cross-sections at (a) 3.0 km AGL, (b) 4.5 km AGL, and (c) 7.5 km AGL. Representative streamlines were derived from the Doppler data. Updraft $>$ 6 m $s^{-1}$ has been lightly shaded. Dark shading corresponds to the 15 and 21 m $s^{-1}$ updrafts respectively. Downdraft regions are hatched at -3 and -9 m $s^{-1}$ intervals. Contours depict relevant precipitation features. V1 and V2 refer to the primary weak echo regions associated with G1. The thin rectangle in (a) and (b) outline the areas where trajectories were released. (d) Horizontal cross-section of the radar derived reflectivity depicting the structure of the squall line. The thin rectangle in (d) denotes the region of the Doppler radar analyses. From Schmidt and Cotton (1989).

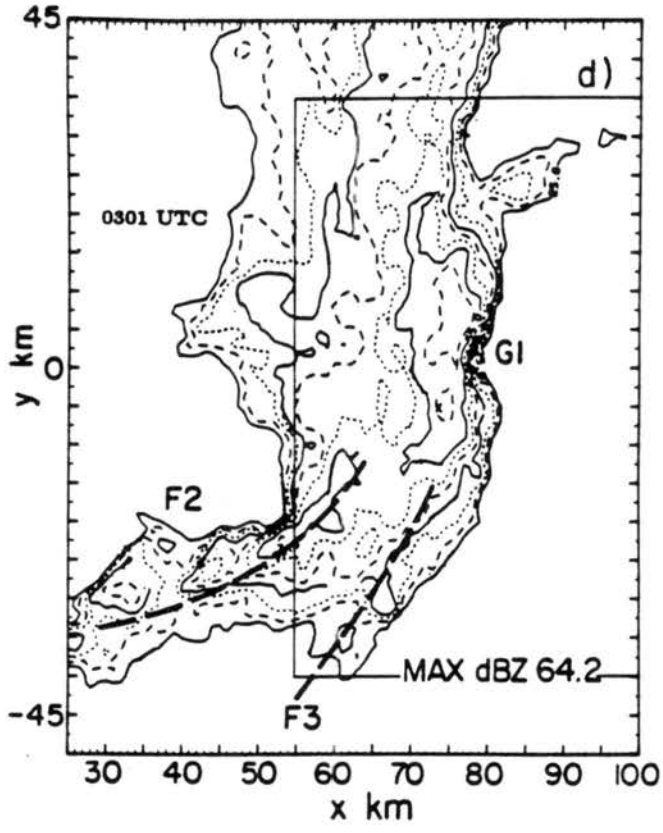


Figure 4.35: Continued.

parcels may have been one factor why the strongest surface winds occurred to the north of the track taken by the supercell (Fig 3.1). These 3-D aspects of the convective and meso-scale flow fields within the bow echo would provide an effective means to maintain the strong surface pressure gradient near the vertex region of the line and, subsequently, the strong northerly surface outflow if they were a persistent feature of the bow echo circulation. We will address this aspect of the bow echo circulation in greater detail in Chapter 6.

## 4.4 Summary

The primary features of the thermodynamic and vertical wind shear profiles of the two derecho cases are summarized in Fig 4.37. In each case the thermodynamic structure within the troposphere consisted of three distinct layers. These include a surface based stable layer 1 to 1.5 km thick, an elevated mixed layer of 3 to 4 km in depth, and an upper tropospheric layer of some intermediate stability. Sufficient moisture was present near the top of the stable layer in each case resulting in the high values of CAPE which fueled the systems.

Each case was also characterized by strong vertical wind shear through the depth of the troposphere. Though the details of the vertical wind shear profiles differed somewhat between the two cases, each showed an easterly flow component near the surface and peak west/southwesterly flow of 40 m $s^{-1}$ to 50 m $s^{-1}$ near the tropopause. The strong flow aloft was typically advecting into the derecho region as both cases formed in the exit region of an upper level jet streak.

In each case a southerly low-level jet was present which provided strong warm air and moisture advection into the derecho region at a level just above the low-level stable layer. The primary difference between the two cases was the magnitude of the jets and their impact on the surface flow fields. The jet in the PRE-STORM environment was nearly twice the magnitude of the CCOPE jet. In the PRE-STORM case the jet also appeared to affect the development of the surface trough within the stable air mass north of the warm frontal zone. This trough became the locus of the low-level easterly wind maximum which tracked through northwest Kansas along a route taken by the observed derecho. This suggests that the regional-scale environment of 12-13 May, unlike the CCOPE case, may have supplied the

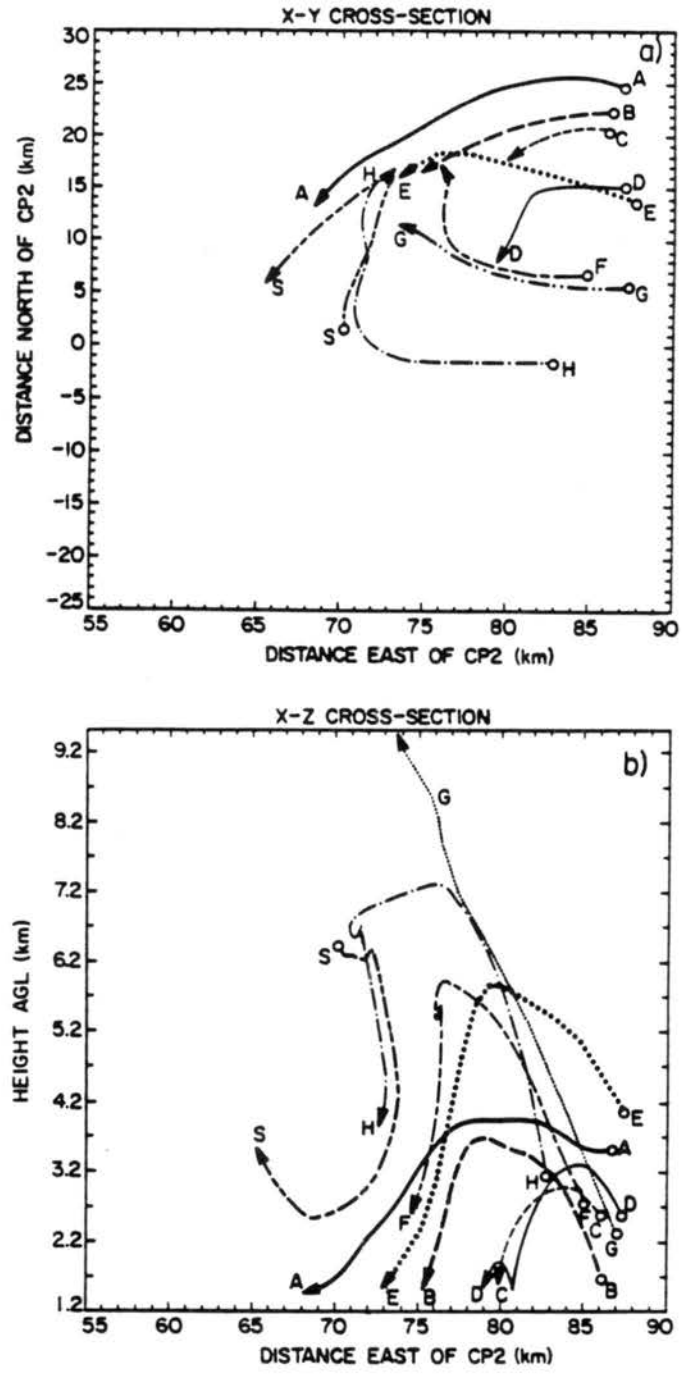


Figure 4.36: Air parcel trajectory released near the primary downdraft on the northern flank of G1 assuming steady state conditions at 0303 UTC 3 August 1981. Trajectory paths are shown in (a) horizontal $x$-$y$ and (b) vertical $y$-$z$ planes. Open circles represent the origin of the trajectory and arrow tips represent the termination point. From Schmidt and Cotton (1989)

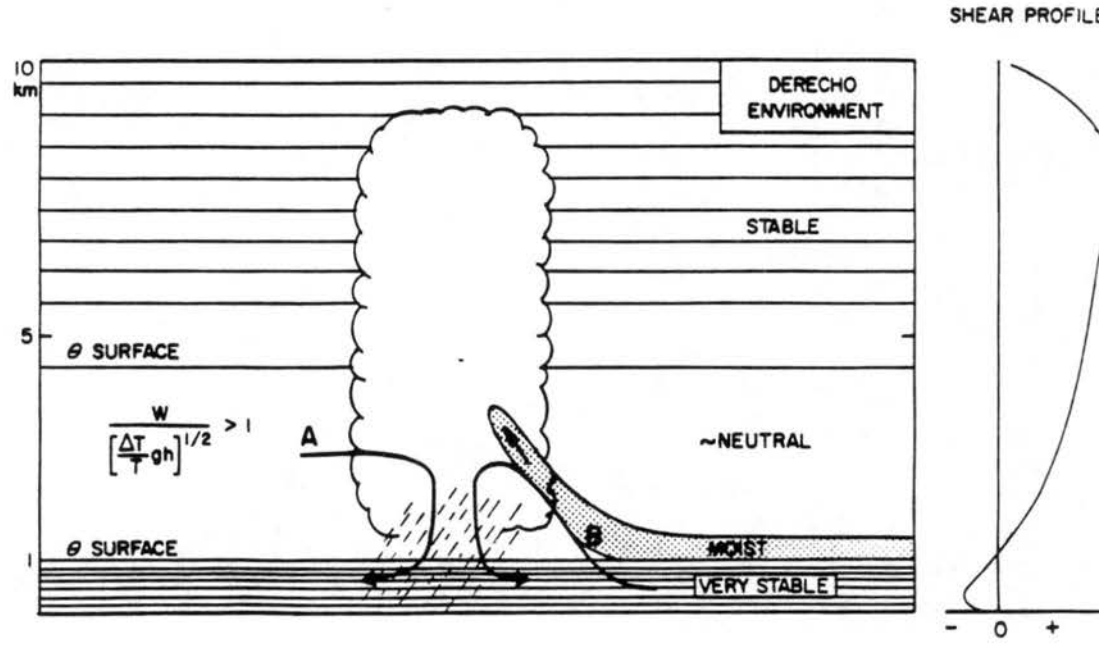


Figure 4.37: Schematic thermodynamic and vertical wind shear profiles summarizing the primary features of the 12-13 May 1985 and 2-3 August 1981 derechos. Horizontal solid lines represent potential temperature surfaces. Trajectories labeled A and B are similar to the downdraft trajectories suggested by Knupp and Cotton (1985) and are meant to suggest possible parcel paths into the primary downdraft. The scalloped outline denotes the cloud boundary and the shaded region denotes the primary source of moisture which fueled the systems. Note that the potential temperature surfaces beneath a storm in nature would likely deviate from the horizontal lines depicted beneath this schematic storm.

low-level momentum which ultimately had a significant impact on the timing, movement, and location of the PRE-STORM derecho.

The nested simulations also revealed other features of regional environment which may have aided the system longevity and track in each case. The PRE-STORM derecho appeared to form in, and remained coupled to, an area of synoptic-scale uplift that developed to the north of a deepening, synoptic-scale lee cyclone and in a region of positive vorticity advection. Thus strong dynamical support was present on the regional-scale throughout the entire lifetime of the derecho.

The CCOPE derecho, meanwhile, propagated along an east-west orientated stationary frontal zone. Though this frontal boundary was presumably instrumental in defining the track of the MCC, results from the nested regional-scale simulations also suggest that the positive vertical motion associated with the left exit region of the upper level jet and the advancing mountain-plains solenoid may have also aided the development, propagation and longevity of this system (Tremback 1990).

In the following chapters, we begin to investigate how this type of environmental setting may have promoted the development of the long-lived MCSs which produced the sustained severe surface winds.

## Chapter 5

# 2-D HORIZONTALLY HOMOGENEOUS EXPLICIT SIMULATIONS

In the previous chapter we established the thermodynamic structure and vertical wind shear profiles which accompanied the 12-13 May 1985 PRE-STORM and the 2-3 August 1981 CCOPE derechos. This was accomplished by supplementing observations of the two cases with regional-scale simulations initialized in a non-homogeneous environment based on the standard NMC analyses. Though these experiments were useful for identifying key features of the regional and mesoscale environment associated with these derechos, we were unable to explicitly resolve the explicit convective and meso$\beta$-scale circulations within the MCSs which may have further impacted the severe surface wind development and system longevity.

The goal of this and the subsequent chapter, therefore, is to investigate these aspects of the derechos within a two and three-dimensional, high resolution framework with explicit microphysics. To ease the interpretation of the results, the MCSs are initialized in a horizontally homogeneous environment consisting of the idealized, three-layer thermodynamic structure discussed in 3.2.2 (see Fig 3.5). The results are first shown for the two-dimensional squall line simulations described in Schmidt and Cotton (1990) [section 5.1]. We extend these results by showing the temporal evolution of the squall line (section 5.2) and by discussing in greater detail the dynamics associated with the surface wind speed maximum for the strong vertical wind shear experiments LS2 and LNU (section 5.3). The results of this experiment are then compared to the sensitivity experiments listed in Table 3.1 (section 5.4). A summary of the two-dimensional experiments may be found in section 5.5.

## 5.1 Idealized simulations in variable vertical wind shear

The initial two-dimensional experiments utilizing the three layer thermodynamic environment of Fig 3.5 were discussed in Schmidt and Cotton (1990). One of the primary

conclusions reached in that paper was the environment supported large amplitude trapped gravity waves which strongly affected the development and longevity of the simulated squall line and the production of the severe surface winds. To see why trapping may have occurred, consider the Boussinesq form of the Taylor-Goldstein equation *viz.*

$$\frac{d^2w}{dz^2} + m^2 w = 0 \tag{5.1}$$

where

$$m^2 = \frac{N^2}{[U(z)-c]^2} - \frac{U''(z)}{[U(z)-c]} - k^2 \quad \text{or} \quad m^2 = l^2 - k^2; \tag{5.2}$$

with $l^2$ being the Scorer parameter, N the Brunt-Väisällä frequency, k the horizontal wave number, and U(z)-c the Doppler shifted phase speed of the wave. This equation describes the conditions of wave trapping for linear waves of a given phase speed c and static stability N. If $l^2 < k^2$ at a given level in the atmosphere, the waves become evanescent with height and considerable wave energy may be retained near the source level of the wave (cf. Eliassen and Palm 1961). We see from (2) that this condition is likely met, for a given k, in a layer of low static stability (small N), in a environment characterized by positive U''(z), or in a sheared environment where the values of U(z)-c become large. For the thermodynamic profile of Fig 3.5, and the range of simulated wave speeds, a negative Scorer parameter was obtained for a $\lambda_x < 28$ km wave in the lower stable layer.

The structure of the simulated waves and their relationship to the squall line development are illustrated in Figs 5.1- 5.4. The field of gravity waves resulting from the upward acceleration of the initial bubble through the various layers within the troposphere was most clearly revealed in the zero flow experiment (Fig 5.1). The initial heating excited waves of differing amplitude and spatial scale within the upper and lower stable layers resulting in a nearly two-to-one difference in the phase speed as they propagated outward from the heat source ($\stackrel{+}{-}$ 30 *vs.* $\stackrel{+}{-}$ 15 m $s^{-1}$ for the upper and lower waves, respectively). The gravity waves, in the form of single waves of elevation or depression, produced large perturbations in the fields of pressure, horizontal flow, and potential temperature within the upper and lower tropospheric stable layers and a relatively weak response within the well-mixed layer.

Except for the field of $u'$, the wave generated perturbations had left/right symmetry about a vertical line through the region of initial heating (applied near x = 0). The asymmetry in the $u'$ field (a change in sign) reflects the effects of mass continuity as the horizontal flow responded to the vertical motion associated with the displacement of the isentropes during the wave passage. The wave-induced circulations may thus be regarded as horizontal vorticity couplets of opposite sign moving outward from the region of initial heating. Similar structures were obtained by Nicholls et al. (1990) who investigated the atmospheric response to a specified heat source in a one layer, linear analytical model.

As the waves encountered the high static stability within the stratosphere their phase lines became inclined from the vertical and their vertical wavelength shortened considerably. The tilt in the phase lines from the vertical is similar to that experienced by light rays passing through a denser medium. Like the light waves, an increase in the refractive index (in this case the static stability within the stratosphere) results in a faster phase propagation. For the phase fronts to remain continuous across the interface (the tropopause) requires a greater tilt of the phase lines in the stratosphere. We will demonstrate later that this simple wave property has an important consequence for the development of the modeled flow within the troposphere.

As vertical wind shear was added to the simulation, the perturbation flow began to resemble the 2-D squall line circulation of Newton (1950), Thorpe et al. (1982), and Smull and Houze (1987) [Figs 5.2 and 5.3]. This development was partially a result of changes in the wave characteristics as they experienced a Doppler shift in phase speed (in this case to the right) and a change in magnitude. The change in wave magnitude was particularly noticeable for the shorter boundary layer waves (compare Figs 5.2a and 5.3a). The positive horizontal vorticity within the ambient shear appeared to enhance the waves having the opposite spin (the LRW in this case). The counterclockwise perturbation flow about the favored LRW [4] formed the convective-scale updraft/downdraft couplet near x = 50 (Fig 5.3a)

---

[4]Though a closed circulation is suggested by the perturbation velocity fields, the wave relative flow remained front-to-rear at all levels.

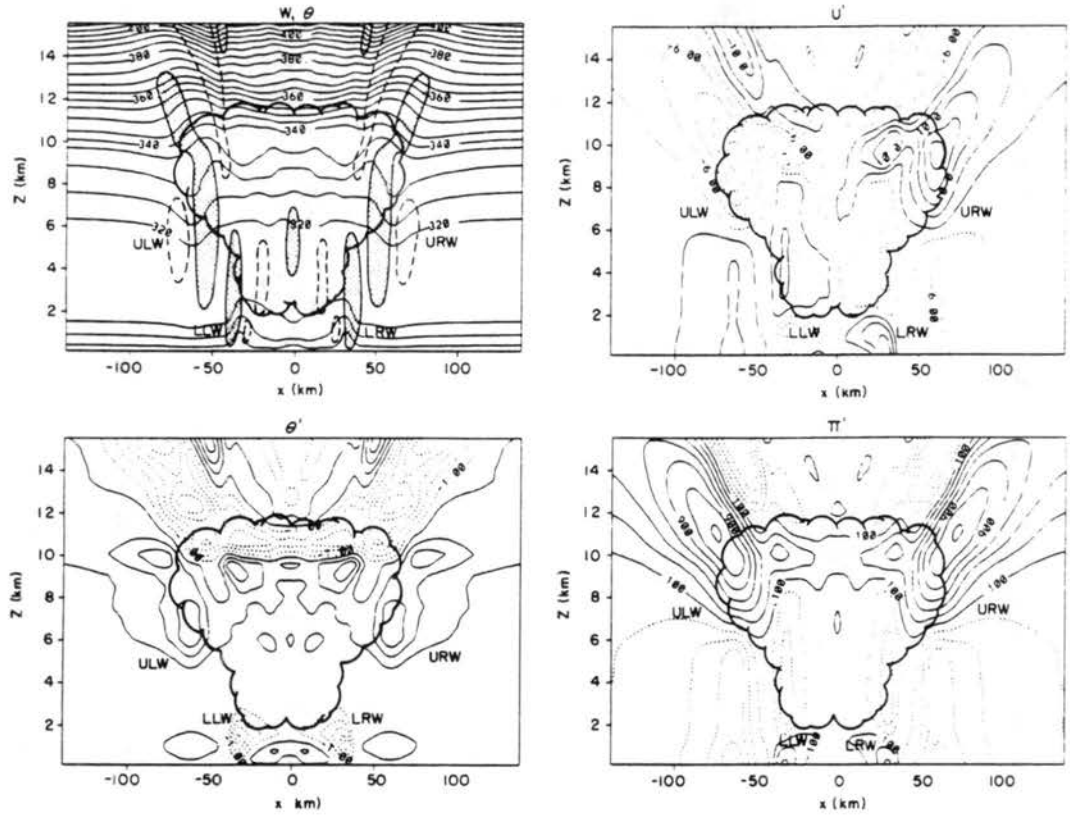


Figure 5.1: Vertical $x$-$z$ cross-sections experiment S0 at 3600 s. (a) Potential temperature ($\theta$) contoured every 5 K and vertical motion (w). Updrafts greater than 1 m $s^{-1}$ are shaded. Downdraft less than -1 m $s^{-1}$ are denoted by the dashed lines. (b) perturbation zonal velocity $u'$ every 4 m $s^{-1}$, (c) perturbation potential temperature $\theta'$ (every 2 K), (d) perturbation Exner function contoured every 0.2 J $kg^{-1}$ $K^{-1}$. Scalloped line in each panel denotes the cloud boundary. The labels ULW, URW, LLW, and LRW denote the primary waves discussed in the text. Note that only a portion of the entire domain is shown.

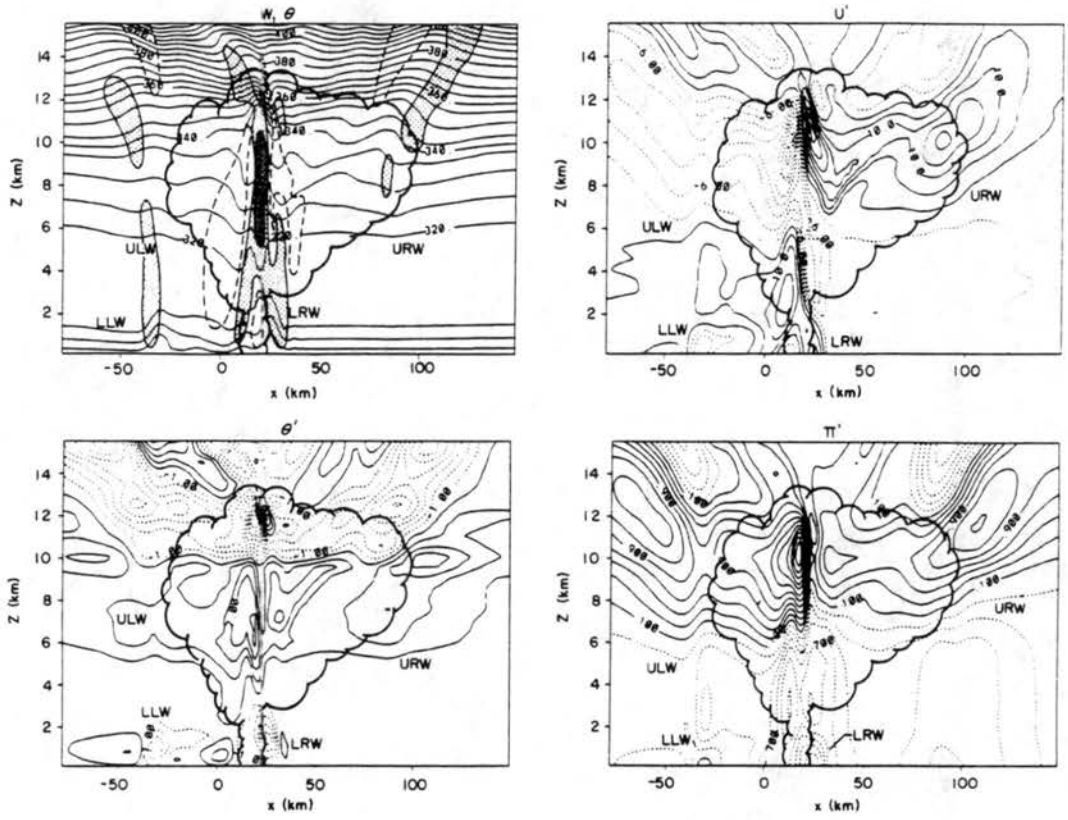


Figure 5.2: As in Fig 5.1 except for experiment S1 (weak shear) at 3600 s. Darker shading denotes updraft in excess of 10 m $s^{-1}$.

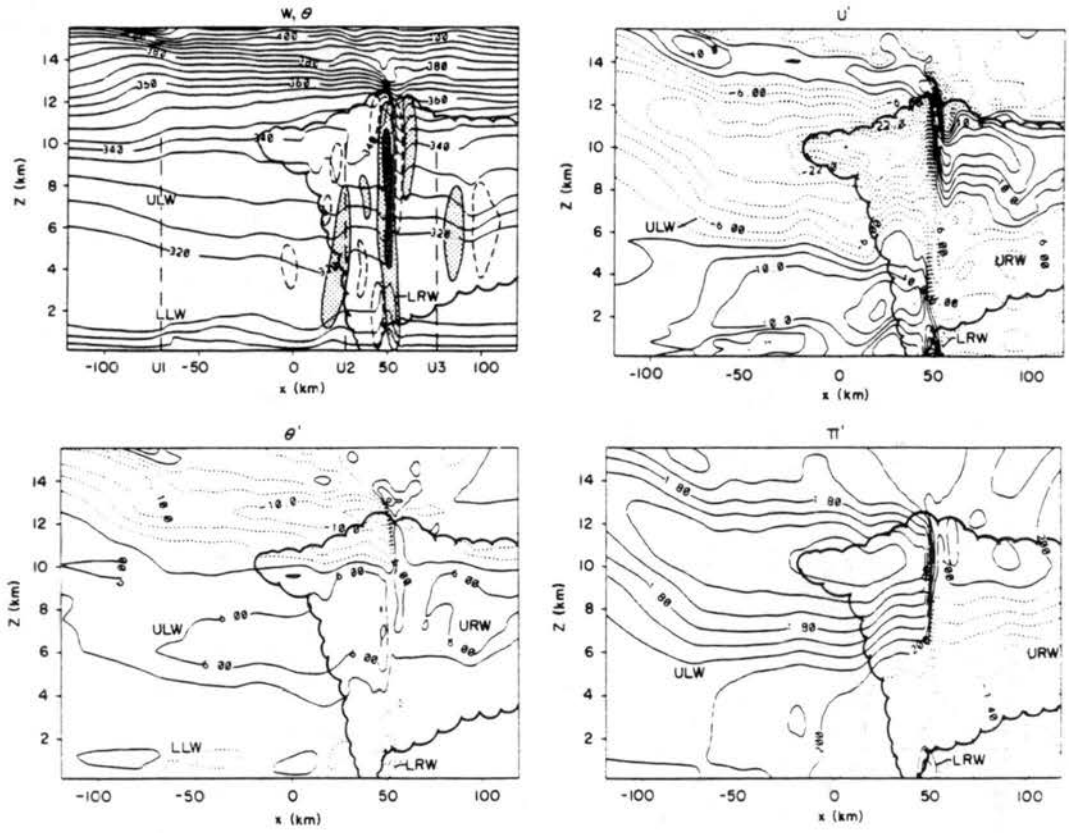


Figure 5.3: As in Fig 5.1 except for experiment S2 (strong shear) at 7200 s. Note that the contour interval in (c) is 4° C and in (d) 0.4 J $kg^{-1}$ $K^{-1}$.

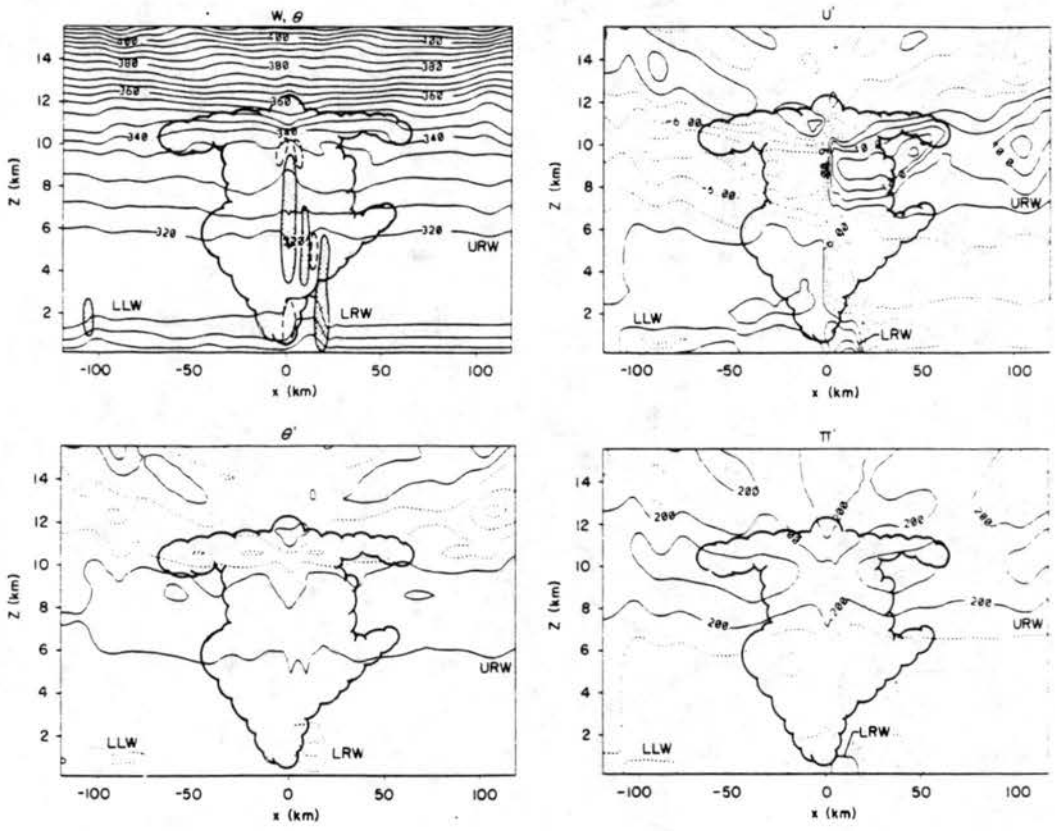


Figure 5.4: As in Fig 5.1 except for experiment S3 (low-level shear) at 5400 s.

and surface $u'$ values of nearly 30 m $s^{-1}$ (Fig 5.3b). Note that the surface wind perturbations within the lower level waves increased in the higher shear experiments (compare Fig 5.1- 5.4). This appears to have resulted, in part, from a greater upward displacement of the isentropic surfaces in the higher shear experiments (Fig 5.3a and 5.4) which increased the cooling and, subsequently, the magnitude of the surface high pressure. As noted by Schmidt and Cotton (1990), the wave also helped sustain the convective-scale updraft by providing a continual source of low-level lift. The wave movement accounted for the rapid speed of the simulated squall line (19 m $s^{-1}$) and closely matched the 21 m $s^{-1}$ movement of the observed squall line reported by Schmidt and Cotton (1989).

The Doppler shift of the waves is evident by comparing Figs 5.1- 5.3. One effect of the Doppler shift on the flow fields was a consolidation of the upshear rear-to-front and front-to-rear flow and an extended region of upper level outflow on the downshear region of the line (Figs 5.2b and 5.3b). The wave contribution to these flow branches are recognized (on comparing with Fig 5.1) as the local maxima and minima $\theta'$, $u'$, and $\pi'$ through the depth of the troposphere on either flank of the line [5]. The Doppler shift also had the affect of retaining the upshear propagating ULW in the near field of the convective-scale updraft for a longer period of time. Since the circulation about this wave opposed the environment shear (Figs 5.1b), it acted to buffer the updraft from the debilitating affects of the upper level ambient flow, a factor which may have aided the longevity of the system.

An important aspect of the upper tropospheric waves was their apparent role in the rapid upshear development of the buoyancy fields on the trailing flank of the squall line (a result also obtained by Nicholls et al. 1990). Such buoyancy fields have been implicated for their role on the development of the rear-to-front jet by Nicholls (1987), Lafore and Moncrieff (1989), and Weisman (1990). In our case the warming in the upper troposphere beyond the trailing stratiform cloud appears to result from the subsidence beneath the high pressure region located near the tropopause. The development of the high pressure region beyond the trailing stratiform cloud appeared to result from the cooling associated

---

[5] We define the line position here as the location of the LRW.

with the upward propagating gravity wave energy in the stratosphere (Fig 5.3c). Since the wave perturbation extended farther upshear in the stratosphere, a result of the change in static stability at the tropopause, parcels approaching the storm in the upper troposphere first experienced a downward directed pressure gradient and began to subside. Since this occurred in a region where the flow was approximately isentropic, we infer that the gravity waves generated by the convective-scale updraft acted to partially block the ambient flow within the upper troposphere well upshear from the trailing stratiform region.

Note that as the isentropes in the upper troposphere were displaced downward, the well-mixed layer depth was reduced. These led to a channeling of the flow within the layer and the formation of the rear-to-front middle-level jet. A comparison of (Fig 5.3) with the weaker shear experiments (Fig 5.2 and (Fig 5.4) suggests that the magnitude of the channeling was enhanced by strong vertical wind shear through the depth of the troposphere. This demonstrates the sensitivity of the simulated flow fields to the vertical wind shear profiles within the upper troposphere and lower stratosphere.

## 5.2 Temporal evolution of the high shear case LS2

The results presented above cover the developments of the simulated squall line through the first two hours of its life-cycle. To determine the temporal evolution of the line, we reran experiment S2 with a domain size of 800 km for a period of five hours (experiment LS2). The results, shown after five hours in Fig 5.5, reveal that the flow structure, other than growing outward laterally, remained remarkably steady throughout the period. The low-level wave remained the focal point of the severe surface winds and continued to provide the low-level lift that supported the convective-scale updraft. In the upper levels, the high pressure region continued to build upshear leading to a elongated region of upper-level blocked flow and a middle-level jet structure that extended well beyond the trailing cirrus cloud shield. Since the upshear development of the line beyond the trailing cloud shield was associated with the ULW (located on the left border of Fig 5.5), the lateral development is easily calculated from the difference in phase speed between the ULW and the downshear propagating LRW (approximately 20 m $s^{-1}$ x 18000 s = 360 km).

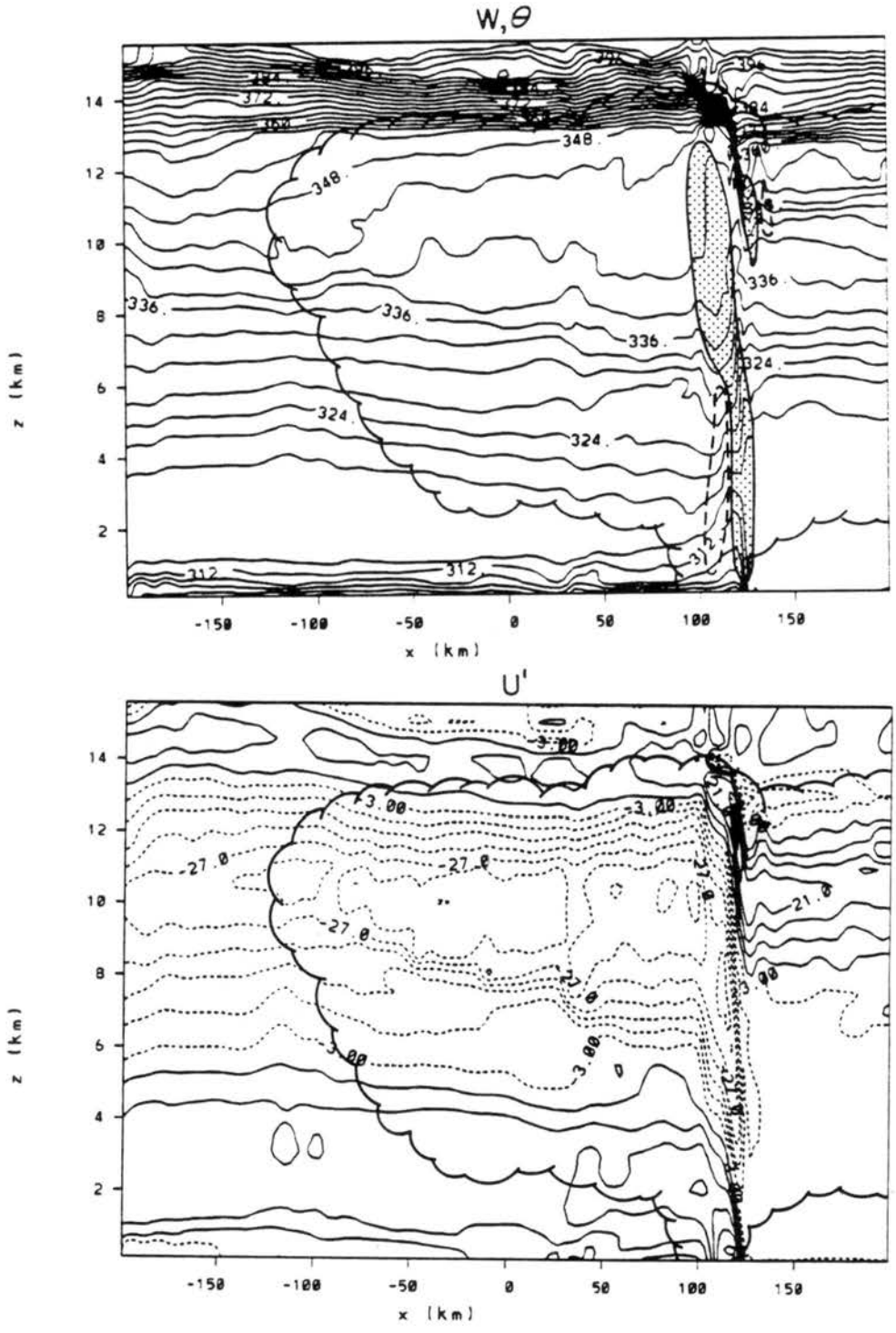


Figure 5.5: Vertical $x$-$z$ cross-sections of experiment LS2 run on the large (800 km) domain at 18000 s. (a) Potential temperature ($\theta$) contoured every 3 K and vertical motion (w). Updrafts greater than 1 m s$^{-1}$ are shaded. Downdraft less than -1 m s$^{-1}$ are denoted by the dashed lines. (b) perturbation zonal velocity $u'$ every 6 m s$^{-1}$, (c) perturbation potential temperature $\theta'$ (every 4 K), (d) perturbation Exner function contoured every 0.4 J kg$^{-1}$ K$^{-1}$. Scalloped line in each panel denotes the cloud boundary.

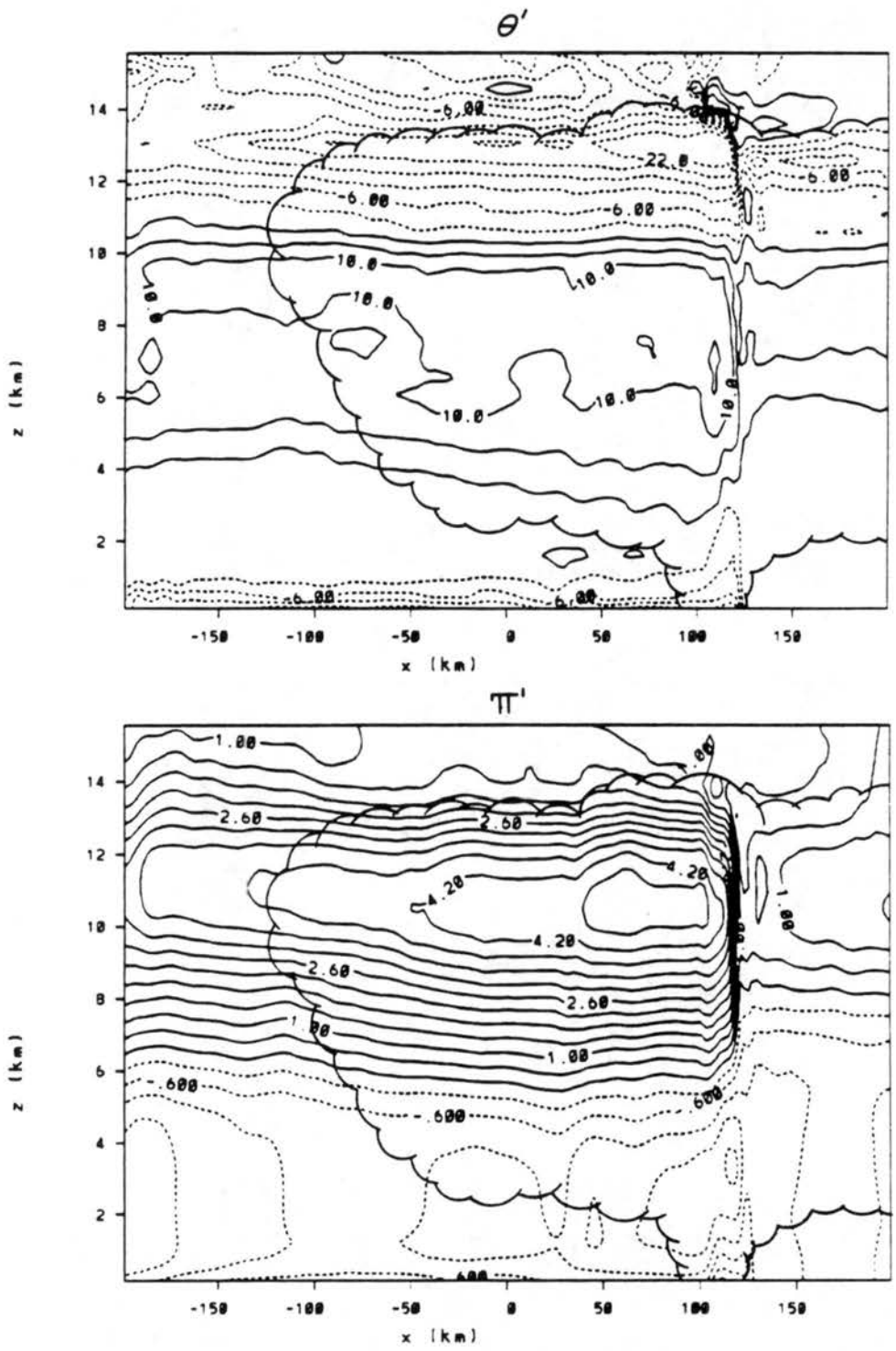


Figure 5.5: Continued.

## 5.3 Surface wind dynamics

The simulations thus far have shown that the magnitude of the surface wind perturbation increased in the environments initialized with a stronger vertical wind shear. Two factors which may have led to this tendency were the increased strength of rear-to-front flow and the larger amplitude of the lower-level wave. In this section we discuss the relative importance of these two developments on the strength of the simulated surface flow for experiment LS2 and the other high shear sensitivity experiments listed in Table 3.1.

### 5.3.1 Temporal evolution of the maximum surface wind gusts.

A time series of the maximum surface wind perturbation for the high shear cases is illustrated in Fig 5.6. Each experiment shows the development of severe, northwesterly, surface winds within the first three hours of the simulation. This is consistent with the time lag between the initial storms and the first report of severe winds discussed by Johns and Hirt (1987). As might be expected, the neutral boundary layer simulation (LNU) produced the greatest surface wind gusts but all experiments appeared to converge toward a common $u$-component value of 30 m s$^{-1}$ by five hours [6]. Since the simulated squall lines would have traveled approximately 360 km during the five hour period displayed in Fig 5.6, we find that a derecho-like swath of strong-to-severe winds was developing at the surface in each experiment.

### 5.3.2 Surface outflow characteristics

Rather than discussing in detail the conditions leading to the strength of the simulated surface outflow for each experiment shown in Fig 5.6, we compare/contrast the characteristics of experiments LS2 and LNU. A comparison of these experiments illustrate important differences which may exist when a stable, rather than neutral, ABL is used to initialize the model. It also generalizes the results by providing a range of thermodynamic conditions

---

[6] To obtain the ground relative flow, subtract 8 m s$^{-1}$ from the $u$-component in Fig 5.6 and, in the usual manner, add the appropriate $v$-component

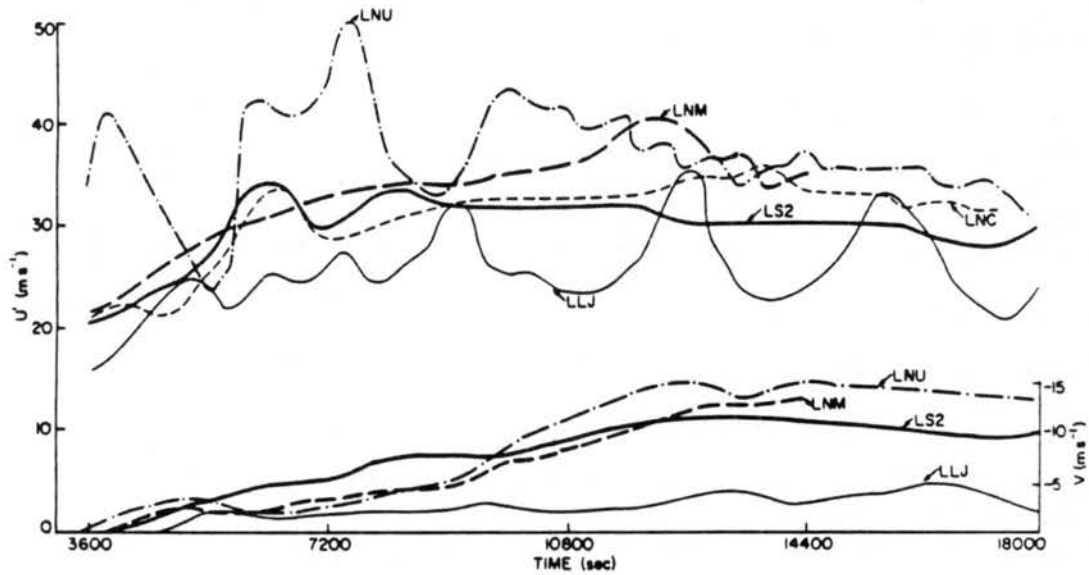


Figure 5.6: Time series of $u'$ and $v'$ (m $s^{-1}$) for the selected experiments listed in Table 3.1.

which individual storms would likely encounter over the extended time periods typical of derecho systems. The remaining experiments will be briefly discussed in section 5.4.

The results of running the simulation with a neutral, rather than stable ABL are shown at 18000 s in Fig 5.7. Note that the overall structure of the flow upshear from the leading convective line (Fig 5.7b) is almost identical with that obtained for experiment LS2. One reason for the similarity is that the upshear propagation of the low-level cold pool in experiment LNU had a similar depth to the pre-existing stable layer in experiment LS2 [7]. This convectively-induced stable layer, combined with the similar downward displacement of the upper tropospheric isentropic surfaces produced by the gravity wave activity, had the same affect on reducing the mixed layer depth and, consequently, on the middle-level channeling of the flow which aided the development of the rear-to-front jet.

Other similarities between the two simulations include the upward directed vertical pressure gradient force located along the leading convective line between the surface meso-high and the middle-level low pressure centered near the level of free convection (LFC) [approximately 3.5 km AGL]. This common feature of propagating convective systems appears to owe its origin to diabatic cooling and precipitation loading within the subcloud layer (Fujita 1955), warming aloft within the updraft (LeMone et al. 1984), nonhydrostatic affects associated with the convergence along the leading gust front (Wakimoto 1982) and/or rapid parcel accelerations within either the convective-scale updrafts or downdrafts (Knupp 1988), or dynamic affects associated with the shear, curvature, and stretching of the flow (cf. Rotunno and Klemp 1982).

A closer view of the kinematic structure along the leading convective line for each experiment (Figs 5.8 and 5.9) reveals that though the magnitude and structure of the high/low couplet were similar, they were produced by entirely different processes. Note in particular that the minimum $\theta'$ values in experiment LNU are located at the surface and extend well upshear from the line (Fig 5.8c) while, in the stable layer experiment (LS2), the surface $\theta'$ values are nearly zero and are confined to the position of the low-level wave

---

[7] Recall that the stable layer used to initialize experiment LS2 was in fact a result of convectively-induced outflow from a previous system

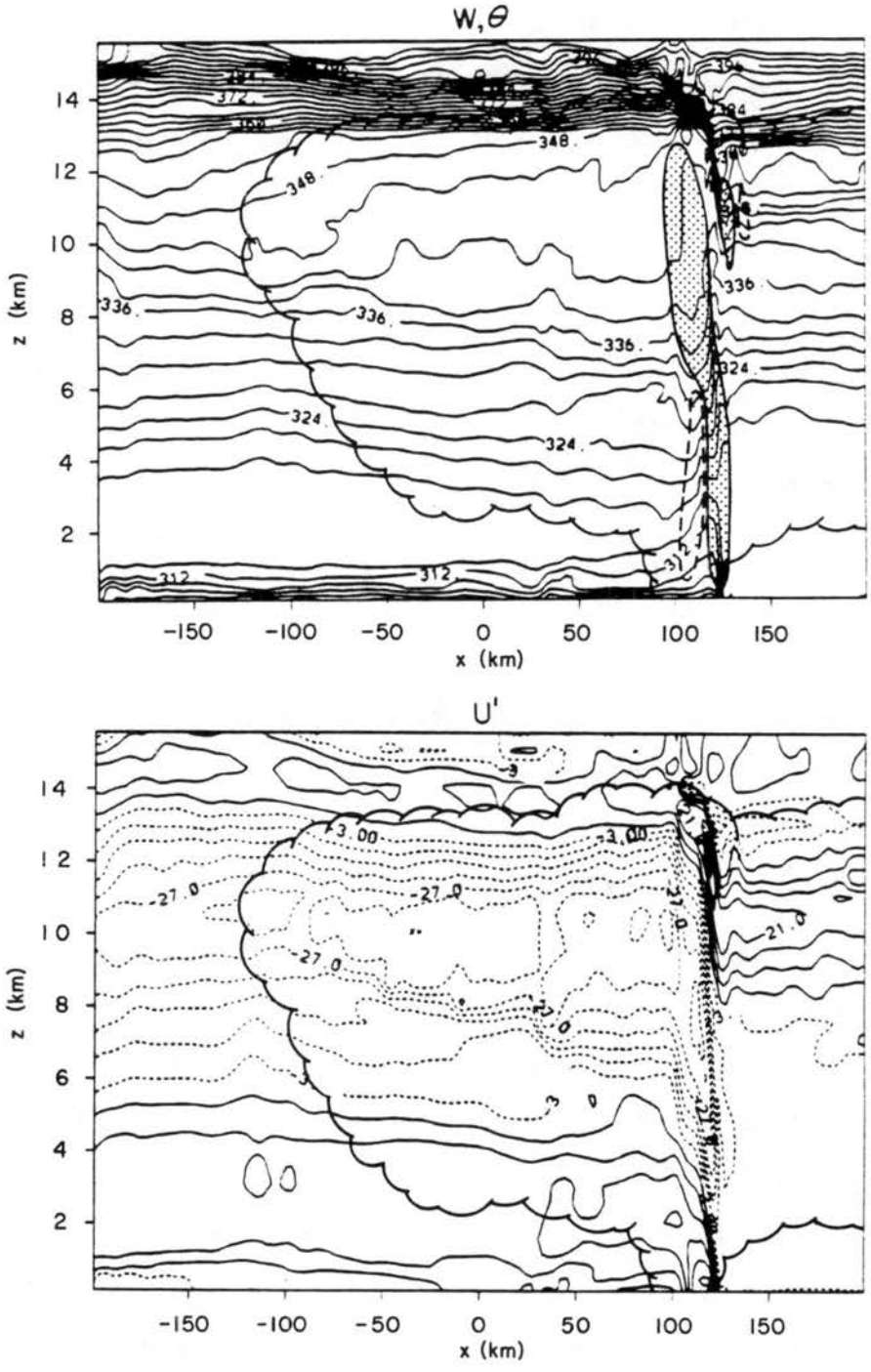


Figure 5.7: Vertical $x$-$z$ cross-sections of the neutral boundary layer experiment (LNU) at 18000 s. (a) Potential temperature ($\theta$) contoured every 3 K and vertical motion (w). Updrafts greater than 1 m $s^{-1}$ are shaded. Downdraft less than -1 m $s^{-1}$ are denoted by the dashed lines. (b) perturbation zonal velocity $u'$ every 6 m $s^{-1}$, (c) perturbation potential temperature $\theta'$ (every 4 K), (d) perturbation Exner function contoured every 0.4 J $kg^{-1}$ $K^{-1}$. Scalloped line in each panel denotes the cloud boundary.

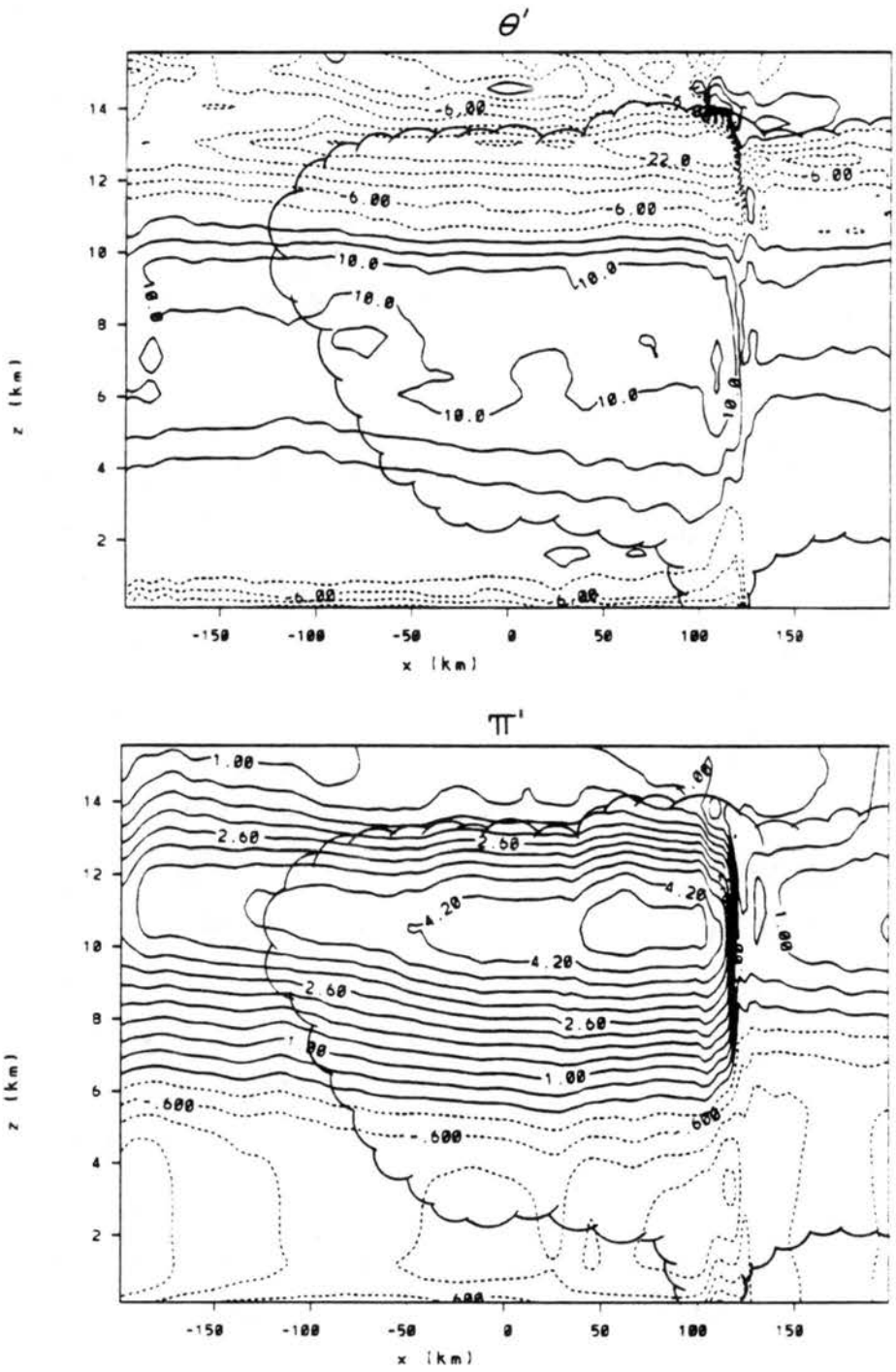


Figure 5.7: Continued.

(Fig 5.9c). We also find much lower $\theta_e$ values within the surface wind maximum in experiment LNU (compare Fig 5.8b and 5.9b) This suggests that surface cooling in experiment LNU resulted from an infusion of middle-level, low-valued $\theta_e$ air into the boundary layer while, in experiment LS2, the low-level cooling resulted from diabatic affects and from the upward displacement of the lower stable layer. Additional differences in the low-level thermodynamic structure likely reflect variations in the diabatic cooling and loading that resulted from the changes in low-level relative humidity, static stability, and updraft source level between the two storms.

In either case the maximum surface winds were located near the leading convective line where the cold air perturbations were deepest (Fig 5.8b and 5.9b). The deeper layer of cold air led to rapid increases in the surface pressure (Fig 5.8d and 5.9d) which, in turn, enhanced the surface outflow strength (Fig 5.8b and 5.9b). In each case the deepest layer of cold air was located beneath the middle-level mesolow suggesting that lifting, generated by the upward-directed, nonhydrostatic, vertical pressure gradient within the storm, had a key role in generating the strong surface winds. The primary difference between the two simulations being that the storm in experiment LNU was drawing up its own outflow while, in experiment LS2, it was drawing up the pre-existing surface-based stable layer.

An inspection of Fig 5.10 shows that the low pressure zone located near the LFC had a significant nonhydrostatic component. This may have been a result of the rapid upward acceleration of parcels within the elevated well-mixed layer. This suggests that a rapid decrease in static stability immediately above the surface-based stable layer may have enhanced the storm's ability to lift the lower layer. *The presence of the elevated well-mixed layer, therefore, may be one factor which determines whether or not a storm overriding a deep surface-based stable layer generates severe surface winds.*

One may argue, however, that an elevated well-mixed layer also increases the amount of warming generated aloft within the updraft. This warming might then negate any surface pressure increase resulting from a greater upward displacement of the lower isentropic surfaces generated by the nonhydrostatic vertical pressure gradient. A comparison of Fig 5.10b and Fig 5.9c shows that this would indeed be the case were it not for the upshear tilt of the updraft. The hydrostatic reduction in pressure beneath the warm updraft extends to

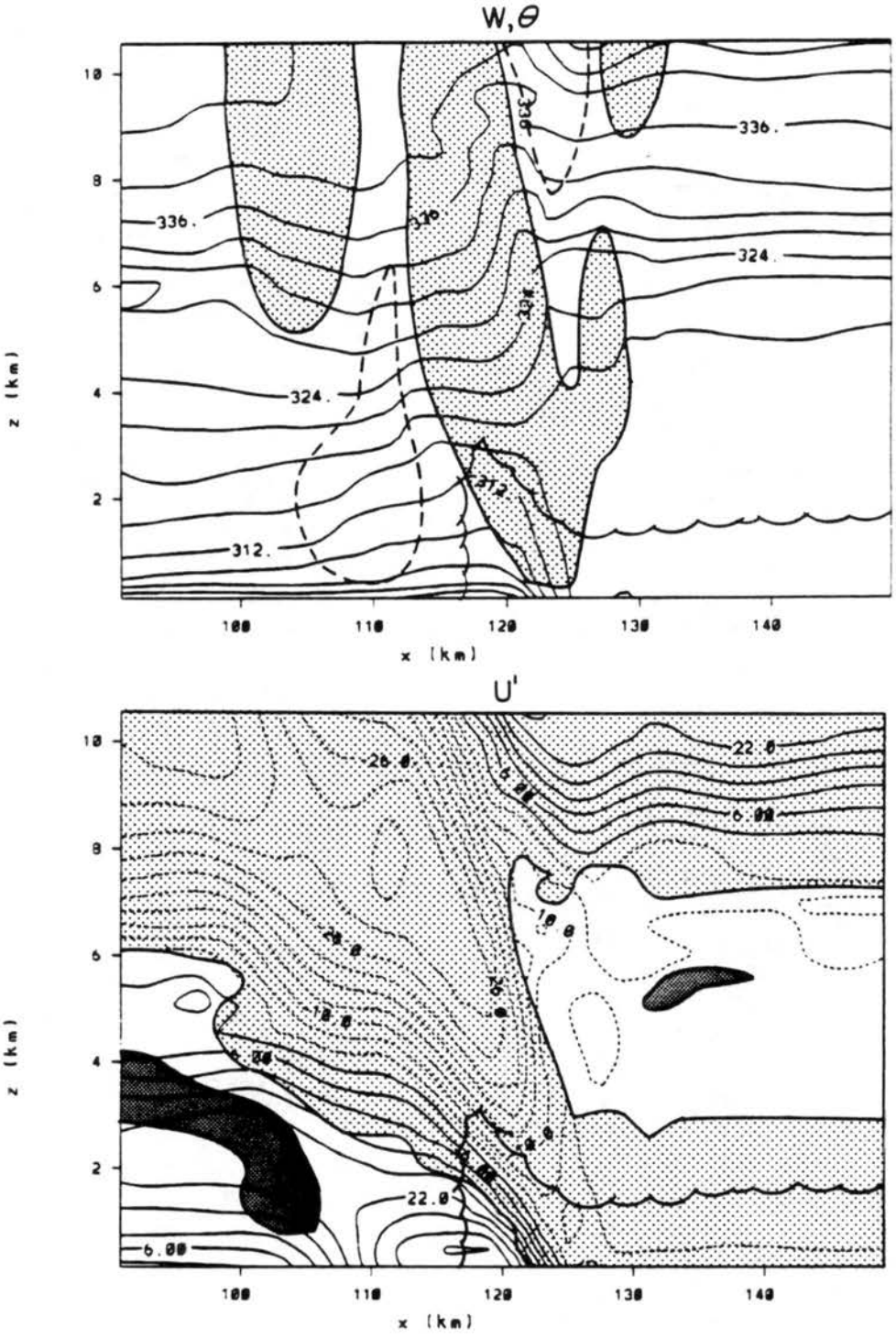


Figure 5.8: Windowed in view of the convective region of Fig 5.7. (a) As in Fig 5.7, (b) $u'$ every 4 m $s^{-1}$ (c) perturbation potential temperature $\theta'$ (every 2 K), and (d) perturbation Exner function contoured every 0.2 J $kg^{-1}$ $K^{-1}$. Scalloped line in each panel denotes the cloud boundary.

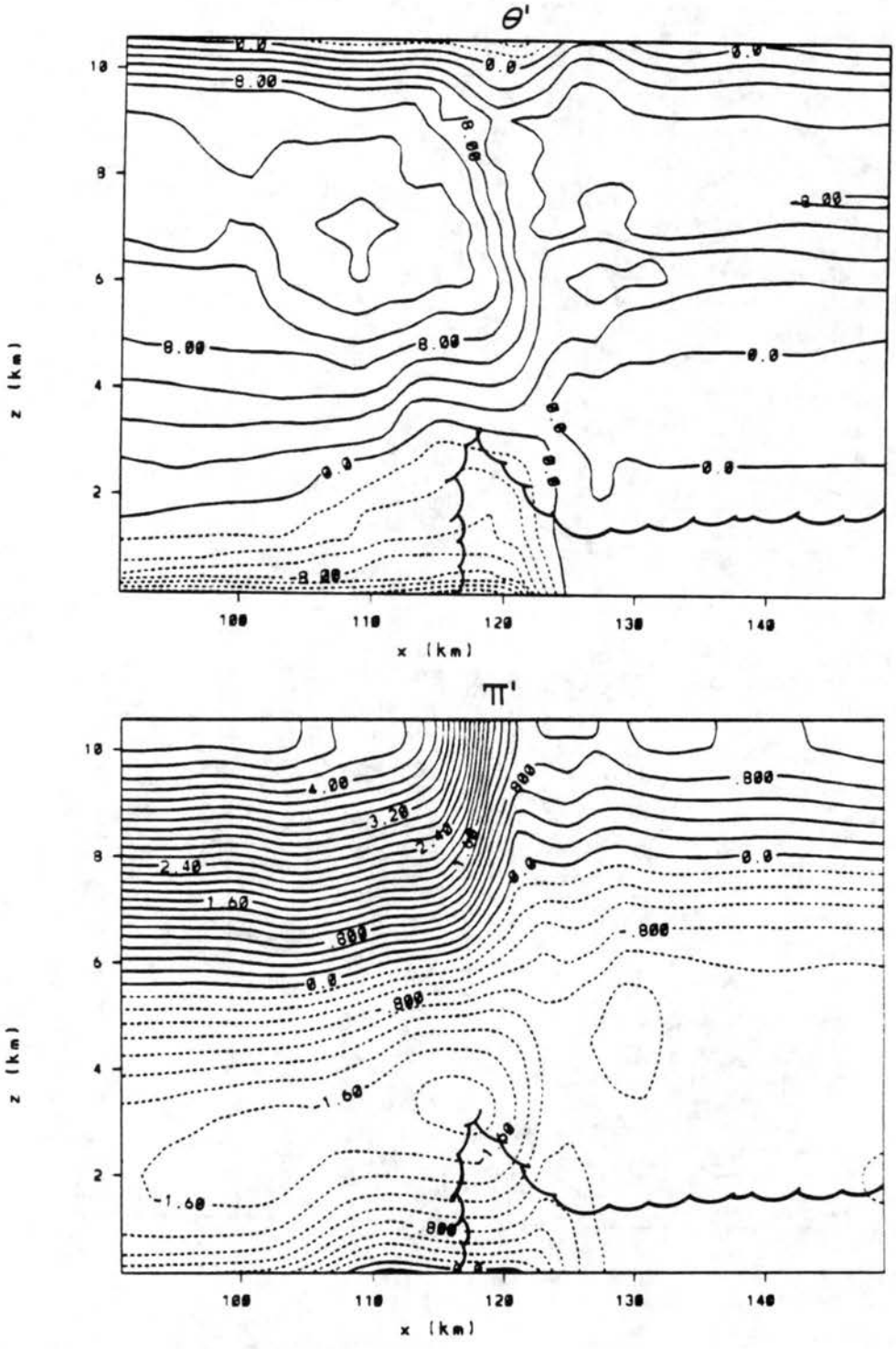


Figure 5.8: Continued.

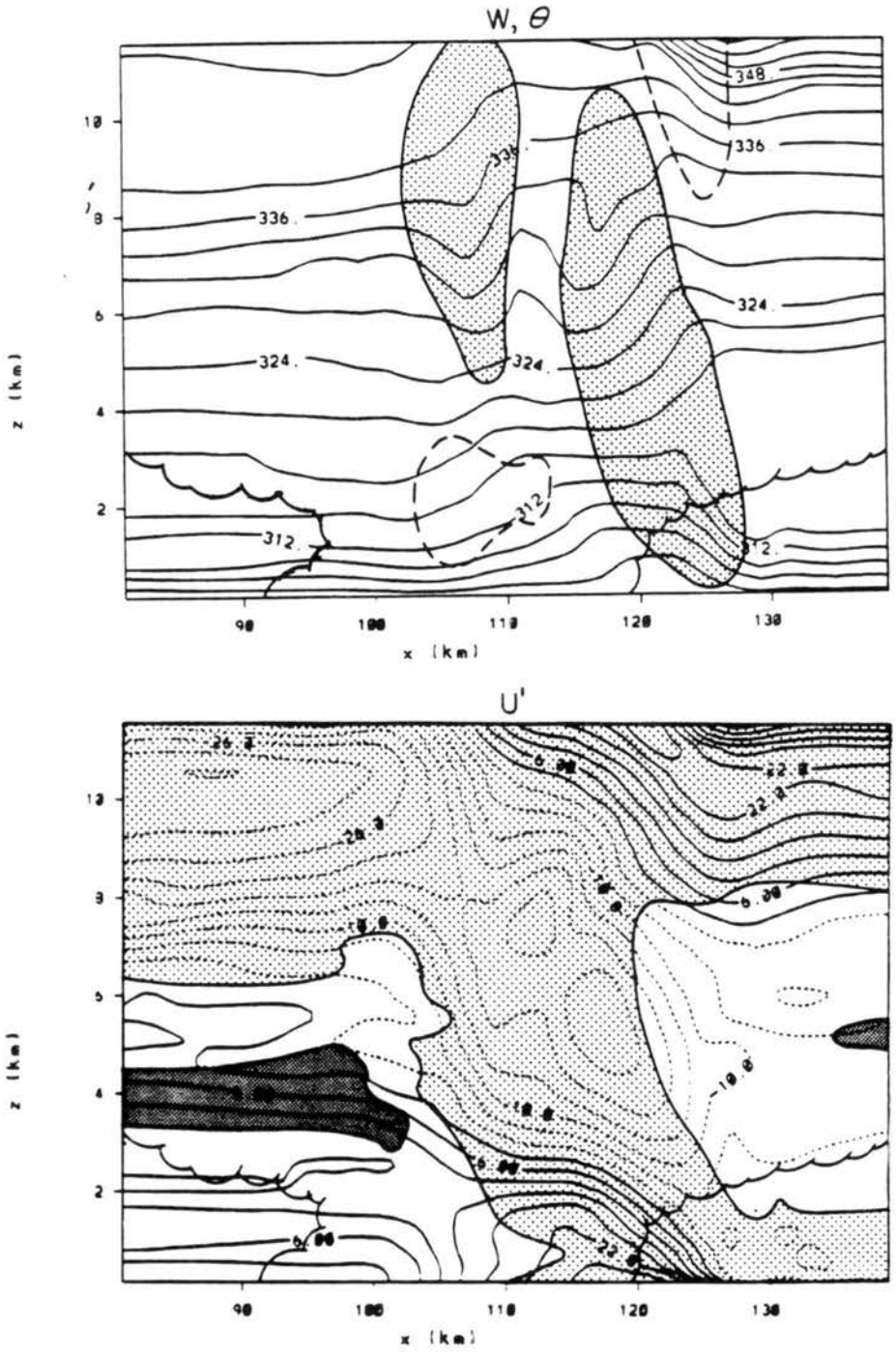


Figure 5.9: Windowed in view of the convective region of Fig 5.5. (a) As in Fig 5.5, (b) $u'$ every 4 m $s^{-1}$ (c) perturbation potential temperature $\theta'$ (every 2 K), and (d) perturbation Exner function contoured every 0.2 J $kg^{-1}$ $K^{-1}$. Scalloped line in each panel denotes the cloud boundary.

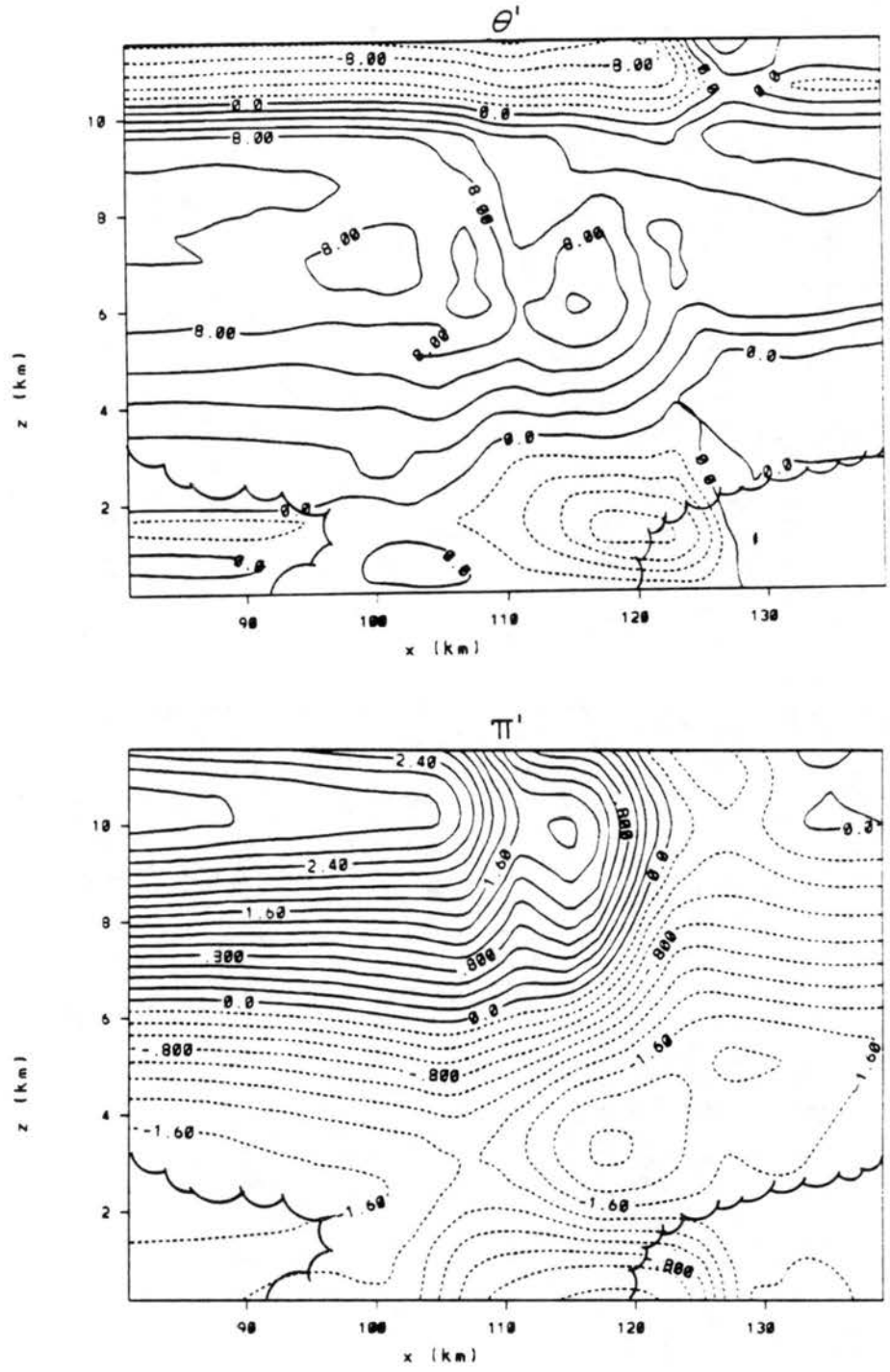


Figure 5.9: Continued.

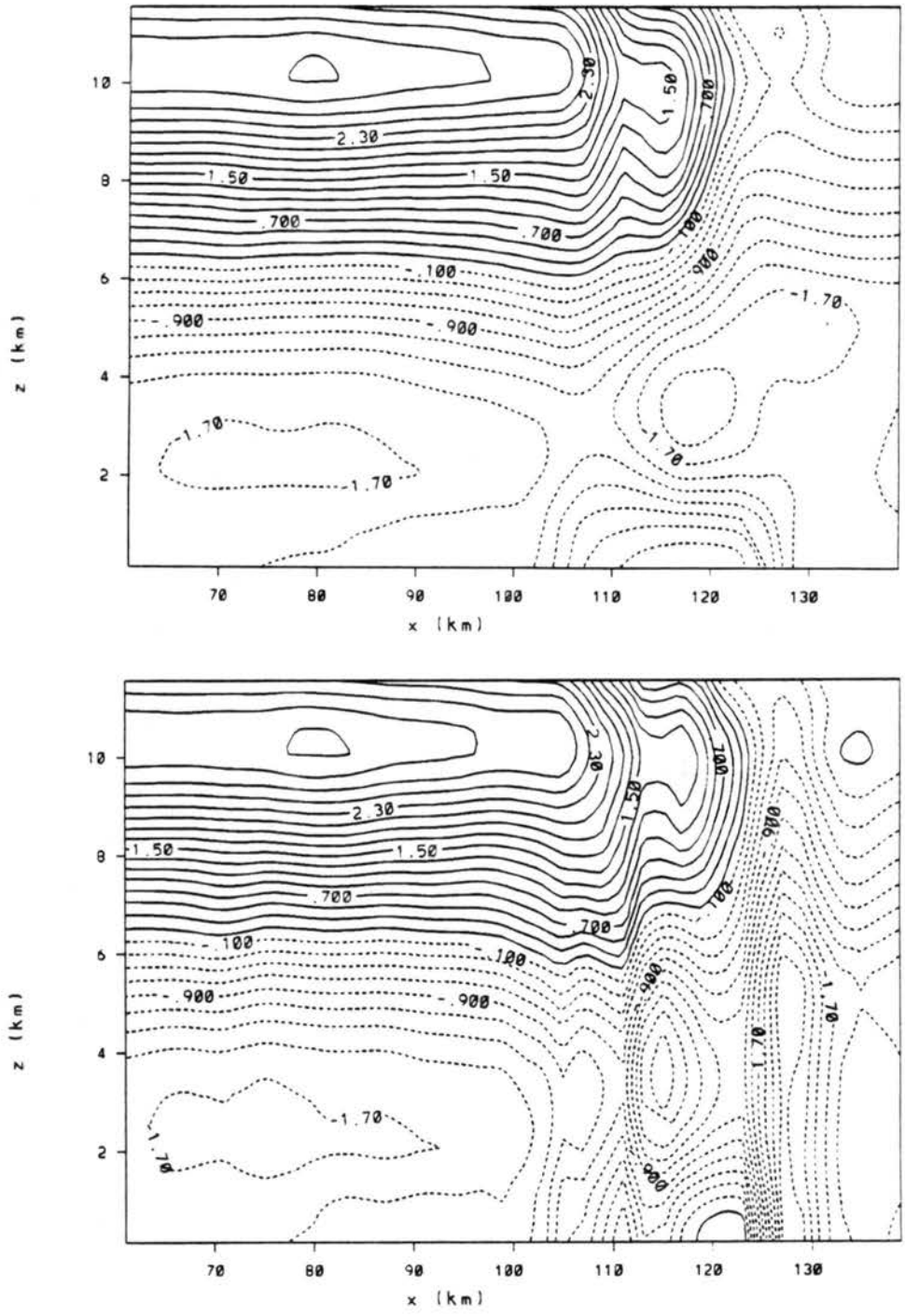


Figure 5.10: Vertical $x$-$z$ cross-sections at 18000 s for experiment LS2 showing (a) total perturbation Exner function $\pi'$, (b) hydrostatic component of $\pi'$, and (c) nonhydrostatic component of $\pi'$. Contour interval is every .2 J kg$^{-1}$ K$^{-1}$. Dashed lines denote negative values of $\pi'$.

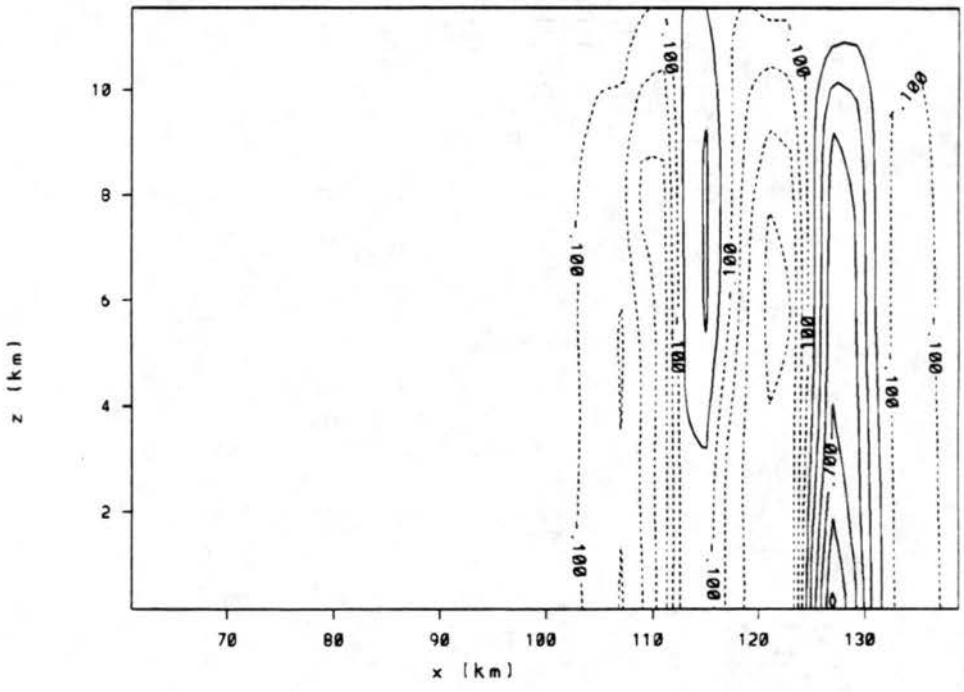


Figure 5.10: Continued.

the surface just upshear of the maximum upward displacement in the lower isentropic surfaces. This produces the broad elevated low pressure region above the stable layer that extends upshear from the leading convective line. Were it not for this dual nature of the low, it appears doubtful that the simulated surface high pressure field would be of sufficient magnitude to produce such outstanding surface wind perturbations in these stable layer simulations.

### 5.3.3 Role of the middle-level, rear-to-front jet

Another possible factor contributing to the strength of the surface flow in the high shear cases was the development of the strong, rear-to-front middle-level jet (compare Figs 5.2-5.4). This common squall line feature (cf. Smull and Houze 1987) has been implicated for its impact on the propagation, longevity, and surface outflow strength of such systems. In this section we discuss the possible role of the thermodynamic and vertical wind shear profiles on the simulated jet strength and discuss the implications of a surfacing, versus, an elevated jet structure on the development of the surface winds and the system longevity.

As mentioned previously, the jet in our simulations appeared to have resulted both from a direct contribution to the flow associated with the gravity wave circulations and the downward displacement of the isentropic surfaces in the upper troposphere beneath the upper level high that produced the channeling of the flow within the middle-troposphere. The amount of upper level blocking and/or middle-level channeling within this two-dimensional framework should depend, in part, on the static stability profiles within the upper troposphere and lower stratosphere. This follows from the condition that a given, hydrostatically-induced high pressure centered near the tropopause generates a greater vertical displacement of the isentropic surfaces as the static stability decreases. This suggests that the presence of a layer aloft with weak static stability, such as an elevated well-mixed layer, may be conducive to the formation of exceptionally intense rear-to-front middle-level jets.

Since each experiment was initialized with the same thermodynamic profile and yet produced different jet strengths, the thermodynamic structure alone cannot account for the differences arising among the simulations. As mentioned previously the simulations suggest

that the displacement of the isentropic surfaces aloft became greater as the upper-level vertical wind shear increased (compare Fig 5.2- 5.4).

A possible explanation for this behavior may rest with either the mass continuity constraints placed on the fluid or on the interaction between the vertical wind shear and the buoyancy fields generated on the upshear flank of the line. We expect the mass continuity constraints to lead to a stronger jet when the ambient environmental flow has a pre-existing, storm-relative, rear-to-front component. Such a flow would enhance the effects of the middle-level channeling as it encountered and then subsided beneath the mesohigh aloft. It is significant, in our view, that derecho type systems all appear to have a such an ambient storm-relative flow (recall that the mean flow at 50 kPa for the derecho systems in the Johns and Hirt (1987) study was 20 m $s^{-1}$). Determining whether such a flow exists may prove to be a useful guide in forecasting derecho occurrence.

A qualitative argument for the later case follows from a consideration of the two-dimensional circulations generated by a buoyancy field in an incompressible fluid *viz.*

$$\frac{d\eta}{dt} = -\frac{\partial B}{\partial x} \tag{5.3}$$

where $\eta = \frac{\partial w}{\partial x} - \frac{\partial u}{\partial z}$ and upshear from the trailing stratiform region $B = \frac{g\theta'}{\theta_o}$. In the region of warming/cooling, the R.H.S of 3 is negative/positive giving the sense of the circulation shown in Fig 5.11.

Note that the horizontal vorticity associated with the buoyancy fields opposes that of the environmental vertical wind shear if, as in the usual mid-latitude case, a westerly jet is centered at the tropopause level (Fig 5.11). Applying the matched vorticity arguments of Rotunno et al. (1988) to the upper level buoyancy and vertical wind shear structure, leads to the result that the upper-level blocking and middle-level channeling on the upshear flank of the squall line may be enhanced in cases of stronger upper-level vertical wind shear. This follows from their argument that a balance between the opposing sources of horizontal vorticity lead to a deeper layer of convergence. In the upper troposphere this would act to enhance the subsidence at the leading edge of the warming and, consequently, the amount of channeling in the middle-troposphere.

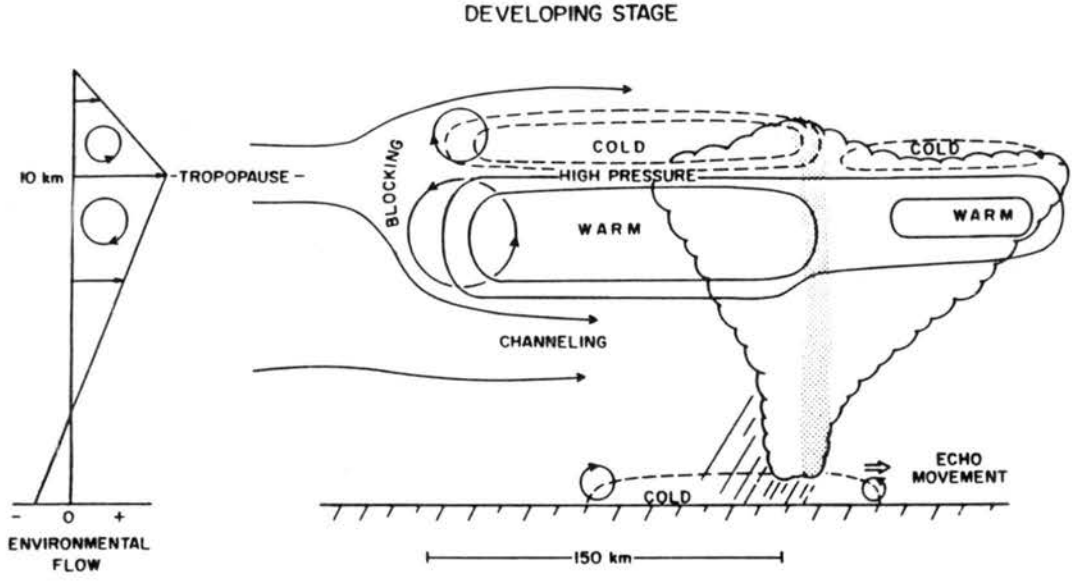


Figure 5.11: Conceptual diagram showing the relationship between the buoyancy fields (solid lines denote warm regions and dashed represent cold regions), pressure, and the streamlines as they approach the upshear flank of the line. The scalloped region denotes the cloud boundary and the stippled region denotes the convective-scale updraft. Circles with arrows denote the sense of horizontal vorticity arising from either the environment shear or from horizontal gradients in the buoyancy field.

Once the jet forms, the question becomes how it may impact the development of the surface flow or system longevity. The simulations of Weisman (1990) have suggested that if the jet remains elevated it enhances the middle-level convergence and, consequently, supports a long-lived squall line. A jet which which surfaces, on the other hand, although increasing the surface outflow, may limit the life expectancy of the system. This is somewhat of a dilemma from the standpoint of derecho systems which are long-lived and yet produce sustained severe surface winds.

It is interesting that the squall line initialized with the pre-existing, surface-based stable layer appears to have the best of both worlds. The analyses of $\theta_e$ shown in (Figs 5.9b) suggest that the jet either remained aloft or, at best, surfaced after considerable mixing with the updraft air. The elevated jet may reflect the difficulty of the simulated system in producing strong penetrating downdrafts. It may also reflect the absence of the surface cold pool which has been suggested by Weisman (1990) to have a significant impact on whether or not the jet surfaces (Fig 5.12). *The severe surface winds, meanwhile, appeared to result from the hydrostatically-induced pressure increases associated with the upward displacement of the lower stable layer and diabatic cooling and loading. This combination may be a unique feature of severe storms which form over surface-based stable layers and offers a possible explanation for both their longevity and their ability to produce sustained severe surface winds.*

## 5.4 Other sensitivity experiments

Of the remaining sensitivity experiments, experiment LNM (the dry boundary layer case) produced the most dramatic increase in the surface winds. The dryer subcloud layer had the affect of increasing the potential cooling realized through a lifting of the lower stable layer as well as the diabatic cooling associated with melting and evaporation. Although not entirely realistic, this simulation suggests that a drier, low-level, stable air mass such as observed in the PRE-STORM derecho, could indicate the potential for severe surface wind development. It also illustrates that the storm development relied entirely on the moisture available at the top of the lower stable layer.

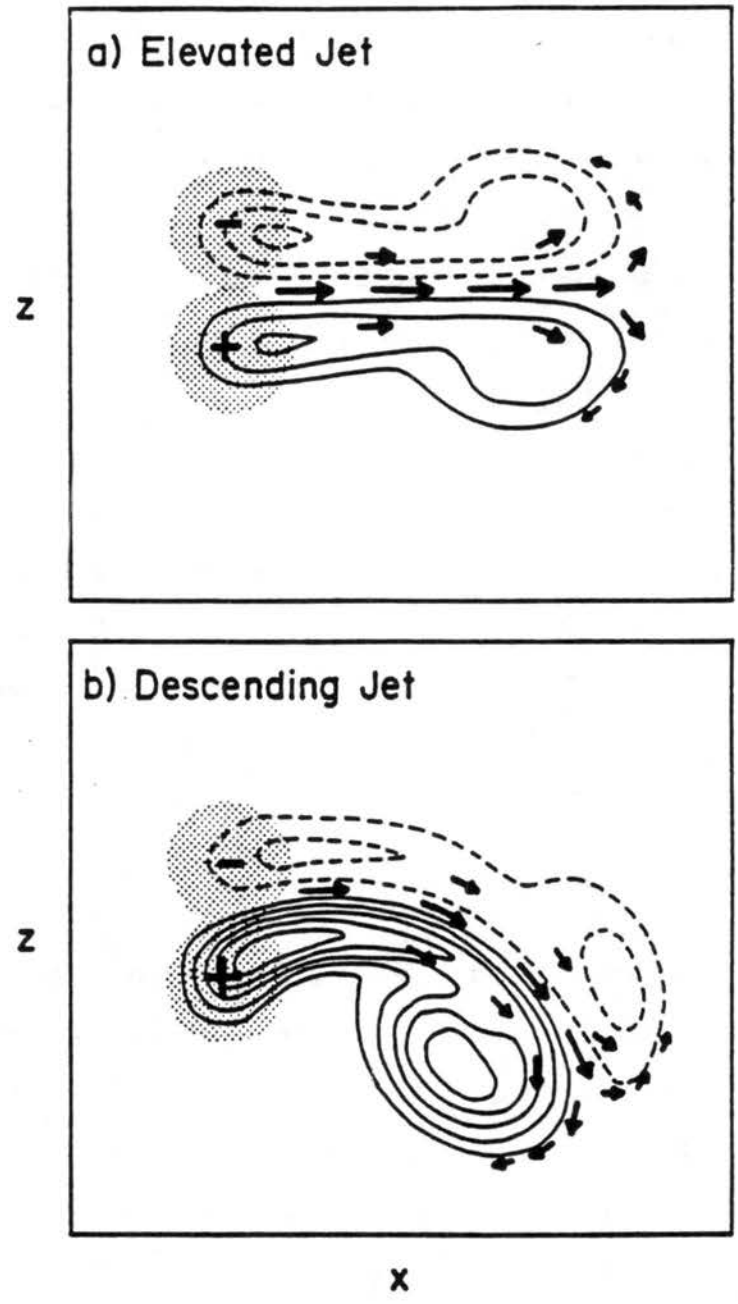


Figure 5.12: Jet structure produced by a two-dimensional vorticity model at t=60 min for (a) a symmetric vortex forcing couplet and (b) a vortex forcing couplet with the positive forcing twice the magnitude of the negative forcing. Vorticity is contoured using a 100 x $10^{-3}$ $s^{-1}$ interval, with zero contour omitted. Regions of vorticity forcing are denoted by the shading, with the sense of the forcing indicated by the sign at the center of the shaded regions. The vectors approximately depict the flow associated with vorticity field. From Weisman (1990).

The experiment initialized with a low-level jet profile (LLJ), also produced a long-lived squall line which produced severe surface wind gusts. The wind gusts were greater in magnitude than experiment LS2 but more periodic in nature. The stronger surface gusts may be related to the low-level curvature in the shear profile which has been shown by Crook (1988) to enhance the wave trapping characteristics of a wave duct. This affect arises through the second term on the right hand side of (Equation 5.1) which becomes strongly negative for positive $U''(z)$ within the sheared layer. A greater amount of wave energy retained in the lower layer, may have led to an increase in the wave amplitude and, consequently, the surface pressure perturbations.

Finally, the experiment initialized without the coriolis force (LNC), produced only marginal increases in the surface wind strength over those obtained in experiment LS2. This occurred despite a stronger rear-to-front flow throughout the entire simulation. This reinforces the impression that the rear-to-front middle-level jet did not have a significant impact on the strength of the simulated surface flow in these two-dimensional stable layer simulations.

## 5.5 Summary of the two-dimensional simulations

Results from a high resolution, non-hydrostatic simulation with explicit microphysics illustrated the role of the vertical wind shear and the three-layer static stability profile on the development of a meso$\beta$-scale squall line. The model results suggest that the three-layered thermodynamic profile supported the development of long-lived, high-amplitude gravity waves which had an important role on the structure, propagation, and longevity of the simulated squall line. One such wave formed in the surface-based stable layer and helped sustain the convective-scale updraft by providing a source of low-level lift throughout the entire simulation. This wave also accounted for the strong surface pressure high which generated the sustained severe surface winds.

Gravity waves generated within the upper troposphere and lower stratosphere by the convective-scale updraft were also found to directly aid the development of the front-to-rear and rear-to-front flows in the simulated squall line. The waves also appeared to aid the rapid upshear development of the mesohigh aloft and the deep buoyancy fields which were

generated in the upper troposphere and lower stratosphere. The wave-induced hydrostatic high pressure located near the tropopause that extended beyond the trailing cirrus cloud shield acted to block the environmental flow impinging on the upshear flank of the squall line. This resulted in a reduced flow aloft and a channeling of the flow below which, together with the middle-level low pressure region, helped establish the rear-to-front, middle-level jet.

The static stability and vertical wind shear profiles had several important impacts on the development of the severe surface winds and system longevity. For one, they provided a wave duct which supported the development of the high amplitude, long-lived, gravity wave in the surface stable layer. The lower stable layer, if it could only be lifted by the advancing storm, also provided a potential source of strong low-level cooling and, consequently, strong hydrostatically-induced surface pressure increases which helped generate the severe wind development. The elevated well-mixed layer provided sufficient instability to support vigorous convection and appeared to enhanced the magnitude of the non-hydrostatically-induced low pressure zone located near the LFC. The role of this low was on lifting the lower stable layer. It was also suggested that weaker static stability and stronger vertical wind shear within the middle-to-upper troposphere affected the vertical displacement of the upper isentropic surfaces and, consequently, the simulated strength of the middle-level rear-to-front jet. This argument was based on the mass continuity constraints placed on the two-dimensional flow and the interactions between the vertical wind shear and the upper level buoyancy fields.

Finally, an elevated well-mixed layer may determine the nature of the vertical wind shear profile within the layer. To see this, simply take a vertical derivative of the thermal wind equation *viz.*

$$\frac{\partial^2 U}{\partial z^2} = \frac{g \partial^2 \theta}{\theta \partial y \partial z} \tag{5.4}$$

This implies a unidirectional shear vector should be present within a layer having nearly neutral static stability (see the hodograph within the neutral layer of Fig 3.4). The fact that a unidirectional shear vector has been implicated as an outstanding environmental signature

# Chapter 6

## 3-D HOMOGENEOUS EXPERIMENTS

The homogeneous experiments thus far have identified many key features of the MCS and its interaction with the ambient environment which may have further impacted the development of the severe surface winds within the observed derecho environment. Yet these experiments were limited by the two-dimensional constraint which may have over emphasized certain aspects of the flow, such as the amount of subsidence-induced channeling on the upshear flank of the line and the amplitude of the low-level gravity wave. These experiments were further restricted by the range of vertical wind shear profiles which could be studied, by not allowing the development of rotation within the updraft, and by confining the development of the cirrus cloud shield and other circulations features in the cross-line sense only. These may be serious restrictions considering the highly 3-D structure apparent in the kinematic fields of the CCOPE bow echo squall line (Fig 4.35) which were suggested in section 4.5 to have had important consequences for the development of the severe surface winds.

The purpose of this chapter therefore is to address some of these issues within a 3-D horizontally homogeneous initial field. As before the idealized thermodynamic structure will be used to initialize the experiments. Particular emphasis is placed on the affects of a unidirectional versus curved environmental hodograph on the evolution of the flow within the MCS and its impact on the surface outflow (section 6.1 and 6.2, respectively). We will also investigate the possible role of rotation within the updraft as a further source of lift for the negatively buoyant parcels within the surface-based stable layer (section 6.2). A summary of the primary findings is presented in section 6.3.

## 6.1 The unidirectional vertical wind shear experiment

One of the primary characteristics of the observed bow echo squall line was the development of a severe northerly wind component in the trailing stratiform region of the storm. This was a long-lived feature which appeared to result from the storm's ability to maintain an asymmetrical structure in the mesoscale surface pressure field.

To determine the possible role of the vertical wind shear profile on this development, two experiments were run in which the amount of directional shear in the environmental hodograph was varied. In the first case an unidirectional S2 shear profile was used to initialize the simulation (see Fig 3.6). An inspection of Fig 6.1 shows that through four hours of simulation this experiment, though generating a severe bow echo squall line, failed to develop the along-line asymmetries in the surface pressure and flow fields noted in the observed case. The surface pressure field consisted instead of a narrow, bow-shaped, high pressure region beneath a similarly shaped convective line. There was a suggestion of a weak low pressure region within the vertex of the bow echo, but the strong north-south pressure gradient of the observed system was absent. As in the two-dimensional experiments, the high was hydrostatically-induced by cooling associated with the upward displacement of the lower stable layer by a gravity wave. The strongest surface winds (25 m $s^{-1}$) were located beneath the convective line in a region of downdraft which extended along the entire back edge of the bow shaped high pressure axis.

In the middle-levels of the storm, the flow wrapped around either end of the line forming an enhanced region of rear-to-front flow directly into vertex of the bow echo (Fig 6.2). The counter rotating vortices are similar to the middle-level flow structure of the observed case (Fig 4.35) and to the unidirectional shear experiments of Weisman (1990). The rotors did not appear, as suggested in his simulations, to result from the convective-scale vorticity couplets associated with the downdraft circulation between the splitting updraft. Rather they occurred on a much larger, system-wide scale as the bow echo blocked the environmental flow aloft. This is similar to the arguments presented by Verlinde and Cotton (1990).

Vertical cross-sections taken through the vertex region of the bow echo show many similarities with the two-dimensional cross-sections shown in Chapter 5 (Fig 6.3). A low-level rotor circulation, consisting of the convective-scale updraft/downdraft couplet and

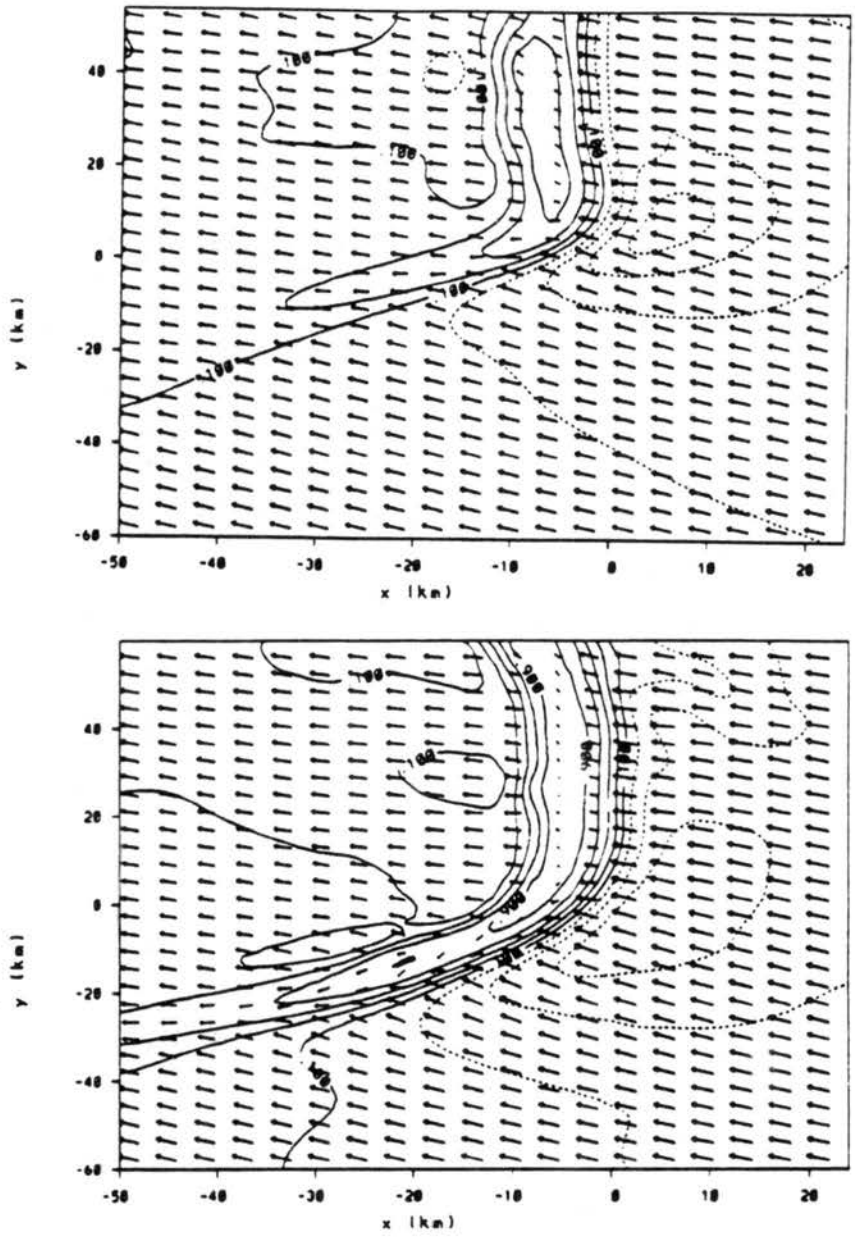


Figure 6.1: Horizontal $x$-$y$ cross-sections of the near surface ($z$= 146 m) storm-relative flow vectors and perturbation Exner function ($\pi'$, contoured every .2 J kg$^{-1}$ K$^{-1}$) for the unidirectional experiment at (a) 7200 s (top panel), (b) 10800 s (center panel), and (c) 14400 s (bottom panel).

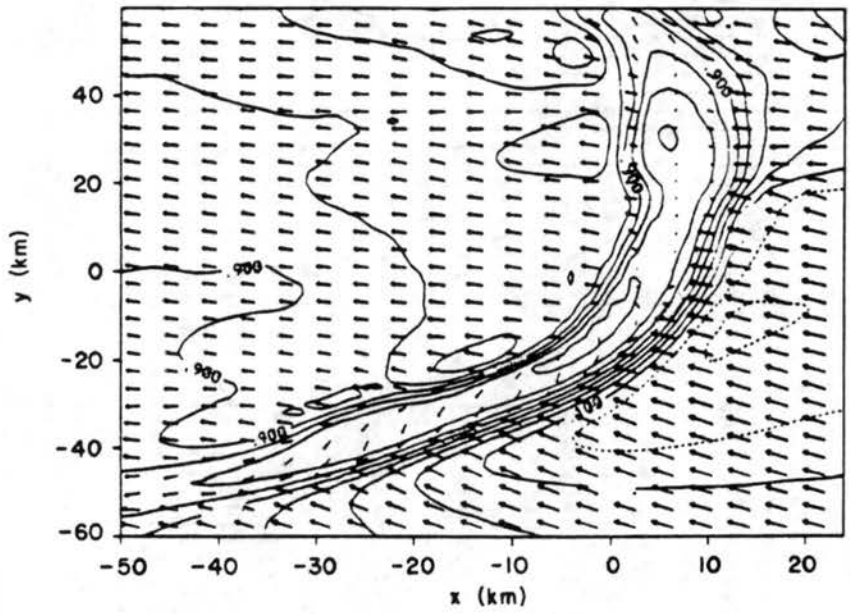


Figure 6.1: Continued.

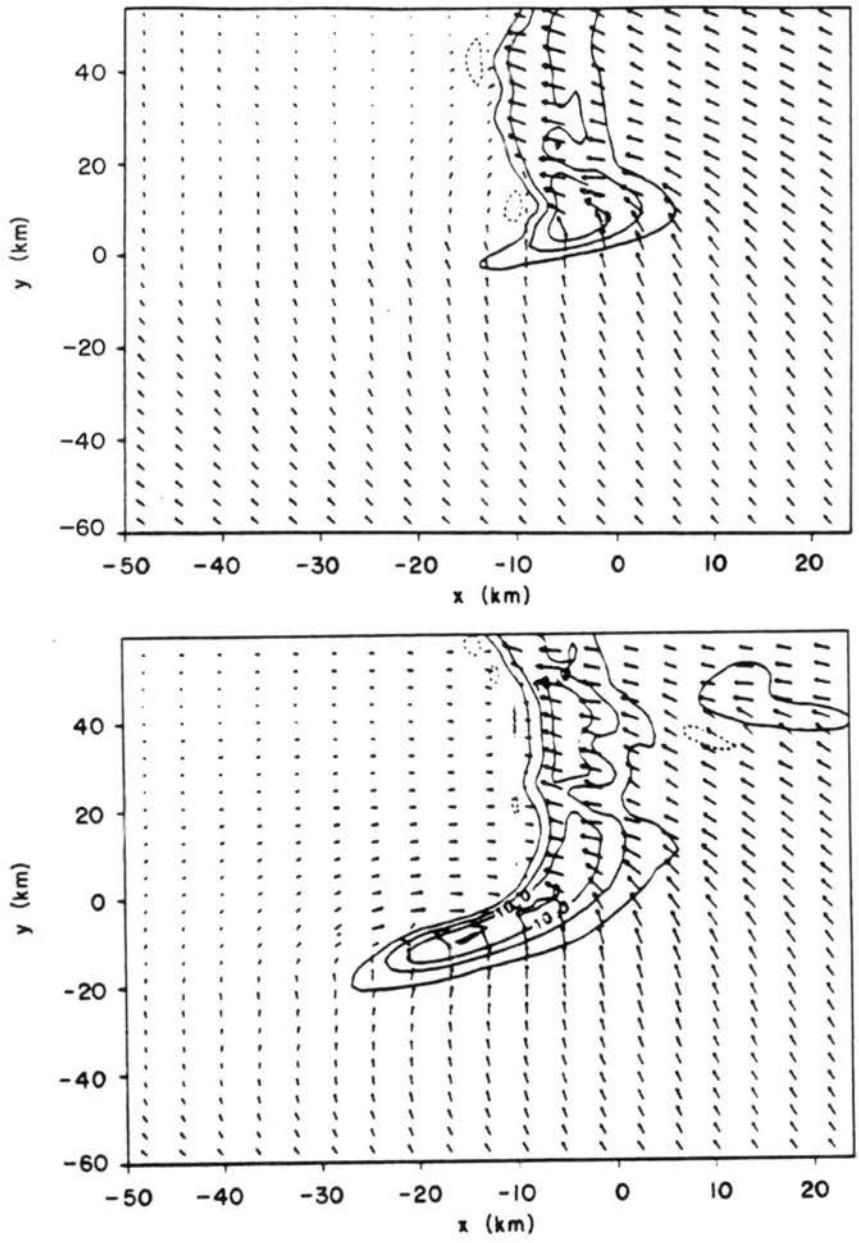


Figure 6.2: Horizontal $x$-$y$ cross-sections of the middle-level (z= 3729 m) storm-relative flow vectors and vertical motion (w, contoured every 4 m $s^{-1}$, solid lines denote positive values) for the unidirectional experiment at (a) 7200 s (top panel), (b) 10800 s (center panel), and (c) 14400 s (bottom panel).

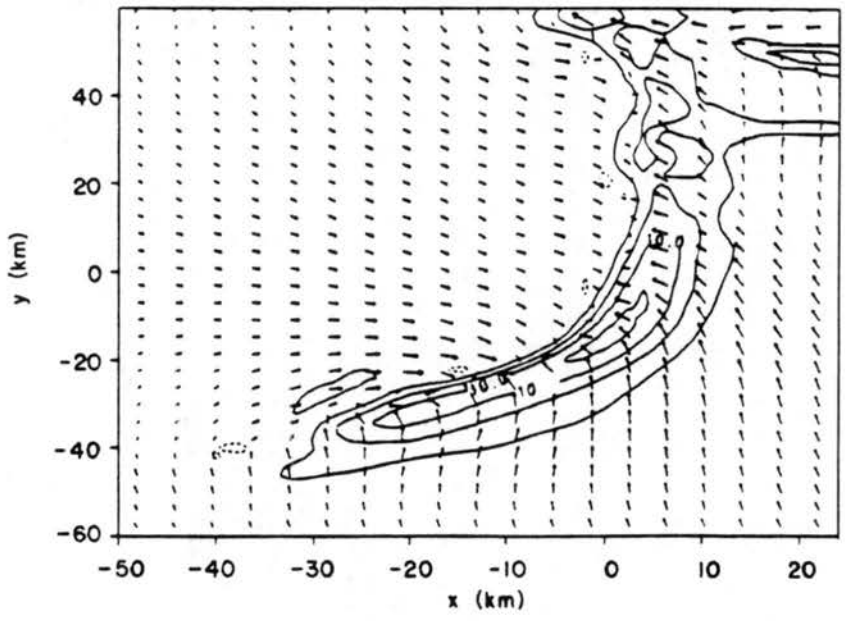


Figure 6.2: Continued.

peak surface wind speeds, was associated with the gravity wave within the surface-based stable layer. As before, the simulation failed to generate a significant cold pool outside the region of cooling within the wave.

The circulation aloft consisted of the familiar front-to-rear and rear-to-front middle-level jets. The strong rear-to-front jet developed in a region of channeling behind the line as the isentropic surfaces were displaced downward beneath the upper level high pressure region. As might be expected, the vertical displacement of the isentropic surfaces was not as great as that observed in the two-dimensional experiment. The stronger jet was primarily a result of the enhanced convergence of the flow wrapping around primary updraft. This is consistent with the findings of Weisman (1990) who showed that the circulation about the middle-level vortices accounted for approximately 50% of the simulated jet strength.

### 6.2 An experiment with a clockwise turning hodograph

Adding curvature to the low-level environmental hodograph used to initialize the model (Fig 3.8) significantly altered the structure of the simulated flow. The kinematic fields shown at 10800 s in Fig 6.4 reveal a highly asymmetric structure having many similarities to those observed in the CCOPE bow echo (compare Fig 6.4 to Fig 4.34 and Fig 4.35). Note the strong north/south pressure gradient between the developing mesohigh over the northern portion of the domain and the mesolow located near the vertex region of the bow echo. As in the observations, a strong northerly flow was generated on the eastern flank of this mesolow. The $\theta_e$ analyses reveals that the air within this outflow region descended unmixed from the middle-troposphere and rapidly advected westward relative to the system. This formed an elongated band of low $\theta_e$ values similar to the pattern shown in Fig 4.34e.

The flow in the middle-levels of the storm was responding to a large low pressure region associated with the southern updraft within the line (Fig 6.5). This was one of two primary updrafts within the simulation which resulted from a split in the initial updraft. As might be expected from the shape of the hodograph (cf. Klemp and Wilhelmson 1978a,b), the southern updraft became the dominant member of the two and, as observed, had a movement to the right of the mean flow aloft. The dominant right moving cell had many supercell characteristics including a forward overhang, a precipitation-free vault, and a

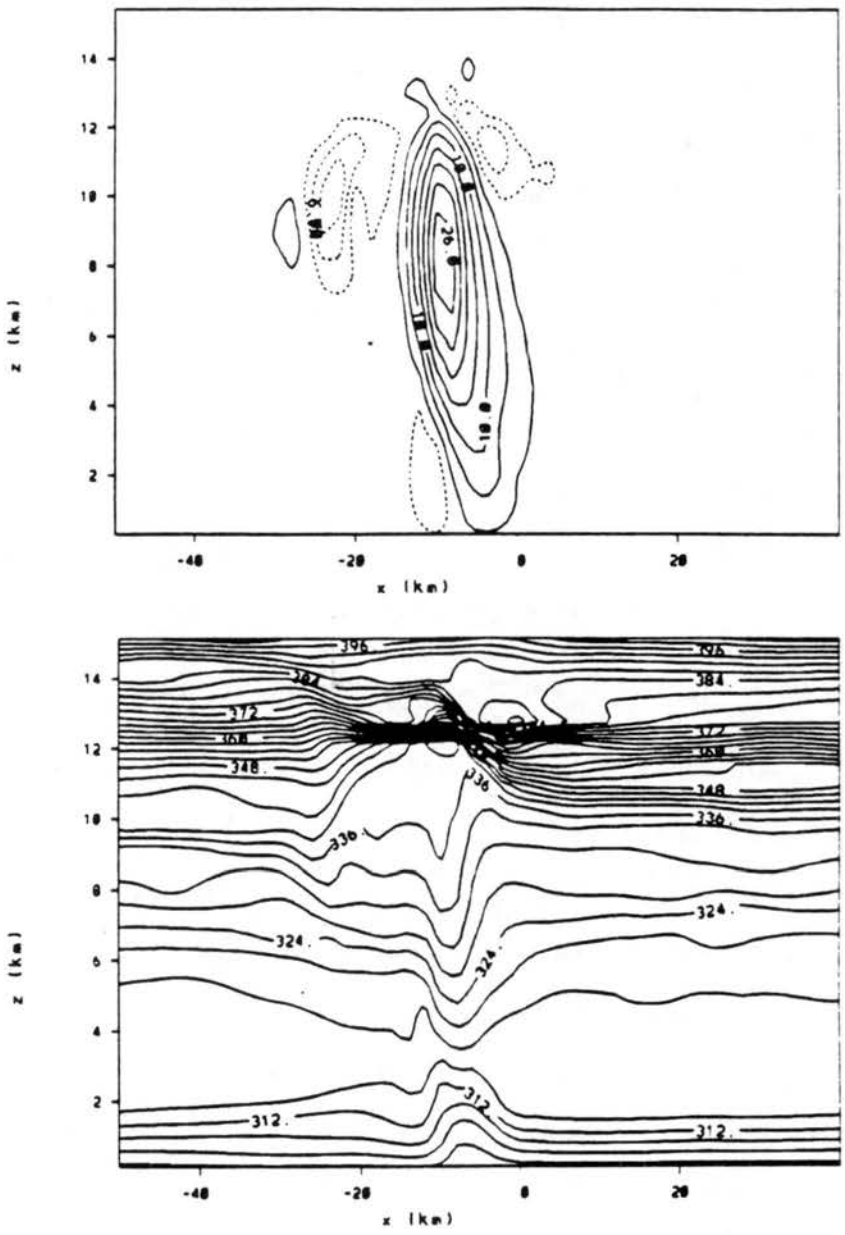


Figure 6.3: Vertical $x$-$z$ cross-sections of the unidirectional experiment at 10800 s along y = 0. (a) vertical motion contoured every 4 m $s^{-1}$ (solid lines denote positive values), (b) potential temperature ($\theta$) contoured every 3 K, and (c) u′ contoured every 6 m $s^{-1}$ (solid lines denote positive values).

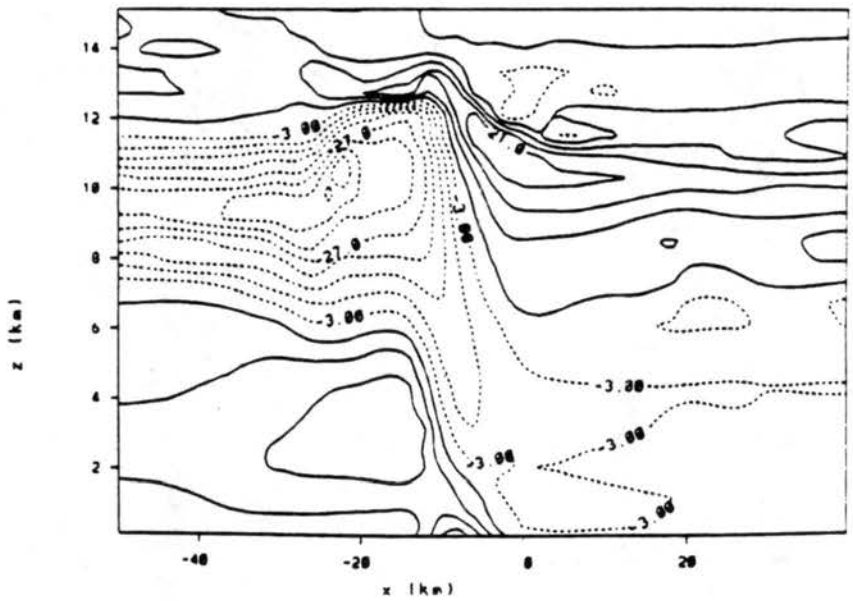


Figure 6.3: Continued.

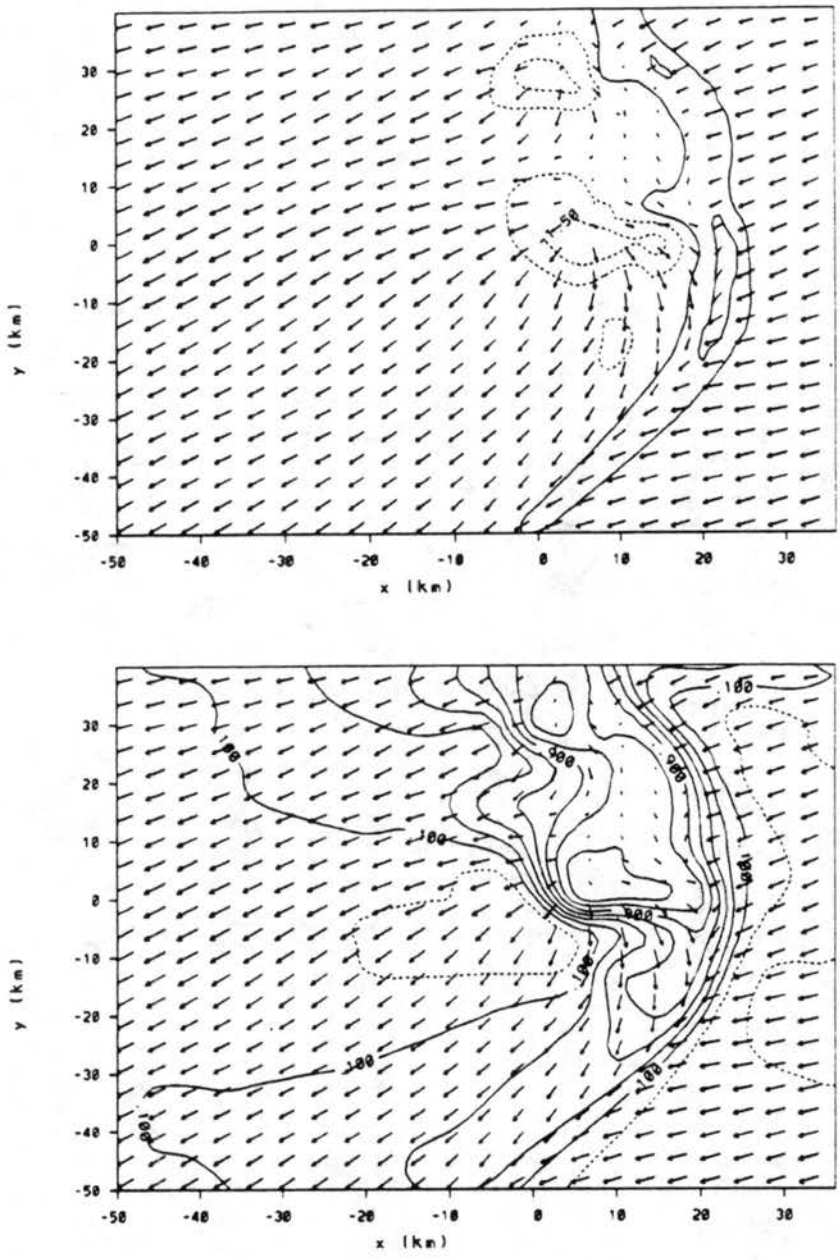


Figure 6.4: Horizontal $x$-$y$ cross-sections of the near surface (z= 146 m) fields for the curved hodograph experiment at 10800 s. The fields shown are (a) storm relative flow vectors and vertical motion (w) contoured every 1 m $s^{-1}$, (b) storm relative flow vectors and perturbation Exner function ($\pi'$, contoured every .2 J $kg^{-1}$ $K^{-1}$), (c) equivalent potential temperature ($\theta_e$), (d) storm relative flow vectors and u' (contoured every 4 m $s^{-1}$), and (e) storm relative flow vectors and v' (contoured every 4 m $s^{-1}$). Solid lines denote positive values of contoured variable in each panel.

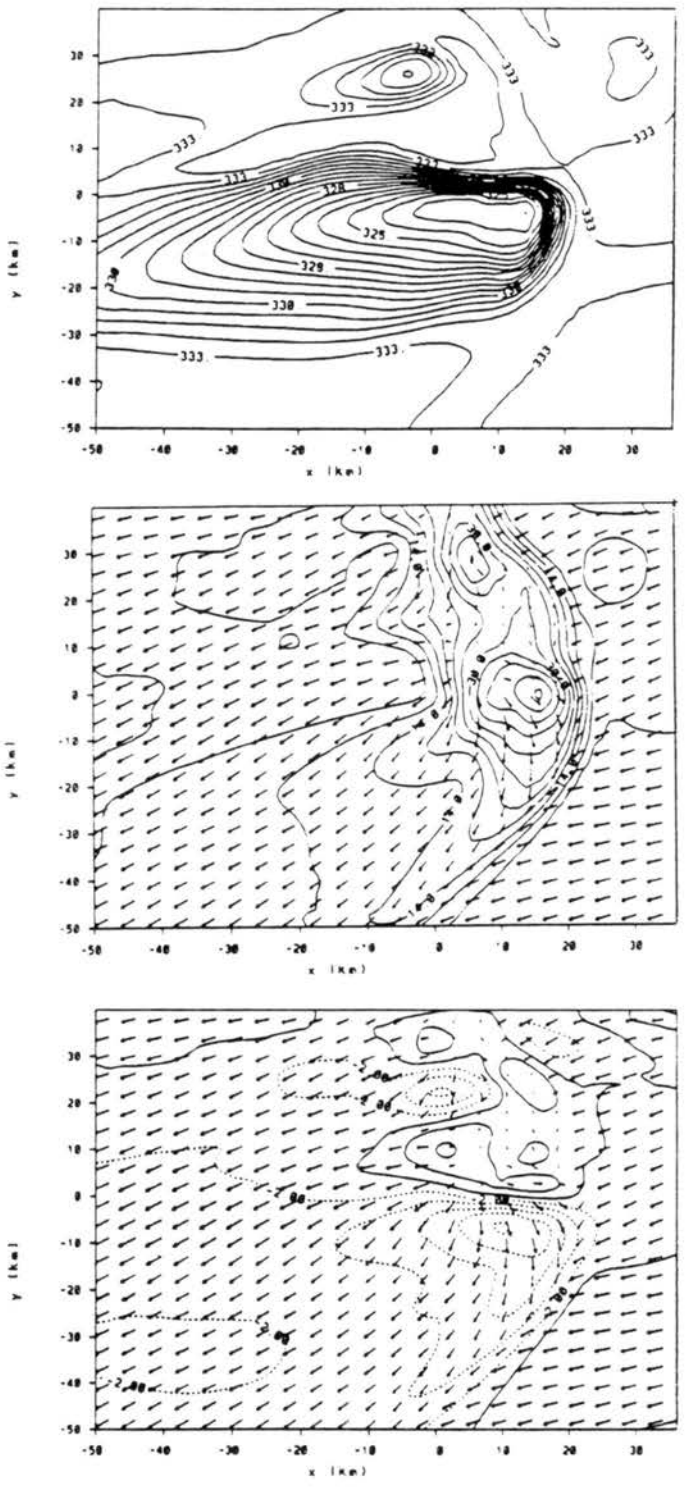

Figure 6.4: Continued.

strong convective-scale downdraft colocated with the primary precipitation core on the northern flank of the updraft. This downdraft penetrated to the surface and was responsible for the strong pressure gradient and surface outflow near the vertex of the bow echo.

As in the previous experiment, the middle-level flow wrapped around the ends of the convective line forming an enhanced rear-to-front flow into the vertex of the bow echo. A vertical $x$-$z$ cross-section taken through the vertex region of the bow echo (Fig 6.6) shows that the jet terminated within the northern flank downdraft where it descended essentially unmixed to the surface. Note that the strength of the simulated $u$-component of the surface flow exceeds that obtained in the 2-D experiments by a factor of nearly 1.5. Note too that the surface wind maximum, unlike the 2-D experiments, occurred slightly upshear of the maximum upward displacement of the lower isentropic surfaces and within a region of low-valued $\theta_e$ air. This suggests that a downward transport of middle-level westerly momentum played a key role in the simulated increase of the surface $u$-component. This illustrates the importance of loading and diabatic cooling, which were enhanced in the three-dimensional experiment beneath the large precipitation core on the northern flank of the supercell, on aiding the transport of middle-level momentum to the surface when a pre-existing, surface-based stable layer is present.

Another factor which may have aided the simulated increase of the surface wind maximum was the "up-down" downdraft component associated with the initial lifting and then descent of the parcels along the leading convective line. That these trajectories were present within the downdraft is suggested by the vertical $y$-$z$ cross-sections which show that the downdraft was being fed by much higher $\theta_e$ from ahead of the system (Fig 6.7). Other cross-sections (not shown) reveal that the upward displacement of the lowest stable layer was greatest beneath the primary updrafts within the line. This suggests that middle-level low pressure zone, as in the previous experiments, played a key role in lifting the negatively buoyant parcels with the surface-based stable layer. Since the updrafts in this case were accompanied by middle-level rotation (Fig 6.5) we expect there to be an dynamically-induced low pressure region (Weisman and Klemp 1984) which would further enhance the lifting capabilities of the storm.

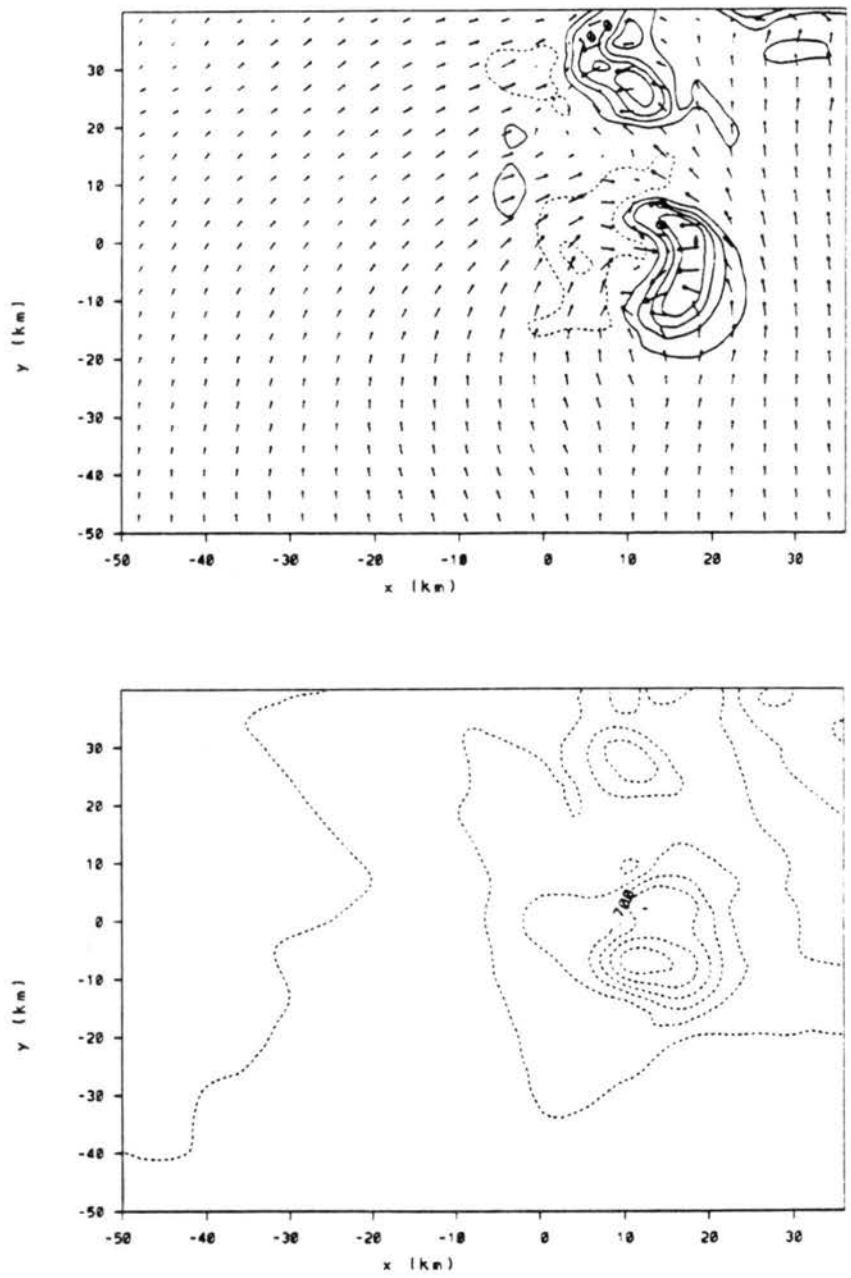


Figure 6.5: Horizontal $x$-$y$ cross-sections of the middle-level (z= 3729 m) fields for the curved hodograph experiment at 10800 s. The fields shown are (a) storm-relative flow vectors and vertical motion (w) contoured every 4 m $s^{-1}$ (solid lines denote updraft), (b) perturbation Exner function ($\pi'$, contoured every .2 J $kg^{-1}$ $K^{-1}$, dashed lines denote low pressure), and (c) total ice mixing ratio contoured every 2 g $kg^{-1}$.

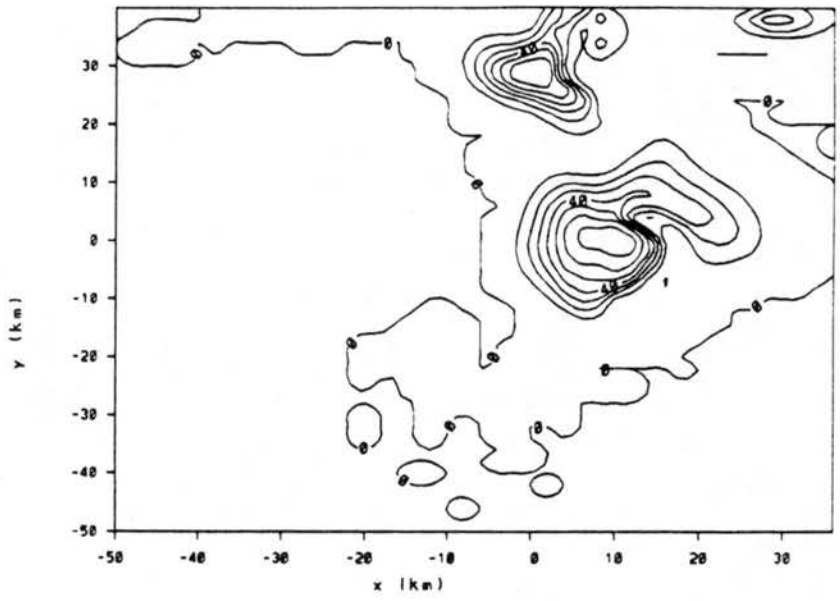


Figure 6.5: Continued.

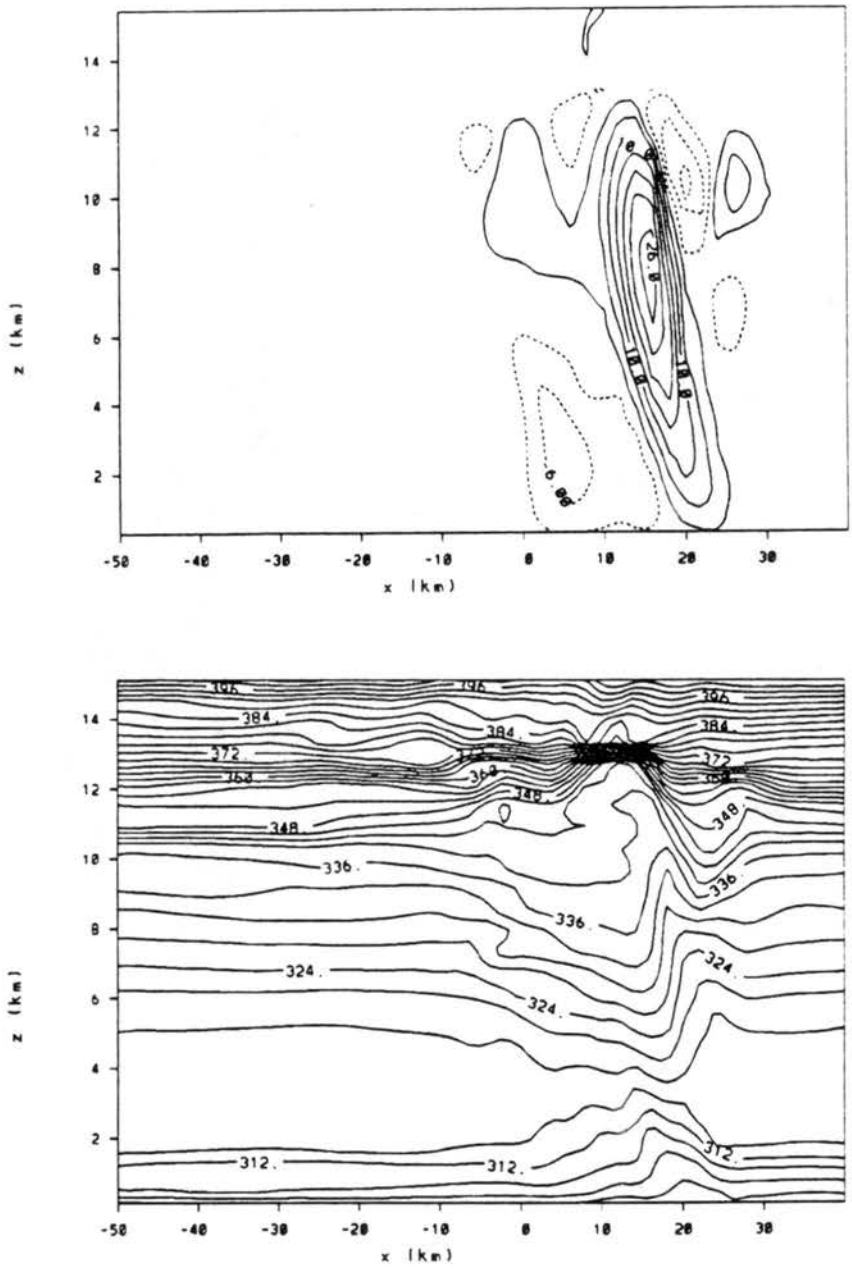


Figure 6.6: Vertical $x$-$z$ cross-sections for the curved hodograph experiment at 10800 s along y = -2. The fields displayed are (a) vertical motion contoured every 4 m $s^{-1}$, (b) potential temperature ($\theta$) contoured every 3 K, (c) u′ contoured every 6 m $s^{-1}$, (d) perturbation Exner function ($\pi'$, contoured every .2 J $kg^{-1}$ $K^{-1}$), (e) equivalent potential temperature $\theta_e$ contoured every 3 K, and, $\theta'$ contoured every 4 K. Solid/dashed contours denote positive/negative values, respectively.

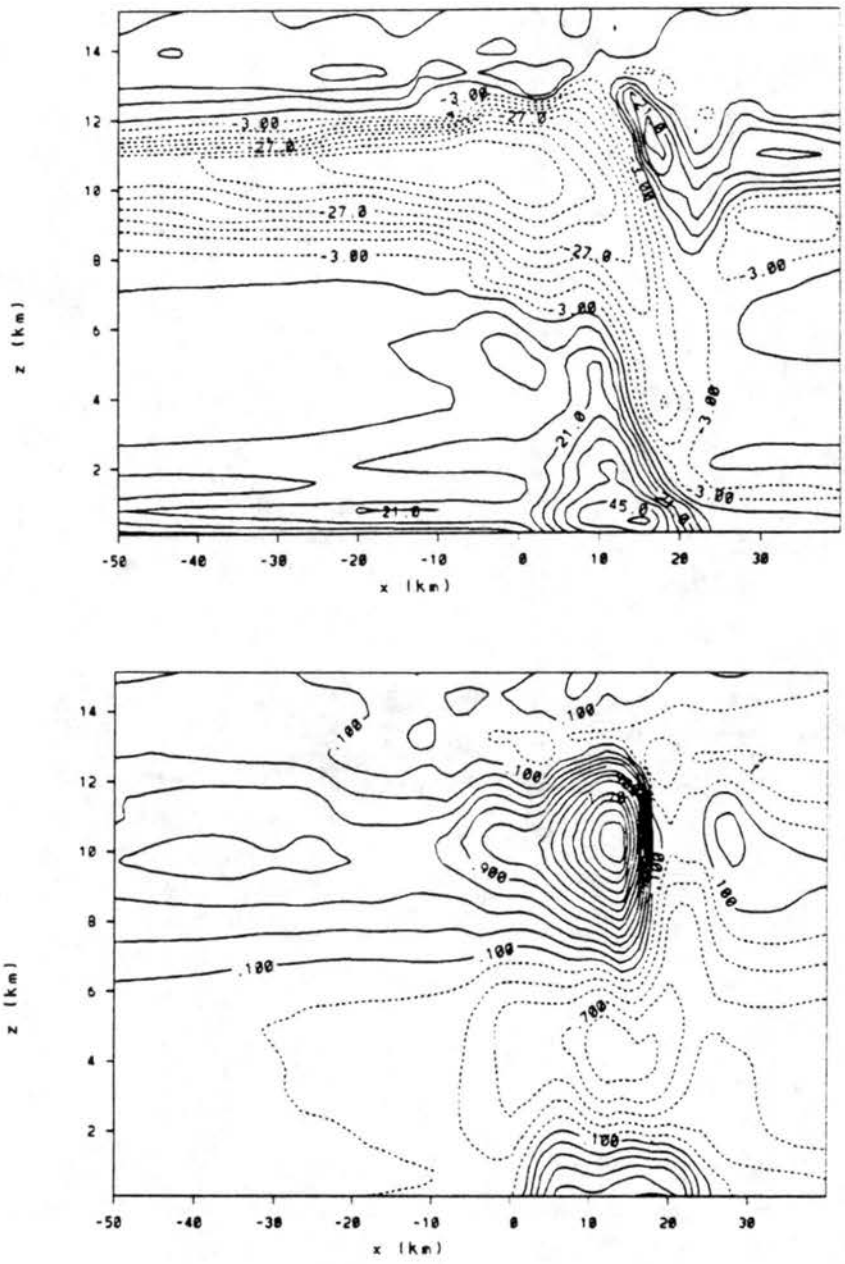


Figure 6.6: Continued.

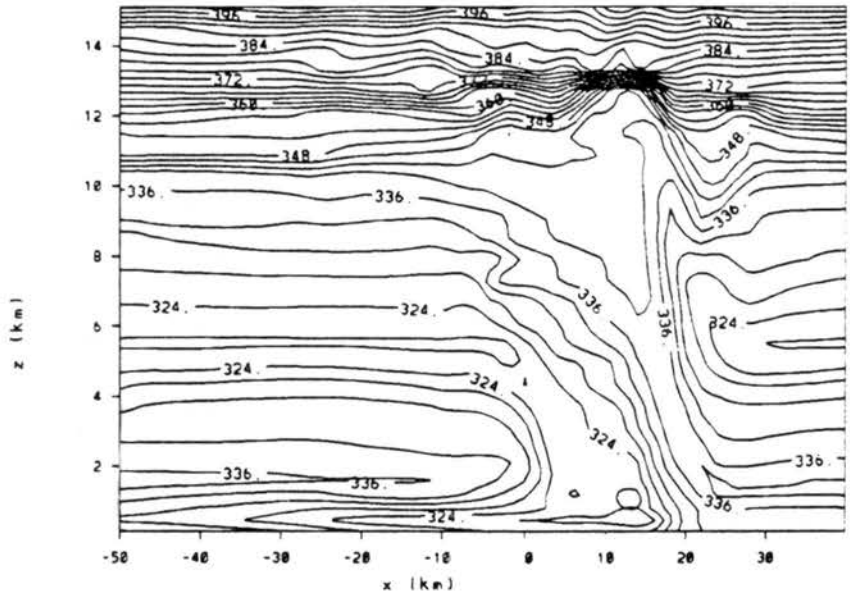


Figure 6.6: Continued.

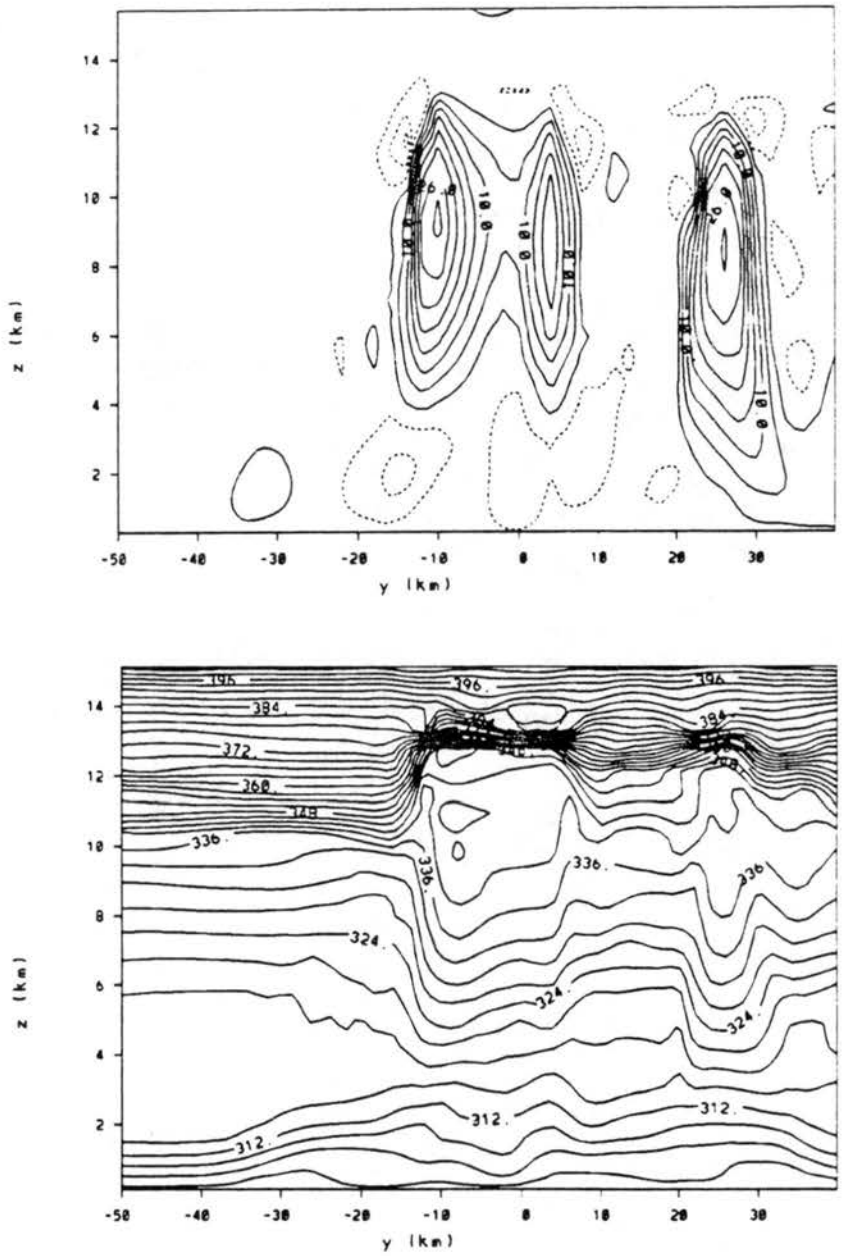


Figure 6.7: Vertical $y$-$z$ cross-sections for the curved hodograph experiment at 10800 s along x = 10. The fields displayed are (a) vertical motion contoured every 4 m $s^{-1}$, (b) potential temperature ($\theta$) contoured every 3 K, (c) perturbation Exner function ($\pi'$, contoured every .2 J $kg^{-1}$ $K^{-1}$) (d) u′ contoured every 6 m $s^{-1}$, (e) u′ contoured every 6 m $s^{-1}$, (f) equivalent potential temperature $\theta_e$ contoured every 3 K Solid/dashed contours denote positive/negative values, respectively.

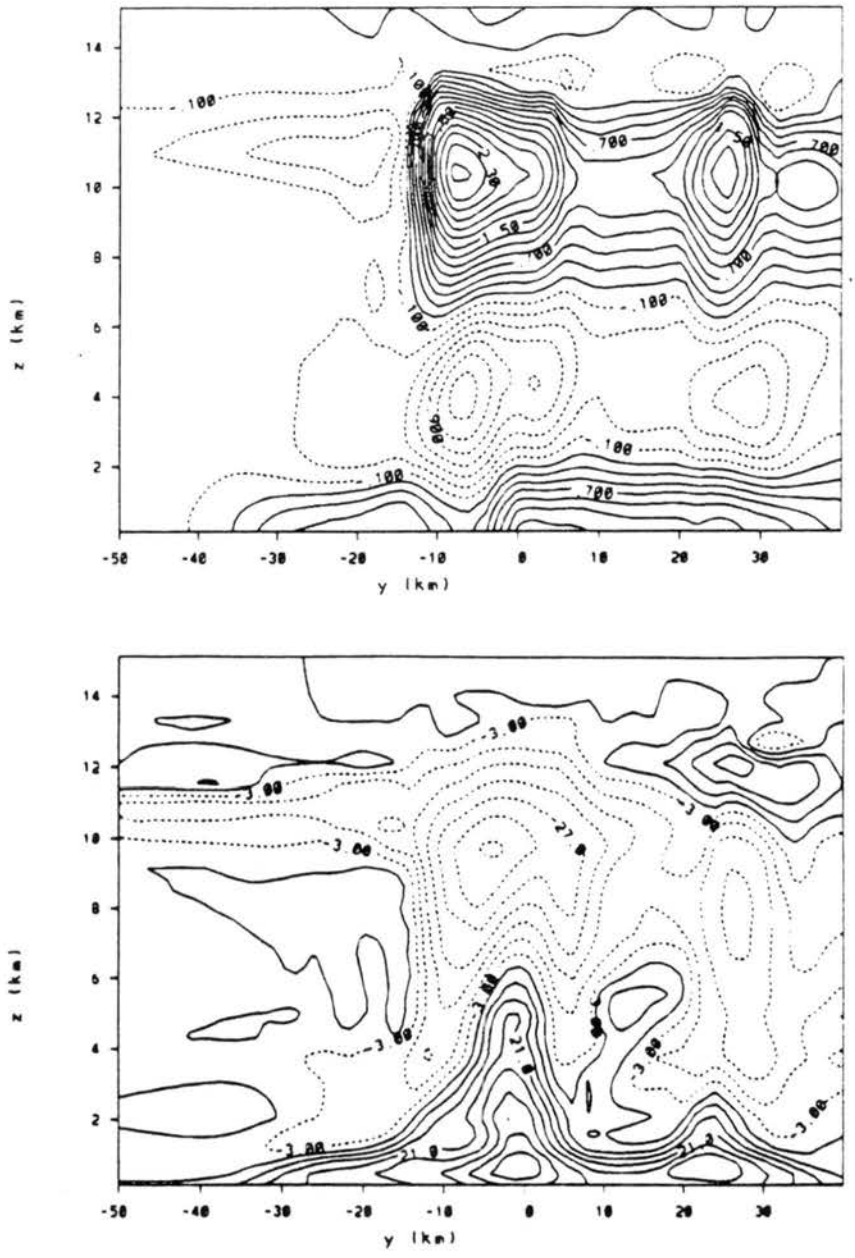


Figure 6.7: Continued.

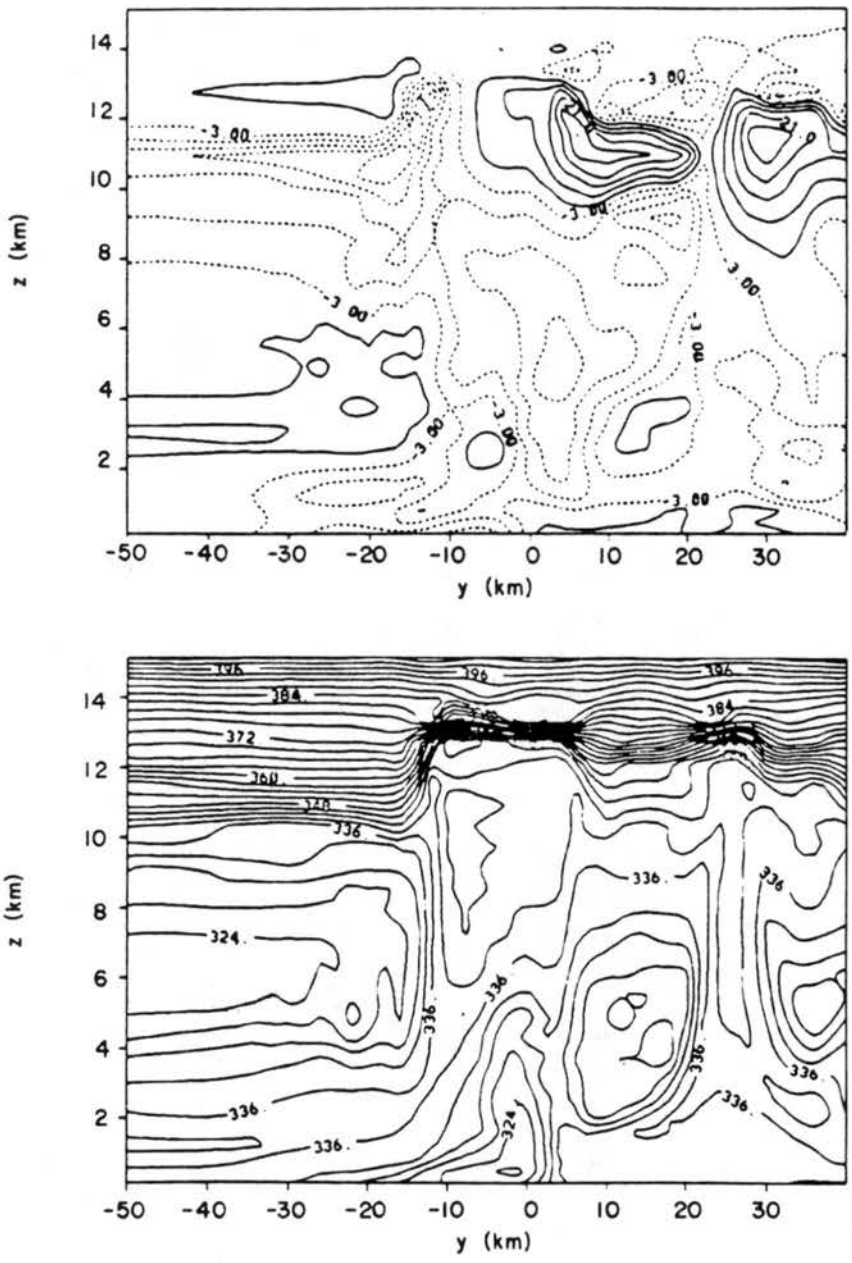


Figure 6.7: Continued.

## 6.3 Summary

A comparison of three dimensional simulations initialized in a homogeneous environment having different vertical wind shear profiles revealed that the asymmetric structure of the observed bow echo squall line may have resulted from the curvature present in the lower portion of the environmental hodograph. The simulated structure had many similarities with the observed storm including the development of a bow echo squall line with strong northerly flow behind the convective line within the vertex region of the bow echo, middle-level wrap around flow, an enhanced meso$\beta$-scale pressure field which fanned outward to the north of wake low, and a strong downdraft on the northern flank of the primary cell within the line.

Both the observations and the simulations revealed that the northerly flow and surface pressure gradient was strongest near a low-level downdraft which formed on the northern flank of the dominant cell within the line. This may explain the often observed relationship (see the discussion by Johns and Hirt (1987) and Fig 3.1), that the strongest surface winds occur slightly north of the vertex region of the bow echo. It also illustrates the process where by outflow from a convective-scale downdraft enhanced the northerly flow component generated by the meso$\beta$-scale pressure field, to generate the severe surface flow located on the southern flank of the downdraft. As suggested by Knupp and Jorgensen (1985), this superposition of the two sources of low-level momentum may be an important mechanism in long-lived, severe surface wind events.

# Chapter 7

# SUMMARY AND CONCLUSIONS

This dissertation has investigated long-lived, MCS-induced, severe surface wind events of extratropical origin otherwise known as derechos (Hinrichs 1888). The basic goals of the research were to determine what environmental or storm-induced features may have led to the following derecho characteristics discussed by Johns and Hirt (1987): (i) a sustained swath of severe surface winds of at least 400 km in length, (ii) an average lifetime of nine hours, (iii) an average speed of 24 m $s^{-1}$, and (iv) an average lifted index of -9 (Johns and Hirt 1987). To keep the discussion focused we investigated a particular type of derecho, namely those which formed in environments having a deep, surface-based stable layer. This choice was based on the personal interest of the author and on the climatological studies of Johns and Hirt which showed that a significant percentage of derechos ( approximately 90% of their sample ) initiate on the the cold side of a synoptic-scale frontal boundaries.

## 7.1 Regional-scale environmental structure and forcing mechanisms

The basic strategy used in the dissertation was to first establish the thermodynamic and vertical wind shear profiles which accompanied the two observed derecho cases (the 12-13 May 1985 PRE-STORM and 2-3 August 1981 CCOPE derechos) and to identify features of their regional-scale environments which may have aided the system longevity and/or production of the sustained surface winds. These goals were accomplished by supplementing detailed observational analyses of the two cases with regional-scale simulations initialized from standard NMC analyses.

Observations of the regional-scale conditions of the 12-13 May 1985 and 2-3 August 1981 derechos revealed similar environments of strong vertical wind shear throughout the troposphere and high values of CAPE. The thermodynamic structure within the troposphere

for each case consisted of three distinct layers: (i) a surface-based stable layer of less than 2 km in depth, (ii) a deep, elevated well-mixed layer, and (iii) an upper tropospheric layer of intermediate stability. The thermodynamic structure was such that parcels lifted from near the surface had significant negative buoyancy to overcome and, provided they could reach the LFC, resulted in relatively small positive area on the Skew-T log-P diagram. The high values of CAPE fueling the storms resulted instead from parcels lifted from near the top of the surface-based stable layer where there was typically an ample supply of moisture.

The vertical wind shear profiles of each case, though differing in detail, generally consisted of a low-level easterly flow and strong southwesterly to westerly flow aloft. The flow aloft was typically increasing during the period as each derecho formed in the exit region of an advancing upper level jet system. We believe it is significant that the ambient flow aloft had a storm-relative rear-to-front flow which may have enhanced the development of the rear-to-front middle-level jet. Each case also had a pronounced southerly low-level jet which was advecting heat, momentum, and moisture into the region of resolved upward vertical motion of the simulated MCS at a level just above the surface-based stable layer. The warm air advection near the top of the stable layer was one factor that acted to enhance the pre-existing, low-level static stability and to destabilize the soundings aloft through a steepening of the environmental lapse rates above the stable layer.

The primary difference between the two cases was in the strength of the low-level jet and its impact on the near surface flow fields. The PRE-STORM southerly low-level jet was nearly twice as strong as the CCOPE case and was associated with an inverted surface low pressure trough that formed in the stable airmass north of the warm frontal zone. This correspondence suggests that the surface trough was hydrostatically induced by the deeper layer of warming aloft within the jet core. This trough became the focal point of a strong (25 m $s^{-1}$), low-level, easterly wind maximum which tracked through northwest Kansas on coarse similar to the observed derecho. Thus, the timing, location, longevity, and track of the PRE-STORM derecho may have been strongly affected by the regional-scale development of a this low-level momentum source. This was in stark contrast to the regional-scale environment of the CCOPE derecho which did not have this type of

low-level momentum source. The severe winds in this case appear to have been determined by processes within the meso$\beta$-scale MCS components of the MCC.

The presence of the southerly low-level jet in both cases suggests its possible importance as a forcing mechanism for the derecho. Other forcing mechanisms which were important in the simulated development of the derechos included strong synoptic-scale uplift generated in a region of positive vorticity advection ahead of an advancing trough, ageostrophic uplift within the left exit region of an advancing upper level jet, and the upward vertical motion associated with the advancing mountain plains solenoid (see the discussion of Tremback 1990). Since these features were easily resolved within the model, we are confident that the ability to forecast the development of relevant forcing mechanisms with a nested-grid regional-scale simulation, such as the low-level jet position and strength, may provide useful guidance in forecasting the location, track, and likely occurrence of derecho-type events.

### 7.2 Results from the two-dimensional homogeneous experiments

Having established the environmental thermodynamic and vertical wind shear profiles of the two derecho case studies, we then set out to determine the affects of these profiles on the internal flow characteristics of a simulated MCS initialized in either a two or three-dimensional, horizontally homogeneous environment with relatively fine horizontal resolution and explicit microphysics. The primary goal of these experiments was to identify features of the MCS circulation which may have further impacted the development, longevity, and sustenance of the severe surface outflow. It was also of interest to determine how the three-layered thermodynamic profile of the observed derecho environments may have influenced the development of MCS circulations, such as the rear-to-front, middle-level jet.

One of the primary findings of the two-dimensional experiments was that the environment supported the development of high amplitude, long-lived meso$\beta$-scale gravity waves. Two types of gravity waves had a particularly significant impact on the system. The first type was the high-amplitude gravity wave which formed in the surface-based stable layer. This was a fast moving, long-lived feature that provided a source of low-level lift which helped sustain the convective-scale updraft throughout the entire simulation. Since this

wave lifted the isentropic surfaces within the lower stable layer, it resulted in strong low-level cooling. This cooling, together with the diabatic cooling and loading, enhanced the strength of the surface high and, consequently, the magnitude of the simulated surface winds.

The experiments suggested that the amplitude of the low-level wave may have been enhanced by an increase in the low-level vertical shear and the rapid decrease in static stability just above the surface-based stable layer. The rapid decrease in static stability above the lower stable layer appeared to have two dominant affects on the wave amplitude. First, it provided a wave duct which acted to trap the wave energy in the lower layers. Secondly, the rapid decrease in static stability may have enhanced the strength of the low pressure zone located near the leading edge of the system and near the level of free convection (LFC). It was noted that the peak upward displacement of the lower isentropic surfaces was located beneath this low pressure region. It was suggested that the low had a significant non-hydrostatic component induced by the rapid acceleration of the parcels above the LFC. The significance of this is that storms developing over surface-based stable layers may have a better opportunity to lift the negatively buoyant parcels, through a favorable vertical pressure gradient force, if a well-mixed layer is present immediately above the lower stable layer. The presence or absence of this layer above a surface-based stable layer may thus determine whether or not the storms develop derecho-like severe surface winds.

The second wave type affecting the development of the simulated flow fields formed in the upper tropospheric and lower stratospheric stable layers. The circulation about these waves were noted to directly contribute to the front-to-rear and rear-to-front circulations within the simulated MCS. Particular emphasis was placed on the role of the upshear propagating waves. These waves aided the rapid upshear development of the buoyancy and pressure fields within the upper troposphere and lower stratosphere which extended well beyond the trailing stratiform region. The primary result was a strong hydrostatically induced high located near the tropopause which resulted in a blocking of the upper level flow and a channeling of the flow within the middle troposphere which aided the development of the rear-to-front, middle-level jet.

It was argued that the amount of blocking/middle-level channeling was a function of the upper tropospheric and lower stratospheric static stability and vertical wind shear profiles. Decreased static stability aloft (*i.e.* an elevated well-mixed layer) and stronger vertical wind shear were suggested to have lead to greater vertical displacements of the isentropic surfaces. These arguments were based on the greater amount of subsidence required to maintain the observed hydrostatic balance as the static stability decreased, mass continuity constraints, and the interaction of the vertical wind shear with the resulting buoyancy fields. We noted that the strong channeling resulting from the weaker stability aloft was further enhanced by either a pre-existing, surface-based stable layer or a low level cold pool. This suggests that the three-layer thermodynamic structure of observed derecho environments may be particularly conducive to the formation of exceptionally strong middle-level rear-to-front jets.

Since the jet appeared to remain aloft in the stable layer simulations, the primary impact of the blocking and channeling on the simulated system were to enhance the longevity of the line by: (i) increasing the middle-level convergence along the leading convective-line (cf. Weisman 1990) and, (ii) by protecting the updraft from the debilitating affects of the upper level shear. This is an interesting aspect of the observed thermodynamic structure which may help explain the longevity of derecho type systems.

### 7.3 Results from the three-dimensional horizontally homogeneous experiments

The three-dimensional experiments presented in this dissertation were designed to compliment the detailed observations of the severe, CCOPE bow echo squall line. This was one of two meso$\beta$-scale convective systems that passed through the data network which showed the importance of the meso$\beta$-scale surface pressure fields on the development of the severe surface winds. Bow echoes are well known MCS radar signatures indicating the potential development of sustained, severe surface winds (Fujita 1978) and are thought to be present in a number of derecho cases (Pryzblinski and DeCaire 1985). One objective, therefore, was to compare detailed Doppler radar and surface analyses of the observed CCOPE bow echo with the model generated system in an attempt to shed further insight on their dynamics and flow structure.

One of the primary features of the observed bow echo squall line was the highly three-dimensional character of the storm relative flow and the along-line asymmetry in the surface pressure and flow fields (Fig 4.34). This was primarily a result of a supercell which was present within the line and the system-scale wrap around flow within the middle-levels of the line. Results from the horizontally homogeneous, three-dimensional experiments suggest that these asymmetries may have resulted from the structure of the environmental hodograph. Experiments run with a unidirectional shear profile, though successfully producing a severe bow echo squall line, failed to generate the observed near-surface along-line asymmetry.

An experiment with the observed clockwise turning hodograph, however, successfully replicated many features of the observed bow echo. The primary similarities between the observed case and the curved hodograph experiment include the dominant meso$\beta$-scale high/low couplet in the trailing stratiform region, the location of the northerly surface wind maximum within the vertex region of the bow echo and on the eastern flank of the mesolow, the presence of a strong convective-scale downdraft on the northern flank of the dominant cell within the line, and the downward transport of the middle-level momentum and low-valued $\theta_e$ air. In the middle-levels there was a pronounced wrap around flow with an enhanced region of rear-to-front flow between two counter rotating vortices located on either flank of the simulated bow echo, while the upper level outflow aided the northwest development of the cirrus cloud shield.

It was suggested that the highly three-dimensional circulations which were established in the bow echo may have contributed to the longevity and severity of the surface wind maximum in the following manner. First of all, the northward bias in the surface high pressure and the development of a north-south pressure gradient were likely a result of diabatic cooling associated the northwest spreading cirrus cloud shield and residual convective debris from the decaying left moving supercell that resulted from the split in the initial updraft. The north-south pressure gradient was intensified near the vertex region of the bow echo beneath a strong convective-scale downdraft which formed on the northern flank of the supercell. The pressure gradient may have been further intensified by subsidence associated with the rear-to-front jet. In this case the jet was located in the vertex region of the bow

echo between counter rotating middle-level vortices which formed on either end of the line. Thus, there was a tendency of the convective and mesoscale circulations to intensify the surface pressure and flow fields within the vertex region of the bow echo. This may explain the observed tendencies of these systems to produce the strongest winds within and slightly north of the vertex region of the bow echo (Fig 3.1 and Johns and Hirt 1987). Further, since the simulations have shown that these features are long-lived (also see the results of Weisman 1990) they may have provided an effective means to sustain derecho-like winds.

One final aspect of the bow echo circulation which may have affected the strength of the surface outflow was the up/down downdraft circulation. The observations have shown that the parcels nearest the supercell experienced the greatest amount of lift and would thus generate the potential for the strongest downdrafts once they moved out of the upward directed vertical pressure gradient force and into the region of increased water loading, melting, and evaporational cooling within the heavy precipitation core on the northern flank of the supercell. In the CCOPE case, the strongest downdraft was on the northern flank of a right moving supercell, a location which may have enhanced the surface winds within the vertex region of the bow echo generated by the meso$\beta$-scale surface pressure fields. Environments which support this type of supercell development (*i.e.* high values of CAPE and strong vertical wind shear with clockwise curvature in the hodograph) may also be conducive to derecho type development. It is our opinion that the midlevel pressure reduction, resulting from the rotational component of the flow near the updraft, would be particularly effective in aiding the upward displacement of the lower stable layer in the type of derecho environments presented in this dissertation.

## 7.4 Conceptual Derecho Model

The primary two-dimensional aspects of the MCS flow characteristics and their relationship to the idealized environmental thermodynamic and vertical wind shear profiles of the observed derecho environments are illustrated schematically in Fig 7.1. The derecho environment in each case was characterized by strong vertical wind shear through the depth of the troposphere and a distinct three-layer thermodynamic structure consisting of a surface-based stable layer, a deep elevated well-mixed layer, and an upper tropospheric layer of

intermediate stability. The stable layer resulted from pre-existing static stability associated with a synoptic-scale frontal boundary, but was reinforced by strong warm air advection near the top of the stable layer and either low-level nocturnal and/or diabatic cooling associated with the evaporation of precipitation. The elevated well-mixed layer resulted from differential temperature advection in the 70 to 50 kPa layer or from the eastward advection of the ABL that formed over the heated elevated terrain of the Rocky Mountains. Each case also had a southerly low-level jet which provided an ample moisture supply near the top of the surface-based stable layer.

The primary storm-relative circulations of the two dimensional simulations resemble the previous schematics of midlatitude squall lines depicted in (Newton 1950 and Thorpe et al. 1982). One primary difference is that the storm had an elevated inflow source of moist air from near the top of the surface based stable layer which was lifted to the level of free convection (LFC) by a high amplitude gravity wave that developed in the surface-based stable layer. This fast moving, long-lived feature accounted for the rapid movement of the system and helped sustain the convective-scale updraft by providing a continual source of low-level lift.

The wave-induced pressure fields also accounted for the severe surface wind production. The winds were produced by the hydrostatically induced high pressure region (labeled H) associated with the upward lifting of the isentropic surfaces within the surface-based stable layer and diabatic cooling and precipitation loading affects. The maximum uplift of the lower isentropic surfaces occurred beneath the middle-level low (labeled $L_{NH}$) centered near the LFC. The simulations suggested that this low had a significant nonhydrostatic component induced by rapid acceleration of the parcels within the well-mixed layer above the LFC. The presence of the elevated well-mixed layer immediately above the lower stable layer may thus aid the storms ability to lift the lower stable layer.

The flow within the upper levels was dominated by a strong, hydrostatically-induced high pressure region centered near the tropopause. The development of this feature near the convective line appeared to result from the cooling associated with the overshooting tops and the mass divergence from the convective-scale updraft. The development of this feature beyond the trailing stratiform region appeared to result from the cooling associated with the

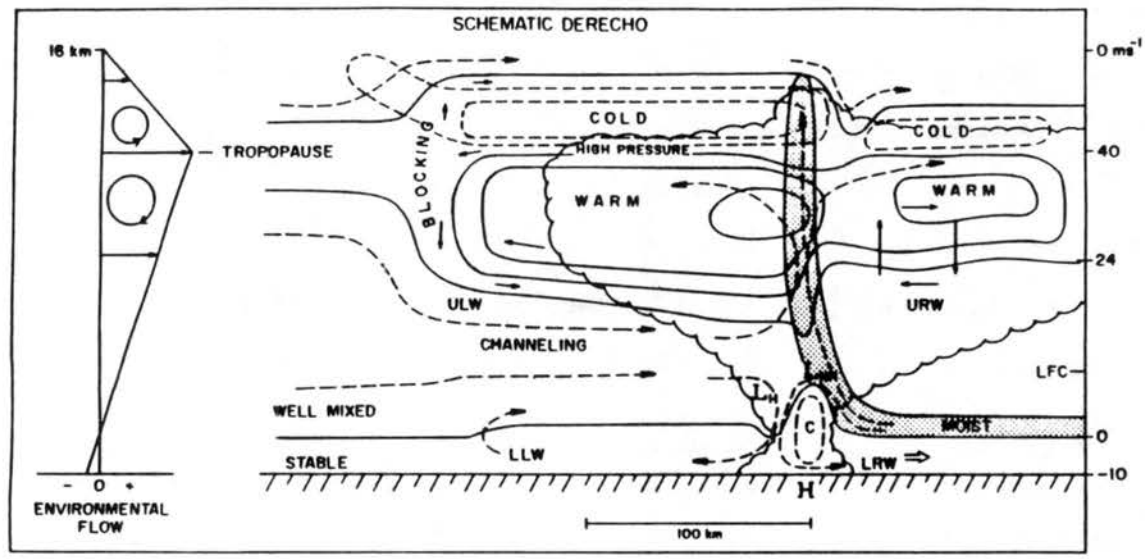


Figure 7.1: Conceptual diagram illustrating the primary two-dimensional features of the simulated MCS structure based on the three-layered thermodynamic and strong vertical wind shear profiles (denoted on the left of the diagram) of the observed derecho case studies. The bold solid lines denote representative isentropic surfaces. The dashed lines terminating with an arrow are meant to suggest representative storm relative streamlines. The light solid and dashed lines denote regions of warming and cooling, respectively. The double arrow gives the storm motion, the thin arrows represent perturbation flow resulting from the primary gravity waves labeled LRW, URW, ULW, and LLW. The numbers along the right boundary of the figure refer to the ambient horizontal flow in m $s^{-1}$ at a given level used to initialize the high shear experiments. The scalloped line denotes the cloud boundary. The labels $L_{NH}$ and $L_H$ denote contributions to the middle-level low pressure region from nonhydrostatic and hydrostatic affects, respectively. The bold H refers to the surface high pressure region and denotes the location of the severe surface wind maximum.

rapid upshear propagation of the gravity waves within the stratosphere. The gravity wave induced portion of the upper-level mesohigh was responsible for the initial blocking of the upper level flow and subsidence-induced channeling of the middle-level flow which aided the development of the rear-to-front jet. Since the gravity wave induced blocking occurred well beyond the trailing cirrus cloud shield, it in essence provided a favorable environment for the continued sustenance of the convective-scale updraft and for the upshear development of the line as a whole.

The simulations showed that a strong, rear-to-front middle level jet formed above the lower stable layer and beneath the downward displaced isentropic surfaces within the upper troposphere. It is hypothesized that the amount of channeling increases with decreasing middle-to-upper tropospheric static stability, stronger upper tropospheric vertical wind shear, and either the presence of a pre-existing, surface-based stable layer or a storm induced cold pool on the upshear flank of the line. This follows, in part, from the greater vertical displacement of the upper tropospheric isentropic surfaces required to hydrostatically balance a given high pressure zone located near the tropopause in environments having weaker static stability aloft (i.e. an elevated well-mixed layer). It also reflects mass continuity constraints and possible shear interactions with the buoyancy fields.

The primary three dimensional aspects of the observed and simulated severe bow echo squall line is illustrated Figs 7.2 and 7.3. The severe winds in this storm were located along the leading gust front and in the trailing stratiform precipitation region near the wake low located in the vertex region of the bow echo. An analyses of the Doppler radar and three-dimensional simulations suggest that the intense north/south horizontal surface pressure gradient in the vicinity of the wake low resulted from a combination of convective-scale and mesoscale flow patterns within the storm. The primary mesoscale flow features include the northwest outflow emanating from the supercell, the middle-level wrap around which led to a concentrated middle-level rear-to-front flow into the vertex of the bow echo, and the cyclonic flow about the supercell within the lower portion of the storm.

The primary convective-scale component was the dominant low-level downdraft on the northern flank of the supercell. Parcels entered this downdraft from the rear flank of the line within the middle-level jet and in an "up-down" downdraft circulation from ahead of

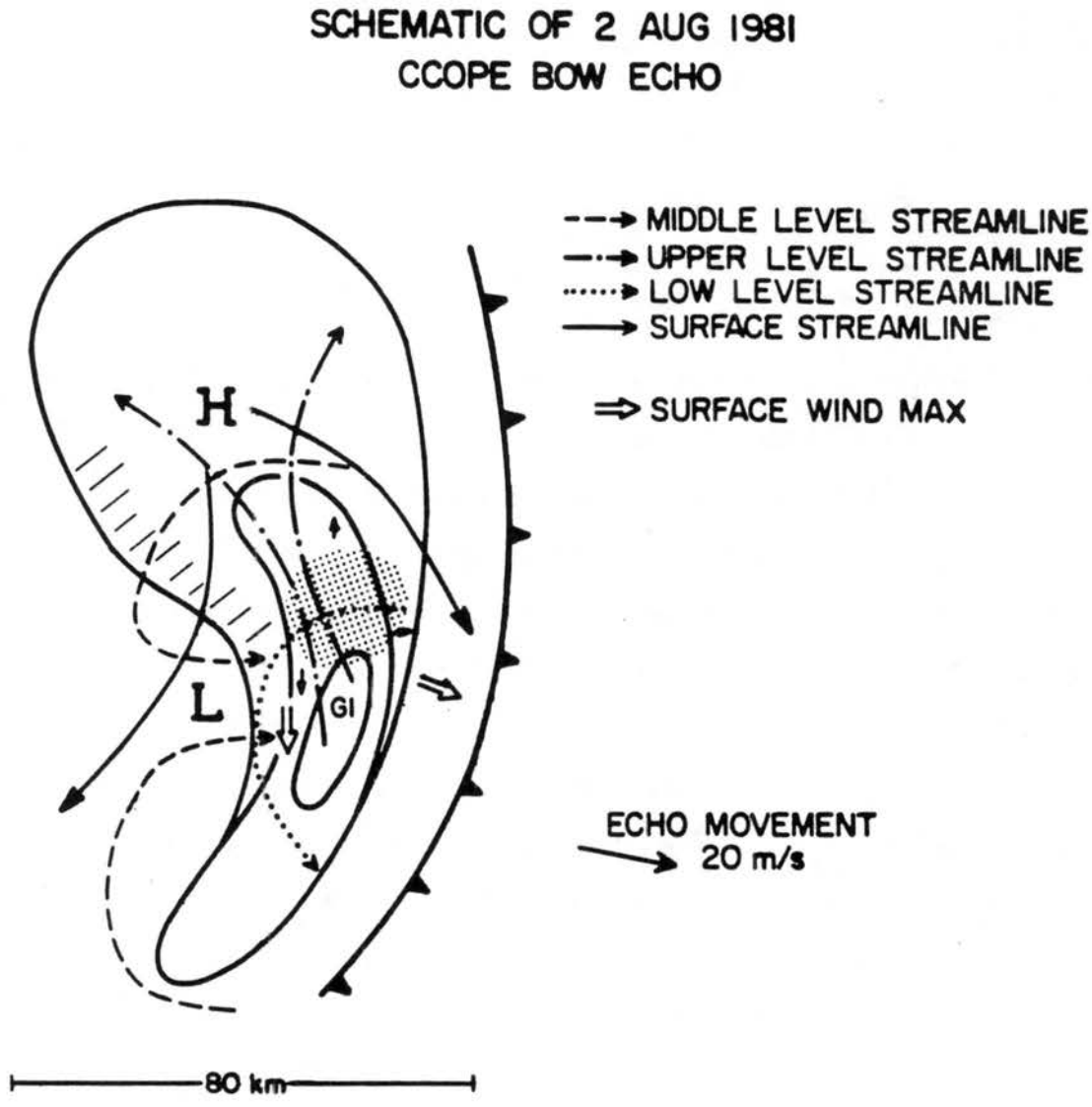


Figure 7.2: Schematic flow structure of the 2 August 1981 CCOPE bow echo squall line. The bold H and L denote regions of meso$\beta$-scale surface pressure perturbations. The double arrow represents the location and direction of the surface wind maxima. The cold frontal symbol denotes the leading edge of the storm induced outflow. The solid lines denote the convective and stratiform precipitation shield of the storm. The hatching denotes the region of strong flow that was observed well behind the bow echo. The symbol G1 denotes the location of the supercell.

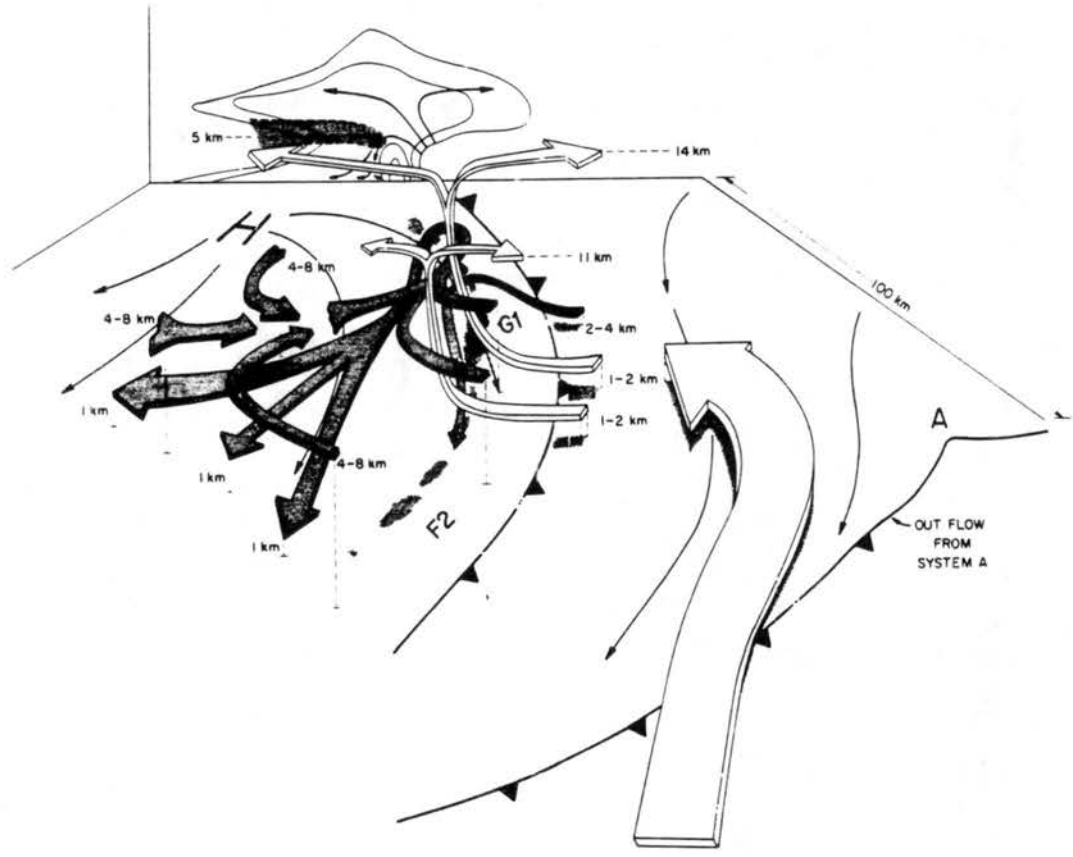


Figure 7.3: Schematic depiction summarizing the 2-D and 3-D flow features discussed in the text for the 2 August, 1981 CCOPE squall line showing mesoscale outflow boundaries, surface streamlines (thin arrows) convective reflectivity structure (stippled), overriding flow (bold arrow), and storm relative flow (thin ribbons). The vertical cross-section corresponds to a representative depiction of the storm core G1 and shows reflectivity (thin solid lines), schematic storm relative flow (thin arrows) and location of the middle-level upshear inflow (shaded). The Bold A refers to the supercell system discussed in the text, G1 and F2 represent the cell groups along the squall line and the bold H represents the location of the surface meso-high. Labeling of the storm relative flow ribbons refers to height AGL.

the line. The vertical displacement of the "up-down" downdraft trajectories were greatest near the supercell. This suggests that dynamically-induced low pressure on the northern flank of this cell also contributed to the storms ability to draw up the lower stable layer and, consequently, to the severe surface wind production of the bow echo. Detailed analyses of the "up-down" downdraft within supercell type storms that form in environments characterized by a deep surface-based stable layer may provide useful insight into the dynamics of derecho-type systems.

## Chapter 8

# SUGGESTIONS FOR FURTHER RESEARCH

Although this dissertation has attempted to cover as extensively as possible the broad range of time and spatial scales which come into play with derechos, the discussion was limited to a particular type of thermodynamic profile. Clearly, much more could be done to expand the parameter space in which derechos occur in nature and below we offer a few suggestions toward this end which may serve as a guide.

• The numerical simulations revealed a strong sensitivity to the strength and depth of the vertical wind shear profile within the troposphere and lower stratosphere. The vertical wind shear appeared to have a particular impact on the gravity waves generated by the convective system. Additional work is necessary to further clarify the role of wave/mean wind shear interactions on producing upper-level blocking and middle-level channeling. For instance, one could determine the vertical shear and thermodynamic profiles which enhance wave/mean flow interactions, the transmission/reflection of gravity wave energy near the tropopause and its subsequent impact on the upper-level mesohigh and outflow characteristics of the storm. One could also determine the impact of varying the depth of the various thermodynamic layers used in the simplified soundings on the resulting storm and gravity wave structure. We strongly believe that more attention should be paid to the vertical structure of the atmosphere within the upper troposphere and lower stratosphere for derecho systems. As discussed by Weisman and Klemp (1984), vertical wind shear and buoyancy calculations are important in determining storm type, but so too are the way in which these parameters are arranged in the vertical.

• More detailed studies on the dynamics of the convectively-generated gravity waves, such as the factors affecting their horizontal scale, energy transports, and relationship to convective-scale regeneration of the updraft and mesoscale flow both within and beyond the observable

cirrus cloud shield are required. This study has only identified a few of the possible roles of gravity waves on the overall structure, propagation, and longevity of mesoscale convective systems. It would be useful to compare the results of the numerical simulations to the results obtained from linear analytical solutions with a specified heat source and linear vertical wind shear. With an analytical model one could determine the growth rates and phase speeds of the dominant wave modes for the simplified thermodynamic and vertical wind shear profiles. Since the thermodynamic structure used in this study strongly resembles the profiles conducive to severe downslope wind storms (cf. Klemp and Lilly 1975), one could address whether the constructive wave interference leading to the severe downslope windstorms also enhances the surface wind strength in derecho-type environments.

- Studies are required to determine if some derecho events, particularly those which occur to the north of synoptic-scale frontal boundaries and in the exit region of upper level jets, are a form of high amplitude inertia-gravity waves. Such a linkage is suggested by the nearly identical environmental conditions which favor both derechos and inertia-gravity waves.
- The model simulations suggest that a hydraulic jump may be occurring near the tropopause in the strong vertical wind shear experiments. This is suggested by the rapid downward displacement of the isentropic surfaces near the position of the ULW. Additional work could be carried out to determine if this is the case. If this is occurring, it seems possible that the magnitude of the jump could be predicted with a knowledge of the thermodynamic and vertical wind shear profiles of the ambient environment. Such knowledge could lead to a prediction of the expected rear-to-front jet strength for a given environment. In any case, one could inspect current cases to determine if weak or strong jets stratify along certain environmental conditions.
- It was evident in the model simulations that the phase lines of the gravity waves within the stratosphere and on the upshear flank of the line became increasingly inclined from the vertical as time progressed. As a result the perturbation flow (initially upward and outward from the storm) developed a significant horizontal component which directly contributed to the front-to-rear flow component over a relatively deep layer within the lower stratosphere. It thus appears that the upper level outflow structure is considerably more complex than what one might expect from simple mass detrainment from the overshooting

convective towers. It would be of interest to determine what produces this affect (possibly the differential horizontal advection of the phase lines by the basic state sheared flow) and how it impacts the structure of the upper level outflow.

• We suggest that future field programs obtain more detailed observations of the upper tropospheric and lower stratospheric thermodynamic and vertical wind shear profiles in and around MCSs. The simulations presented here suggest that storm-induced modifications in the clear air surrounding a MCS may have an important consequence on the flow fields observed within the MCS. Experiments should be designed to determine the temporal and spatial distributions of these modifications and their impact on the system evolution, propagation, and longevity.

• It was noted that the "up-down" downdraft component may have played an important role in both the strength and location of the severe surface winds for the CCOPE bow echo squall line case. It was suggested that the middle-level pressure reduction associated with the rotation of the primary updraft ( a supercell) within the squall line, may have been instrumental in a further lifting of the parcels within the surface-based stable layer. Since this would ultimately affect the strength of the surface outflow, there is a further need to analyse the dynamics of this circulation branch in supercell-type systems, particularly when the supercell forms in an environment characterized by a deep, pre-existing, surface-based stable layer.

• Finally, the need to sample additional derecho systems in detail, to better characterize their environmental structure and the structure of the convective systems, cannot be overemphasized. The CCOPE case provided data on the storms during the intial stages of the derecho event, but detailed information of the storm structure during the later stages of a derecho event have yet to be documented. The PRE-STORM case provided data on the regional-scale throughout the lifecycle of the event yet no information was available on the convective structure of this derecho because it formed on the outer fringe of the network. It is hoped that future field programs, such as STORM, will provide an opportunity to sample a number of mature derechos.

## REFERENCES


Abdullah, A.J., 1954: The meridional growth of squall lines. *J. Meteor.*, **11**, 301-308.

Baliji, V., and T.L. Clark, 1988: Scale selection in locally forced convective fields and the initiation of deep cumulus. *J. Atmos. Sci.*, **45**, 3188-3211.

Barnes, S.L., 1973: Mesoscale objective map analysis using weighted time series observations. NOAA Tech. Memo. ERL NSSL-62, 60 pp. [NTIS COM-73-10781].

Barnes, S.L., and C.W. Newton, 1985: Thunderstorms in the Synoptic Setting. Chapter 5, *Thunderstorm Morphology and Dynamics*, Second edition, edited by E. Kessler, pp. 75-112.

Benjamin, S.G., and T.B. Carlson, 1986: Some effects of surface heating and topography on the regional severe storm environment. Part I: Three-dimensional simulations. *Mon. Wea. Rev.*, **114**, 307-329.

Blackadar, A.K., 1957: Boundary layer wind maxima and their significance for the growth of nocturnal inversions. *Bull. Am. Met. Soc.*, **38**, 283-290.

Bolton, D., 1984: Generation and propagation of African squall lines. *Quart. J. R. Met. Soc.*, **110**, 695-721.

Bonner, W.D., 1963: Thunderstorms and the low-level jet. Mesometeorology Research Paper No. 22, University of Chicago, 5734 S. Ellis Ave., Chicago, IL 60637, 23 pp., [NTIS No. AD-602 540].

Bonner, W.D. and J. Paegle, 1970: Diurnal variations in boundary layer winds over the south-central United States in summer. *Mon. Wea. Rev.*, **98**, 735-744.

Booker, J.R., and F.P. Bretherton, 1967: The critical layer for internal gravity waves in a shear flow. *J. Fluid Mech.*, **27**, 513-539.

Bosart, L.F., and A. Seimon, 1988: A case study of an unusually intense atmospheric gravity wave. *Mon. Wea. Rev.*, **116**, 1857-1886.

Brunk, I.W., 1949: The pressure pulsation of April 11, 1944. *J. Meteor.*, **6**, 395-401.

Byers, H.R., and R.R. Braham, 1949: The thunderstorm. U.S. Dept. of Commerce, Washington, 287 pp.

Carlson, T.N., 1980: Airflow through midlatitude cyclones and the comma cloud pattern. *Mon. Wea. Rev.*, **108**, 1498-1509.

Carr, F.H., and J.P. Millard, 1985: A composite of comma clouds and their association with severe weather over the Great Plains. *Mon. Wea. Rev.*, **113**, 370-387.

Charba, J., 1974: Application of gravity current model to analysis of squall line gust front. *Mon. Wea. Rev.*, **102**, 140-156.

Cotton, W.R. 1990: Storms. ASTeR Press, P.O. Box 466, Ft Collins CO 80522.

Cotton, W.R., and R.A. Anthes, 1989: Storm and cloud dynamics. Academic Press Inc., San Diego, CA.

Cotton, W.R., R. McAnelly, J. Schmidt, and M.-S. Lin, 1984: A multi-scale observation investigation of the formation mechanisms of a mesoscale convective complex. 9th Int. Cloud Physics Conference, Tallinn, USSR, 21-28 August 1984.

Cotton, W.R., and G.J. Tripoli, 1978: Cumulus convection in shear flow-Three-Dimensional numerical experiments. *J. Atmos. Sci.*, **35**, 1503-1521.

Crook, N.A., 1988: Trapping of Low-level internal gravity waves. *J. Atmos. Sci.*, **45**, 1533-1541.

Crook, N.A., and M.W. Moncrieff, 1988: The effect of large-scale convergence on the generation and maintenance of deep moist convection. *J. Atmos. Sci.*, **45**, 3606-3624.

Cunning, J.B., 1986: The Oklahoma-Kansas Preliminary Regional Experiment for STORM Central. *Bull. Amer. Met. Soc.*, **67**, 1478-1486.

Droegemeier K.K., and R.B. Wilhelmson, 1987: Numerical simulation of thunderstorm outflow dynamics. Part I: Outflow sensitivity experiments and turbulence dynamics. *J. Atmos. Sci.*, **44**, 1180-1210.

Eliassen, A., and E. Palm, 1961: On the transfer of energy in stationary mountain waves. *Geofys. Publ.*, **22**, 1-23.

Emanuel, K.A., 1982: Inertial instability and mesoscale convective systems. Part II: Symmetric CISK in a baroclinic flow. *J. Atmos. Sci.*, **39**, 1080-1097.

Eom, J., 1975: Analysis of the internal gravity wave occurrence of April 19, 1970 in the Midwest. *Mon. Wea. Rev.*, **103**, 217-226.

Farrell, R.J., and T.N. Carlson, 1989: Evidence for the role of the lid and underrunning in an outbreak of tornadic thunderstorms. *Mon. Wea. Rev.*, **117**, 857-871.

Fawbush, E.J., and R.C. Miller, 1954: The types of air masses in which North American tornadoes form. *Bull. Amer. Meteor. Soc.*, **35**, 154-165.

Fortune, M.A., 1989: the evolution of vortical patterns and vortices in mesoscale convective complexes. Ph.D Thesis, Colorado State University, Dept. of Atmospheric Science, Fort Collins, CO 80523.

Freeman, J.C., 1948: An analogy between the equatorial easterlies and supersonic gas flows. *J. Meteor.*, **5**, 138-146.

Fujita, T.T., 1955: Results of detailed synoptic studies of squall lines. *Tellus*, **7**, 405-436.

Fujita, T.T., 1963: Analytical mesometeorology. A review. *Meteor. Monogr.*, **5**, 77-125.

Fujita, T.T., 1978: Manual of downburst identification for project NIMROD. Satellite and Mesometeorology Research Paper No. 156, Dept. of Geophysical Sciences, Univ. of Chicago, 104 pp. [NTIS No. N78-30771/7GI].

Fujita, T. and H. Byers, 1977: Spearhead echo and downdraft in the crash of an airliner. *Mon. Wea. Rev.,* **105,** 129-146.

Fujita, T. and R.M. Wakimoto, 1981: Five scales of airflow associated with a series of downbursts on 16 July 1980. *Mon. Wea. Rev.,* **109,** 1438-1456.

Fulton, R., D.S. Zrnić, and R.J. Doviak, 1990: Initiation of a solitary wave family in the demise of a nocturnal thunderstorm density current. *J. Atmos. Sci.,* **47,** 319-337.

Hamilton, R.A, and J.W. Archbold, 1945: Meteorology of Nigeria and adjacent territory. *Quart. J. Roy. Meteor. Soc.,* **71,** 231-264.

Hinrichs, G., 1888: Tornadoes and derechos. *Amer. Meteor. J.,* **5,** 306-317, 341-349.

Hoskins, B.J., E.C. Neto, and H.R. Cho, 1984: The formation of multiple fronts. *Quart. J. Roy. Meteor. Soc.,* **110,** 881-896.

Humphreys, W.J., 1914: The thunderstorm and its phenomena. *Mon. Wea. Rev.,* **42,** 348-380.

Johns, R.H., and W.D. Hirt, 1985: The derecho of 19-20 July 1983... A case study. *National Science Digest,* **10,** 17-32.

Johns, R.H., and W.D. Hirt, 1987: Derechos: Widespread convectively induced windstorms. *Weather and Forecasting,* **2,** 32-49.

Johns, R.H., K.W. Howard, and R.A. Maddox, 1990: Conditions associated with long-lived derechos–An examination of the larger-scale environment. Preprints, 16th Conf. on Severe Local Storms, 22-26 October 1990, Kananskis Prov. Park, Canada, AMS.

Johnson, R.H. and P.J. Hamilton, 1988: The relationship of surface pressure features to the precipitation and air flow structure of an intense midlatitude squall line. *Mon. Wea. Rev.,* **116,** 1444-1472.

Kamburova, P.L., and F.H. Ludlam, 1966: Rainfall evaporation in thunderstorm downdrafts. *Quart. J. Roy. Meteor. Soc.,* **92,** 510-518.

Klemp, J.B. and D.K. Lilly, 1975: The dynamics of wave-induced downslope winds. *J. Atmos. Sci.,* **32,** 320-339.

Klemp, J.B. and R.B. Wilhelmson, 1978a: The simulation of three-dimensional convective storm dynamics. *J. Atmos. Sci.,* **35,** 1070-1096.

Klemp, J.B. and R.B. Wilhelmson, 1978b: Simulations of right- and left-moving storms produced through storm splitting. *J. Atmos. Sci.,* **35,** 1097-1110.

Knight, C.A., 1982: The Cooperative Convective Precipitation Experiment (CCOPE), 18 May - 78 August 1981. *Bull. Amer. Meteor. Soc.,* **63,** 386-398.

Knupp, K.R., 1988: Downdrafts within High Plains cumulonimbi. Part II: Dynamics and Thermodynamics. *J. Atmos. Sci.,* **45,** 3965-3982.

Knupp, K.R., and W.R. Cotton, 1985: Convective cloud downdraft structure: An interpretive study. *Rev. Geophys. and Space Physics,* **23,** 183-215.

Knupp, K.R., and D.P. Jorgensen, 1985: Case study analyses of a large-scale and long-lived downburst producing storm. Preprints, *14th Conf. on Severe Local Storms,* Indianapolis, Amer. Meteor. Soc.,

Koch, S.E., R.E. Golus, and B. Dorian, 1988: A mesoscale gravity wave event observed during CCOPE. Part II: Interaction between mesoscale convective systems and the antecedent waves. *Mon. Wea. Rev.,* **116,** 2545-2569.

Koch, S.E., and J. McCarthy, 1982: The evolution of an Oklahoma dryline. Part II: Boundary-layer forcing of mesoconvective systems. *J. Atmos. Sci.,* **39,** 237-257.

Kuo, H.L., 1974: Further studies of the parameterization of the influence of cumulus convection on large-scale flow. *J. Atmos. Sci.,* **31,** 1232-1240.

Lafore, J. and M.W. Moncrieff, 1989: A numerical investigation of the organization and interaction of the convective and stratiform regions of tropical squall lines. *J. Atmos. Sci.,* **46,** 521-544.

LeMone, M.A., G.M. Barnes, and E.J. Zipser, 1984: Momentum flux by lines of cumulonimbus over the tropical oceans. *J. Atmos. Sci.,* **41,** 1914-1932.

Ley, B.E., and W.R. Peltier, 1978: Wave generation and frontal collapse. *J. Atmos. Sci.,* **35,** 3-17.

Lin , Y.L., and S. Li, 1988: Three-Dimensional response of shear flow to elevated heating. *J. Atmos. Sci.,* **45,** 2987-3002.

Lin , Y.L., and R.B. Smith, 1986: Transient dynamics of airflow near a local heat source. *J. Atmos. Sci.,* **43,** 40-49.

Lindzen, R.S., 1974: Wave-CISK in the tropics. *J. Atmos. Sci.,* **31,** 156-179.

Lindzen, R.S., and K.K. Tung, 1976: Banded convective activity and ducted gravity waves. *Mon. Wea. Rev.,* **104,** 1602-1617.

Mahrer, Y., and R.A. Pielke, 1977: A numerical study of the airflow over irregular terrain. *beitrage zur Physik der Atmosphare,* **50,** 98-113.

Marwitz, J.D., 1973: Trajectories within the weak echo regions of hailstorms. *J. Appl. Meteor.,* **12,** 1174-1182.

McNider, R.T., and R.A. Pielke, 1981: Diurnal boundary-layer development over sloping terrain. *J. Atmos. Sci.,* **38,** 2198-2212.

Means, L.L., 1954: A study of the mean southerly wind-maximum in low-levels associated with a period of summer precipitation in the middle west. *Bull. Amer. Meteor. Soc.,* **35,** 166-170.

Miller, D.A., and F. Sanders, 1980: Mesoscale conditions for the severe conditions of 3 April 1974 in the east-central United States. *J. Atmos. Sci.,* **37,** 1041-1055.

Miller, L.J., J.D. Tuttle, and C.A. Knight, 1988: Airflow and hail growth in a severe northern High Plains supercell. *J. Atmos. Sci.,* **45,** 736-762.

Nehrkorn, T., 1986: Wave-CISK in a baroclinic basic state. *J. Atmos. Sci.,* **43,** 2773-2791.

Newton, C.W., 1950: Structure and mechanism of the prefrontal squall line. *J. Meteor.,* **8,** 210-222.

Newton, C.W., 1956: Mechanisms of circulation change during lee cyclogenesis. *J. Meteor.,* **13,** 528-539.

Newton, C.W., 1966: Circulations in large sheared cumulonimbus. *Tellus,* **18,** 699-713.

Nicholls, M.E., 1987: A comparison of the results of a two-dimensional numerical simulation of a tropical squall line with observations. *Mon. Wea. Rev.* **115,** 3055-3077.

Nicholls, M.E., R.A. Pielke, and W.R. Cotton 1990: Thermally forced gravity waves in an atmosphere at rest. Submitted to J. Atmos. Sci.

Orlanski, I., and B.B. Ross, 1986: Low-level updrafts in stable layers forced by convection. *J. Atmos. Sci.,* **43,** 997-1005.

Pielke, R.A., 1974: A three-dimensional numerical model of the sea breezes over south Florida. *Mon. Wea. Rev.,* **102,** 115-139.

Proctor, F.H., 1989: Numerical simulations of an isolated microburst. Part II: Sensitivity experiments. *J. Atmos. Sci.,* **46,** 2143-2165.

Przybylinski, R.W., and D.M. DeCaire, 1985: Radar signatures associated with the derecho, a type of mesoscale convective system. Preprints, 14th Conf. on Severe Local Storms, Indianapolis, Amer. Meteor. Soc., 228-231.

Raymond, D.J., 1984: A wave-cisk model of squall lines. *J. Atmos. Sci.,* **41,** 1946-1958.

Raymond, D.J., 1986: Prescribed heating of a stratified atmosphere as a model for moist convection. *J. Atmos. Sci.,* **43,** 1101-1111.

Rotunno, R., and J.B. Klemp, 1982: The influence of the shear-induced pressure gradient on thunderstorm motion. *Mon. Wea. Rev.,* **110,** 136-151.

Rotunno, R., J.B. Klemp, and M.L. Weisman, 1988: A theory for strong, long-lived squall lines. *J. Atmos. Sci.,* **45,** 463-485.

Schmidt, J.M., and W.R. Cotton, 1989: A High Plains squall line associated with severe surface winds. *J. Atmos. Sci.,* **46,** 281-302.

Schmidt, J.M. and W.R. Cotton, 1990: Interactions between upper and lower tropospheric gravity waves on squall line structure and maintenance. *J. Atmos. Sci.,* **47,** 1205-1222.

Shapiro, M.A., 1982: Mesoscale weather systems of the Central United States. Cooperative Institute for Research in Environmental Sciences, National Oceanic and Atmospheric Administration, University of Colorado, Boulder, Colorado, 78 pp.

Smull, B.F., and R.A. Houze, 1987: Dual-Doppler radar analysis of a mid-latitude squall line with a trailing region of stratiform rain. *J. Atmos. Sci.*, **44**, 2128-2148.

Srivastava, R.C., 1987: A model of intense downdrafts driven by the melting and evaporation of precipitation. *J. Atmos. Sci.*, **44**, 1752-1773.

Stobie, J.G., F. Einaudi, and L.W. Uccellini, 1983: A case study of gravity waves-convective storms interaction: 9 May 1979. *J. Atmos. Sci.*, **40**, 2804-2830.

Tepper, M., 1950: A proposed mechanism of squall lines: the pressure jump line. *J. Meteor.*, **7**, 21-29.

Thorpe, A.J., M.J. Miller, and M.W. Moncrieff, 1982: Two-dimensional convection in non-constant shear: A model of mid-latitude squall lines. *Quart. J. Roy. Meteor. Soc.*, **108**, 739-762.

Tremback, C. J., 1990: Numerical simulation of a mesoscale convective complex: model development and numerical results. Ph.D. dissertation, Atmos. Sci. Paper No. 465, Colorado State University, Dept. of Atmospheric Science, Fort Collins, CO 80523.

Tripoli, G.J., and W.R. Cotton, 1982: The Colorado State University three-dimensional cloud/mesoscale model - 1982. Part I: General theoretical framework and sensitivity experiments. *J. Rech. Atmos.*, **16**, 185-219.

Tripoli, G.J., and W.R. Cotton, 1986: An intense, quasi-steady thunderstorm over mountainous terrain. Part IV: Three-Dimensional numerical simulations. *J. Atmos. Sci.*, **43**, 894-912.

Tripoli, G.J., and W.R. Cotton, 1989a: A numerical study of an observed orogenic mesoscale convective system. Part 1. Simulated genesis and comparison with observations. *Mon. Wea. Rev.*, **117**, 273-304.

Tripoli, G.J., and W.R. Cotton, 1989b: A numerical study of an observed orogenic mesoscale convective system. Part 2. Analysis of governing dynamics. *Mon. Wea. Rev.*, **117**, 305-328.

Uccellini, L.W., 1975: A case study of apparent gravity wave initiation of severe convective storms. *Mon. Wea. Rev.*, **103**, 497-513.

Uccellini, L.W., 1980: On the role of upper tropospheric jet streaks on lee-side cyclogenesis in the development of low-level jets in the Great Plains. *Mon. Wea. Rev.*, **108**, 1689-1969.

Uccellini, L.W., and Koch S.E., 1987: The synoptic setting and possible energy sources for mesoscale wave disturbances. *Mon. Wea. Rev.*, **115**, 721-729.

Van Tuyl, A.H., and J.A. Young, 1982: Numerical simulation of nonlinear jet streak adjustment. *Mon. Wea. Rev.*, **110**, 2038-2054.

Verlinde, J., and W.R. Cotton, 1990: A mesoscale couplet observed in the trailing anvil of a multicellular convective complex. *Mon. Wea. Rev.*, **118**, 993-1010.

Vescio, M.D., 1990: The wind's response to transient mesoscale pressure fields associated with squall lines. Cooperative M.S., Cooperative Institute for Research in the Atmosphere and Colorado State University, 86 pp.

Wade, C.G., 1982: A preliminary study of an intense thunderstorm which moved across the CCOPE research network in Southeastern Montana. Preprints, 9th Conf. on Wea. Forecasting and Analysis, Seattle, Washington, 28 June - 1 July 1982, 388-395.

Wakimoto, R.M., 1982: The life cycle of thunderstorm gust fronts as viewed with Doppler radar and rawinsonde data. *Mon. Wea. Rev.*, **110**, 1050-1082.

Weisman, M.L., 1990: The genesis of bow echoes: A rear-inflow induced meso-convective structure. Cooperative thesis No. 125, The Pennsylvania State University and the National Center for Atmospheric Research, Boulder, CO, 150 pp.

Weisman, M.L., and J.B. Klemp, 1984: The structure and classification of numerically simulated convective storms in directionally varying wind shears. *Mon. Wea. Rev.*, **112**, 2479-2498.

Weisman, M.L., J.B. Klemp, and L.J. Miller, 1983: Modeling and Doppler analysis of the CCOPE August 2 supercell storm. Preprints, 13th Conf. on Severe Local Storms, Amer. Meteor. Soc., 223-226.

Williams, D.T., 1953: Pressure wave observations in the central midwest, 1952. *Mon. Wea. Rev.*, **81**, 278-298.

Xu, Q., and J.H.E. Clark , 1984: Wave-CISK and mesoscale convective systems. *J. Atmos. Sci.*, **41**, 2089-2107.

Zhang D., and J.M. Fritsch, 1988: Numerical simulation of the meso-*beta* scale structure and evolution of the 1977 Johnstown flood. Part III: Internal gravity waves and the squall line. *J. Atmos. Sci.*, **45**, 1252-1268.

Zipser, E.J., 1977: Mesoscale and convective-scale downdrafts as distinct components of squall-line structure. *Mon. Wea. Rev.*, **105**, 1568-1589.